THÈSE EN COTUTELLE PRÉSENTÉE

POUR OBTENIR LE GRADE DE

DOCTEUR DE

L'UNIVERSITÉ DE BORDEAUX
ET DE L'UNIVERSITÉ DE PAÍS VASCO

ÉCOLE DOCTORALE DES SCIENCES CHIMIQUES

PROGRAMA DE DOCTORADO FÍSICA DE NANOESTRUCTURAS Y MATERIALES AVANZADOS

SPÉCIALITÉ : Chimie des Matériaux

Par **Valentina MUSUMECI**

A supercritical water-based technology for calcium silicate hydrate nanoparticles production

Sous la direction de : Cyril AYMONIER & Jorge SÁNCHEZ DOLADO

Soutenance prévue le 31 Mars 2021 sous réserve d'acception par les rapporteurs

Rapporteurs :

M. MARTIN, François	Professeur, GET, Université de Toulouse
M. KOENDERS, Eddie	Professeur, Technische Universität Darmstad

Examinateurs :

M. MAGLIONE, Mario	Directeur de Recherche CNRS, ICMCB
Mme PETIT, Sabine	Directrice de Recherche CNRS, IC2MP
Mme ARRESE-IGOR, Silvia	Docteure, CFM-CSIC-UPV/EHU

Contents

Acronyms

A Al_2O_3.

AFm $Ca_2(Al,Fe)(OH)_6 \cdot X \cdot nH_2O$ (where X indicates a single charged anion or a 'half' doubly charged anion), Calcium monosulphoaluminate.

AFt $Ca_3(Al,Fe)(OH)_6 \cdot 12\,H_2O2 \cdot X_3 \cdot nH_2O$ (where X indicates a doubly charged anion or, sometimes, two singly charged anions), Calcium trisulphoaluminate hydrate.

C CaO.

C_2S Ca_2SiO_4, Belite.

C_3A $Ca_3Al_2O_6$, Aluminate or celite.

C_3S Ca_3SiO_5, Alite.

C_4AF $Ca_4Al_nFe_{2-n}O_7$, Tetracalcium aluminoferrite or ferrite.

$C_6A\bar{S}_3H_{32}$ $(CaO)_6(Al_2O_3)(SO_3)_3 \cdot 32\,H_2O$, Ettringite.

C-A-S-H $CaO\text{-}Al_2O_3\text{-}SiO_2\text{-}H_2O$, Calcium aluminosilicate hydrate.

C-S-H $CaO\text{-}SiO_2\text{-}H_2O$, Calcium silicate hydrate.

CSH Calcium silicate hydrate, when referring to crystalline minerals.

H H_2O.

S SiO_2.

$\bar{F}$ Fe_2O_3.

$\bar{S}$ SO_3.

BDS Broadband dielectric spectroscopy.

CP-SSNMR Cross polarisation solid-state nuclear magnetic resonance.

FTIR Fourier transform infrared.

HP-XRD High-pressure X-ray diffraction.

HT-XRD High-temperature X-ray diffraction.

ICP-OES Inductively coupled plasma/optical emission spectrometry.

LCA Life cycle assessment.

LCI Life cycle inventory.

LCIA Life cycle impact assessment.

PXRD Powder X-ray diffraction.

SAED Selected-area electron diffraction.

SCFs Supercritical fluids.

SEM Scanning electron microscopy.

SHFS Supercritical hydrothermal flow synthesis.

SSNMR Solid-state nuclear magnetic resonance.

TEM Transmission electron microscopy.

TGA-MS Thermogravimetric analysis-Mass spectrometry.

X-ray μCT X-ray computed microtomography.

General introduction and thesis objectives

A natural mineral is defined as a solid with a specific chemical composition and a highly ordered atomic arrangement that has been formed as a result of a geological process [1]. From the beginning of civilisation, natural minerals played a key role as raw materials for the social, economic and technological development of modern society [2]. Among the large variety that can be found in nature, calcium silicate hydrates are members of a large family of minerals related to cement-based materials. They form as a consequence of geological hydrothermal processes in which hyperalkaline fluids react with basic igneous rocks, or as a product of chemical reactions during cement hydration. In the latter case, the calcium silicate hydrate (C-S-H) gel represents the principal hydration product of cement paste and the primarily responsible for its strength and performance.

In the last years, two minerals which belong to this mineral family, namely xonotlite and tobermorite, have attracted increasing interest in several fields, as orthopaedic applications [3], insulating materials [4], stabilising agent for trapping impurities in wastewater and as additions for reinforced cement [5]. In particular, the idea of employing these mineral phases in cement relies on their high chemical compatibility. Recent studies have shown the effect of xonotlite and tobermorite particles as seeds to trigger the autocatalytic formation of the C-S-H gel [6, 7]. The acceleration of cement hydration allows to develop faster a denser and harder cement paste, which from an application point of view permits to reduce the time and the costs of construction.

However, xonotlite and tobermorite are scarce in nature, and that strongly limits their potential use. Therefore, to fulfil the necessities related to the increasing of the demand, several techniques have been developed to produce synthetic specimens. So far, the most common route for their production is the hydrothermal synthesis. Unfortunately, this conventional methodology requires very long synthesis times, in the order of tens of hours or even days, to obtain crystalline materials.

Chapter 1

State of the art of calcium silicate hydrate minerals: xonotlite and tobermorite

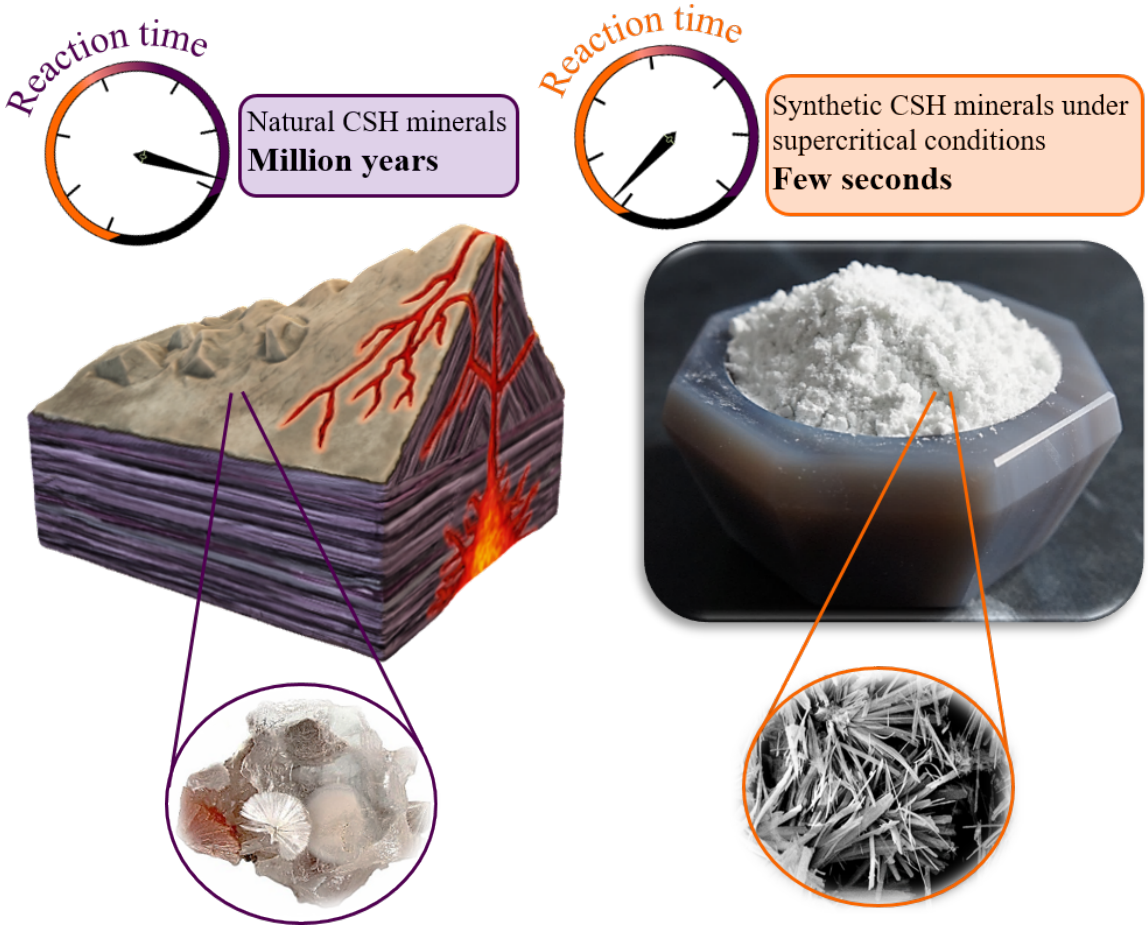

In this chapter, we introduce the most relevant concepts for the chemistry of cement and the CaO - SiO_2 - H_2O system. This family of minerals can form in nature due to geological hydrothermal processes in which hyperalkaline fluids react with basic igneous rocks or as a product of chemical reactions that occur during cement hydration. The extensive interest in studying these minerals relies on several reasons for both fundamental and application orientated researches. As an example, the chemistry of hydrated cement at the microscopic scale strongly influences its macroscopic properties, such as resistance, strength and durability. In this way, a deep investigation of the calcium silicate hydrate mineral structures could help to better understand and control the performance of cement. With this in mind, our work has improved an innovative methodology which allows producing highly crystalline calcium silicate hydrate (CSH) minerals in only a few seconds, contrarily to the several hours or days characteristics of the conventional hydrothermal route.

The first part of the chapter addresses particular attention to the hydration process of cement, emphasising the central role of water on the chemical reactions that take place. Then, the structure of the hydration products of cement is described at different scales (macro, micro and nano). Instead, the second part is dedicated to the description of the CaO - SiO_2 - H_2O system, with particular attention to the structures of xonotlite and tobermorite. Lastly, the hydrothermal manufacturing route of these materials will be presented distinguishing between conventional subcritical hydrothermal synthesis and the innovative supercritical hydrothermal synthesis. A brief overview of the key properties of supercritical fluids will be reported, highlighting some specific features of supercritical water that has been used in this work.

1.1 Introduction to cementitious materials

1.1.1 History and properties of cementitious materials

Construction of buildings and infrastructures had a key role in the civilisation process and continues its vital role in the rapid advancement and the well-being of modern society. Nowadays, cement is defined as a hydraulic binder, i.e. a fine inorganic powder that by reacting with water transforms into a fluid paste, easy to shape and mould, which hardens and develops strength as a consequence of the hydration process [10].

The first archaeological discovery of cement consisted of several layers of limestone ($CaCO_3$) and it dates back to 7000 B.C. in Israel [11]. Successively, the Mesopotamian civilisation developed a mixture made of sand, lime (CaO), and gravel. Throughout history, different mixture compositions and production methods of cement were used by the ancient Greeks, Egyptians and Romans [12, 13]. During the Roman Empire, a hardened paste produced by mixing the blend with water, similar to the modern concept of hydraulic cement, was used for the first time. The Romans used a mixture of slaked slime and volcanic ash, as calcium and siliceous sources, and water to form a hardened material that has resisted over time in optimal conditions [13].

However, after the Roman Empire fall, the discoveries and the expertise acquired in making hydraulic cement were essentially lost. Consequently, during the dark middle ages, the constructions were built by using poor mortars, in which the only active ingredient was lime without any addition of water. Since cured lime mortar can be easily degraded by atmospheric agents contact, many Gothic structures suffered over the centuries.

Many years later, the Industrial Revolution in Europe was the origin of a breakthrough step towards the development of modern cement. In 1756, the contributions of the British constructor John Smeaton in the reconstruction of Eddystone lighthouse in Cornwall led to the discovery of a more modern approach for the production of hydraulic cement [11]. After several researches, he has found out that the use of a hydraulic lime mortar, obtained by burning limestone containing some clay, provided better performance to cement paste. He has also discovered that the hydraulicity (i.e. the property to set and harden with water) of lime was directly correlated to the limestone's clay content [14].

In 1818, another important contribution to the development of modern cement was provided by Louis-Joseph Vicat thanks to his deep research on hydraulic lime properties. As a result of that study, it was concluded that synthetic hydraulic lime should also contain silica and alumina and be produced by calcining a ground mixture of clay and

limestone.

Finally, in 1824 Joseph Aspdin has created a three-step process for producing hydraulic cement, which consisted of: (i) calcining the limestone to obtain lime, (ii) mixing and burning that compound with clay, and (iii) recalcining that blend to form the final product. Aspdin named this "Portland" cement due to the similarity to strong building stones from Portland, England. Isaac Charles Johnson successively refined the method of Aspdin by increasing the production temperature up to the point of vitrification, resulting in the production of the modern cement clinker.

Nowadays, the term cement strictly refers to the clinker powder obtained through a well optimised pyrochemical process [10]. Several different types of cement clinker exist and differ for the proportion between calcium silicates, sulphoaluminate, aluminium and iron oxides, *etc.* Among them, the most common type of cement is the ordinary Portland cement (OPC). In that clinker, the most abundant component is alite (Ca_3SiO_5, named C_3S in cement chemist notation) and a smaller but not negligible amount is composed by belite (Ca_2SiO_4, referred as C_2S), tricalcium aluminate, tricalcium aluminoferrite and gypsum. Depending on the impurities incorporated in the raw materials, the final clinker could also contain low quantities (< 3 wt.%) of MgO, Na_2SO_4, and K_2SO_4 [10]. The composition of a typical OPC clinker is reported in Table 1.1.

Table 1.1: Summary of the typical and most abundant raw materials and final components of OPC clinker reported with the respective weight percentages [10, 15]. The main phases of the clinker are also identified as in the cement notation.

Raw materials		Final components	
CaO	60 - 90%	Alite (C_3S)	50 - 70%
SiO_2	18 - 24%	Belite (C_2S)	15 - 30%
Al_2O_3	4 - 8%	Tricalcium aluminate (C_3A)	5 10%
Fe_2O_3	1 - 8%	Tetracalcium aluminoferrite (C_4AF)	5 - 15%
SO_3	1 - 3%	Tetracalcium aluminoferrite (C_4AF)	5 - 15%
		Gypsum ($CaSO_4 \cdot 2H_2O$)	$\sim 5\%$

The chemical reaction of that cement powder with water, commonly referred to the hydration of cement, leads to the formation of the so-called cement matrix or cement paste. The typical setting and hardening characteristics of the material are developed as a result of that reaction, as it will be presented in the next section. Lastly, concrete is defined as the mix of cement paste with coarse and fine aggregates, like gravel, sand and crushed stone [16].

In the last decades, the efficiency of cement production has been improved, making cement the most used construction material in the world, as shown in Figure 1.1 [17].

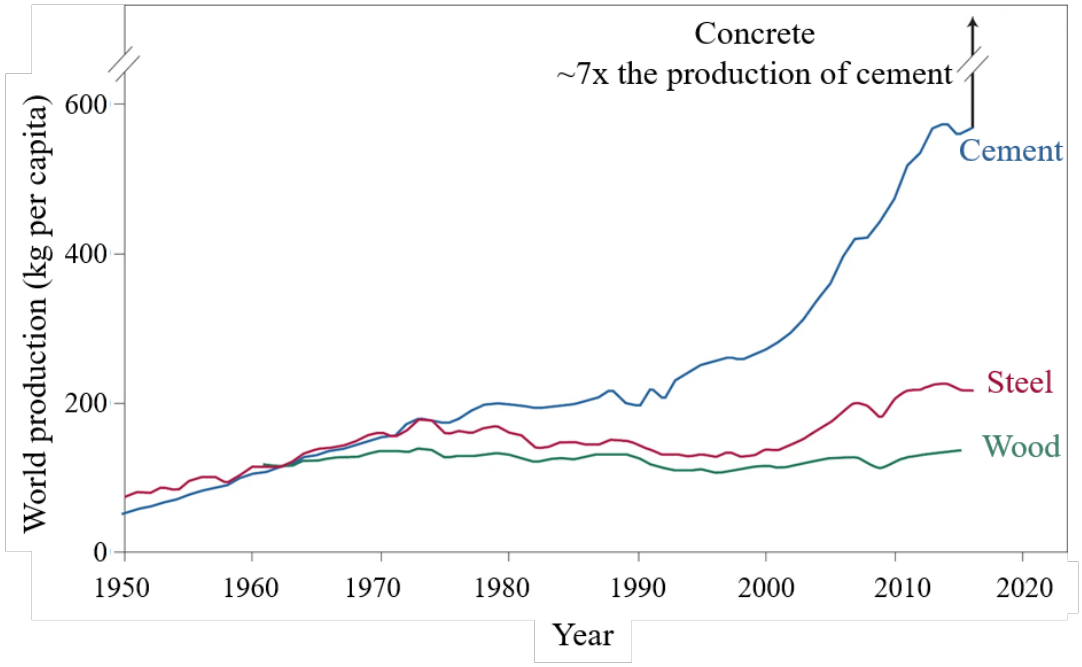

Figure 1.1: Historical growth in construction material production: cement (blue line), steel (red line) and wood (green line) per capita [17].

In the last 65 years, the cement production has grown by ten times compared to the approximately threefold increase in steel production and the almost stagnant production per capita of wood. Of additional importance, cement is related to the production of concrete, whose content is approximately seven times larger than that of cement alone [17]. The reasons for the rapid increase of cement production and consumption, despite other construction materials, are several. Among them, there are:

- The cost, cement is very cheap: 60 - 70 euro per ton,
- It is resistant to fire and it shows good mechanical properties when subjected to compression stress,
- Freshly mixed cement paste can properly flow into all corners of prefabricated mould or formwork to fill it completely, and consequently, it is easy to use.

Nowadays, the demand for cement is particularly strong in the most populated regions of the world, as in China, which is also one of the fastest growing economy, as displayed in Figure 1.2 [18]. The data reported in the annual activity reports published from 2015

by the *European Cement Association, Cembureau* show that China is the first producer of cement in the world, followed by other Asian countries, India and Japan. As an example, the global cement production has been estimated at approximately 4.1 Gt in 2017 [19]. That year, China accounted for 56.5 wt.% of the worldwide cement production, and India for 6.8 wt.%. The following year, the worldwide cement production dropped at approximately 3.99 Gt due to slower growth in China (where accounted for 54.5 wt.%), on the contrary, the production in India increased to 8.2 wt.% [20]. According to a forecast reported by the *World Cement Association*, by 2030 China production is expected to drop by 18%, and Pakistan will replace Japan in the top 10 cement producer countries [19, 20, 21].

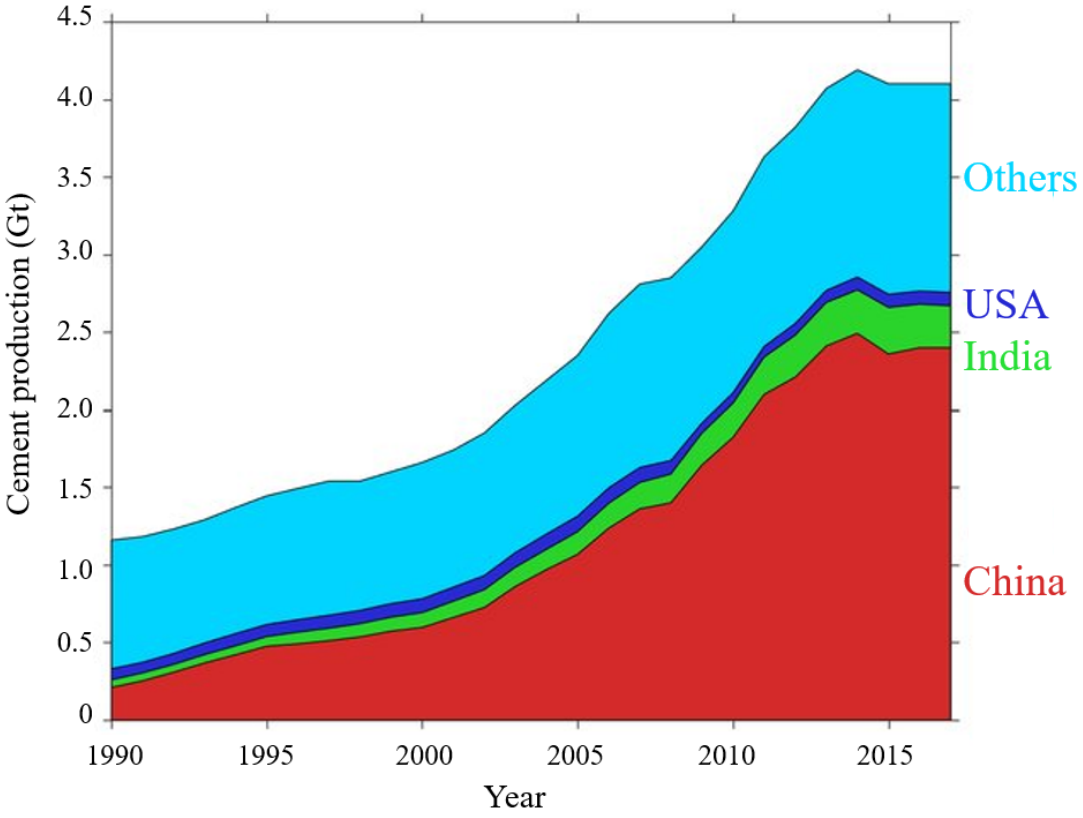

Figure 1.2: Global cement production by country in the period range 1990 – 2017 [18].

From the analysis of these data, it appears clear that cement is the most consumed product in the world, just after water [22]. As a consequence of the high production of clinker, every year around 7 - 8% of the global CO_2 anthropogenic emissions is released into the atmosphere by the cement manufacturing industry [17]. In fact, the clinker production involves the calcination of limestone in the range of temperature 700 - 900 °C,

which decomposes into lime (CaO) and carbon dioxide, according to [23]:

$$CaCO_3 \rightarrow CaO + CO_2 \tag{1.1}$$

This reaction and the thermal emission due to the fuel burning to heat the raw materials, make the pyrochemical process the principal responsible for the CO_2 footprint during the clinker production. The production of one ton of OPC clinker requires between 60 and 130 kg of fuel oil (depending on the cement type) and around 110 KWh of electricity, resulting in the emission of 0.9 ton of CO_2 [22]. As a consequence, the CO_2 emissions from clinker production reached around 1.50 ± 0.12 Gt during 2018, and the cumulative CO_2 emissions over 1928 - 2018 are estimated to $\sim 38.3 \pm 2.4$ Gt, 71% of which have been released since 1990 [18].

This introduction to cementitious materials highlights the role of cement as the most used construction material in the world. As a consequence of the great quantity of clinker produced, every year, the manufacturing industry of cement accounts for 7 - 8% of the global CO_2 anthropogenic emissions. In this context, research for producing more ecological cement is a challenge of fundamental importance to reducing the environmental footprint. The sustainability can be improved by enhancing the material performance, making the life cycle of cement structures more resilient and durable. In this way, it appears clear the importance of studying the chemical structure and the microscopic properties of cement, which in turn affect its performance.
In the next section, the main concepts related to cement hydration will be introduced. As we will show later, the mechanisms involved during the hydration are not completely established and still under debate. We will discuss the main theories and models, reported in the literature, which are the most accepted from the research community.

1.1.2 Mechanisms of the cement hydration process

Hydration of cement is an extremely complex process which involves numerous chemical reactions and physicomechanical changes. After mixing the clinker with water, at the water to cement ratio ranging from 0.3 and 0.6 (hereon referred to w/c, in wt.%), the reacting system evolves to form the 'fresh cement paste'. As the hydration progresses, such paste sets and transforms into a 'hardened cement paste'. The process is characterised by the release of energy in the form of heat and consequently is exothermic.

The cement hydration is the subject of research investigation since the beginning of 1900s [24], however, the mechanism is still not fully elucidated in some aspects due to the numerous involved variables. Among them, there are:

- the wide variety of components contained in the clinker, and the common presence of impurities and ions within the crystalline lattices of each phase,
- the different morphological properties of clinker grains, as shape, particle size, and specific surface area,
- the presence of chemical admixtures which modify the hydration rate.

Several other external parameters can affect the final properties of the cement matrix, such as the used w/c and the reaction curing temperature [25].

Based on *in situ* characterisation techniques, as nuclear magnetic resonance and X-ray diffraction, some authors suggested the classification of the hydration process into five different periods, which can also be recognised by monitoring the heat evolution curve during the hydration, as shown in Figure 1.3 [10, 26].

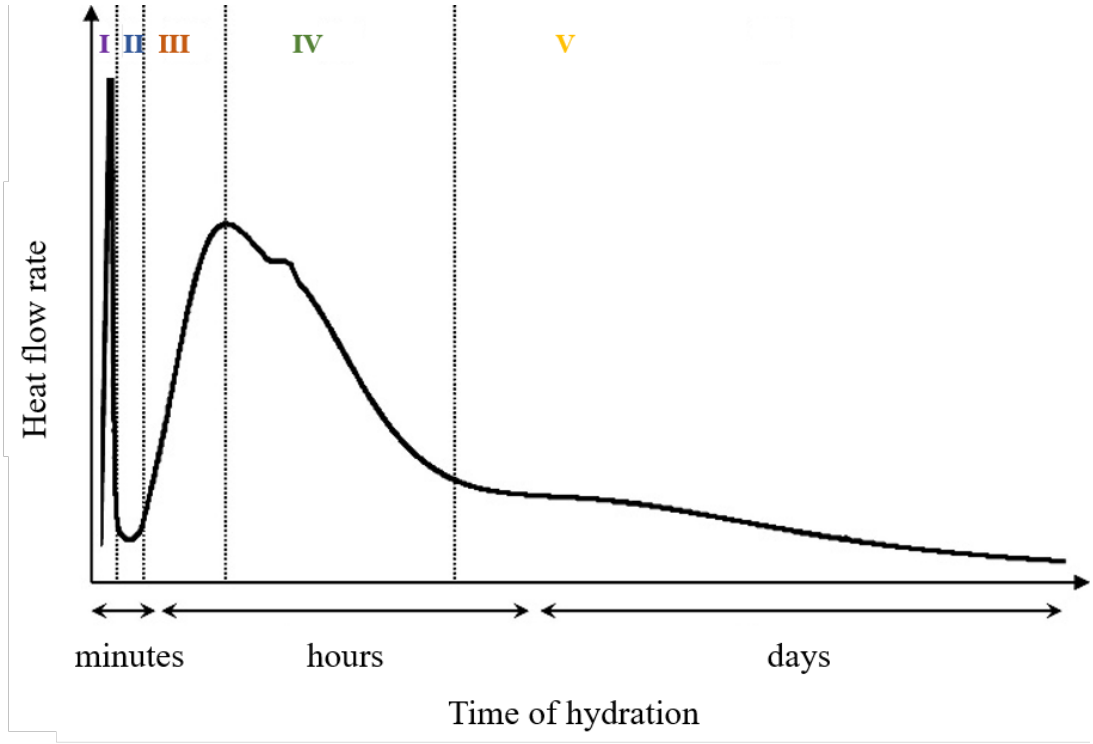

Figure 1.3: Schematic representation of the typical heat release evolution and the proposed classification of different stages during the hydration process of OPC cement [26].

However, it is worth mentioning that the tentatively assignment of the duration of

each stage can vary depending on several parameters, as curing temperature and cement type. Consequently, the classification in five steps and the explanation of the involved mechanisms have to be considered a proposed model supported by some authors, but still not fully established.

The progression of the clinker phases consumption and the hydrates formation over the hydration time are shown in Figure 1.4.

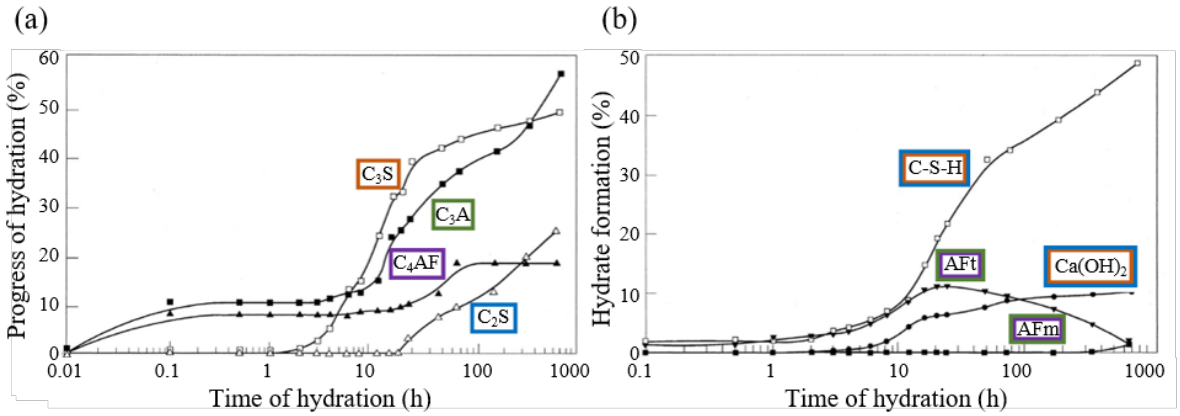

Figure 1.4: Hydration kinetics of an ordinary Portland cement: (a) consumption of clinker phases, (b) formation of hydrate products over time. The hydration was investigated at ambient temperature [10].

- **Stage 1: Pre-induction**

  Upon contact of cement with water, the anhydrous clinker grains start reacting releasing ionic species into the solution. In the first few seconds of the reaction period, the alkali sulphates dissolve completely, contributing with Na^+, K^+, and SO_4^{2-} ions, while calcium sulphate dissolves contributing with two ionic species, Ca^{2+} and additional SO_4^{2-} [11]. As above mentioned, alite is the principal and most important constituent of OPC clinker and also the main responsible for setting and hardening. During the first minutes of this stage, C_3S grains react with water and the protonolysis of the silicate and oxygen ions takes place at their surface. The dissolution of alite grains leads to an additional release of Ca^{2+} simultaneously to those of hydroxide and silicate ions in accordance with [10, 15]:

$$3CaO \cdot SiO_2 + 3H_2O \rightarrow 3Ca^{2+} + H_2SiO_4{}^{2-} + 4\,(OH)^- \tag{1.2}$$

  Initially, the rate of the C_3S dissolution is higher than that of ions to diffuse away from the grains. This phenomenon causes a concentration gradient near the surface. Here, the concentration of ions continues increasing until the liquid phase becomes oversaturated and a layer of amorphous gel starts to precipitate at the alite surface.

From that moment, the amount of free SiO_4^{2-} ions starts decreasing. On the contrary, the amount of Ca^{2+} and OH^- continues increasing, as the CaO/SiO_2 ratio of formed gel is lower than that of the clinker phases [10, 27, 28]. However, another proposed theory suggests that, at the beginning, a SiO_2-rich layer grows on the C_3S surface, and only at a later time, Ca^{2+} ions, dissolved in the liquid phase, are incorporated in it [10, 29, 30].

Regarding the second principal phase in the clinker, belite, its hydration kinetic is even lower than the one of alite, as shown in Figure 1.4(a): only a minimal fraction reacts during this stage, contributing to increasing the Ca^{2+} and OH^- concentration in the liquid phase. Therefore, tricalcium aluminate (C_3A) dissolves in accordance with:

$$3CaO \cdot Al_2O_6 + 6H_2O \rightarrow 3Ca^{2+} + 2\,Al(OH)_4^- + 4\,(OH)^- \tag{1.3}$$

Afterwards, the reaction of ions present in the solution, Ca^{2+}, $Al(OH)_4^-$ and SO_4^{2-}, leads to the formation of calcium trisulphoaluminate hydrate, also called ettringite ($Ca_6Al_2(SO_4)_3(OH)_{12} \cdot 26\,H_2O$, in the cement chemist notation abbreviated as $C_6A\bar{S}H_{32}$) that consequently precipitates in the form of short rods at the cement grain surface [31]. Ettringite is the main compound of the so-called AFt phase; other compounds of this phase are obtained for substitution of Fe to Al due to the reaction of ferrite in the clinker in a similar way as tricalcium aluminate.

To conclude, in Figure 1.3 the initial exothermic peak in the stage I (the so-called pre-induction period from some authors) is related to the intense liberation of heat, within the first few minutes, due to the rapid dissolution of C_3S and C_3A.

- **Stage 2: Induction or dormant period**

  As the process progresses, the hydration slows down and the reaction rate decreases significantly, consequently, the liberation of heat is also reduced, Figure 1.3 stage II. In addition, the microstructure of the hydration product does not present relevant changes, and the paste remains workable and fluid for several hours. The reasons for the drastic slowing down of the hydration rate during the dormant period are still not completely understood.

  In the literature, some authors have explained this phenomenon in relation to the growth of the precipitated product, which forms a layer around the alite grains. The exact structure of that layer is still unknown, but it is thought to be a metastable calcium silicate hydrate compound. That hydrated phase could act as a permeable barrier between the bulk solution and the non-hydrated product, which reduces both the migration of water molecules and the dissolution of ions. According to

this theory, a renewed fast hydration after the end of the induction period could be allowed from some changes, in terms of composition and/or morphology, of the hydrated layer that could make it more permeable [10, 28].

Contrarily, the researchers who claim the formation, in the first minutes of hydration, of a SiO_2-rich layer with absorbed Ca^{2+} ions, propose that the electric double layer hinders the flow of further ions at that stage [10, 29, 30].

Other researchers have proposed a different theory, explaining that it is the low concentration of silicate ions and the consequent slow nucleation of hydration product that controls and limits the reaction rate [10, 32]. During this period, the concentration of Ca^{2+} and OH^- ions continues increasing, and at the end, the pH value is very high, around 12 - 13.

- **Stage 3: Acceleration**

  The acceleration period coincides roughly with the beginning of the main heat evolution peak, Figure 1.3 stage (III). At that time, the concentration of calcium, hydroxyl and silicate species in the liquid phase reaches the critical supersaturation level; consequently, the principal hydration product of cement, Calcium-Silicate-Hydrate (C-S-H) gel, can nucleate, and meanwhile calcium hydroxide begins to precipitate in the form of portlandite crystals, Figure 1.4(b). Therefore, this main peak corresponds to the massive precipitation of the principal hydration products. This phenomenon is coupled with the simultaneous increase of C_3S dissolution, which is mainly responsible for the heat release [10]. It is generally agreed that, in this period, the reaction rate is controlled by the heterogeneous nucleation and growth of hydrated products, which is thought to be dependent on the C-S-H surface area. During that stage, about 30 wt.% of cement reacts to form portlandite and C-S-H gel. It is widely accepted that the setting of cement takes place during this stage, and the end of the acceleration period corresponds with the maximum rate of heat evolution.

- **Stage 4: Deceleration**

  After several hours of reaction, the surface of clinker grains is completely covered by the hydration products and both the amount of unreacted material and the hydration rate decrease, Figure 1.3 (stage IV). Consequently, it is believed that the kinetics could be controlled by the diffusion of ion species through the porous structure of the hydration shell. During this deceleration, a second peak could occur based on the cement type. This heat release is linked to the sulphate depletion and corresponds to faster precipitation of ettringite, and a higher dissolution of C_3A [26].

- **Stage 5: Diffusion**

  A low activity characterises this last period due to the slow diffusion of water and ion species as the cement paste hardens and gains strength [10]. Furthermore, in Figure 1.3 (stage V), a third low peak could be related to the formation of the AFm phase (constituted by monosulphoaluminate compounds, Al_2O_3-Fe_2O_3-monosulpho) from the reaction between AFt and C_3A [26, 33]. After approximately 1 day, the microstructure of C-S-H gel is formed and the gel phase appears dense, whereas the other crystalline phases, such as portlandite as well as monosulphoaluminate, continue growing. Theoretically, the hydration process is considered completely finished after one year, however, the C-S-H gel and cement paste microstructure could continue to evolve over one year.

In this section, cement hydration has been illustrated as several coupled chemical processes, each of which occurs at a rate that is determined by numerous parameters. As above mentioned, the mechanisms involved during the hydration of cement are very complex. Here, we have reported a summary of the most accepted theories related to the hydration process through a classification of five different steps.
However, it is worth mentioning that, despite cement hydration has been the subject of many studies, important aspects have not been carefully addressed and are still not fully established. In the next section, we will show that this complexity is also reflected into the structure of the material. In fact, if at the macroscale, the properties of cement paste are widely investigated, at the micro- and mostly at the nanoscale, the characterisation and the knowledge of the material are limited in part by its amorphous nature and inhomogeneous composition. The final composition and structure of the cement matrix will be illustrated in more detail in the following.

1.1.3 Structures of hydrated cement matrix

The structure of cement paste is very complex due to the numerous involved mineral phases. Among them, there are crystalline components bounded to a semi-amorphous hydration product of variable stoichiometry, the C-S-H gel. The crystalline agglomerates, characterised by different sizes, could be either hydration products such as ettringite and portlandite, or even unreacted, and thus unhydrated, clinker particles.

The C-S-H gel is the principal hydration product in the cement matrix and accounts for the 70% of the total cement paste volume. That amorphous component has a strong influence on the mechanical properties of set cement, as strength and cohesion, and con-

sequently, it is crucial to investigate and explore its structure. However, due to its dissimilarity in structure and size, the cement paste features several hierarchical levels of organisation, showing a distinctive pore structure at each scale level [23]. Consequently, the description of the hydration product has to be illustrated separately for each scale.

a) Macroscale

At the macroscale, the cement matrix can be defined as a homogeneous material containing macropores with diameters ranging from 0.1 to 5 mm [23]. These pores are produced by air inclusions introduced during the paste preparation and generally negatively affect the mechanical properties [10]. In Figure 1.5, pores and aggregates into the cement paste are easily distinguishable [34].

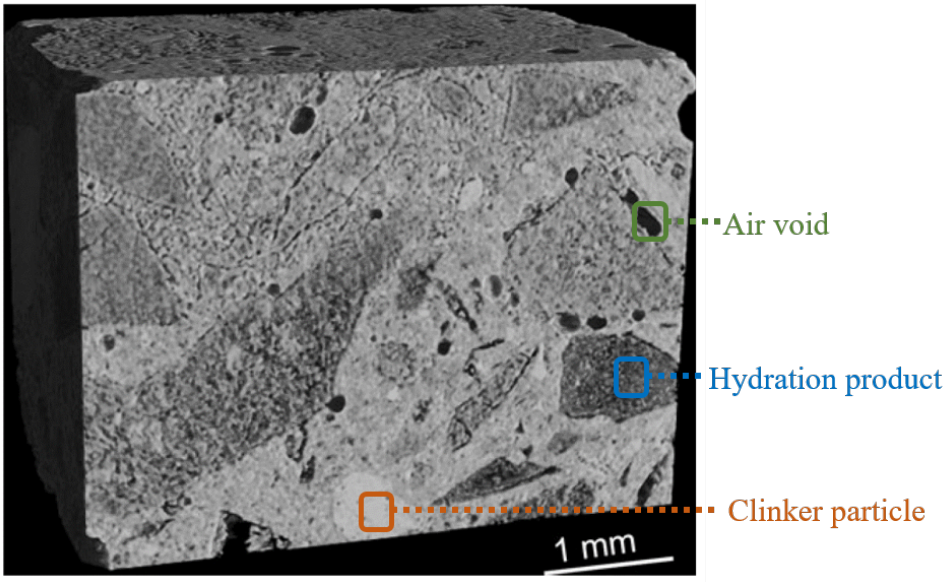

Figure 1.5: Three dimensional representation of concrete specimen obtained by synchrotron X-ray microtomography. Grey levels allow to distinguish the different components: clinker and hydration products in light and dark grey and air voids in black, respectively [34].

b) Microscale

The heterogeneous and multiphase composition of the hydrated cement matrix becomes more evident at the microscale. At this level, it is possible to observe pores, named mesopores or capillary voids, as a consequence of the empty vacancies left when the hydration products replace the spaces initially occupied by cement grains and water [10]. The diameter of these pores is related to the age of cement. For early age of hydration, the capillary voids reach about 5 μm, whereas, for old cured cement, they range within 10 to 50 nm [32, 35]. Furthermore, the pores abundance is directly proportional to the w/c

ratio employed to prepare the paste.

At the microscale, C-S-H gel appears as an amorphous material which surrounds the other crystalline aggregates present in the matrix. The morphology of the C-S-H compounds depends on numerous factors, such as cement type, the water/cement ratio, and the hydration stage at which it grows and the available free space. In the literature, many different morphologies are reported; among them, some examples are flakes, needles, foils, and honeycomb-like [32].

The crystalline phases which are possible to identify at the microscale are mostly ettringite and portlandite, as shown in Figure 1.6. Ettringite crystallises in the form of tiny needles preferentially on the surface of the cement grains [23, 35]. Portlandite, under ideal conditions, forms crystals of several micrometres in size with hexagonal plates-like morphology. In the cement paste, depending on several factors such as temperature, w/c and available growing space, $Ca(OH)_2$ although perfect hexagonal crystals could appear as unshaped crystals, conserving the characteristic layered structure, Figure 1.6(b).

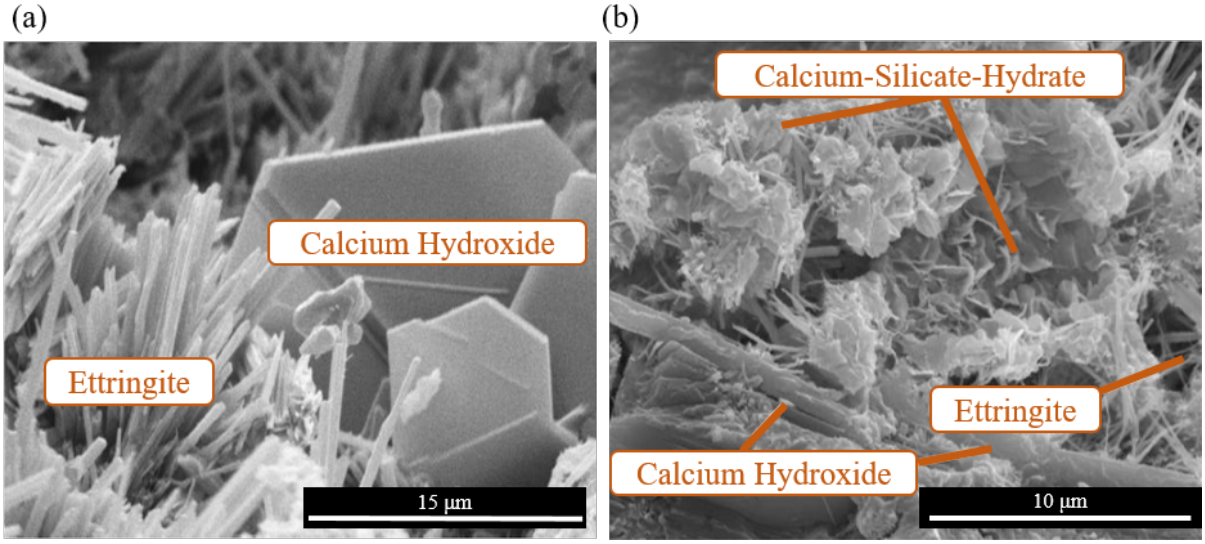

Figure 1.6: Scanning electron images of cement paste showing the morphology of hydration products at different setting times. (a) Crystal phases growth in fresh-cement under conditions of minimal space restrictions, allowing the development of hexagonal-like $Ca(OH)_2$, needle-like ettringite. (b) Crystal phases in more mature paste with limited space, exhibit forms which are more subhedral than anhedral [36].

c) Nanoscale

The description of the cement matrix at the nanoscale results quite challenging due to the heterogeneous and amorphous nature of the C-S-H gel [35]. The nanopores identified at that scale (diameter $< 10\,\text{nm}$) are an intrinsic characteristic of the C-S-H structure

and can have an effect on shrinkage and creep [23, 35]. The C-S-H structure has been investigated at the nanoscale by several techniques, such as nuclear magnetic resonance, and infrared spectroscopy, in contrast, it is difficult by microscopy techniques and X-ray diffraction. For that reason, the exact structure of C-S-H gel is not completely resolved by experimental results. As a consequence, several theoretical and modelling-based models have been proposed for describing this material [37, 38, 39, 40]. Figure 1.7 shows a TEM image of cement matrix where the foil-like morphology of C-S-H can be observed, together with the most widely accepted representation of the C–S–H particles at the nanoscale [41, 42].

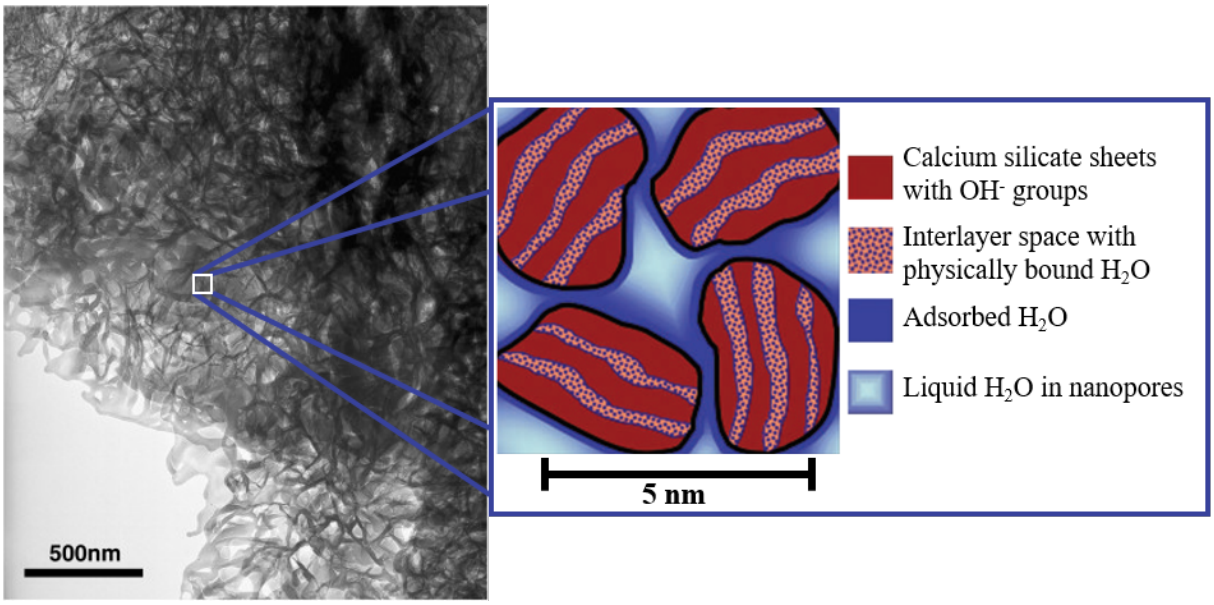

Figure 1.7: TEM image of a cement sample hydrated for 20 years, showing the foil-like morphology of C-S-H [42]. In the adjacent inset, a schematic representation at the nanoscale of the C–S–H particles, with sheet-like structure held together with interlayer water. This representation is based on the model proposed by Jennings and his group [41].

In this section, the structure and properties of the hydrated cement matrix at different scales were described, with a particular attention to the limitation related to the in-depth investigation of the C-S-H gel phase. As we will show later, that phase shares some similarities with the chemical structure of minerals which belong to the $CaO\text{-}SiO_2\text{-}H_2O$ system. For that reason, the chemistry of calcium silicate hydrate minerals will be discussed in the following. Particular interest will be addressed to the description of xonotlite and tobermorite, which represent the analogous crystalline forms of C-S-H gel, and are thus, an excellent model system for mimicking its properties.

1.2 Chemistry of calcium silicate hydrate phases

The very complex system identified as CaO-SiO_2-H_2O is composed of about thirty crystalline phases, characterised by different Ca/Si molar ratios. The existence in nature of such many species is based on the large ionic radius of calcium and its electropositive character, which allow various types of coordination with oxygen [43]. Calcium silicate hydrate minerals can form in nature as a consequence of geological hydrothermal processes in which hyperalkaline fluids react with basic igneous rocks or as a product of chemical reactions that take place during cement hydration.

The great interest in studying calcium silicate hydrate phases, as xonotlite and tobermorite, relies on two main reasons. First, the complex structure of these phases in some aspects are still not fully elucidated, and thus this work pretends to throw some light on this. In particular, a deep understanding of the tobermorite structure is crucial due to the similarity of its structure with the one of C-S-H gel. Consequently, tobermorite represents the most convenient mineral for capturing the structural characteristics of the semi-amorphous C-S-H gel.

Second, in the last years, tobermorite and xonotlite have been highlighted as attractive materials due to their potential applicability in numerous fields. Among them, there are orthopaedic applications [3], insulating materials [4], stabilising agent for the trap of impurities in wastewater and as an addition for reinforced cement [5]. Furthermore, tobermorite phase has been found in Roman cement and is widely accepted to be the reason for the durability of Roman cementitious structures. However, these minerals are scarce in nature, and therefore the increase in the demand goes together with the request for new and green approaches, which can provide fast production at the industrial scale. For those reasons in this work, we are focusing on both the synthesis of xonotlite and tobermorite and the study of their properties and applications.

1.2.1 The xonotlite phase

Natural xonotlite mineral was first discovered in 1866 in Xonotla (Mexico), hence its name. Natural xonotlite is commonly found nearby to a contact between igneous rocks and calcium bearing rocks [44]. In the structure of natural specimens, in addition to Ca, Si, O and H atoms, some traces of Na^+, Fe^{3+}, K^+, and Mn^{2+} can be present in the form of impurities. In this way, synthetic xonotlite production offers the solution to obtain the mineral phase with high crystallinity and chemical purity.

Xonotlite is usually described as having the following ideal stoichiometric formula

$Ca_6Si_6O_{17}(OH)_2$ [45]. Mamedov and Belov first described the structure of xonotlite as closely related to that of its dehydrated correspondent phase: wollastonite ($CaSiO_3$) [46]. Furthermore, they classified xonotlite as a monoclinic crystal with space group *P2/a*. Later, Kudoh *et al.* [45] and Hejny *et al.* [44] investigated the structures of different polytypisms of the mineral. Based on these studies, the basic elements of the xonotlite structure have been identified as CaO-polyhedral layer and Si_6O_{17}-double chains.

The Ca-polyhedral layer is composed of three different calcium sites depending on the Ca coordination in the structure. Two of them are seven-fold coordinated by oxygen, whereas the third calcium atom has octahedral coordination, as shown in Figure 1.8(a).

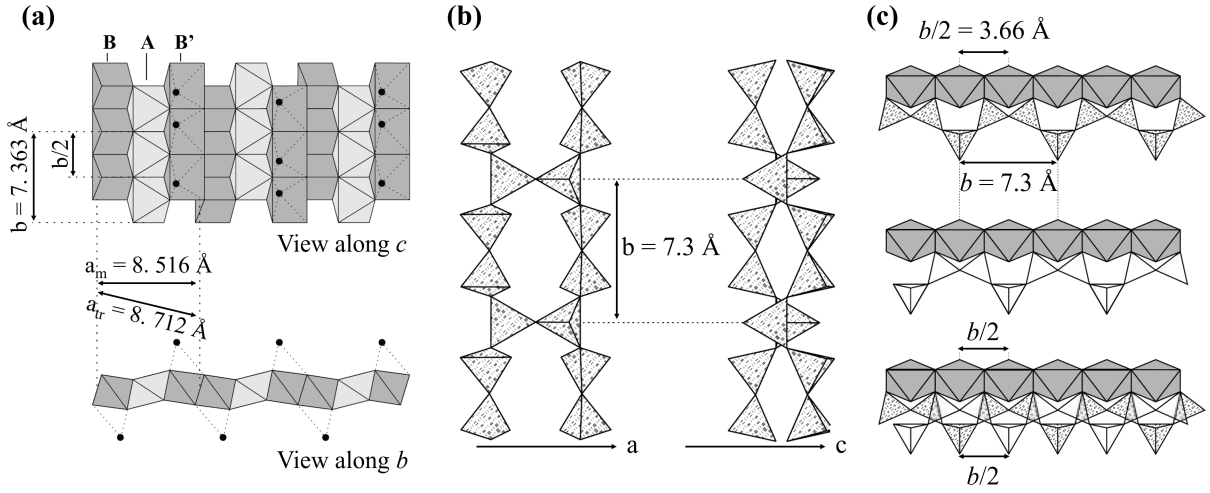

Figure 1.8: Representation of (a) CaO-polyhedral sheet in the structure of xonotlite. Chains of Ca atoms seven-fold coordinated, type B and B', Ca atoms octahedrally coordinated, type A, are represented in dark grey and light grey, respectively. The seven-fold coordination structure forms a trigonal prism where black dots represent a seventh oxygen atom; (b) Si_6O_{17}-dreier-doppelkette double chain in the structure of xonotlite seen along the **c**-axis (left) and along the **a**-axis (right); (c) the two different possibilities of connecting a silicon tetrahedra chain (with a periodicity of three SiO_4) to a column of calcium octahedra (type A) in xonotlite (top and middle) and column of calcium octahedra with two superimposed SiO_4 chains (bottom) [44].

The calcium atoms in seven-fold coordination are located in trigonal prism structure where six of the oxygen atoms are in the apices of that prism, and the seventh coordinated oxygen is placed at one prism face. The other Ca site in octahedral coordination is located in edge-sharing position to form an infinite chain along the **b**-axis (chains A in Figure 1.8(a)). Along the same direction, a chain of edge-sharing polyhedra is formed by Ca seven-fold coordinated (chains B and B' in Figure 1.8(a)). The totality of the chains is linked together through edge-sharing to constitute a layer with a BAB'-arrangement structure. The chains B and B' are related through a two-fold axis parallel to **b**-axis and

a mirror plane perpendicular to it. The arrangement of Ca-O polyhedra in this structure has been described in a cell with symmetry of *C2/m* and parameters equal to a = 17.031 Å, b = 3.682 Å, c = 7.012 Å, and $\beta = 90.37°$ [44].

The other basic xonotlite structural elements are Si_6O_{17}-double chains, bonded via sheets of edge-sharing Ca-polyhedra. Each Si_6O_{17}-double chains is formed by condensation of two wollastonite-like Si_3O_9-dreier-einfachketten chains [44, 45, 46]. That single unit consists of repetitive silicon–oxygen tetrahedra with a periodicity of three SiO_4. Among them, two are paired together to form Si_2O_7, and the third one corresponds to a single tetrahedron in bridging position to connect the paired SiO_4. Consequently, in xonotlite, the Si_3O_9 chains are linked together by sharing the apical oxygen atoms of two bridging tetrahedra, forming what is known as Si_6O_{17}-dreier-doppelkettedouble chain. The two double chains have a symmetry *2/m*, being the two single chains related to each other by an inversion centre, a two-fold axis, and a mirror plane perpendicular to the two-fold axis [44]. The silicate double chain has the same length as two Ca-polyhedra, and thus each silicon–oxygen tetrahedra can be bounded to the Ca octaedra at two structurally different positions, as shown in Figure 1.8(c). This gives rise to a number of various xonotlite polytypes characterized by distinct relative arrangement of the Si_6O_{17}-double chains in neighbouring Ca sheets [44]. To study and compare the different xonotlite polytypes, a small common unit, labelled 'cell of hypothetical protoxonotlite (or p-xonotlite)', was defined [45, 46]. That unit was described with a monoclinic symmetry and cell parameters equal to $a_p = 8.516$ Å, $b_p = 7.363$ Å, $c_p = 7.012$ Å, and $\beta = 90.37°$ [45]. Using this convention, the structures of different polytypes can be interpreted as distinct arrangements of the protoxonotlite subcell.

In the ideal xonotlite structure, the OH groups are placed at the free apices of the calcium octahedra where any bridging silicon–oxygen tetrahedra are linked. However, several studies have shown that both natural and synthetic xonotlite contain an excess of water, which is present partially as Si–OH groups and partially as water molecules [44, 45]. As a consequence, the exact chemical formula should be closer to $(CaOH)_2Ca_{3.6}(H_{0.8}Si_6O_{17})\,H_2O$, with $m \leq 2$, as suggested by Grimmer *et al.* [47].

Xonotlite has been used as an appealing mineral in several application fields, in brake linings of cars to improve the properties in terms of resistance and thermal conductivity [48], or as a pigment in paper and dye compounds, or even as potential biocompatible candidate for preparation of bioactive composites [3]. Xonotlite represents one of the components which can be found in well cement [49], and due to its compatibility with the cement chemistry has been further used as seed addition to improve the performance, in

terms of strength, of cement paste [5, 6]. Another interesting application of xonotlite relies on using this mineral phase as starting material to produce the respective calcium silicate, wollastonite, upon dehydration. This application of xonotlite has also been investigated in this Ph.D. work, and the results will be presented in chapter 4.

In this section, the crystal structure of xonotlite was presented as constituted of two basic units: the Ca-polyhedral layers and the silicate chains. Depending on the relative arrangement between these elements, various xonotlite polytypes can be identified. The structure of xonotlite was first described as similar to that of another mineral phase, wollastonite. In fact, each Si_6O_{17}-double chain of xonotlite consists of two wollastonite-like Si_3O_9-dreier-einfachketten chains, highlighting the similarity between the two materials.
In the following, the crystal structure of tobermorite will be introduced. As we will show later, the two mineral phases, xonotlite and tobermorite, are constituted by the common basic units: Ca-polyhedra layer and tetrahedral dreiereinfachketten-type silicate chains.

1.2.2 The tobermorite phase

Natural tobermorite mineral was discovered in 1880 in Tobermory (Scottland), hence its name. Natural tobermorite is considered a rare and scarce mineral that crystallises in the form of plates or flat fibres. In nature, it is commonly found in or nearby cavities of basic rocks, or at the contact between dolerite and limestone, or granodiorites [50]. Depending on the degree of hydration (i.e. content of water molecules), the basal distance ranges from 9Å, to 11Å or 14Å. As a consequence, three structural varieties of tobermorite exist: 9Å tobermorite, 11Å tobermorite or 14Å tobermorite. The three varieties show different d_{002} values in the diffraction patterns: 9.3, 11.3 or 14.6Å, from the least to the most hydrated type, respectively. It has been observed by X-ray diffraction that upon heating at 100 °C, 14Å tobermorite transforms into 11Å tobermorite, which in turn can give rise to 9Å tobermorite by a further dehydration process at 300 °C. However, some natural samples of 11Å tobermorite, labelled anomalous, contrarily from those labelled normal, despite the heating treatment preserves their structure without any changing in the basal distance value [51].

It is widely accepted that the variety with closer resemblances to the cementitious C-S-H gel is the 14Å tobermorite [52]. Instead, the most common and stable variety to produce as synthetic form is the 11Å. For that reason, our attention in the next section

will be focus only on the 11Å tobermorite.

a) 11Å tobermorite

As previously mentioned, the structure of tobermorite is complex, and consequently, its description has been, for many years, a matter of debate. It is worth mentioning that the difficulties in ascertain the exact structure of the material are also related to the poorly crystalline character of the studied specimens.

The first study on natural 11Å tobermorite, in the form of fibrous aggregates (from Northern Ireland), was performed in 1954 [53]. Through X-ray diffraction, the material structure was classified with an orthorhombic symmetry, space group of *C222*, and unit cell parameters: a = 11.3, b = 7.33, and c = 22.6 Å. Two possible formulas were suggested as result of the study: $Ca_5Si_6O_{16}(OH)_2 \cdot 4H_2O$ or $Ca_5Si_6O_{17} \cdot 5\,H_2O$ [53].

Later, Megaw and Kelsey proposed a first structural model to describe this mineral [54]. They defined 11Å tobermorite as formed by a central layer with CaO_2 octahedra bonded on both sides to wollastonite-type silicate chains running along [010]. The proposed formula in that work was: $Ca_5Si_6O_{16}(OH)_2 \cdot 4\,H_2O$. Further work towards the understanding of the 11Å tobermorite structure was performed on a specimen originating from Germany [55]. The structure of the sample was classified in the *Imm2* group (dimensions of the unit cell parameters: a = 11.172, b = 7.392 and c = 22.779 Å) [55]. In that study, the material was more precisely described as constituted by a continuous seven-fold coordinated Ca-polyhedral sheets, linked to tetrahedral dreiereinfachketten-type single chains in both sides. In that configuration, it was stated that the bridging SiO_4 of each chain could occupy two alternative orientations related by the mirror plane normal to the **a**-axis. The results of this study suggested the following formula to characterise the material: $Ca_{4.5}Si_6O_{15}(OH)_3 \cdot 2H_2O$.

The most substantial attempt to describe this mineral was made by Merlino *et al.* to finally overcome the disagreement between previous studies [50, 56]. They investigated two specimens of 11Å tobermorite: a normal one from Baščenov (Urals, Russia) and an anomalous one originating from Wessels mine (South Africa). The samples were formed of extraordinary well developed crystals, which helped the characterisation analysis. Common structural features to both forms are the double silicate chains (built up through condensation of dreiereinfachketten wollastonite-type chain) running along **b**-axis and bonded on both sides to infinite layers of seven-fold coordinated calcium polyhedra. A schematic representation of how silicate chains are connected to the Ca-polyhedral layer is shown in Figure 1.9. The Ca-polyhedra were defined as monocapped trigonal prism

running along **b**-axis. The calcium cations are not placed in the basal plane of the 'pyramid' but are displaced towards the centre of the trigonal prisms. In that representation, the 'capping' ligand is a water molecule (W6) with the corresponding Ca-O bond perpendicular to the 'pyramidal' basis. Each silicate chain can be described as formed by 'paired' Si_2O_7 units linked together by a bridging tetrahedron. That chain is bounded to a column of Ca trigonal prisms, through the 'paired' tetrahedra that share oxygen atoms of the edges opposite to the capping ligands. In contrast, the bridging tetrahedron (Si2) shares an oxygen atom (O6) with the adjacent column. As shown in Figure 1.9(a), consecutive silicate chains are shifted by $\mathbf{b}/2$; the silicate chains on the hidden side are likewise linked to the Ca-layer, with paired tetrahedra bounded to the alternate Ca-columns, and shifted by $\mathbf{b}/4$ relatively to those on the visible side.

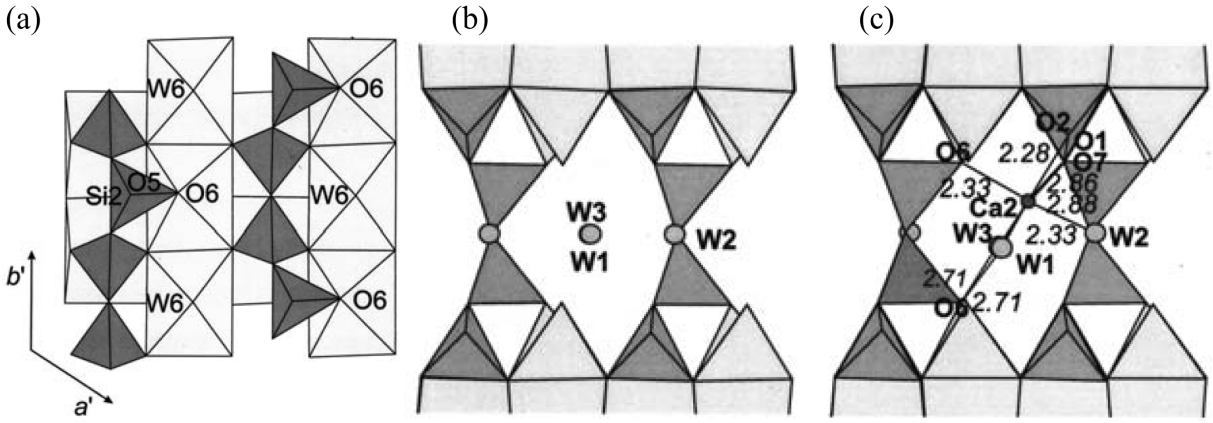

Figure 1.9: Representation of (a) the connection between silicate chains (dark grey) and Ca-polyhedral layer (light grey), and structural cavities in (b) anomalous and (c) normal 11Å tobermorite, as seen along [001] [50].

Furthermore, the structure formed from consecutive layers of Ca-polyhedra and the respective bounded double silicate chains, shows channels running along **b**-axis. From Figure 1.9(b) and 1.9(c), it appears clear that one of the differences between the anomalous and normal structures regards the content of these cavities. In the first case only water molecules are present in the structural channels, Figure 1.9(b), whereas in the normal specimen both water molecules and calcium ions are hosted, Figure 1.9(c). Through an accurate analysis on the anomalous specimen, Merlino *et al.* have proposed a reliable model of the structure and defined two main polytypes. The first one was classified as orthorhombic with a space group *F2dd*, whereas the second one has a monoclinic symmetry and a space group *B11m*. The normal 11Å tobermorite sample was described with a *2mm* symmetry and a space group *B11m*. Figure 1.10 shows the crystal structures of the monoclinic polytype of both anomalous and normal 11Å tobermorite samples. As a result

of this exhaustive work, they proposed for the anomalous sample the following chemical formula: $Ca_4Si_6O_{15}(OH)_2 \cdot 5H_2O$, and for the normal one: $Ca_{4.5}Si_6O_{16}(OH) \cdot 5H_2O$.

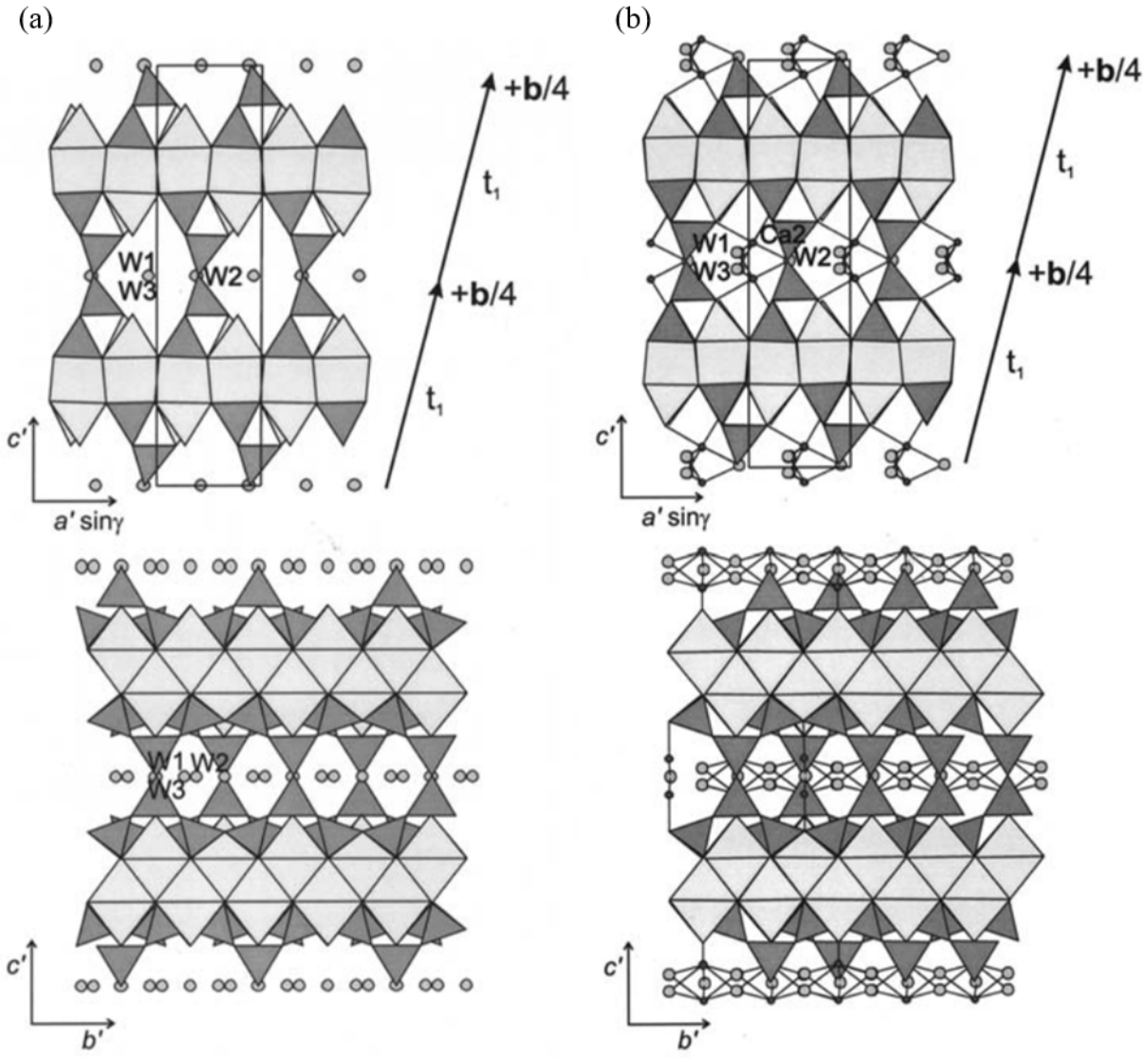

Figure 1.10: Crystal structures of the monoclinic polytypes of (a) anomalous tobermorite 11Å and (b) normal tobermorite 11Å. The crystal structures are represented on the top as seen along [010], and on the bottom as seen along [210]. The double silicate chains are represented in dark grey and the seven-fold coordinated calcium polyhedra in light grey. Grey circles indicate the water molecules W1, W2, and W3 trapped in the structural cavities [50].

Tobermorite exists in nature in the form of three different varieties, depending on the content of interlayer water molecules. In this work, we are particularly interested in 11Å tobermorite, which represents the most stable variety to synthesise. In this introduction, the 11Å tobermorite crystal structure, and the properties of its calcium layers and silicate chains were presented. We have observed that, the similarity

between different mineral phases, as xonotlite and tobermorite, relies in the presence of the common units: calcium polyhedra and dreiereinfachketten wollastonite-type silicate chains.
In the next section, the structure of aluminium-substituted tobermorite will be presented, being this variety very common in both natural and synthetic samples.

b) Al-substituted tobermorite

In nature, the formation of tobermorite usually occurs with the presence of aluminium, or in more rare cases other elements (Mg, Fe or Na), as a partial substitution in its structure. As a result, Al-substituted tobermorite is found more commonly than the pure specimen. Furthermore, the presence of the Al-tobermorite has also been detected in Roman archaeological submarine cementitious specimen [57]. The formation of Al-substituted tobermorite is associated with the pyroclastic puzzolans, a Si-poor and Al-rich specie, used in the Roman concrete binders.

Regarding the hydrothermal synthesis of tobermorite, the results of several studies have shown the advantage of adding aluminium to stabilise synthetic tobermorite under specific hydrothermal conditions and avoid the transformation into xonotlite, as will be more detailed in the following, section 1.3.1. In the literature, several studies have been conducted to study where and how the aluminium atoms enter in the tobermorite structure. The first attempt in producing Al-tobermorite has been reported by Kalousek in 1957, who suggested that the Al^{3+} ions probably assumed tetrahedral coordination when replacing Si^{4+} [58]. Afterwards, Diamond *et al.* have confirmed that theory on the incorporation of aluminium in tetrahedrally coordinated Si-sites of tobermorite chains through X-ray fluorescence spectroscopy [59].

An important parameter to be considered when discussing the Al-coordination and entering positions, is the value of employed aluminium content. In an ideal tobermorite structure, Al ions enter only in branching and not in bridging positions. Consequently, the maximum amount of excepted Al is such that Al/(Al+Si) = 0.165 [7]. Whit the aim of investigating the effect of the Al percentage on the material structure, several ^{27}Al nuclear magnetic resonance studies have been reported. Based on these results, it has been confirmed the presence of tetrahedrally coordinated aluminium in the aluminium-silicate chains when the Al/(Al+Si) molar ratio is about 0.15. On the contrary, octahedrally coordinated aluminium has been detected in the structure when employing higher aluminium content. This experimental evidence can be explained as follows. A first hypothesis con-

siders that the Al excess does not react or enter into the structure but instead leads to the formation of secondary impurity products, as hydrogarnet, in which aluminium is octacoordinated [59, 60]. Instead, a second explanation proposed by Guio *et al.* predicts that aluminium could enter in the position of calcium atoms [61]. Figure 1.11 shows the multiplicity of possible positions for Si and Al tetrahedra into the structure.

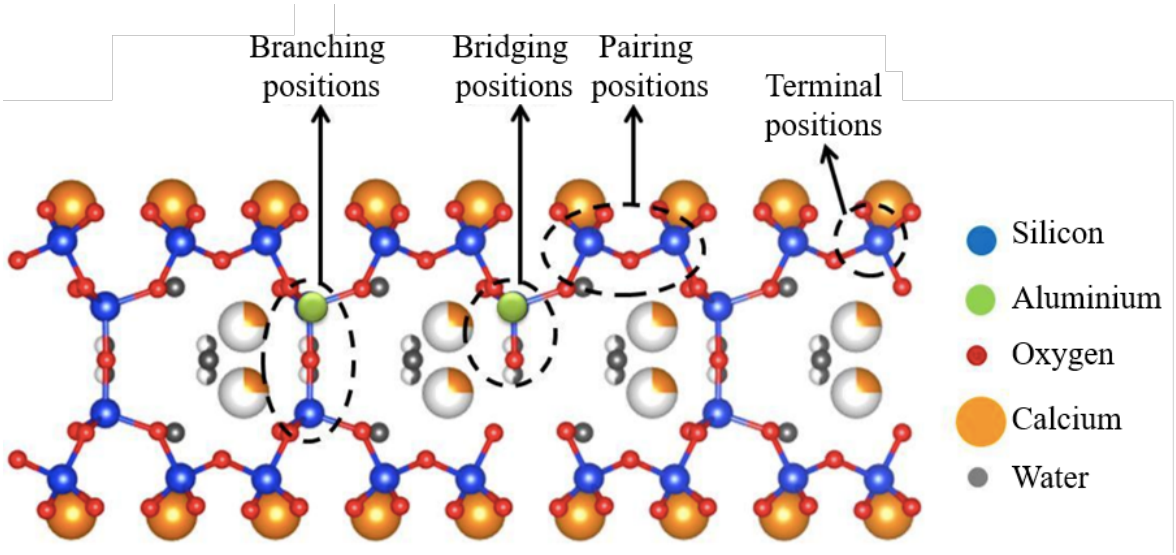

Figure 1.11: Schematic representation of Al-substituted tobermorite structure, according to the description of Wang *et al.* [62]. The different positions of Si and Al atoms within a chain (branching, bridging, paired and terminal) are reported. The legend shows the colours of the involved atoms: Si, Al, O, Ca and H. The spheres depicted partially in withe represent atom that belongs, in part, to another unit cell [7].

To better explain how Al^{3+} ions replace Si^{4+} and enter into the tobermorite structure, the charge deficit due to this substitution should be taken into account. Kalousek proposed three different hypotheses in agreement with the principles of isomorphous substitution [58]. The first proposition relies on the substitution of $Al^{3+} + H^{+}$ for one Si^{4+}, and represents the most favourable case. The second proposition involves the substitution of $2Al^{3+}$ for $(Si^{4+} + Ca^{2+})$, and despite being less probable, can also occurs punctually. A third possibility is the substitution of $4Al^{3+}$ for $3Si^{4+}$, which requires special geometrical arrangement due to the introduction of a different number of cations, and thus is the less accepted one. In conclusion, the case of Al-tobermorite is commonly described by the first proposition, even if the second is not necessarily precluded.

1.2.3 The C-S-H gel phase

As mentioned before, the C-S-H gel is a semi-amorphous and porous material with short-range order at the atomic scale and variable stoichiometry. Furthermore, it is char-

acterised by a Ca/Si ratio ranging from 0.7 to 2.3, and a variable content of structural water [23, 63]. The exact composition and structure of C-S-H gel have been investigated for many years and are still the subject of intense debate. A basic description defines this material as composed of calcium oxide planes surrounded by silicate chains, forming a layered structure. The space between layers is occupied by water molecules and ions, such as Na^{+} or Ca^{+2}, dissolved in the solution [64]. In this representation, the silicate chain lengths, following the 3n-1 rule (dimers and pentamer), are ordered according to the dreiereinfachketten wollastonite-like structure [43, 65, 66]. An ideal representation of the C-S-H gel structure is shown in Figure 1.12.

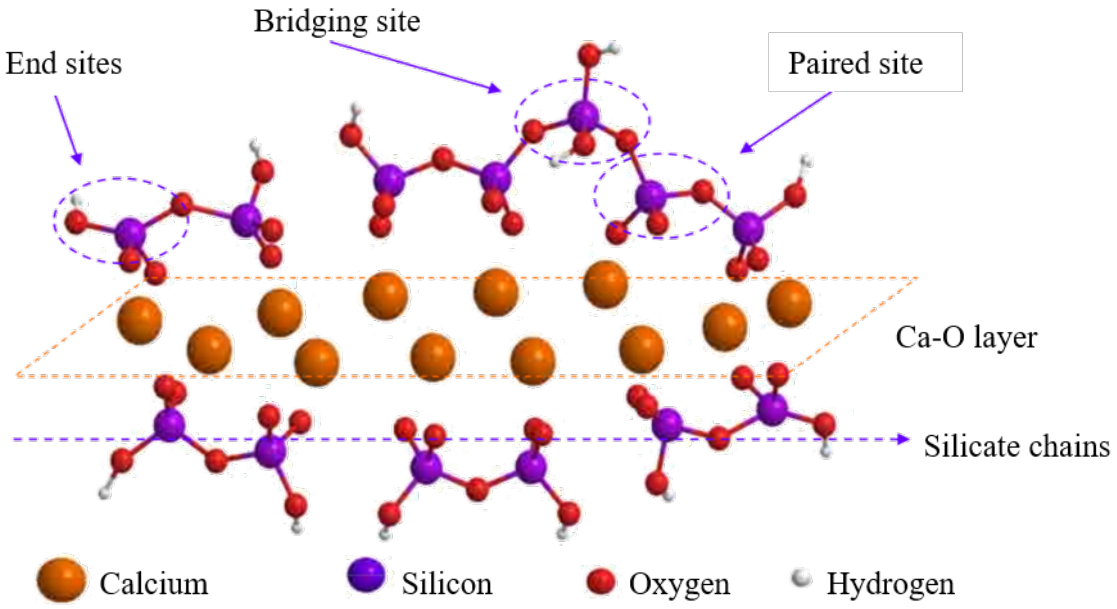

Figure 1.12: Schematic representation of the C-S-H gel atomic structure. The different positions within a chain (end, paired and bridging) are represented. The legend shows the size and the colours of the involved atoms: Ca, Si, O, and H [64].

A general accepted formula for describing C-S-H gels is $Ca_xH_{2(n+1-x)}Si_nO_{(3n+1)} \cdot z\,Ca(OH)_2 \cdot mH_2O$, where n is the silicate chain length, $2\,(n+1-x)$ is the number of –OH groups linked to the chain and z is the number of calcium hydroxide units surrounded by m water molecules [65]. In this proposed model, the structural distribution of the Ca is not clarified, therefore in the formula the Ca ions are divided into those necessary to charge balancing the silicate chain (x) and the remaining z are involved in forms of $Ca(OH)_2$ in the "solid-solution".

Due to the semi-amorphous nature of C-S-H gel and its high propensity for structural variations, many of the knowledge about its structure have been achieved from the com-

parison with some of the analogous crystalline calcium silicate hydrates materials. For instance, in 1952 Bernal and Taylor proposed for the first time the analogy between the C-S-H gel and the tobermorite phases based on X-ray diffraction studies of hydrated C_3S pastes [67]. Such results became the base of many further models proposed afterwards. However, the C-S-H gel has an average Ca/Si ratio equal to ~ 1.7, which is higher than that of tobermorite, Ca/Si $= 0.8$. Because of such disagreement, it was proposed that the higher Ca/Si ratio in C-S-H gel is related to the lack of some bridging tetrahedra in the silicate chains and their substitution with interlaminar Ca^{2+} ions [68]. Finally, thirty years later from his first model, Taylor suggested the possibility of a combination of tobermorite-like and jennite-like structures to explain the higher Ca/Si ratio in C-S-H gel [43]. This result has been widely accepted in successive researches [41, 65, 69]. More recently, Dolado *et al.* have proposed a model for the structure of C-S-H gel, depending on the Ca over Si ratio. At low Ca/Si ratio, the system is formed of long polymerised chains (pentamers and more) with principally 11Å tobermorite, 14Å tobermorite, and jennite phases, whereas increasing the Ca/Si ratio, the polymeric chains are mainly short (dimmers) composed of 14Å tobermorite and jennite [63].

1.2.4 Water in calcium silicate hydrate materials

In mineral structures, oxygen-bound hydrogen species can exist in many different forms. They can occur as part of the crystal structure, organised as stoichiometric hydronium ions, hydroxyl groups, and water molecules. The water content can exist in the form of "evaporable" or "nonevaporable", to distinguish between relatively free and strong bounded or structural water [70]. The first type is typically present as adsorbed on the external surface of mineral particles or in macroscopic fluid inclusions and can be easily evacuated by heating up [71]. The "nonevaporable" water in minerals can be present in vacant anion and cation sites, zeolitic sites, or interlayer regions as well as in small micrometre or nanometer sized cavities, due to the hydrogen-bonded interactions with the material interfacial atoms.

Understanding nanoconfined water dynamics, especially in terms of molecules trapped in nanocavities or strongly bonded to the material surface, is a theme of great interest across numerous scientific fields [72, 73, 74]. The features of nanoconfined water are highly dependent on surface interactions and confinement geometry and are further modified by different chemical environments. Several previous studies have investigated the dynamics of nanotrapped water in minerals using several experimental techniques such as nuclear magnetic resonance, neutron scattering, and molecular dynamics simulations

[71, 75, 76, 77]. Among these techniques, broadband dielectric spectroscopy (BDS), due to its large frequency (10^{-6} - 10^{12} Hz) and temperature (100 - 670 K) ranges, allows exploring the dynamic features of water over an extremely broad time range, from 10^{2} to 10^{-8} s [78].

In the context of calcium silicate hydrate minerals system, the extensive interest in the study of water dynamics is due to the strong influence of the water molecules on the macroscopic properties of cement, such as resistance, strength, and durability [79]. In the literature, three main water dynamics were observed in C-S-H gel in the supercooling region (100 K - 250 K) by BDS [79, 80]. The weak and broad components at low temperature (110 K) were independent of the amount of water, and were the only dynamics observed in the sample dried at 120 °C. For these reasons, this contribution was associated with the dynamics of hydroxyl groups; on the other hand, the processes observed at a higher temperature (190 K) presented dynamical features typical of water in confined systems and, consequently, were associated with the dynamics of water molecules in small and large pores of C-S-H gel. Apart from the study of nanotrapped water in this material, the only other research on calcium silicate hydrate minerals is an investigation of tobermorite. Monasterio *et al.* compared the BDS results of natural and synthetic tobermorite (synthesised at 200 °C in 4 h) [81, 82]. Unlike in previous works on C-S-H, a well-defined contribution of the dielectric response was observed at low temperature (110 K) in both natural and synthetic tobermorite specimens. As evidenced by the different shapes of this contribution in the dielectric spectra of C-S-H and tobermorite, and the presence of aluminium in the tobermorite samples, it was suggested that the origin of this component is related to the dynamics of water confined in aluminium-rich zeolite cavities. On the other hand, at a higher temperature, the process behaviour was similar to that observed for water molecules in small C-S-H gel pores.

Despite all these previous studies, the definitive description of water dynamics in these systems is still incomplete. In this way, this work pretends to throw some light on this, as it will be discussed in chapter 3.

In this section, the main characteristics of the crystal structure of calcium silicate hydrate minerals, xonotlite and tobermorite, were introduced. Furthermore, an introduction to the oxygen-bound hydrogen species that can be found in these minerals was reported.
In the following, the state of the art of the hydrothermal synthesis of xonotlite and tobermorite will be presented, highlighting the crucial role of experimental parameters like temperature, precursors and time.

1.3 Hydrothermal synthesis of xonotlite and tobermorite

The hydrothermal synthesis can be defined as any homogeneous (nanoparticles), or heterogeneous (bulk materials) reaction which takes place in a closed system in the presence of an aqueous media kept above 25 °C and 1 atm [83]. When the chemical reaction occurs in a non aqueous solvent, we refer as solvothermal synthesis [84, 85, 86]. The term hydrothermal was first used in the XIX century by the British geologist Sir Roderick Murchison to describe the mimicking of natural and geothermal reactions of water at elevated temperatures and pressures which provided the formation of numerous minerals and rocks [87]. The hydrothermal method was first employed to produce fine particles of quartz. Afterwards, the manufacturing process was largely exploited, and by 1900, more than 150 mineral species were synthesised including zeolites, large single quartz crystals, clay and diamond [88, 89]. Nowadays, the hydrothermal route provides an excellent methodology for processing a wide variety of materials, such as native elements, hydroxides, metal oxides, as well as silicates and carbonates, *etc.*, either in the form of bulk single crystals, or fine particles, or even nanostructures as nanowires, nanotubes, and nanorods [87].

When heating up, a fluid in a tank tends to expand as the molecules are transferred from the liquid to the gaseous phase. As a consequence, the pressure increases and at the same time the density of the liquid phase decreases; in contrast, the density of the corresponding gaseous phase increases up to the critical point, where both phases have the same density value. During the hydrothermal process, water plays two different roles: it acts as a solvent and as a pressure-transfer medium. Consequently, the physicochemical properties of water at high temperatures and pressures are extremely relevant. For example, the diffusivity in the solvent media, as well as the reactivity, are improved under hydrothermal conditions due to the lower value of viscosity. Furthermore, the direct influence of the density variation on the solvation power of water and, therefore, its feasibility to react, is one of the most important advantages provided by the hydrothermal methodology. These phenomena are accentuated the higher is the temperature, as described in more detail in the section 1.4.

1.3.1 Phase diagram of the $CaO - SiO_2 - H_2O$ system

Most of the minerals of the CaO-SiO_2-H_2O system can be obtained through hydrothermal route. The formation of one synthetic specie or another depends on the control of numerous parameters, such as the Ca/Si ratio, the time and the temperature of the reac-

tion. Furthermore, the synthesis of calcium silicate hydrate minerals is quite challenging due to the difficulty in manufacturing crystalline and pure single phase materials. Several studies in the literature have investigated the stability between these phases, such as xonotlite, tobermorite, and gyrolite [90, 91, 92, 93]. Figure 1.13 shows the distribution of the numerous crystalline phases of the $CaO\text{-}SiO_2\text{-}H_2O$ system.

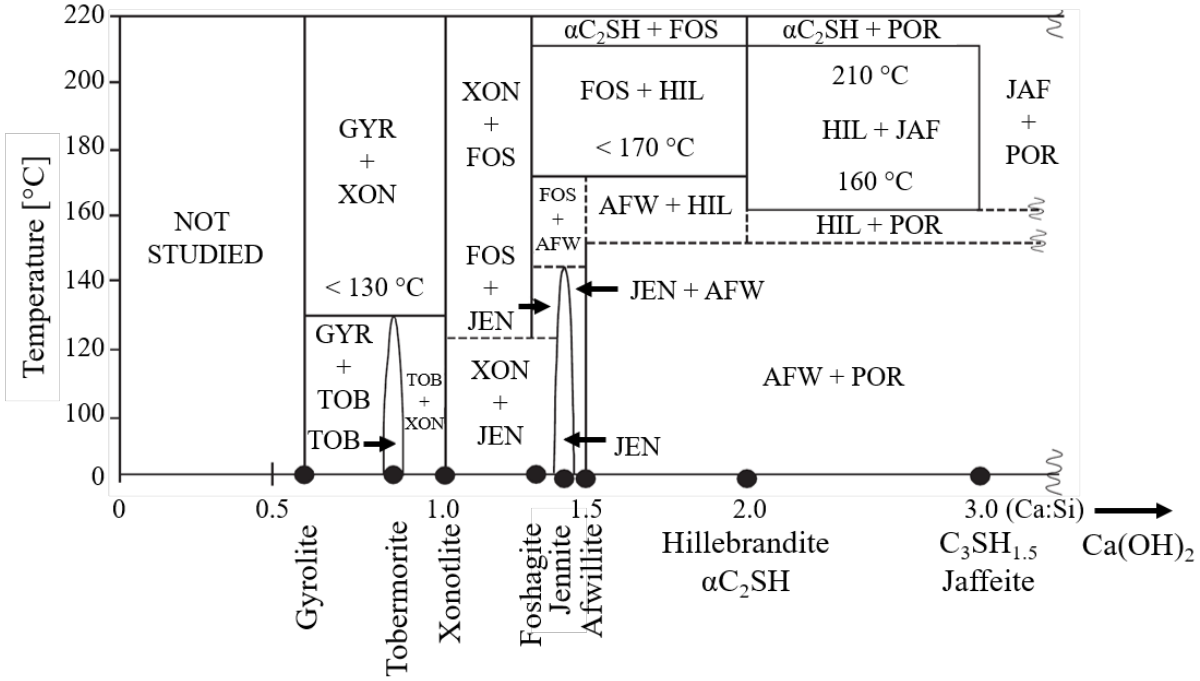

Figure 1.13: Phase diagram of the $CaO\text{-}SiO_2\text{-}H_2O$ system where the Ca/Si molar ratio and the stability region of each phase are shown. The dashed lines indicate uncertainties [93].

This phase diagram was determined as a result of a study based on the hydrothermal synthesis of calcium silicate hydrates with different Ca/Si ratios [93]. From an experimental point of view, it is very challenging to determine the exact conditions for which each phase is stable due to the high complexity of the system and the high number of parameters involved. In this work, we are principally interested in the xonotlite/tobermorite boundary region, as described in the following.

Black *et al.* stated that the 11Å tobermorite has lower stability at high temperature due to the lower polymerisation, in terms of condensation of Si-tetrahedra, if compared with xonotlite [94]. To explain this, the structure of tobermorite must be recalled. An indication of the decreased polymerisation in 11Å tobermorite is related to its structure composed of "dreienfachketten" silicate chains with the typical double chains disposition. They proposed that such double chains in tobermorite structure are not as stable as the xonotlite chains. Preliminary study on the thermal stability of tobermorite reported by

Speakman has shown that below 100 °C only amorphous C-S-H phase can be formed, while above 140 °C crystalline synthetic tobermorite transforms into xonotlite [95]. Furthermore, the thermal stability between these two phases depends, apart from the temperature, on several other experimental parameters, such as the Ca/Si ratio and the pressure. Buckner *et al.* demonstrated that the formation of tobermorite is more favourable at lower Ca/Si molar ratio, more specifically at 0.8 rather than at 1 [96]. Furthermore, pressure plays an important role in determining the xonotlite/tobermorite boundary region. Several studies have been reported that by increasing the pressure, up to 200 MPa, the phase transformation from tobermorite to xonotlite occurs around 280 °C, and so much higher than the value (140 °C) reported by Speakman [95].

Another parameter that can affect the stability of synthetic tobermorite is the addition of aluminium, due to its important effect on the material structure, as previously described. The phase diagram in Figure 1.14 summarises the results obtained for different synthesis of tobermorite over a wide range of temperatures (200 - 310 °C) and aluminium contents (Al/Si+Al = 0 to 0.15).

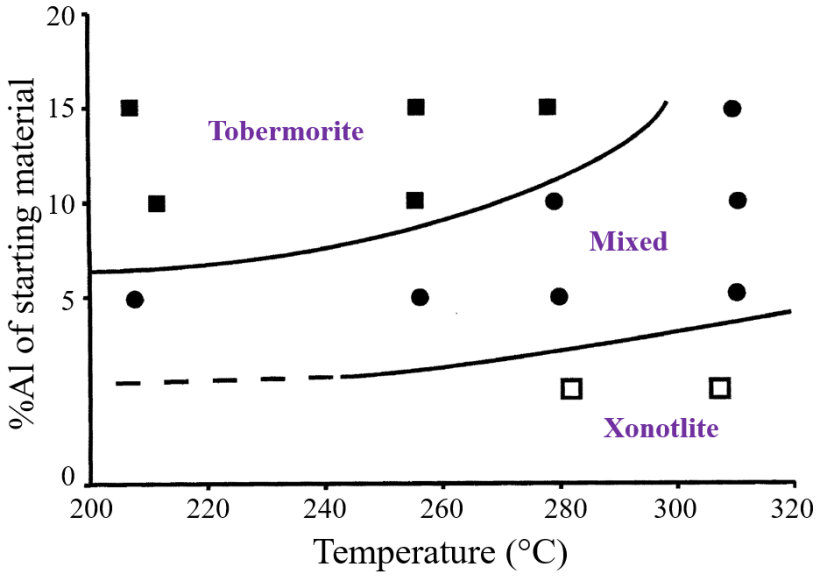

Figure 1.14: Phase diagram of the tobermorite/xonotlite system over a temperature range of 200 - 310 °C at the saturated vapour pressure value. The effect of the aluminium content substituted to silicon (0%, 5%, 10%, and 15%) on the stability of the phases is shown. The different experimental syntheses were performed over a 3 - 5 h time period [92].

As the temperature decreases and the Al/(Al + Si) molar ratio increases, tobermorite becomes the most stable phase; contrarily, by decreasing the Al content and increasing the temperature, xonotlite is the most stable phase, highlighting the thermodynamically unstable nature of tobermorite at high temperature.

To conclude, the unstable nature of tobermorite at high temperature should be related to the lower stability of its double "dreienfachketten" silicate chains, rather than in the case of xonotlite.
The stability of tobermorite is improved, over the transformation into xonotlite, the more the pressure and the Al content are high (up to 200 MPa and Al/(Al + Si) molar ratio equal to 0.15, respectively) and the Ca/Si ratio is low (down to 0.8). However, when comparing the synthesis parameters (temperature, pressure and Al content) to determine the better conditions at which tobermorite is stable, another variable should be taken into account: the duration of the synthesis. In fact, higher is the temperature, lower should be the time to avoid the transformation into xonotlite.
In the following sections, a summary of the state of the art of the hydrothermal synthesis of xonotlite and tobermorite will be reported.

1.3.2 Hydrothermal synthesis of xonotlite

As mentioned in the previous paragraph, xonotlite is one of the most stable phases of the CaO-SiO_2-H_2O system. Consequently, the hydrothermal synthesis of xonotlite and the effects of the experimental parameters as temperature, pressure, type of precursors, and pH of the precursor solution have been widely investigated in the literature.

In 1938, Flint and his research group were the first to explore the synthesis of calcium silicate hydrate phases at different Ca/Si ratios, temperatures, pressures, and reaction times [97]. The experiments were carried out by placing the precursors and the solvent, water, in a closed vessel, which in turn was positioned in a furnace to reach the desired temperature. In this work, the chosen precursors were silica gel as Si-source and lime as Ca-source. Their results have shown that by employing three different Ca/Si ratios, as 0.8, 1 and 1.5, the xonotlite formation was favoured. However, only in the first two cases, the synthesis of pure xonotlite was observed; on the contrary, by increasing the Ca content to 1.5 times over the content of Si, the formation of an additional unknown secondary phase took place. The synthesis of xonotlite was explored within a range of temperatures from 175 °C up to 390 °C. The experimental observations have shown that, as a consequence of the temperature increasing, the reaction time could be shortened: crystalline xonotlite was formed at 175 °C and 0.9 MPa in 79 days, while at 390 °C and 7 MPa only 4 days were required. As results of their numerous experiments, they have fixed the upper temperature limit at which xonotlite is stable at 395 ± 10 °C. This work reported the first xonotlite

synthesis by employing high temperature water (in the vapour phase) in a batch reactor. However, the process was not well described, and the produced materials not accurately characterised. Afterwards, all the studies reported in the literature describe the synthesis in a range of temperature between 150 and 250 °C [98].

The most common employed precursors are CaO and SiO_2 in crystalline or amorphous forms [93, 94, 97, 98, 99, 100, 101, 102]. In addition, also other precursors, such as $Na_2SiO_3 \cdot 9H_2O$ as Si-source, and $Ca(NO_3)_2 \cdot 4H_2O$ [3, 103] or carbide slag [104] as Ca-sources have been investigated. Besides experimental parameters as temperature, pressure and type of precursors, the effect of the precursor solution pH on the synthesis of xonotlite was also investigated [105]. The results have suggested that different pH values, ranging between 12.0 and 13.5, have a slight effect on the material crystallinity, but a strong impact on the particle size: the higher pH value is, the larger the xonotlite fibres are. During a synthesis at 220 °C for 15 h in a solution with pH 13.5, the formation of xonotlite fibres 10 - 30 μm long and 100 - 200 nm wide was observed [105].

To conclude, the most common temperature conditions reported in the literature for the hydrothermal synthesis of xonotlite ranges within 150 and 250 °C [98]. The synthesis time strongly depends on the specific temperature value, from a minimum of few hours ($\sim$ 17h to obtain crystalline single phase material) at 250 °C [7], to much longer times (133 days) at 150 °C [95]. Furthermore, at temperature below 200 °C, the observation of other secondary phases is often observed.

1.3.3 Hydrothermal synthesis of 11Å tobermorite

As above mentioned, the most common type of synthetic tobermorite is the 11Å variety, being the most stable one under hydrothermal conditions. The formation of tobermorite is much more complicated than that of xonotlite, due to the low stability of that phase at high temperature. For that reasons, the challenging synthesis of tobermorite has attracted increasing interest from researchers. As for xonotlite, the most investigated synthesis parameters in the hydrothermal production of 11Å tobermorite are temperature, pressure, type of precursors, and pH of the precursor solution. Two more variables play a crucial role in that synthesis, rather than for xonotlite: the reaction time and the aluminium content. For each parameter, a wide range of values has been explored, making it difficult to ascertain the optimal conditions for synthesising this material. The temperature values range from 140 °C to 240 °C. The synthesis of tobermorite at such low temperature was performed at saturated steam pressure by using C-S-H gel (formed

during 6 - 24 months) and $Ca(OH)_2$ in a Ca/Si ratio equal to 0.83 for 90 days [93]. On the other hand, the synthesis at higher temperature was carried out in 5 h using calcsilicate alkoxide gel as a precursor in a quantity to have Ca/(Si+Al) = 0.83 and Al/(Si+Al) = 0.15 [92].

Regarding the precursors, most of the studies in the literature report the use of CaO and SiO_2. Furthermore, other employed Ca- and Si-source are calcium silicate nitrate, $Ca(OH)_2$, sodium metasilicate [106], C-S-H gel [93], and calcsilicate alkoxide gel [92]. Particular attention has been focused on the Si source: silica acid, silica fume, C-S-H gel, nano SiO_2 have been tested. The synthesis of tobermorite has also been performed by using industry waste products, like cement kiln dust [107], soda-lime-silica container glass [108], and oil shale ash [109]. A very exhaustive study was performed by Mitsuda *et al.* employing CaO as Ca-source and three different silicon/aluminium precursors: colloidal silica with and without γ - Al_2O_3, aluminosilicic (Al_2O_3 - SiO_2) gel and clinoptilolite ($Ca_3(Si_{30}Al_6)O_{72} \cdot 20\,H_2O$) [110]. For each precursor, two different Ca/(Si+Al) molar ratios were tested: 0.8 and 1. Furthermore, they took into account the effect of Al content by employing several $Al/(Al + Si)$ molar ratios, 0%, 5%, 10% and 15%, at two different temperature values, 90 °C and 120 °C, respectively. These experiments have provided important knowledge related to the formation of synthetic tobermorite. First, the Al content promotes the stabilisation and formation of this mineral phase, and the process is more favoured using $Ca/(Si + Al) = 0.8$, rather than $Ca/(Si + Al) = 1$. Second, higher temperature synthesis gives rise to a faster crystallisation of tobermorite. Third, they stated that the most advantageous Si-source in terms of material crystallinity, and rapidity of the process, is the aluminosilicic gel. Using this precursor, the optimal conditions determined in that work for producing crystalline tobermorite were $Ca/(Si + Al) = 0.8$, $Al/(Al + Si) = 0.15$ at 120 °C for 16 h. Nevertheless, the impact of the precursors on the synthesis process was not fully elucidated.

The effect of the precursor solution pH on the morphology of tobermorite particles was also investigated in the literature [111]. As previously discussed, tobermorite phase can crystallise either as platelets or as fibres. Commonly, the reported hydrothermal syntheses give rise to the formation of platy tobermorite. However, controlling the pH value or using surfactants can help to get fibre-like morphology. As an example, the results of Huang *et al.* have shown that the use of EDTA and pH values above 13 promotes the formation of platelets, conversely, fibres can be obtained at higher pH values [111].

To conclude, it appears clear that only an accurate control on the reaction/crystallisation can promote the formation of pure single phase tobermorite and inhibit the formation of other mineral phases. That control is challenging to be achieved in a traditional batch method, where the mild temperatures commonly used involve either the formation of other stable phases or very long synthesis time. For these reasons, a methodology that allows to curtail the synthesis times and capture more truthfully the tobermorite formation process that takes place in nature is needed. In the next section, a manufacturing route which fulfils these requirements will be introduced.

1.4 Current challenges: the supercritical hydrothermal flow synthesis

1.4.1 Definition and properties

A fluid is described as *supercritical* when its pressure and temperature exceed the critical pressure (p_c) and temperature (T_c) [112]. Figure 1.15 shows a schematic representation of the phase diagram of water and the corresponding organisation of molecules in the solid, liquid, gas, and supercritical domains.

In the supercritical domain, the fluid behaves as a media which combines properties of both gas and liquid phases. From a macroscopic point of view, a supercritical fluid (SCF) is considered homogeneous: at the critical point, the density of the gas phase becomes equal to that of the liquid phase, and the interface between gas and liquid disappears. On the other hand, a supercritical fluid is not microscopically homogeneous due to strong fluctuations of the local density. In fact, at the microscopic level, the local organisation of molecules leads to the simultaneous existence of both low (gas-like) and high (liquid-like) density regions. In addition, the local organisation of molecules is dynamic and evolves with a lifetime of about 100 ps, contributing to form high local density inhomogeneities [112, 113].

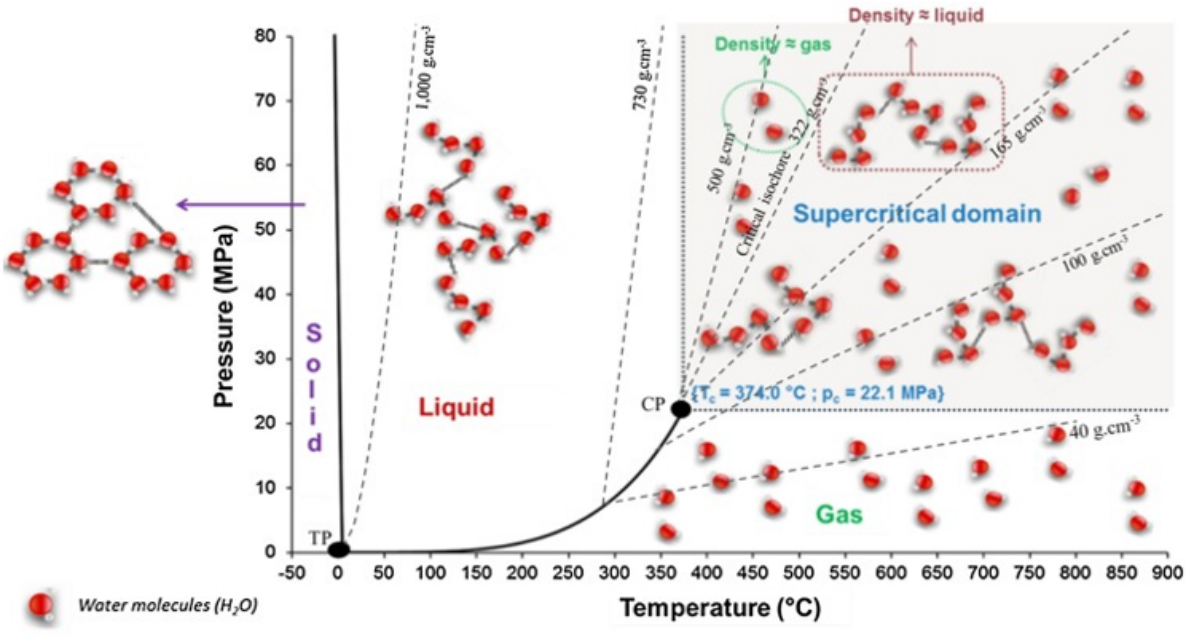

Figure 1.15: Pressure-temperature phase diagram of pure water. *TP* is the triple point ($p_{tp} = 0.612$ MPa, $T_{tp} = 0.01$ °C) and *CP* is the critical point ($p_{cp} = 22.1$ MPa, $T_{cp} = 374$ °C). Some isochoric curves are drawn (dotted lines). A schematic representation of the density and organisation of molecules in the solid, liquid, gas and supercritical domain are shown [114].

The supercritical domain is characterised by unique thermophysical properties, such as high density (solute solubilisation as liquid-like) and low viscosity (transport matrix penetration as gas-like). Supercritical fluids offer the opportunity to vary density, diffusivity, viscosity or surface tension continuously from gas-like to liquid-like values through the control of temperature and pressure, as shown in Table 1.2. These specific properties of SCF are particularly useful to manipulate as desired the reaction environment for applications in material processing [115, 116].

Table 1.2: Principal properties of liquids, supercritical fluids, and gas [112].

	Liquids	Supercritical Fluids	Gas
Density (g/cm^3)	0.4 - 1.5	0.1 - 1	0.001
Diffusivity (m^2/s)	10^{-9}	10^{-7}	10^{-4}
Viscosity ($\mu Pa \cdot s$)	10^3 - 10^5	10 - 100	10
Surface Tension (mN/m)	1 - 100	~ 0	0

In 1992 Tadafumi Adschiri *et al.* were the first to explore the properties of near- and supercritical water (SCW) for chemical reactions and processes [117]. The use of SCW-based technology results particularly interesting to replace hazardous, expensive and polluting organic solvents. Since then, the supercritical fluid technology has become an interdisciplinary field shared by chemists, chemical engineers, physicists, agronomists, as well as researchers in biotechnology [118].

The critical temperature and pressure of water are 374 °C and 22.1 MPa, respectively. The physicochemical properties of SCW, such as the density of molecules (ρ), viscosity (η), dielectric constant (ϵ), diffusion coefficient, and heat capacity differ largely from those of water at ambient conditions [114]. In Table 1.3 the most important water properties are summarised as a function of pressure and temperature [119].

Table 1.3: Physiochemical properties of water as a function of pressure and temperature (liquid, subcritical, supercritical and superheated vapour domain) [119].

	Liquid	Subcritical water	Supercritical water	Superheated vapour
T (°C)	25	250	400	400
p (MPa)	0.1	5	25	0.1
ρ (kg/m^3)	997	800	170	0.3
ϵ	78.5	27.1	5.9	1
η (μPa·s)	890	110	30	20

At room temperature and pressure (25 °C and 0.1 MPa), the density and the dielectric

constant of water assume values equal to 997 kg/m^3 and 78.5, respectively. It has been observed that increasing the temperature, these values are subjected to a drastic fall: in the supercritical region (400 °C and 25 MPa) they assume values equal to 170 kg/m^3 and 5.9, respectively. The low value of ϵ of water under supercritical conditions is nearly equal to those of nonpolar organic solvents under ordinary conditions. This behaviour is related to the reduction of the number and the strength of hydrogen bonds present in water [120, 121, 122]. To explain this phenomenon, it has been suggested that due to strong compression, the double well potential of the hydrogen bond should degenerate into a single well potential [123]. In addition, molecular-based modelling studies proposed that the structure of water evolves from a three-dimensional network of hydrogen bonds, at ordinary conditions, to a hydrogen-bonded configuration of dimers and small clusters, at high temperature and pressure [124]. As a consequence of all these evidence, under supercritical conditions, the polarity of water is as low as nonpolar solvents, which allows the solubilisation of organic compounds and the precipitation of inorganic compounds [125]. In a hydrothermal synthesis, the effect of the dielectric permittivity of water on the material product is significant, as it influences the reaction rate, the equilibrium and solubility of salts in the medium. The evolution of density and dielectric constant as a function of the temperature at 25 MPa is shown in Figure 1.16.

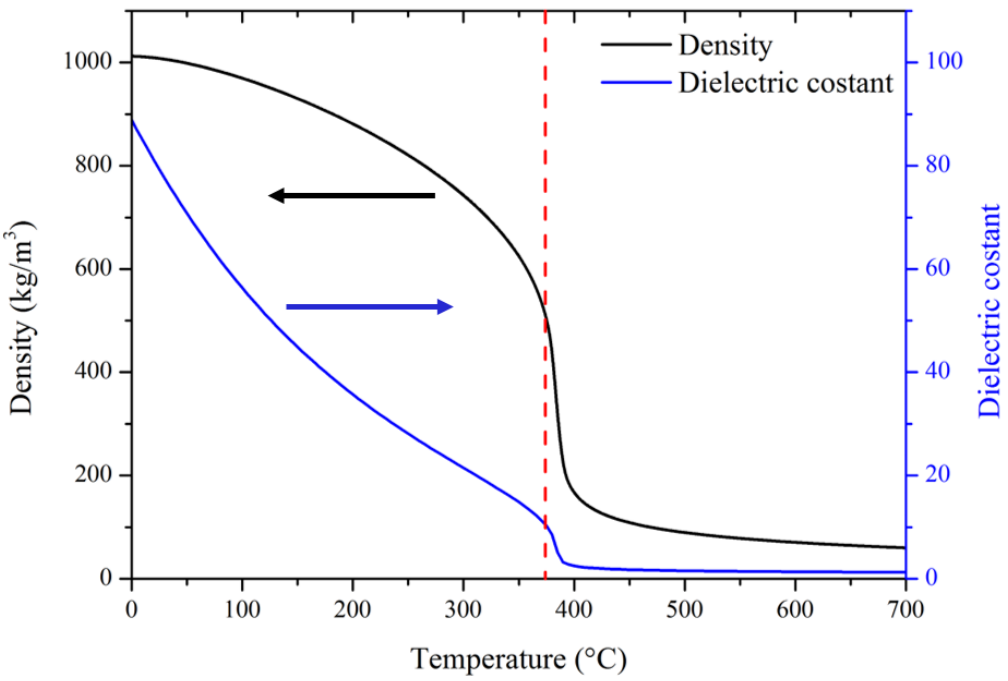

Figure 1.16: Evolution of density (solid black line) and dielectric constant (solid blue line) of pure water as a function of the temperature at 25 MPa. The dotted red line represents the critical temperature. The data were collected from the National Institute for Standards and Technology database, NIST [126].

In terms of kinetics, one of the key properties of supercritical water is related to faster hydrothermal synthesis reactions if compared to the respective reactions at lower temperature. One explanation for this "booster" effect was proposed by Adschiri *et al.* as the enhancement of the reaction rate (k) with the decreasing of the dielectric permittivity, according to the theory of Born:

$$\ln k = \ln k_0 - \frac{\omega}{RT}\left[\frac{1}{\epsilon} - \frac{1}{\epsilon_0}\right] \tag{1.4}$$

where k_0 is the reaction rate at the vacuum permittivity value ϵ_0, ω is a constant related to the reaction system, R is the gas constant, and T is the absolute temperature [85].

Increasing the temperature and pressure, the viscosity of water η is subjected to a considerable decreasing to gas-like values, as shown in Figure 1.17. This phenomenon results in high fluidity, which is very attractive in chemical processes due to the enhancement of the molecular mobility and mass transfer.

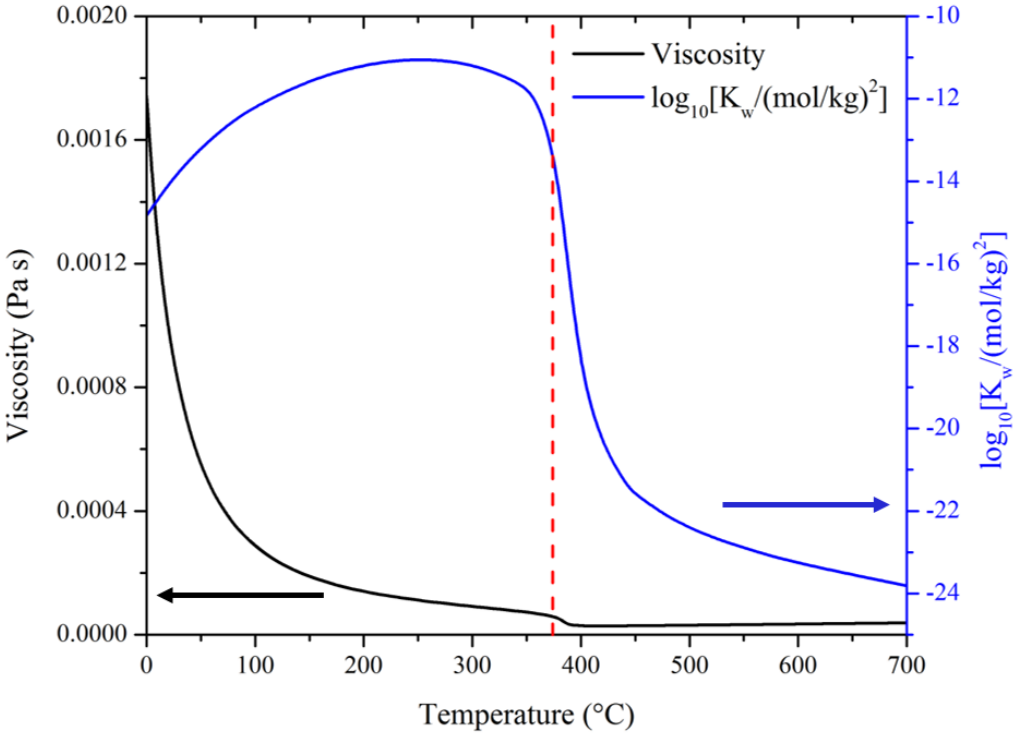

Figure 1.17: Evolution of viscosity (solid black line) and ion product (solid blue line) of pure water as a function of the temperature at 25 MPa. The dotted red line represents the critical temperature. The data were collected from the NIST database [126].

Another interesting property of water, in terms of many applications, is related to its non-dissociating nature. The dissociation equilibrium of water, characterised by the ion

product K_w, can be expressed as:

$$\begin{aligned} H_2O &\leftrightarrows H^+ + OH^- \\ K_w &= [H^+] \quad [OH^-] \end{aligned} \tag{1.5}$$

Under ambient conditions, K_w is equal to 10^{-14} for liquid water and the proton concentration assumes the value of 10^{-7} mol/L [123]. Thermodynamic calculations show a monotone increasing of the ion product with temperature, by about three orders of magnitude, up to 10^{-11} in nearcritical conditions ($K_w = 10^{-11.4}$ at $T = 320$°C and $p = 25$ MPa), as shown in Figure 1.17. Afterwards, as soon as the critical point is reached, a decreasing of the ion product ($K_w = 10^{-20.9}$ at $T = 420$°C and $p = 25$ MPa) is observed [114]. As shown in Figure 1.17, the ion product of SCW is reduced by nine orders of magnitude at 550 °C and 25 MPa if compared with room temperature conditions. Consequently, the pH value of water from ambient to supercritical conditions decreases by three units, resulting in much more hydronium ions for acid-catalysed reactions [127]. This phenomenon provides further evidence of the nonpolar nature of SCW, and has a strong impact in reactions-based on acid–base equilibrium.

To conclude, supercritical water exhibits unique thermophysical properties which differ largely from those of water at ambient condition. SCW is completely miscible with nonpolar compounds, making it an interesting solvent for numerous processes, such as the hydrolysis of organic compounds, pyrolysis [123], and oxidation [125]. In addition, another application field of major interest for SCW is the green and ultrafast synthesis of synthetic minerals, where it acts as a solvent for mimicking the natural conditions of the geological process [2]. In the next section, the advantages of using a supercritical water-based technology for the synthesis of xonotlite and tobermorite will be discussed. Among them there are fast reaction times and the opportunity to finely adjust the reaction kinetics to control the properties of the synthesised material.

1.4.2 Supercritical hydrothermal flow synthesis of xonotlite and tobermorite

In 2017, M. Diez-Garcia in our group provided the first proof of supercritical hydrothermal flow synthesis (SHFS) of calcium silicate hydrates minerals, namely xonotlite and tobermorite [7, 8, 9]. During her Ph.D. work, M. Diez-Garcia exploited both the conventional subcritical hydrothermal synthesis as well as the supercritical water-based

technology for the xonotlite and tobermorite nanoparticles production [7]. She reported the formation of crystalline xonotlite and tobermorite at 400 °C and 23.5 MPa by employing a continuous flow reactor. In that research work, calcium nitrate tetrahydrate and sodium metasilicate nonahydrate were employed as precursors for Ca- and Si-sources, respectively. Furthermore, in the case of tobermorite, aluminium nitrate nonahydrate was added as Al-source, investigating the influence of reaction time and the Al dosage.

The most remarkable result regards the synthesis time: under supercritical hydrothermal conditions, it was shortened from tens of hours, as reported in the literature for the conventional subcritical hydrothermal route, to a few seconds. In particular, their results have shown the opportunity of obtaining highly crystalline xonotlite and tobermorite in 20 and 7 s, respectively.

The new and fast synthesis route reported by Diez-Garcia *et al.* is considered revolutionary in the area of the calcium silicate hydrates synthesis. However, the study of the mineral structures and properties was limited by the trace amount of the produced material, motivating in our work the development of a new set-up.
The first objective of this Ph.D. research has been focused on the design and the development of a more suitable reactor for a higher and more effective minerals production to allow their deep characterisation.
In this context, the development of the reactor represented the first challenge of our work, as several requirements must be met and satisfied. A successful development must maintain both productivity and quality of the chemical process, and the larger-volume process should be at least as robust as the smaller-volume process. In the next chapter, the design to develop the employed user-customised equipment will be described in more detail.
In this contest, this work could open the door to a more flexible and effective production for the industrial uses of the tobermorite and xonotlite in several application fields.

1.5 Conclusions

This first chapter provides an exhaustive overview of the main topics concerning the entire Ph.D. work. First, it has been described the important role of cement in the civilisation process through history, and the development of modern society. Then, the chemical reactions and the complex chemistry involved in the hydration process for the formation of hardened cement paste have been introduced.

In the second part, the structure of minerals which belongs to the CaO-SiO_2-H_2O system, namely xonotlite and tobermorite, and C-S-H gel have been presented. In particular, the similarities between tobermorite and the principal hydration product of cement were described, highlighting the role of tobermorite in the cementitious world.

In the third part, state of the art summarising the most important knowledge on the hydrothermal synthesis of xonotlite and tobermorite was described. The extensive bibliography reported so far in the literature on the production of xonotlite and tobermorite presents a wide and broad range of conditions, resulting in a confusing compilation of information. Especially for tobermorite, due to its metastable nature under certain conditions, it is very difficult to ascertain the optimal synthesis parameters to obtain single and pure phase material, avoiding the xonotlite production as a secondary product. Consequently, we studied the xonotlite/tobermorite boundary regions to find the key parameters in the synthesis of the two phases. The results of several studies revealed that the synthesis of xonotlite is promoted when the Ca and Si sources are mixed with a Ca/Si molar ratio equal to 1. On the contrary, for the synthesis of tobermorite is preferable to add a small quantity of Al, and employing $Ca/Al{+}Si = 0.8$ and $Al/Al{+}Si = 0.15$.

The last part of the chapter described the synthetic route based on the innovative supercritical water technology. Above its critical point (374 °C and 22.1 MPa), water exhibits unique physicochemical properties, which differ largely from those of water under ambient conditions. This methodology, due to its versatility, offers the possibility to finely adjust the process parameters and the reaction kinetics. Consequently, supercritical hydrothermal flow synthesis is particularly useful to manipulate, as desired, the reaction environment for application in materials processing. In the context of CSH production, the main advantage of this technique regards the ultra-fast reaction kinetics: it is possible to synthesise crystalline calcium silicate hydrate nanoparticles, such as xonotlite and tobermorite, in a few seconds in a continuous mode. Furthermore, it should be emphasised that xonotlite and tobermorite obtained under these conditions, are more similar to the natural phases, in terms of morphology, crystallinity and structure, than the synthetic

minerals reported so far in the literature. This experimental evidence suggests that, in addition to the reduced synthesis times, this innovative technology more accurately captures the formation process that takes place in nature.

In the next chapters, we propose to study the effect of different synthesis parameters on the properties of xonotlite and tobermorite through the supercritical water-based methodology. Later, we will explore the application of these synthetic minerals in several fields.

Chapter 2

Experimental set-up and characterisation techniques

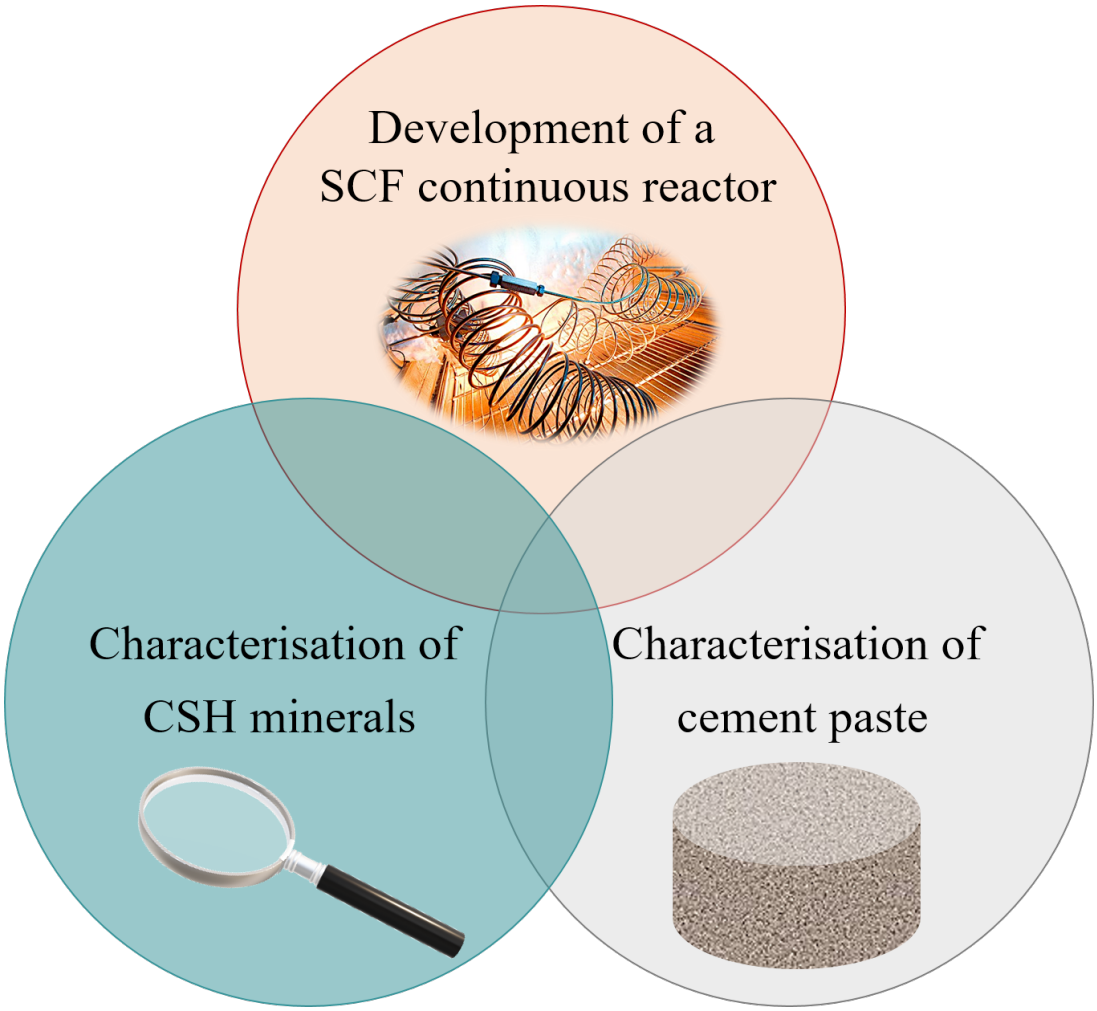

In chapter 1, the interesting peculiarities of supercritical water were presented, highlighting the advantages that a supercritical hydrothermal flow synthesis offers for processing materials.

In the last four years, new perspectives for the supercritical hydrothermal flow synthesis of nanominerals have been opened up, especially thanks to the innovative research work carried out at Institut de Chimie de la Matière Condensée de Bordeaux (ICMCB). The developed methodology combines a flow process and the use of supercritical water for producing different minerals as talc, a phyllomineral [128], tobermorite and xonotlite, two inominerals [2, 7, 8, 9].

The synthesis of xonotlite and tobermorite in supercritical water has been firstly reported by Diez-Garcia *et al.* in 2017 [7, 8, 9]. However, in these studies, the trace amount of produced nanoparticles strongly limited both the deep investigation of structure and properties of the materials, as well as their use in applications, as seeds in cement paste. Consequently, the first main challenge of this Ph.D. research relies on the development of a new experimental set-up being able to produce a significant quantity of CSH nanominerals. To achieve this objective, a work of process engineering was carried out to design and construct a suitable home-made user-customised synthesis equipment.

In this way, this chapter is dedicated to introducing the experimental tools employed in this study for the synthesis and the characterisation of calcium silicate hydrate nanominerals, xonotlite and tobermorite. Firstly, a brief review will summarise the state of the art of the supercritical hydrothermal flow synthesis, providing information on the different approaches. In the second part, a detailed description of the customised home-made continuous flow reactor and the methodology developed as part of this work, will be presented. Lastly, the third section will introduce the different characterisation techniques used to analyse the structural, chemical and physical properties of the synthesised materials.

2.1 An overview of the supercritical hydrothermal flow synthesis

The supercritical hydrothermal flow synthesis has been reported for the first time by Adschiri *et al.* at the beginning of the 90's [117]. Various metal oxides were produced through this methodology, as AlOOH, Co_3O_4, NiO, ZrO_2, Fe_2O_3, Fe_3O_4. In the field of materials science, their work represented a breakthrough, demonstrating the promising role of supercritical water and continuous flow reactors for the rapid and versatile production of highly crystalline nanomaterials of different natures [112, 116, 118]. The flow chemistry offers several advantages over the batch process: faster reactions, feasible scale-up and enhanced safety. Furthermore, a flow synthesis allows better control and a quicker optimisation of the reaction variables. The versatility of the SHFS route permits manipulating the architecture of the nanostructures to obtain different morphologies, such as nanowires and nanotubes as well as composite nanomaterials [115]. For all these reasons, the supercritical technology attracts significant interest for application in microelectronics, optoelectronics and barrier material applications (gas barriers, oxygen barriers, food packaging) [118, 129].

In the last thirty years, numerous research groups have proposed different reactor designs for the SHFS of materials and two main classes of strategy are reported in the literature [116]. The first approach was described by Adschiri *et al.* [117]. A schematic of the set-up developed for producing various metal oxides by rapid and continuous route is shown in Figure 2.1. The experimental strategy can be described as follows. A reagent stream containing the metal salt is brought at the inlet of the reactor and then mixed with a separate stream of water, preheated at near- or supercritical conditions, fed from another line. Here, due to the high concentration of OH^- species in the preheated water stream, a rapid hydrolysis (Equation 2.1) and the consequent production of metal (hydrous) oxide, immediately take place. In the reactor, the dehydration (Equation 2.2) of these hydrous species occurs to produce the metal oxide which precipitates as nanoparticles due to supersaturation of the solution, according to the following equations:

$$ML_x + xOH^- \rightarrow M(OH)_x + xL^- \tag{2.1}$$

$$M(OH)_x \rightarrow MO_{x/2} + \frac{x}{2}H_2O \tag{2.2}$$

Lastly, at the reactor outlet, the reaction solution is cooled down and continuously recovered as a particle-water suspension.

To summarise, the working principle of this approach is based on mixing a cold pre-

cursor solution, and a preheated water stream [85, 130].

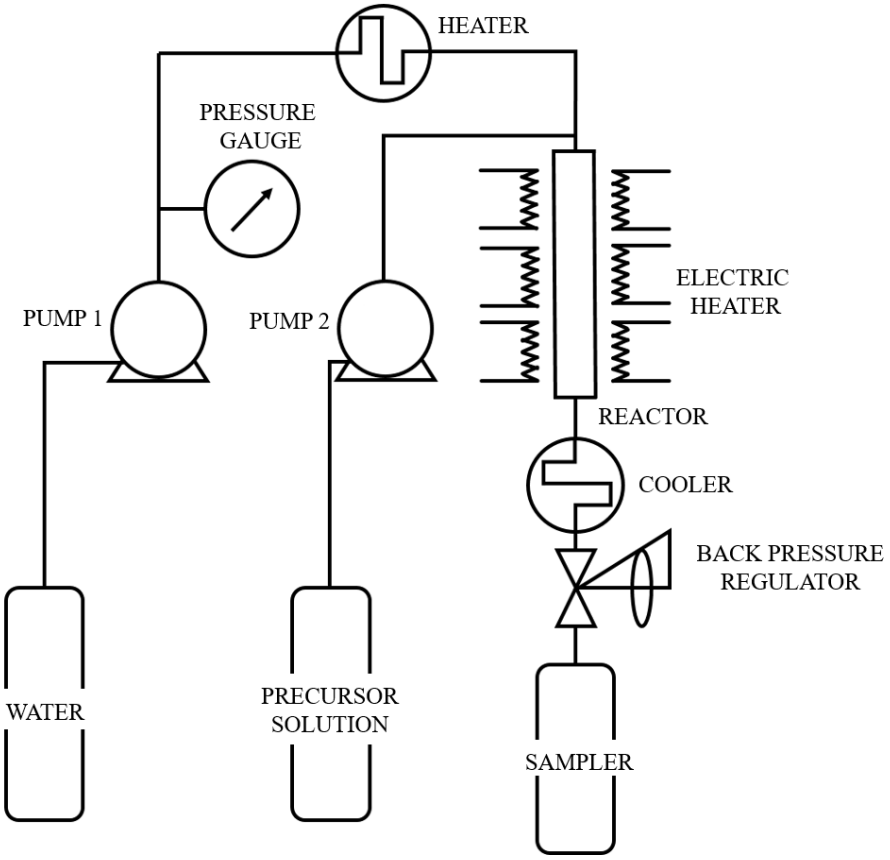

Figure 2.1: Schematic diagram of the reactor configuration developed for the hydrothermal flow synthesis of nanoparticles by Adschiri *et al.*. The reactor was made of a stainless-steel vertical tube, 400 mm long with 9.5 mm internal diameter, and was operating at 400 °C and 30 MPa [117].

This first result represents the starting point for numerous research works focused on studying the mixing, which plays a crucial role in the synthesis process. As an example, Lester and coworkers have deeply investigated the mixing of the flows in a T-piece reactor by the development of *in situ* observations through Light Absorption Imaging (LAI) as well as Computational Fluid Dynamics (CFD) simulations [131]. Through these studies, they proposed some criteria for an ideal optimised mixer.

A different strategy based on a coupling chemistry/chemical engineering/materials science to prepare advanced materials has been developed at ICMCB by researchers within the *Supercritical Fluids Group* [116]. This approach involves the use of one or more pump(s) and injection line(s) maintained at room temperature for the transportation, at specific flow rates, of the precursor solution(s) into a heated, pressurised tubular reactor. Here, the reaction takes place, and the stream containing the produced materials is collected at the outlet. A schematic diagram of this reactor configuration is shown in Figure

2.2. This methodology was applied to study the nucleation and growth of materials of different natures, among them also several nanominerals [2].

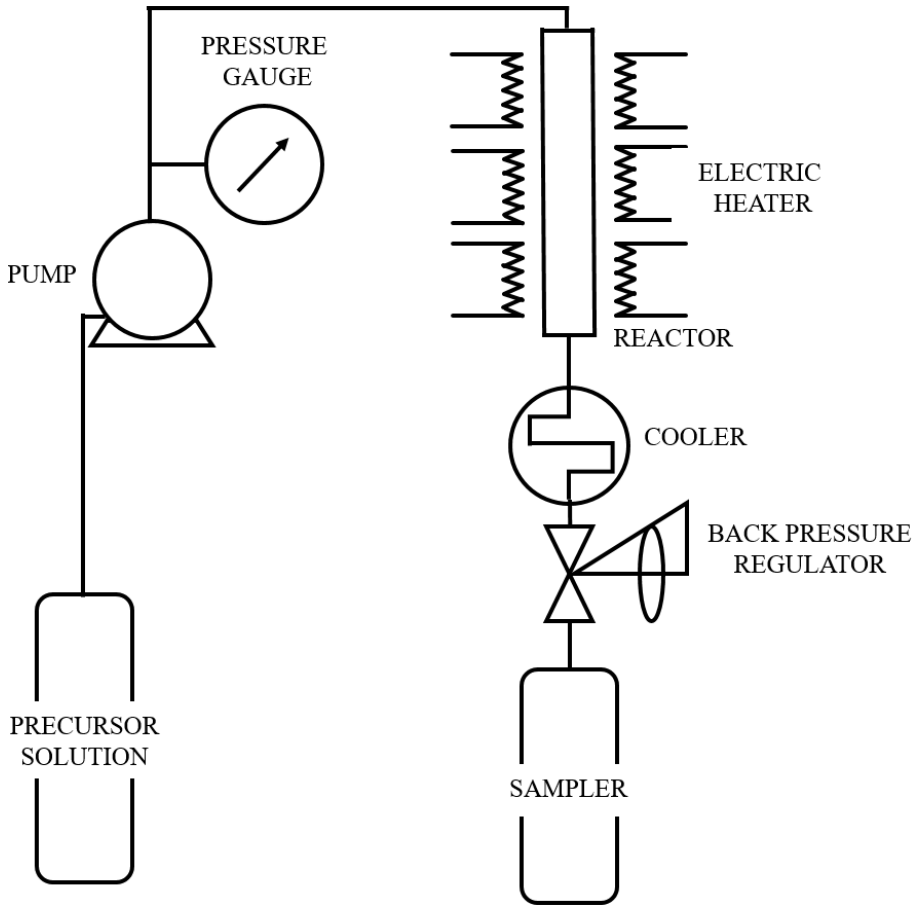

Figure 2.2: Schematic diagram of the reactor configuration developed for the hydrothermal flow synthesis of nanoparticles at ICMCB by researchers within the *Supercritical Fluids Group*.

Independently of the type of approach, some variables must be taken into account for an optimal design. Among them, the most important one to control the nature and the crystallinity of the material product is the residence time. That parameter refers to the time that the growing particles spend flowing through the reactor, and therefore is linked to the reactor's volume, the operating temperature, pressure and flow rate, according to the formula:

$$\tau = \frac{V_r}{Q} \cdot \frac{\rho(T,p)}{\rho(T_0,p)} \tag{2.3}$$

with τ the residence time (s), V_r the volume of the reactor (L), Q the volume flow rate of the solutions (L/s), $\rho(T_0,p)$ and $\rho(T,p)$ the density of the solvent at the inlet of the reactor (kg/m^3; at 25 °C and working pressure), and inside the reactor (kg/m^3; at reaction conditions), respectively.

To conclude, the control on the physicochemical properties of the produced materials in terms of structure, composition, size and morphology, can be achieved by selecting the optimal choice for (i) the type and concentration of precursors, (ii) the solvent, (iii) the temperature, (iv) the pressure, and (v) the residence time.
In this work, supercritical hydrothermal flow synthesis has been investigated as a highly promising process for the synthesis of calcium silicate hydrate nanoparticles. The main interests in using this technology for the production of synthetic nanominerals are:

- Ability to synthesise high quality nanoparticles by using a one-step process,
- Ultra-fast reaction kinetics (tens of seconds),
- Possibility to operate in a continuous mode, which results in higher control of the synthesis parameters,
- Possibility to employ green reaction medium as water,
- Scalability of this methodology towards industrial-scale production.

The next section is dedicated to the detailed description of the designed system, highlighting its advantages.

2.2 Development of a supercritical flow reactor for CSH nanoparticle production

As described previously, the synthesis of xonotlite and tobermorite in supercritical water has been reported firstly by Diez-Garcia *et al.* [7, 8, 9]. However, in their work, beyond the proof of concept, the study of the structure, as well as the applications of the minerals, was limited by the trace amount of the produced material. In fact, most of calcium silicate hydrate minerals have fibre-like morphology which, from an experimental point of view, results in clogging problems. Consequently, the first objective of this work relies on developing an experimental set-up that allows the production of significant quantities of xonotlite and tobermorite, to assess the impact of the experimental parameters on the material properties, and then to be able to use them in several application fields.

To achieve this goal, a work of process engineering was carried out to design, construct, develop, implement and monitor the synthesis equipment. This process has been a challenging and critical part of this thesis work, and can be summarised in two main steps: the design and the construction. Firstly, to avoid any clogging problems, we have decided to scale up a conventional laboratory-scale reactor. The developed supercritical continuous system consists of a home-made user-customised equipment, composed of several task-specific units, some of them commercially available and others specially designed, assembled together. The set-up is highly modular and consequently offers the opportunity to easily configure the equipment with specific requirements. Once the design of the experimental system was refined, the second step was based on the choice of the materials and the construction. To build an effective and robust reactor, the use of appropriate materials for working at high pressure and temperature is crucial. Also, the material must be chemically inert and resistant to corrosion over a reasonable period of time. To fulfil that mentioned requirements, 316L grade stainless steel was an obvious material of choice for the pipes and the fittings.

The supercritical flow reactor for producing calcium silicate hydrate nanoparticles was built at ICMCB in collaboration with Guillaume Aubert. The set-up is composed of three different sections: the injection of the chemical precursors, the reactor where the crystallisation of the CSH nanoparticles takes place, and the product recovery. A process flow diagram and a picture of the entire experimental system are shown in Figure 2.3.

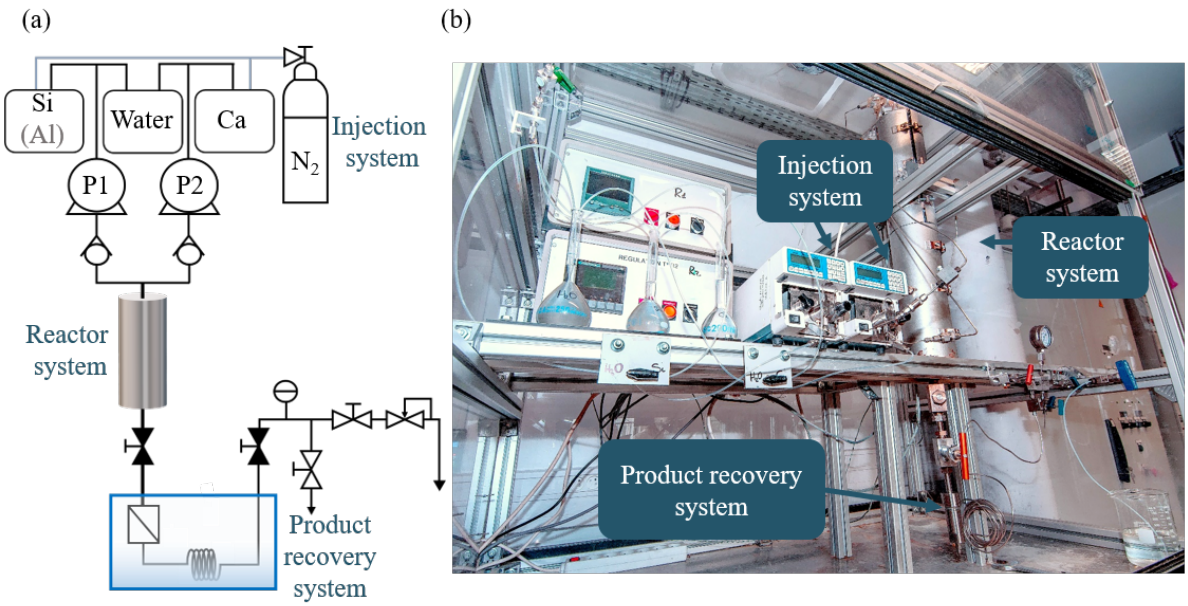

Figure 2.3: (a) Schematic representation and (b) picture of the set-up designed and developed in this work for the flow synthesis of xonotlite and tobermorite in near- and supercritical water.

2.2.1 The injection system

The precursor solutions, the Ca-aqueous solution and the Si-aqueous solution are injected into the system using two separately Jasco Isocratic HPLC pumps (Model PU-2080). This pumping method provides the most stable, accurate, and reliable solution delivery possible. A guaranteed flow rate precision within $\pm 0.1\%$ over the flow rate range 0.1 mL - 10 mL per minute ensures high reproducibility of the process, allowing to study the effect of the residence time on the characteristic of the produced materials. According to Equation 2.3, in our system (reactor volume $= 1.33 \cdot 10^{-5}\,m^3$) the range of residence time accessible for chemical reaction under supercritical hydrothermal conditions (400 °C and 25 MPa) is 6 s - 600 s. Furthermore, the versatility of this technology allows to widen these values range by changing the volume of the reactor.

It has to be highlighted that this model of pump uses soluble precursors due to the susceptibility to solid particles. Consequently, in this work sodium metasilicate nonahydrate ($Na_2SiO_3 \cdot 9H_2O$) and calcium nitrate tetrahydrate ($Ca(NO_3)_2 \cdot 4H_2O$) were chosen as precursor source for Si and Ca, respectively, due to their high solubility in water, used as solvent. Also, a nitrogen line was added to the experimental set-up to prevent the carbonation of the precursor solutions. The line has two branches to keep under a positive flow of nitrogen each of the precursor solutions. The two injection lines, connecting each pump to the inlet of the reactor, were built with 1/8" wide (1.57 mm internal diameter) stainless steel pipes. The reaction of precipitation to form an amorphous calcium sili-

cate hydrate compound occurs at room temperature as soon as the precursors are mixed in the T-mixing piece at the inlet of the reactor. Afterwards, the crystallisation of calcium silicate hydrate nanoparticles occurs inside the reactor under near- or supercritical conditions.

2.2.2 The reactor system

The tubular reactor is the central element of the continuous apparatus. It consists of a 0.74 m of 9/16" diameter stainless steel pipe. The internal and the external diameters are 4.78 mm and 14.29 mm, respectively. The width of the reactor was chosen to prevent clogging problems that could occur due to the fibrous nature of calcium silicate hydrate nanoparticles. Likewise, the reactor length and the volume of the reactor were chosen by taking into account the allowed limit flow values of the pumps to have access to a wide range of residence times, according to Equation 2.3.

Two ceramic band heaters are used to obtain a fast and homogeneous heating up. Each heating element is connected to a Eurotherm temperature controller, which heats via resistive heating by applying electrical power. Two thermocouples in contact to the external walls of the tubular reactor are connected to the temperature controllers to adjust the supplied power depending on the designated set-point value of the temperature. In addition, the reactor part is embedded in an isolating glass wool to prevent heat losses.

In some cases, to achieve very high flow rates and maintain high temperature, an additional preheating unit was incorporated to the system before the inlet of the reactor. This unit was developed by rolling a 1/8" tube of the injection line around a metallic tube placed inside a ceramic band heater and filled with glass wool.

The set-up pressure is controlled and maintained with a manual Tescom Back Pressure Regulator (BPR). In addition, a manometer was added to monitor the pressure. A purge valve was placed after the tubular reactor to evacuate an eventual over-pressure, which could occur during the supercritical synthesis.

2.2.3 The product recovery system

At the outlet of the reactor, the chemical reaction is quenched thermally downstream with an ice bath. Inside the cooling system, a stainless steel fritted filter (5 μm porous size) is placed to collect the produced nanoparticles. Figure 2.4 shows the design of the recovery system: the fritted filter is placed inside a vessel with an inlet and an output through which the reagent stream flows. The filter offers two advantages: firstly, it avoids

the clogging of the tubing in the final part of the set-up, and secondly, it prevents damage to the BPR valve. The fritted filter and the vessel were moulded at the workshop of the ICMCB by Bertrand Guillaume. The home-made user-customised equipment was designed to be highly modular, to easily configure it with specific requirements. For example, the quantity of collected material can be increased by only changing the fritted filter volume, if needed.

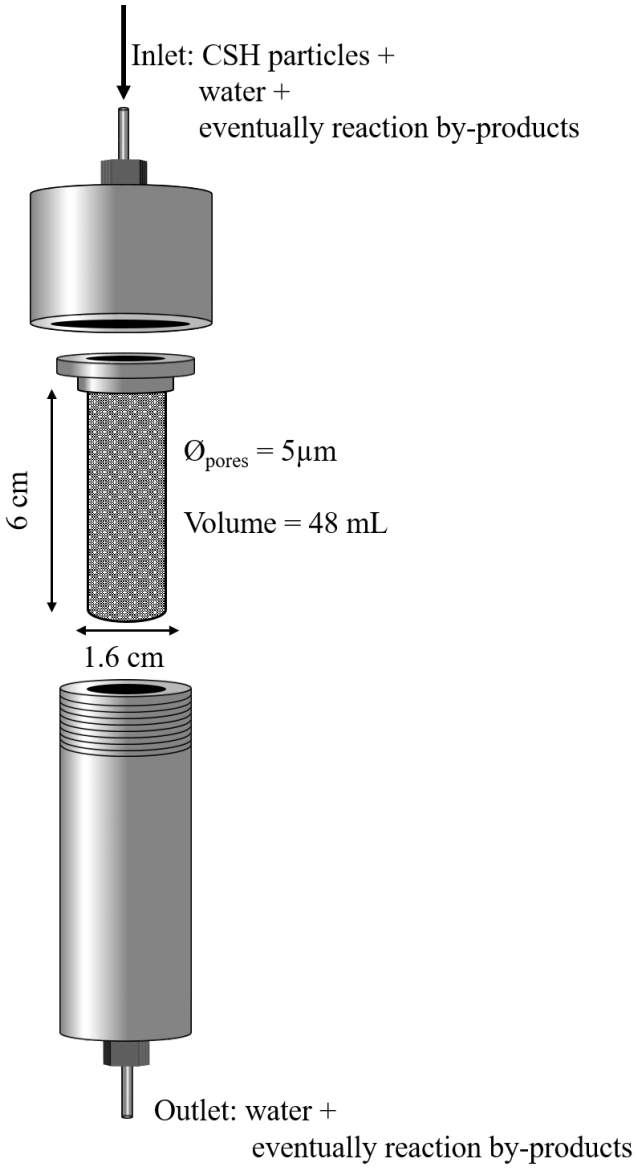

Figure 2.4: Schematic representation of the product recovery system employed in this work.

The work of process engineering, described so far, was followed by an important procedure to make operative the experimental set-up: the temperature calibration of the reactor. To do this, a thermocouple was inserted inside the reactor to control, in different points, the internal variation of temperature over a wide range of flow rates. By this

procedure, it was ascertained the correct value of temperature, at each flow rate, to set in the two Eurotherms to have the desired temperature inside the reactor. After these procedures (design, construction and temperature calibration) the equipment was operational for the syntheses of xonotlite and tobermorite minerals. The accessible operating conditions for the system are summarised in Table 2.1.

Table 2.1: Operating conditions accessible for the calcium silicate hydrates production with the designed reactor.

Section	Accessible Conditions
Injection	0.1 mL - 10 mL
Preheating	25 °C - 200 °C
Reactor	25 °C - 400 °C
	R_t = 6 s - 600 s (T = 400 °C, p = 25 MPa)
Entire system	1 - 350 MPa

The developed experimental set-up allows to produce ∼2.9 g/h of xonotlite (at M = 0.1 mol/L and 7 s) and ∼1.4 g/h (at M = 0.05 mol/L and 8 s) of tobermorite, respectively. Behind the high modularity of the system, two more advantages rely on the fine control of the reaction kinetics through the chosen residence times, and on the possibility to use high molar concentration precursor solutions for an effective production of materials, without the risk of clogging.
In the next section, a detailed description of the characterisation methods used in this work to study the synthesised minerals will be introduced.

2.3 Material characterisation techniques

In this work, several experimental techniques were used to characterise and analyse the structural, chemical and physical properties of the materials from the macro- down to the nanolevel (Figure 2.5).

The first part of the chapter focuses on the description for each characterisation method of the main operating parameters, sample preparation, and the most useful information extracted from the data analysis. The background principles on which the techniques rely are reported in Appendix A.

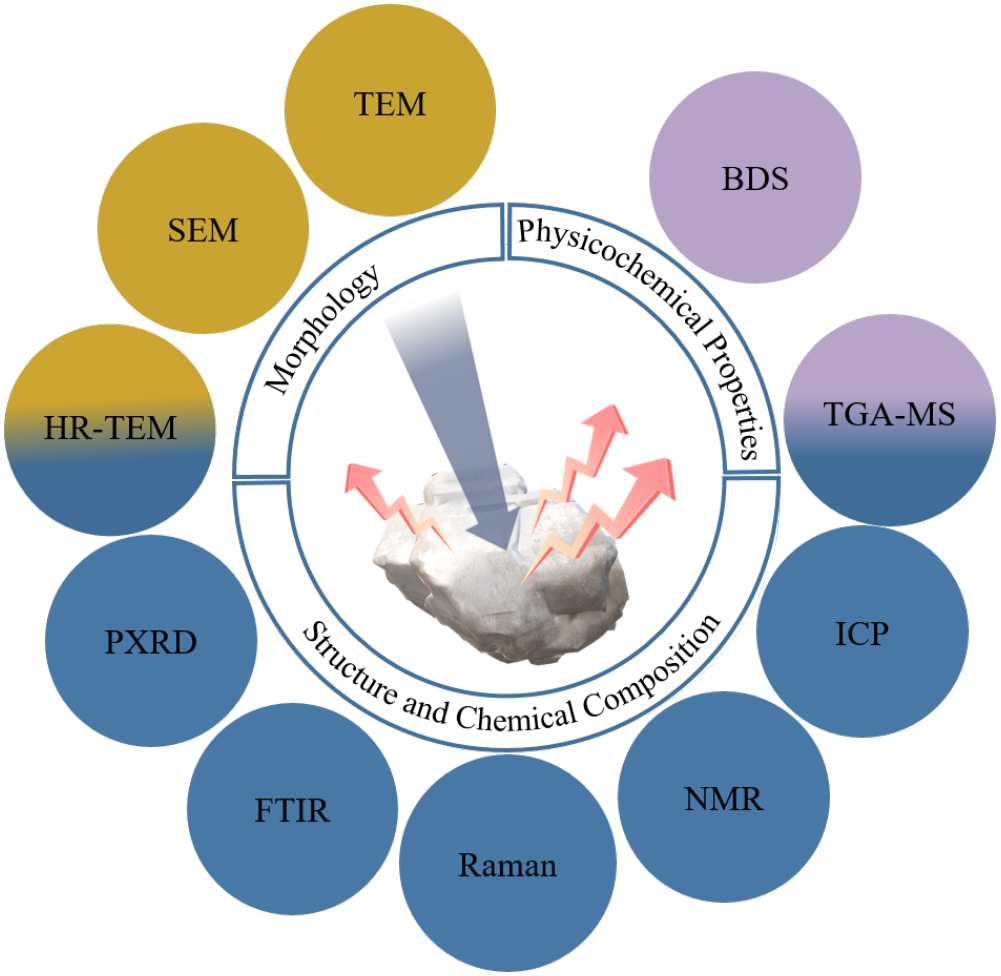

Figure 2.5: Characterisation techniques used for the investigation of the materials synthesised in this work. The morphology has been explored by scanning electron microscopy (SEM), transmission electron microscopy (TEM) and high-resolution transmission electron microscopy (HR-TEM). The structure and chemical compositions have been investigated by powder X-ray diffraction (PXRD), HR-TEM, Fourier transform infrared (FTIR) spectroscopy, Raman spectroscopy, nuclear magnetic resonance (NMR) spectroscopy, and inductively coupled plasma (ICP), thermogravimetric analysis coupled with mass spectrometry (TGA-MS). The physicochemical properties have been analysed by TGA-MS and broadband dielectric spectroscopy (BDS).

2.3.1 Scanning electron microscopy

To investigate the size and the morphology of the minerals synthesised in this work, scanning electron microscopy (SEM) was employed. The analyses were performed at ICMCB on a scanning electron microscope Jeol JSM 6360A. The electron beam operated in the range of voltage between 0.4 - 40 kV, allowing magnification between 10× and 300 000 ×. Also, a high-resolution field emission gun SEM-FEG HR (JEOL 6700F) was employed at PLACAMAT (PLateforme Aquitaine de CAractérisation des MATériaux) in collaboration with Philippe Legros. To carry out a SEM analysis, the dry powder samples were placed in an aluminium stub by using a two-sided carbon tape. Before imaging, as CSH minerals are non-conductive materials, an electrically grounded layer of gold was deposited on the surface using a 108 manual sputter coater equipment. The metal coating allows improving the conductivity of the sample, minimising the negative charge accumulation of the electrons beam.

2.3.2 Transmission electron microscopy

Further investigation of the morphology and the crystallinity of the synthesised mineral powders were performed through transmission electron microscopy (TEM). Transmission electron imaging was carried out at PLACAMAT using a JEOL 1400+ microscope, operating at an acceleration voltage of 120 kV. High resolution imaging was performed at PLACAMAT in collaboration with Marion Gayot and François Weill, by using a JEOL Jem 2200FS FEG high resolution microscope, operating at 200 kV with a range of accessible magnification within 4000× - 600 000× and a resolution of 0.1 nm.

Samples for the TEM analysis were prepared by drop-casting a colloidal suspension containing the nanoparticles on an appropriate support, as described in the following. Firstly, a small amount of powder (< 2 mg) was suspended in ~ 1 mL of ethanol. Successively, to disperse the nanoparticles properly in the solvent, the solution was subjected to sonication in an ultrasonic bath for approximately 15 minutes. Lastly, the solution was deposited dropwise onto a carbon coated copper grid before being left to air dry for several minutes. This procedure leaves the nanoparticles deposited on the grids, ready to be imaged. A sharp image of the nanoparticles deposited onto the carbon film can be achieved due to the very low contrast of the carbon film in transmission mode, related to the low atomic number of carbon and the nanometric thickness of the film.

2.3.3 Powder X-ray diffraction

In this work, the study of the synthesised materials in terms of crystalline structure, chemical composition and identification of the mineral phases was performed through powder X-ray diffraction (PXRD). The measurements were performed at ICMCB by Eric Lebraud and Stanislav Pechev.

The diffraction patterns were collected on a PANalytical X'Pert PRO MPD X-ray diffractometer in Bragg-Brentano θ - θ geometry equipped with an automatic sampler. The radiation source, Cu K_α ($K_{\alpha1}$ $\lambda = 1.5418$ Å, $K_{\alpha2}$ $\lambda = 1.5444$ Å), operated at a generator voltage of 45 kV and a current of 40 mA. Continuous scans were recorded by a X'Celerator multi-strip detector within the range 8.012 - 99.991° (2θ) with a minimum step size of 0.017° (2θ). For the X-ray diffraction measurements, proper sample preparation is a crucial requirement to enhance the signal over noise ratio, avoid fluctuations in intensity, and attenuate preferred orientations. In this work, the samples were finely ground into powder and sieved employing a 100 μm mesh sieve. Afterwards, the powder was placed and uniformly distributed into the sample holder ring to form a flat pellet.

The diffraction patterns of samples used to conduct Rietveld refinement were acquired on a PANalitycal Bragg-Brentano θ - 2θ geometry diffractometer over an angular range within 9.022 and 109.985° (2θ) with a minimum step size of 0.017°. The radiation source, Cu $K_{\alpha1}$ generated at 45 KV and 40 mA, was made monochromatic by using a Ge(111) monochromator. For this measurement, the samples were prepared on a silicon sample holder to avoid any diffraction contribution from the sample holder.

In situ X-ray diffraction studies at high temperature were performed on PANalytical X'Pert Pro diffractometer in Bragg-Brentano θ - θ geometry equipped with a Anton Paar HTK-1200N high temperature chamber. The radiation source was Co K_α ($\lambda = 1.789$ Å). This set-up allows studying phase transformations in different atmospheres at temperature up to 1200 °C. The measurements were performed under N_2 at different temperatures by using a heating ramp of 10 °C/min.

A more sophisticated measurement was carried out on tobermorite through high pressure X-ray diffraction (HP-XRD). This experiment was performed at the beamline 12.2.2 of the Advanced Light Source at the Lawrence Berkeley National Laboratory, Berkeley, California, United States. A BX-90 diamond anvil cell was used in an axial geometry, and the culet diameter of the diamond pair was 400 μm. A cylindrical chamber with a diameter of ~ 110 μm and a thickness of ~ 90 μm was drilled on a stainless-steel gasket using a laser milling machine. Over half volume of the chamber was loaded with densely packed tober-

morite powder. Then, a ruby sphere (α-Al_2O_3 doped with 0.05 wt.% Cr^{3+}) was loaded into the chamber. The ruby was used as a gauge for applied hydrostatic pressure in the chamber. Subsequently, the chamber was filled with a methanol-ethanol solution (4:1 by volume), as the pressure-transmitting medium, and then sealed immediately. The incident X-ray beam energy was 25 keV ($\lambda = 0.4959$ Å and beam size $= \sim 30\,\mu$m). 2D diffraction images were collected by a MAR345 image plate, and then integrated into 1D diffraction patterns. The measurements and the data analysis were performed in collaboration with Jiaqi Li, Postdoctoral researcher in the research group led by Paulo J. M. Monteiro at the University of California, Berkeley.

2.3.4 Fourier transform infrared spectroscopy

Fourier transform infrared (FTIR) spectroscopy was employed in this study as an analytical technique for identifying different types of chemical bonds present in the material of interest. The employed set-up at ICMCB was a BRUKER Equinox 55 FTIR spectrometer which allows detecting the infrared spectra at room temperature over the range 400 - 4000 cm^{-1}. To carry out the measurement, the sample was diluted in another material powder, KBr, which is optical transparent within the mid-IR region.

2.3.5 Raman spectroscopy

The vibrational properties of mineral crystals were also characterised using a Raman spectrometer (HORIBA Jobin-Yvon Xplora) at Centre de Recherche Paul Pascal (CRPP). The system was equipped with a laser of excitation wavelength and spot size equal to 532 nm and $\sim 1\,\mu$m, respectively. Prior to analysis, the instrument was calibrated using the 520.5 cm^{-1} line of a silicon wafer. The measurements were performed using a 50× objective, gratings with 1200 or 2400 lines/mm and a CCD detector. Repeated acquisitions of the spectra in the 200 - 3800 cm^{-1} range with an exposure time of 30 s were acquired to improve the signal-to-noise ratio.

2.3.6 Solid-state nuclear magnetic resonance spectroscopy

Solid-state nuclear magnetic resonance (SSNMR) is a probe for the local structure at the atomic nearest neighbour and next nearest neighbour scale, and thus provides significantly different information than diffraction methods. In this work, we employed it to investigate the environments of proton and silicon sites in xonotlite and Al-substituted tobermorite. In that later mineral, the position of aluminium atoms in the crystal structure

was further analysed. In the following, the four different types of SSNMR measurements (^{29}Si, ^{27}Al, ^{1}H-^{29}Si and ^{1}H SSNMR) conducted in this work will be introduced.

a) ^{29}Si SSNMR

The analysis of ^{29}Si SSNMR spectrum allows to study the structure of silicates and aluminosilicates: the close correlation between the chemical shift and the structural properties provides an analytical 'fingerprints' to reveal complex structural details of the sample. The silicate structures are usually described by the conventional Q^n nomenclature where Q indicates a SiO_4 tetrahedron unit coordinated to other n ($0 \leq n \leq 4$) tetrahedral centres by an oxygen atom. In this notation, the ^{29}Si SSNMR peaks can be identified as Q^0 which represents an isolated tetrahedron, Q^1, Q^2, Q^3 or Q^4 if the tetrahedron shares one, two, three or four oxygen atom(s) with other tetrahedron(a), respectively. The chemical shift depends on the local structural arrangement of the first and second nearest neighbour atoms, and in silicate materials is typically defined within the range between -60 and -120 ppm. Figure 2.6(a) shows that the presence of an additional tetrahedral unit with –O–Si bonding results in a displacement of approximately 10 ppm to more negative chemical shifts. However, the chemical shift regions are not exclusive for each resonance, and the signals can overlap.

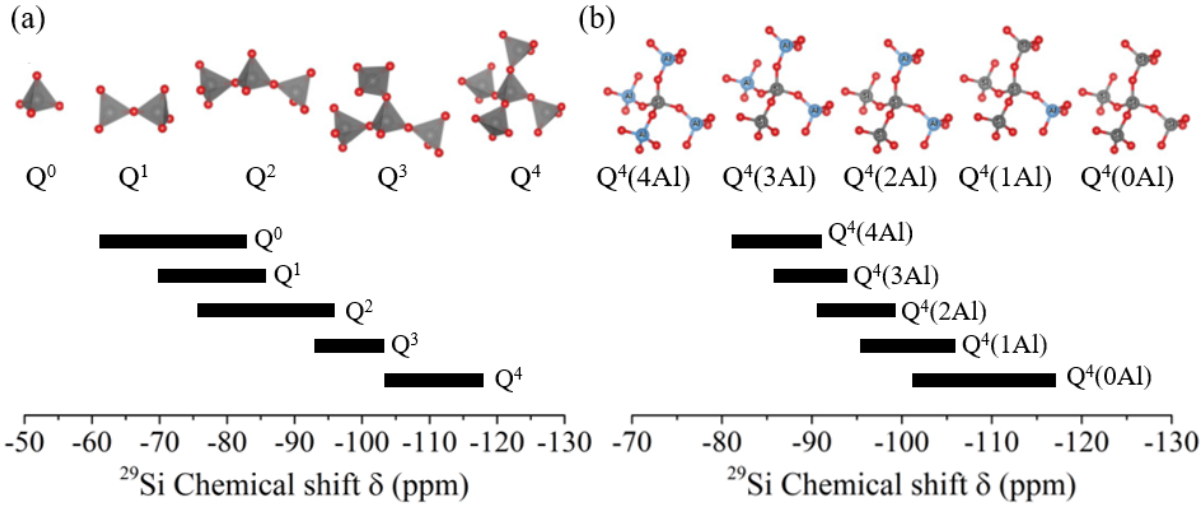

Figure 2.6: Typical ranges of ^{29}Si chemical shifts for (a) Q^n and (b) $Q^n(m\text{Al})$ sites in silicates and aluminosilicates. In the scheme it is possible to identify the different Si positions as a function of n and m values. Si, O and Al atoms are represented by grey, red and blue spheres, respectively (adapted from [132]).

A similar notation is used to study the aluminosilicates, where an isomorphic substitution of aluminium replacing silicon takes place. Silicon sites are commonly identified using the $Q^n(m\text{Al})$ nomenclature with $0 \leq m \leq n \leq 4$, where a silicate tetrahedral centre

(represented by Q) is bonded to n other tetrahedra (m of which are Al atoms) through oxygen bridges. Q^n(1Al) refers to a Si atom surrounded by one Al atom and n oxygen atoms, likewise Q^n(2Al) refers to a Si atom enclosed by two Al and n oxygen atoms, *etc.* Consequently, the introduction of Si–O–Al linkages results in the displacement of the ^{29}Si chemical shift towards less negative values of roughly 5 ppm, as shown in Figure 2.6(b). That phenomenon provides an important tool for differentiating $Q^n(m\text{Al})$ sites as a function of n and m.

b) ^{27}Al SSNMR

^{27}Al SS-NMR analysis is used to identify the aluminium coordination structures based on the resulting chemical shifts. The Al centres are typically differentiated by q^n notation, where q refers to aluminium in tetrahedral coordination bonded to n ($0 \leq n \leq 4$) tetrahedral silicon centres through oxygen bridges. Tetrahedral and octahedral Al centres typically resonate in the ranges 80 - 50 ppm and 20 - 0 ppm, respectively. Although, resonances that refer to highly distorted tetrahedral Al environments and five-coordinated Al are commonly detected within the region 50 - 20 ppm.

c) ^{1}H SSNMR

In the context of this work, ^{1}H SSNMR results notably helpful for exploring local environments in mineral structure where the role of hydrous species, H_2O and OH, is of high relevance. This technique allows to distinguish between Ca–OH and Si–OH chemical environment, and to detect molecular water adsorbed on the mineral surface and eventually interlayer water.

d) ^{1}H-^{29}Si cross polarisation SSNMR

^{1}H-^{29}Si cross polarisation (CP) NMR, contrarily to the direct pulse NMR described up to now in this section, allows the acquisition of the spectra of less abundant nuclei more rapidly and with a higher signal-to-noise ratio. The basic principle of CP SSNMR is based on the transfer of magnetisation from the nucleus with highly-abundant spins to a nucleus with low-abundant spins, by the irradiation of both nuclei at their resonant frequencies during a contact time. Consequently, the response from the less abundant nucleus in the immediate proximity to the more abundant one is amplified. That phenomenon allows obtaining further information on the connectivity or spatial proximity of spins. ^{1}H is the most abundant nucleus in calcium silicate hydrate minerals, and so ^{1}H-^{29}Si CP NMR enhances the signals from Si atoms, which are directly bonded (or in proximity) to ^{1}H

atoms.

e) Experimental implementation of SSNMR analysis

In this work, the SSNMR data were collected and processed in collaboration with Paula Sanz Camacho and Mathieu Duttine. NMR spectra were acquired at European Institute for Chemistry and Biology (IECB) of Bordeaux using either a Bruker Avance 300 MHz spectrometer equipped with a 7.05 T wide-bore magnet, or a Bruker Avance 500 MHz spectrometer equipped with a 11.7 T wide-bore magnet. The experiments were performed at room temperature using a standard 2.5- or 4-mm magic angle spinning (MAS) probe with MAS rates of 10 or 30 kHz, respectively. Magic angle spinning NMR, allows to spin the sample at an angle of $\cos^2(\theta_{MAS}) = 1/3\,(\theta_{MAS} = 54.74°)$ in respect to the static magnetic field to remove anisotropic interactions and obtain narrower spectral lineshapes.

For ^{1}H solid-state NMR a rotor-synchronised Hahn-echo sequence was employed with a $\pi/2$ pulse. The chemical shifts are referenced relative to ultrapure Milli-Q water (shift: + 4.7 ppm). While, for ^{29}Si solid-state NMR, the spectra were acquired either directly (using a short pulse length of 2.4 μs) or using cross polarisation from ^{1}H with square contact pulse of 3, 6 or 10 ms. In that case, chemical shifts refer to silicon oil at -22 ppm. For ^{27}Al, a short pulse of a length of 1 μs corresponding to a selective $\pi/12$ pulse was applied. Chemical shifts are referenced relatively to $Al(NO_3)_3$ at 0 ppm. The operating conditions for each measurement are summarised in Table 2.2

Table 2.2: SSNMR operating conditions employed in this work.

	^{1}H NMR	^{29}Si NMR	^{29}Si CP NMR	^{27}Al NMR
Larmor frequency (MHz)	300.13	59.62	300.13, 59.62	78.20
Pulse length (μs)	2	2.4	2	1
Contact pulse (ms)	-	-	3, 6 or 10	-
Recycling delay (s)	5 or 10	10 or 30	3	1

All the spectra were deconvoluted using DmFIT program [133]. For very thin signals, individual Lorentzian peaks were used, while a combination of Gaussian and Lorentzian (in ratio equal to 0.5) were used when broaden peaks were observed.

2.3.7 Thermogravimetric analysis

Information about physical and chemical phenomena, as phase transition via dehydration, which could occur when the sample is subjected to heating, was obtained by thermogravimetric analysis. The thermal behaviour of xonotlite and tobermorite nanominerlas was investigated at Centro de Física de Materiales (CFM) using a TA Instruments Q500 thermogravimetric analyser. During the analysis, the samples were heated from room temperature up to 800 °C with a rate ramp of 5 °C/min under a constant N_2 flow of 60 mL/min. A thermogravimetric analysis coupled with mass spectrometry (TGA-MS) was performed at ICMCB using a TGA Setaram TAG2400 combined with a Pfeiffer Thermostar mass spectrometer. The measurements were carried out in Ar atmosphere in the range 25 - 1100 °C using a heating rate of 10 °C/min.

2.3.8 Inductively coupled plasma/optical emission spectrometry

A quantitative chemical analysis of the outlet water containing the reaction by-products was conducted at ICMCB using a Varian ICP/OES 720-ES spectrometer. The solution was diluted with Milli-Q water using a properly dilution factor to obtain a similar medium, in terms of chemical species concentrations, to that used for the calibration solutions. During the measurement, the concentrations (mg/L) of Ca, Si, Al and Na present in the outlet water were determined. To test the reproducibility and repeatability of the results, for both xonotlite and tobermorite, the outlet solutions of three different syntheses were analysed.

2.3.9 Broadband dielectric spectroscopy

Broadband Dielectric spectroscopy (BDS) is a versatile and powerful technique to investigate the dielectric properties of a material, and thus it is of particular interest for both fundamental and application-oriented researches. Among its main advantages, there are the opportunity to explore a wide frequency range, and the flexibility in state of matter, size and shape of samples. This technique allows to study the material response, in both the time or frequency domain, to an alternating (sinusoidal) external electric field oscillating at a frequency $\omega = 2\pi\nu$ [78]. The dielectric properties of the material are described by the complex dielectric function, given by:

$$\epsilon^*(\omega) = \epsilon^{'}(\omega) - i\epsilon^{''}(\omega) \tag{2.4}$$

where $\epsilon^{'}(\omega)$ and $\epsilon^{''}(\omega)$ are the real and imaginary part of the complex dielectric function [78, 134].

Under the electric field, a polarisation is induced into the sample due to different involved phenomena. Depending on the typical timescale, the polarisation mechanisms can be classified as (i) electronic or atomic polarisation, (ii) orientational or dipolar polarisation, (iii) ionic polarisation, and (iv) charge migration polarisation [135]. The type of induced phenomenon depends clearly on the frequency of the external field, as shown in Figure 2.7.

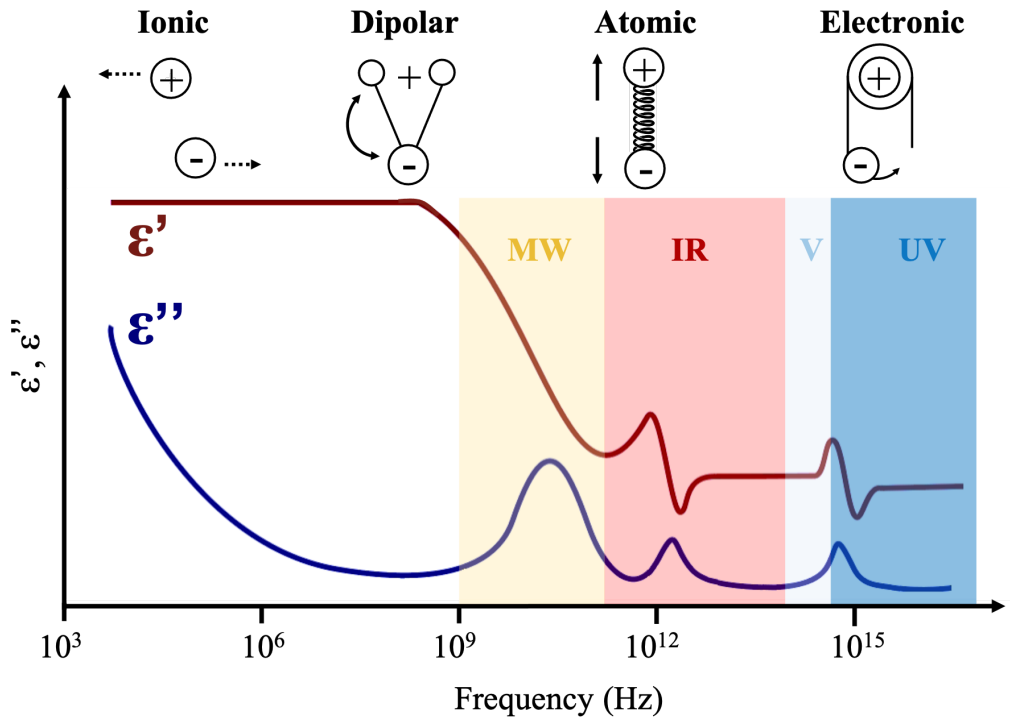

Figure 2.7: Illustration of dielectric response over a wide range of frequencies. $\epsilon^{'}$ and $\epsilon^{''}$ indicate the real and the imaginary part of the permittivity, respectively. Several processes are pictured as a function of the frequency: ionic and dipolar relaxations, and atomic and electronic resonances (adapted from [135]).

Electronic polarisation usually occurs in neutral atoms at high frequencies due to the displacement of the electron cloud slightly away from its equilibrium position [135]. This phenomenon is considered an instantaneous process and is observed in the optical frequency band. At lower frequencies, the atomic polarisation is defined as a deformation of the arrangement of the atomic nuclei in a molecule or lattice. This process is due to a temporary dipole moment generated in all the atoms of the material, and it is also known as vibrational polarisation. Atomic polarisation is around two orders of magnitude slower than that of the electron displacement (due to the higher mass), and thus is characterised

by lower resonant frequencies. As a consequence it can be observed in the frequency region of infrared [135].

In dipolar materials, which possess a permanent dipole moment, the orientational or dipolar polarisation can take place. The phenomenon is related to the alignment of molecular dipoles (initially randomly oriented) in the direction of the applied electric field. The molecular dipole can orient over a wide range of time scales (frequencies), being the process highly dependent on intra- and intermolecular interactions. Consequently, the intermolecular potential, the degree of cooperativity between molecules, the number and the size of involved molecules can affect the dielectric response [135]. It is worth mentioning that this type of polarisation is also influenced by the temperature, as the thermal energy randomises the alignment of the molecules.

On the other hand, a mechanism that is commonly observed in ionic solid, inorganic crystals, glasses and ceramic is the ionic polarisation, also known as displacement polarisation. The phenomenon relies on the asymmetric sharing of electrons between several atoms within a molecule. As a result, the electron cloud shifts towards the stronger-binding atom [135]. The ionic species can highly affect the dielectric properties of the material, giving rise to high permittivity value.

Lastly, charge migration polarisation is observed when in a material there are charge carriers capable of migrating through the sample, creating a macroscopic field distortion. This phenomenon can occur via diffusion, fast ionic conduction, or hopping (i.e. when charges, as ions and vacancies or electrons and holes, can hop from one site to another) [135].

To conclude, at high frequencies, the molecular dipoles are incapable of following the variations in the direction of the field, and consequently the dielectric permittivity will be related to the electronic and atomic polarisation. Nevertheless, as the frequency decreases, the molecular dipoles will start to orient in the electric field's direction, resulting in a partial orientation. The degree of orientation of molecular dipoles will continue increasing with further decreasing of the frequency, which corresponds to an increase in the dielectric permittivity. Finally, the molecular dipoles can reach a state of a full orientation at low enough frequency, which will produce a static value of the dielectric permittivity.

So far, we have described the processes that can occur in a material when subjected to an external electric field. When turning off the field, another phenomenon, termed dielectric relaxation, occurs. The decay of polarisation to zero value is not an immediate process but takes a specific finite time, depending on the time required for the dipoles to

randomly re-orient. The basic principles on which relies the experimental measurement of the complex permittivity will be introduced in the following.

The measurement of the permittivity through a dielectric spectrometer is based on the physical principle for which a sample placed between two metallic disk-shaped electrodes form a capacitor (Figure 2.8). The capacitance, C, of such parallel-plate capacitor is given by [134]:

$$C = \epsilon \cdot \epsilon_0 \frac{A}{d} \tag{2.5}$$

where ϵ is the relative dielectric permittivity of the material under study, ϵ_0 the vacuum permittivity ($8.85 \cdot 10^{-12}$ F/m), A is the area of the plate and d is the distance separating the two plates.

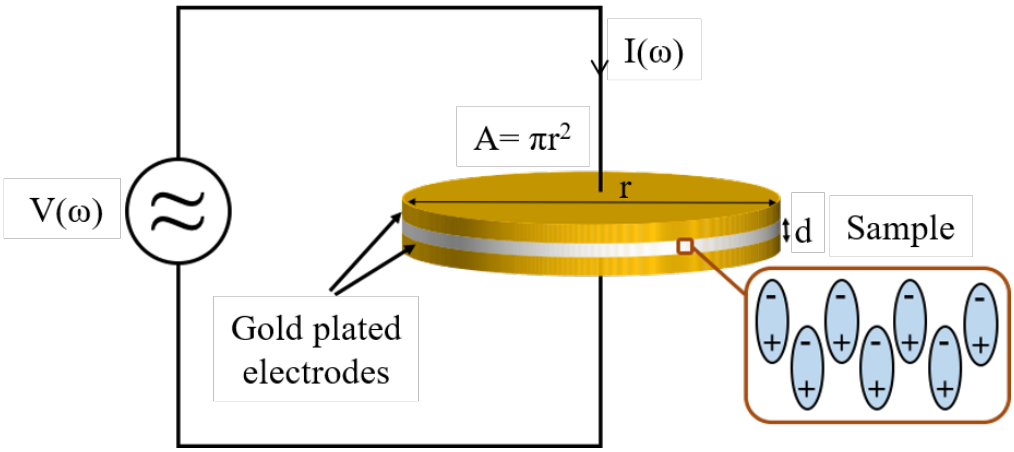

Figure 2.8: Schematic representation of the experimental set-up: the sample, of thickness d, placed between two gold disk-shaped electrodes of area A forms a capacitor of capacitance C.

During the experiment, a sinusoidal voltage is produced by a generator and applied to the capacitor. The voltage signal, $V(\omega)$, can be expressed as:

$$V(\omega) = V_0 \sin(\omega t) \tag{2.6}$$

characterised by an amplitude V_0 and an angular frequency ω [134]. Therefore, the generated current, which flows through the sample, oscillates at the same frequency, but shifted in phase:

$$I(\omega) = I_0 \sin(\omega t + \phi) \tag{2.7}$$

where the amplitude I_0 and phase ϕ are linked to the driving voltage. For easy calculation and representation of the formulas, it is more convenient to use complex notations [136]:

$$V(\omega) = Re(V^*(\omega)\, e^{i\omega t}) \tag{2.8}$$

and

$$I(\omega) = Re(I^*(\omega)\, e^{i\omega\, t + \phi}) \tag{2.9}$$

with

$$V^*(\omega) = V^{'} + i\, V^{''} = V_0 \tag{2.10}$$

and

$$I^*(\omega) = I^{'} + i\, I^{''} \tag{2.11}$$

$$I_0 = \sqrt{I'^2 + I''^2} \tag{2.12}$$

$$\tan(\phi) = \frac{I^{''}}{I^{'}} \tag{2.13}$$

In that mathematical notation, an asterisk immediately following the variable will be used to indicate a quantity that is a complex number [136].

The complex impedance of the system is defined as the ratio between the applied voltage and the response current, and its expression is given by [137]:

$$Z^*(\omega) = Z^{'} + i\, Z^{''} = \frac{V^*(\omega)}{I^*(\omega)} = \frac{V_0}{I^*(\omega)} \tag{2.14}$$

The equation which express the complex dielectric function, Equation 2.4, can be rewritten from Equation 2.5 as:

$$\epsilon^*(\omega) = C^*(\omega) \cdot \frac{d}{\epsilon_0 A} = \frac{C^*(\omega)}{C_0} \tag{2.15}$$

where $C^*(\omega)$ denotes the complex capacitance and C_0 the capacitance of an empty capacitor. Furthermore, the complex impedance for a single parallel plate capacitor can be also expressed as:

$$Z^*(\omega) = \frac{1}{i\omega\, C^*(\omega)} \tag{2.16}$$

Consequently, extracting the value of $C^*(\omega)$ from Equation 2.16 and replacing it in Equation 2.15, the complex permittivity can be redefined as [137]:

$$\epsilon^*(\omega) = \frac{-i}{\omega\, Z^*(\omega)\, C_0} \tag{2.17}$$

From this calculation, it appears clear that the determination of $\epsilon^*(\omega)$ is essentially based on the measurement of the complex impedance of the sample, $Z^*(\omega)$. As a consequence, $\epsilon^*(\omega)$ can be experimentally determined by measuring the applied voltage and the response current over a frequency range.

To study the dielectric response of a sample, the imaginary part of the dielectric

permittivity, $\epsilon^{''}(\omega)$, is plotted as a function of the frequency. $\epsilon^{''}(\omega)$ is also denominated dielectric loss, being a measure of the field energy dissipated into the sample [78]. In a loss spectrum, several peaks can appear at different frequencies and temperatures, related to different relaxation processes. For each process, the characteristic time for the dipole relaxation can be defined as:

$$\tau_{max} = \frac{1}{2\pi\nu_{max}} \tag{2.18}$$

where ν_{max} represents the frequency at the maximum loss (maximum value of $\epsilon^{''}(\omega)$).

In the next part, the analytical tools necessary for understanding the analysis of dielectric data will be presented.

a) Phenomenological and empirical relaxation models

In the literature, several functions have been suggested to describe the dielectric relaxation processes [78, 135]. The most important of these models are examined in the following.

The simplest approach to calculate the time dependence of a polarisation process is illustrated in the Debye model [78]. That approach describes the relaxation response of an ideal, non-interacting population of freely rotating dipoles to an alternating external electric field. Debye assumed that after turning off the field, the decreasing of the orientational polarisation is directly proportional to the polarisation value itself, according to the following first-order differential equation:

$$\frac{\partial\vec{P}(t)}{\partial t} = -\frac{1}{\tau}\vec{P}(t) \tag{2.19}$$

with τ the *Debye-relaxation time*, a parameter linked to the dynamics of the system. In this scenario, the permittivity is estimated from the Debye equation, as follows:

$$\epsilon^{*}(\omega) = \epsilon^{'}(\omega) - i\epsilon^{''}(\omega) = \epsilon_{\infty} + \frac{\Delta\epsilon}{1+i\omega\tau} \tag{2.20}$$

where $\Delta\epsilon$ is the dielectric relaxation amplitude (or dielectric strength) defined as the difference between the low and the high frequency limit of the permittivity, ϵ_s and ϵ_∞, respectively. Figure 2.9(a) shows the plot for both the real and the imaginary parts of the Debye function. It can be noticed that the imaginary part is symmetric around $\omega = \tau^{-1}$.

The Debye model, despite being suitable to describe the relaxation for certain molecular reorientation, i.e. isotropic rotational diffusion, it fails for explaining the relaxation behaviour of many other systems. Generally, the experimentally measured dielectric re-

sponse presents a much broader loss peak than the one predicted by the Debye model. In addition, their shapes are sometimes asymmetric with a high frequency tail. Consequently, numerous other empirical or semi-empirical model functions, mostly extensions of the Debye equation, have been developed for modelling a non-Debye behaviour [78, 135].

Kenneth S. Cole and Robert H. Cole proposed the first empirical expressions for $\epsilon^*(\omega)$ in 1941 [138, 139]. The Cole-Cole equation describes a symmetrically-broadened dielectric function given by the formula

$$\epsilon^*(\omega) = \epsilon_\infty + \frac{\Delta\epsilon}{1 + (i\omega\tau_{cc})^\alpha} \tag{2.21}$$

where the parameter $\alpha \in]0;1]$ describes the symmetrical broadening of the relaxation time distribution around the so-called Cole-Cole relaxation time, τ_{cc}. In that model, τ_{cc} represents the position of maximal loss: $\omega_{max} = 2\pi\nu_{max} = 1/\tau_{cc}$.

In Figure 2.9(b) the real and imaginary part of Cole-Cole equation for different values of α are plotted. It has to be noticed that for α equal to 1, the Cole-Cole equation converts to the Debye equation.

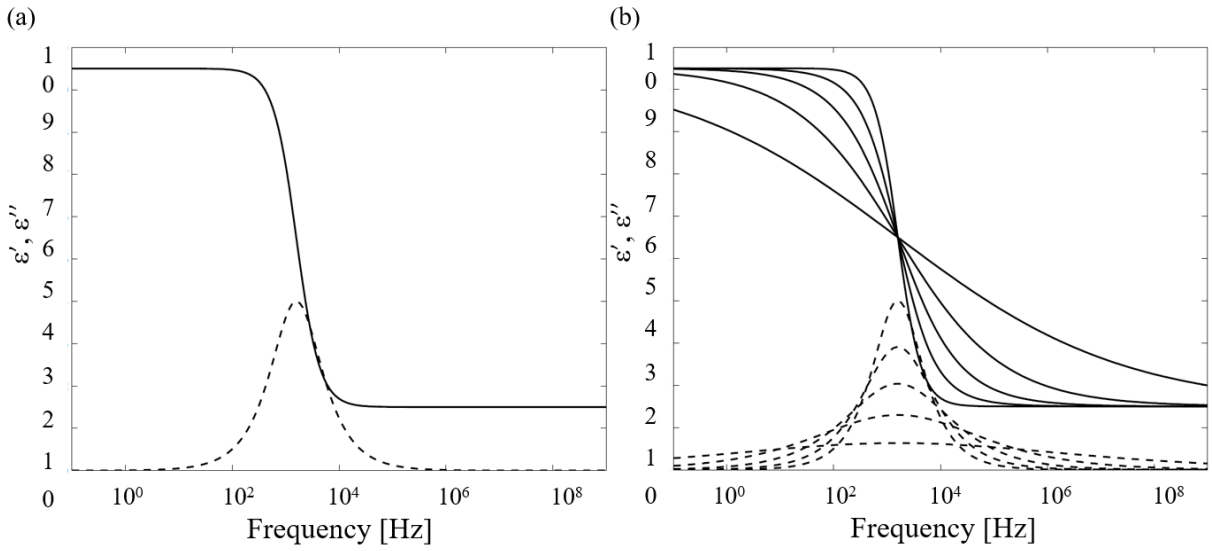

Figure 2.9: The full and the dashed line represent the real part $\epsilon^{'}(\omega)$ and the imaginary part $\epsilon^{''}(\omega)$ of the complex permittivity, respectively. (a) Plot of the Debye relaxation function. The Debye equation is plotted using a semilogarithmic plot and $\epsilon_\infty = 1.5$, $\epsilon - \epsilon_\infty = 8$ and $\tau = 10^{-4}$. (b) Plot of the Cole-Cole relaxation function. The real and the imaginary part of Cole-Cole equation are plotted for $\alpha = 1$, $\alpha = 0.8$, $\alpha = 0.6$, $\alpha = 0.4$, and $\alpha = 0.2$. Decreasing the value of α the peak becomes lower and broader [140].

For describing asymmetric distribution of the imaginary part $\epsilon^{''}$, for example, if the relaxation peak is much broader at the high frequency side, the Cole-Davidson equation

can be employed [141, 142]:

$$\epsilon^*(\omega) = \epsilon_\infty + \frac{\Delta\epsilon}{1 + (i\omega\tau_{CD})^\beta} \tag{2.22}$$

with $\beta \in]\,0\,;1\,]$, for $\beta = 1$ the Cole-Davidson equation corresponds to the one described in the Debye model (Equation 2.20).

A more general model which allows representing simultaneously broad and asymmetric relaxation time distributions is defined by the Havriliak-Negami relaxation function [143, 144]:

$$\epsilon^*(\omega) = \epsilon_\infty + \frac{\Delta\epsilon}{[1 + (i\omega\tau_{HN})^\alpha]^\beta} \tag{2.23}$$

where α and β take into account the broadening and the skewing of the peak at high frequency, respectively. The Havriliak-Negami equation is a combination of Cole-Cole and Cole-Davidson equations, and for $\alpha = 0$ and $\beta = 1$ is identical to the Debye function (Equation 2.20).

b) Temperature dependence of the relaxation process

The temperature dependence of the relaxation times is generally studied by using two main approaches. The simplest one is based on the Arrhenius activation model, in accordance with:

$$\tau = \tau_0 \exp \frac{E_a}{k_B T} \tag{2.24}$$

where τ_0 is a temperature-independent parameter which refers to the molecular vibration time, E_a is the activation energy, i.e. the energy barrier to overcome for the process to take place, and k_B is the Boltzmann's constant. This approach is based on the phenomenon for which the relaxation time (frequency) of a dynamic process increases (decreases) upon decreasing the temperature. The simple Arrhenius model is often not really suited to describe several systems, and instead the Vogel-Fulcher-Tamman (VFT) equation results to be more appropriate [145, 146, 147]. This equation is given by:

$$\tau_\alpha = \tau_0 \exp \frac{B}{T - T_{VFT}} \tag{2.25}$$

where B is a temperature-dependent parameter and T_{VFT} is defined as the Vogel temperature. It can be observed that if $T_{VFT} = 0\,\mathrm{K}$, the VFT function is identical to the Arrhenius equation (2.24) with $B = E_a/k_B$.

c) Experimental implementation of BDS analysis

In the framework of this study, the complex dielectric permittivity of xonotlite and tobermorite was determined by a Novocontrol Alpha-N broadband dielectric spectrometer at CFM. Prior to analysis, the mineral powder was placed between two parallel gold plated electrodes with a diameter of 30 mm. The sample cell was prepared by pressing the powder manually between the electrodes to form a pellet as compact as possible, being careful that the material is completely covering the surface of the electrodes. As shown previously in Figure 2.8, the capacitor plates separation, d, corresponds to the sample thickness, which was determined to be 0.4 mm using a calibre. Once the sample was placed inside the dielectric cell cryostat of the equipment, it was dried at 105 °C for 1 h to remove the evaporable water content. Successively, it was subjected to a fast cooling (rate $>$ 20 K/min), and the measure of $\epsilon^*(\omega)$ was recorded by isothermal frequency scans every 5 K within a temperature range of 100 - 300 K. At higher temperature, the isothermal frequency scans were performed on heating every 10 K. During the experiment, the sample temperature was maintained stable within 0.1 K by a nitrogen gas flow. A totality of 76 frequency points were recorded for each sample in the frequency range from 10^{-2} Hz to 10^6 Hz. The dielectric spectra were analysed using the WINfit software developed by Novocontrol [148]. We have used the Cole-Cole functions to describe broadened loss peaks related to nanoconfined water dynamics in xonotlite and tobermorite minerals. The measurements and the data analysis were carried out in collaboration with Guido Goracci, Postdoctoral researcher in the *Ceramic and Cement-Based Materials* group led by Jorge S. Dolado at CFM.

2.4 Cement paste characterisation methods

In this section, the characterisation techniques employed to analyse the cement paste properties will be presented (Figure 2.10). In particular, the study focused on the role of calcium silicate hydrate nanoparticles to trigger the quick formation of the principal hydration product of the cement, the C-S-H gel.

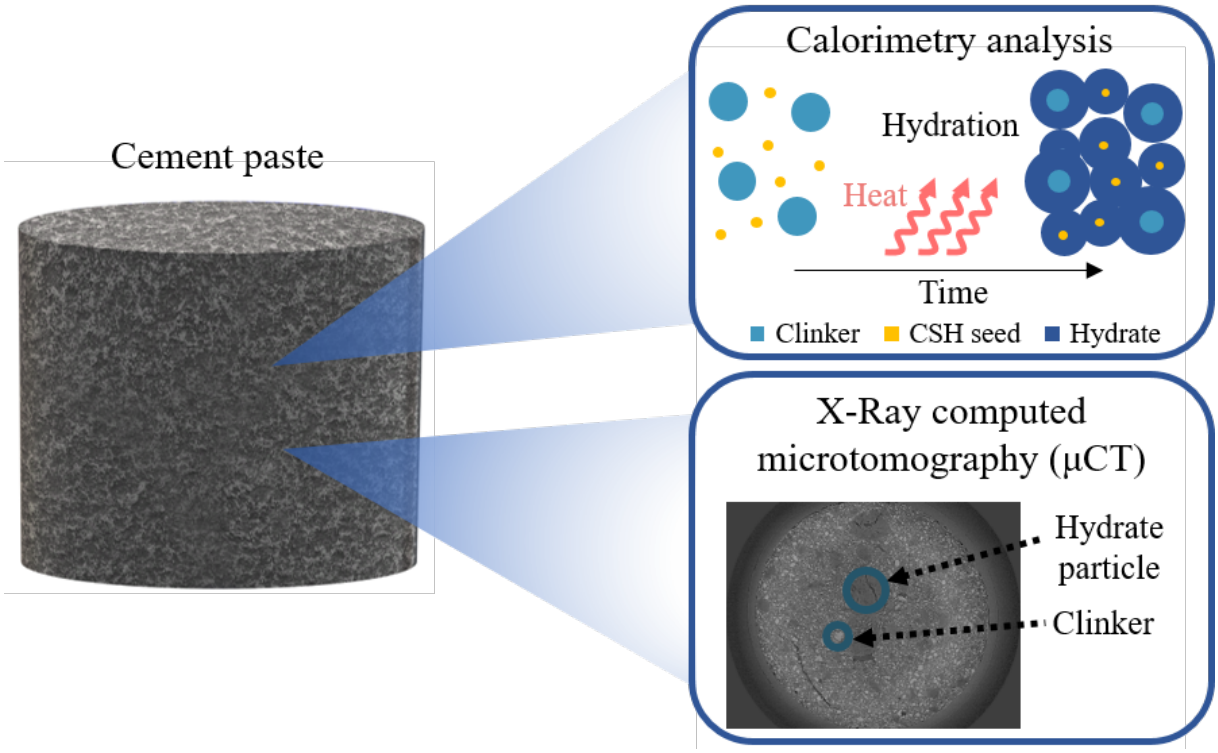

Figure 2.10: Schematic representation of the characterisation techniques employed to study the seeding effect of xonotlite and tobermorite nanoparticles into cement paste.

2.4.1 Calorimetry analysis

The calorimetry analysis is commonly employed to measure the heat released into or absorbed from the environment during a chemical reaction. Within the frame of our work, this technique was used as a sensitive tool for studying the exothermic hydration process of cement over time. As discussed previously in chapter 1, the heat evolution is strongly correlated to the rate of the chemical reactions which take place during hydration, and chemical additions also influence it. Consequently, the effect of calcium silicate hydrate minerals as seeds can be detected by monitoring the hydration curve changes.

In the following, the procedure employed to prepare the cement paste specimens will be presented. The protocol developed in this study comprises the following steps, shown in Figure 2.11:

1. Dispersing the nanoseeds in DI water and sonicating for 120 s,
2. Adding the obtained colloidal suspension to the cement powder,
3. Mixing for 90 s at 800 rpm by using a vortex mixer,
4. Waiting for 60 s,
5. Mixing for 90 s at 1000 rpm by using a vortex mixer.

All cement pastes were prepared using ASTM type I cement and fixing the cement/water ratio to 0.5. In the seeded pastes a variable concentration of dried CSH nanoparticles, 0.5 wt.% or 1 wt.%, per weight of cement was employed.

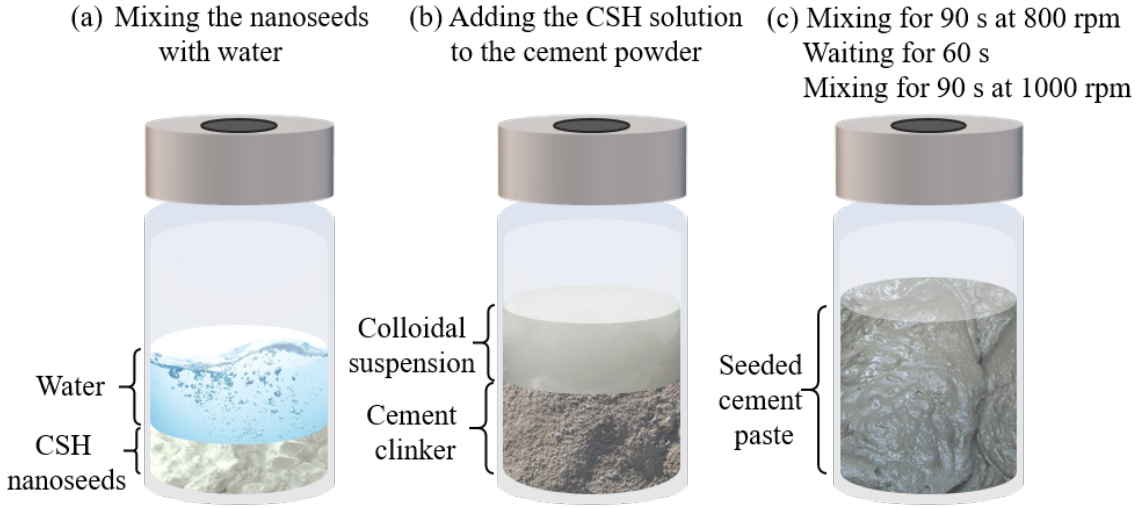

Figure 2.11: Schematic representation of sample preparation for calorimetric measurements.

To carry out the analysis, 5 g of cement paste was placed into the calorimetric ampule, as schematically represented in Figure 2.11(c), and then loaded into the isothermal calorimeter within 6 min after the initial contact of clinker with water. The calorimeter block consists on an air-based thermostat utilising a heat sink to conduct the heat produced by hydration away from the sample. The heat flow is then detected and converted into the heat evolution rate by applying the correction from the reference and the calibration. To ensure reliability and reproducibility of the measurement, the calorimeter is designed to minimise the outside temperature effects. The calorimetric equipment used at CFM was a TAM Air isothermal calorimeter designed with eight separated units, or channels, which allows testing eight samples simultaneously. The sample under investigation was placed into a 20 mL hermetic glass bottle, and the measurement was performed at $25 \pm 0.001\,^{\circ}\mathrm{C}$, using water as a reference. Being interested in the early stage hydration of cement paste, the measurements were carried out for 48 h for each sample.

2.4.2 X-ray computed microtomography

X-ray computed microtomography (X-ray μCT) provides a complementary approach for studying the hydration process of cement paste over time, and thus the seeding effect of CSH nanoparticles. The basic principle is based on the 3-dimensional computed reconstruction of a material specimen from 2-dimensional X-ray images collected at different angles around the axis of rotation of the sample. A schematic illustration of the X-ray computed microtomography measurement is shown in Figure 2.12.

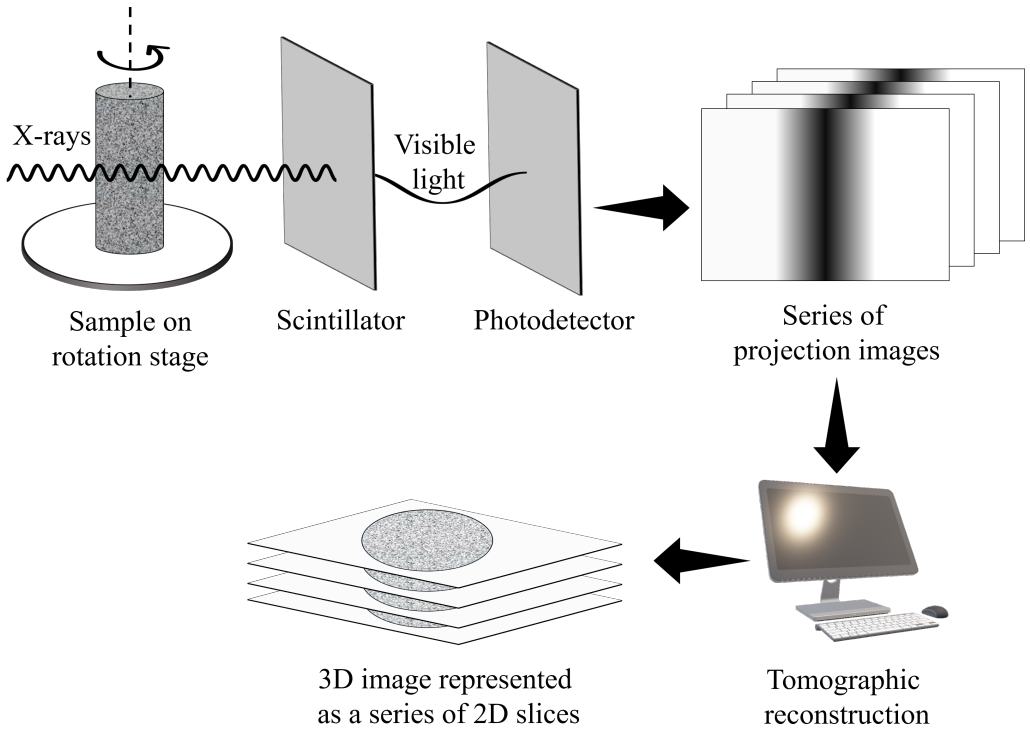

Figure 2.12: Schematic illustration of X-ray computed microtomography workflow. The tomographic apparatus includes the X-ray source, the specimen understudy, a scintillator and a photodetector. The raw output of the tomogram is a series of projection images recorded at different angles during the rotation of the sample. 2D Projections are then digitally 'reconstructed' to produce a 3D map of X-ray absorption in the sample volume.

In this work, synchrotron X-ray microtomography was used to explore the spatial distribution of the crystallographic phases within the cement paste at different hydration times. The use of synchrotron radiation offers several advantages. Among them, there are the feasibility to obtain high quality, low-noise images at the submicron resolution, and phase contrast imaging at very short exposure times. Synchrotron X-ray computed microtomography measurements were carried out at the 8.3.2 beamline of the Advanced Light Source (ALS) at the Lawrence Berkeley National Laboratory, Berkeley, California, United States. The analysis was performed in collaboration with Ke Xu, Ph.D. student in

the research group led by Paulo J. M. Monteiro at the University of California, Berkeley.

Figure 2.13(a) shows a schematic representation of the principal instrument components of the beamline 8.3.2 [149, 150]. The source of the beamline is a 4.7 Tesla magnetic field in a superconducting dipole. As the synchrotron electron beam crosses the magnet, a wide range of light wavelengths is emitted, and successively a specific X-ray wavelength is selected by a monochromator. The sample and detection components are placed inside the hutch, as shown in Figure 2.13(b). The translation of the sample in the plane perpendicular to the X-ray beam propagation is ensured with a 0.1 μm precision by a motorised stage. Translation and rotation stages are used to slide and adjust the material rotation centre to ensure that the sample will remain in the field of view during the rotation. The sample centring is, thus, a critical procedure prior to the measurement.

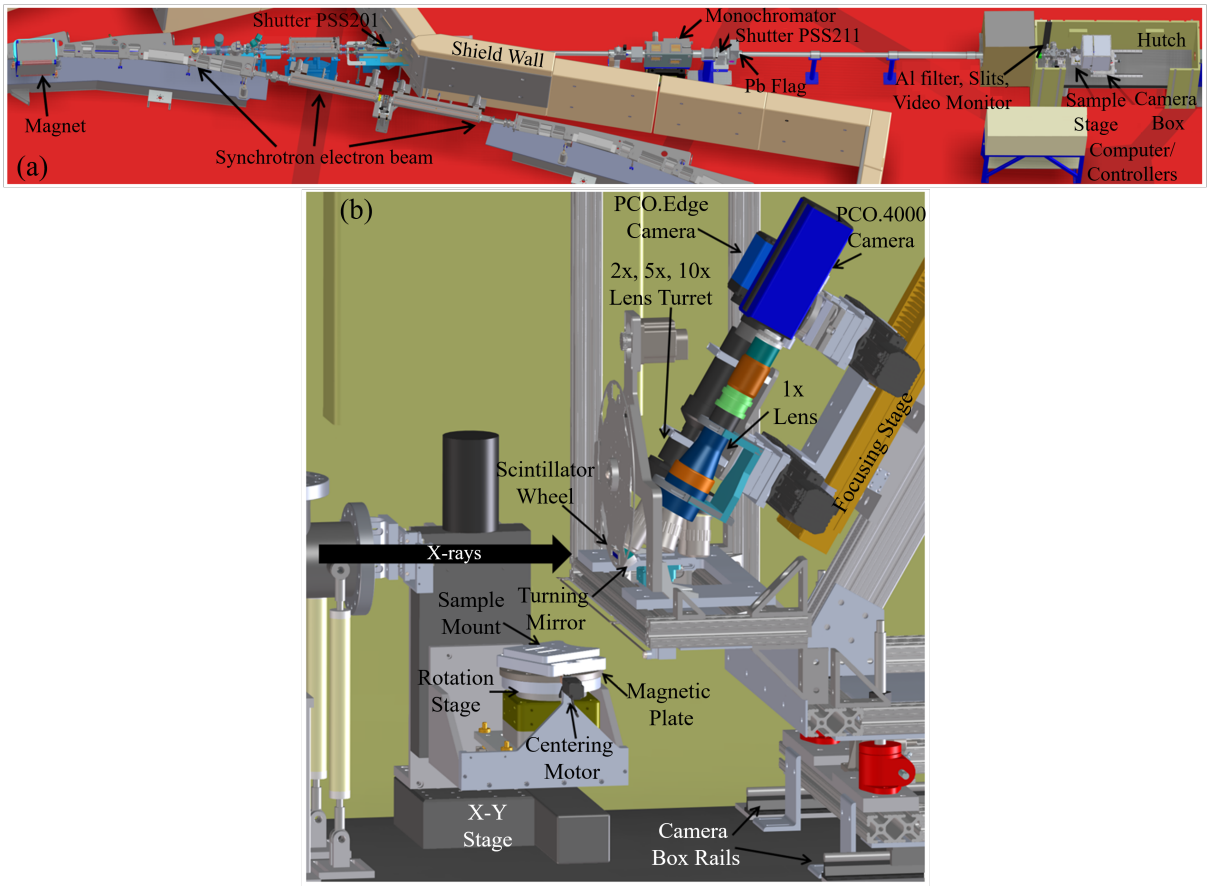

Figure 2.13: (a) Overview of the instrument components and (b) sample and detection components inside the hutch of the beamline 8.3.2 of the Advanced Light Source (ALS) at the Lawrence Berkeley National Laboratory, Berkeley, California, United States [149, 150].

In this study, the cement pastes were prepared with w/c = 0.5 and and 1 wt.% of xonotlite or tobermorite seeds by using the same protocol developed for the calorimetric test. To perform X-ray computed microtomography analysis, each of the as-prepared

pastes was loaded into a cylindrical thin-wall polyimide tube (~ 3 mm diameter). At different setting times, 7 and 36 h, the cylindrical sample was placed into the sample holder of the 8.3.2 beamline of the ALS at ~ 25 °C. During the measurement, the sample was irradiated by a focused X-ray beam of 40 mm $\times \sim 4.6$ mm size (at the sample) with an energy of 35 KeV. To carry out the experiment, the ring energy was 1.9 GeV and the beam current was maintained constant at 500 mA. At each scan, the sample was rotated around the axis perpendicular to the X-ray beam propagation. After the interaction with the sample, the beam passes through a scintillator generating visible light. Then, a 5× Mitutoyo magnification optical lens is used to image the scintillator onto a 2560px PCO.Edge Scientific CMOS camera (Figure 2.13(b)). For each sample, a totality of 4320 projected radiographs with an angle step of 0.09° and an exposure time of 20 ms were acquired. For that analysis, the field of view was 3.3 mm and the pixel resolution was 1.3 μm/voxel. A detailed description of tomographic data processing will be presented in chapter 4.

2.5 Conclusions

The first main goal of this chapter was to highlight the interest and the necessity of combining the supercritical water media with the continuous process technology for the synthesis of xonotlite and tobermorite particles. For that reason, a brief overview of the synthesis methodologies that exploit supercritical water as a solvent has been presented in the first part.

In the second part, it has been highlighted how the implementation of a continuous process for the production of nanominerals strongly depends on the availability of a suitable experimental set-up. Furthermore, the reactor's performance, robustness, and reliability are the most critical factors to fully capitalise on the benefits of a flow process. For all these reasons, the first challenge of this work focused on the design, construction and development of a suited, innovative and home-made set-up which allows the production of significant quantities of CSH powders.

Through this chapter, the employed characterisation set-ups have also been described, together with the information that can be obtained from the analysis. By combining different types of techniques, such as PXRD, NMR, BDS, and HR-TEM, with different levels of analysis resolution, we can achieve a complete understanding of the materials. In addition, the in-depth study of the CSH minerals is essential for interpreting the properties of cement paste at the micro- and macroscale. Consequently, the last part of the chapter was dedicated to the characterisation techniques employed for exploring the seeding effect of CSH particles in the cement matrix.

In the next two chapters, the experimental results for the synthesis, characterisation and applications of the xonotlite and tobermorite particles will be presented and discussed.

Chapter 3

Deep inside into the synthesis and characterisation of xonotlite and tobermorite nanoparticles

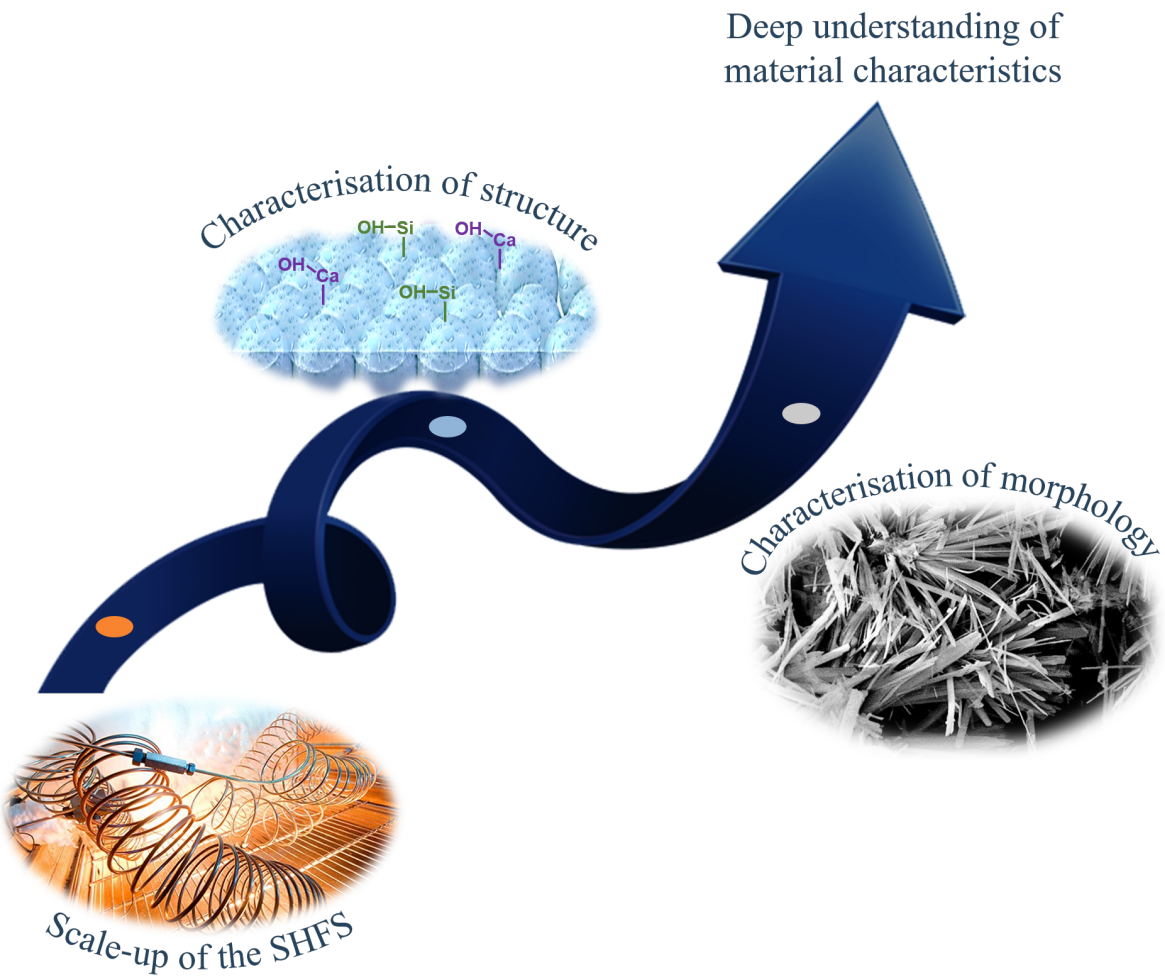

In this chapter, the results obtained during the Ph.D. work in terms of synthesis and characterisation of calcium silicate hydrate nanoparticles, namely xonotlite and tobermorite, will be discussed.

The first part of the chapter will be devoted to presenting the experimental protocol developed in this study. In particular, the effect of operating parameters, as temperature and residence time, on the produced materials will be investigated. As we will show later, long residence time (20 s) and high temperature (400 °C) involves, in the case of xonotlite synthesis, the formation of a secondary phase: wollastonite. Thanks to a systematic parametric study, the optimal conditions to synthesise high crystalline xonotlite were found to be 400 °C, 25 MPa and 7 s. Under these conditions, the newly developed set-up can produce ~ 2.9 g/h of xonotlite (using precursors molar concentration equal to $M = 0.1$ mol/L). It is worth mentioning that also under nearcritical conditions, $T = 250$, 300, and 350 °C and $p = 23.5$ MPa, the formation of xonotlite in ~ 115, 105, and 88 s, respectively, were observed. These findings, observed here for the first time, clearly show the advantages of using a continuous process to synthesise xonotlite in only a few seconds, making this methodology much more profitable than the very long conventional hydrothermal route.

In the case of tobermorite, the difficulties related to the stabilisation of that mineral phase at high temperature are widely reported in the literature. Consequently, to avoid the formation of secondary phases, the reaction kinetics must be finely controlled to boost the synthesis. The protocol and the experimental set-up developed in this work allow to produce ~ 1.4 g/h (at $M = 0.05$ mol/L for Si precursor) of tobermorite at 400 °C, 25 MPa and 8 s. Thanks to supercritical water, the synthesised tobermorite exhibits high crystallinity and polymerisation degree, which make it much more comparable to the natural specimen than the other synthetic samples reported in the literature so far.

For both xonotlite and tobermorite, the SHFS allows producing model nanominerals very close to the natural counterpart in crystallinity and morphologies, by mimicking the environments at high temperature and pressure of the geological natural process.

In the second part of the chapter, an in-depth characterisation of these model nanominerals using a combination of spectroscopic techniques will be reported for the first time. Such study allowed us to unequivocally define the picture of the water dynamics in these systems. As it will be shown later, the local chemical environment of nanominerals (either Ca–OH or Si–OH) has a profound effect on the water molecule dynamics. These results can be potentially applied to other water-containing materials, with a significant impact in many materials science fields.

3.1 Protocol for the SHFS of xonotlite and tobermorite

In this work, the synthesis of high crystalline calcium silicate hydrates in only a few seconds was performed by employing a continuous set-up.

For the production of xonotlite nanoparticles, the two precursors solutions were prepared by dissolving a stoichiometric amount of $Ca(NO_3)_2 \cdot 4\,H_2O$ (calcium nitrate tetrahydrate) and $Na_2SiO_3 \cdot 9\,H_2O$ (sodium metasilicate nonahydrate) in pure water in order to obtain $Ca/Si = 1$. Instead, for the synthesis of tobermorite, a small amount of Al replacing the Si in the structure is necessary, as mentioned above. Consequently, a third precursor, $Al(NO_3)_3 \cdot 9\,H_2O$ (aluminium nitrate nonahydrate) was used in a concentration of $Al/(Al+Si) = 0.15$, while calcium and silicate salts were added in a Ca/(Si+Al) molar ratio of 0.83. Afterwards, the precursor solutions were kept under a N_2 flow, by using a two outlets line equipping the experimental set-up, to prevent their carbonation. Initially, only pure water was injected by the two Jasco Isocratic HPLC pumps into the system, and the pressure was progressively increased by closing the BPR. Once the chosen value of pressure was reached, a test of the pumps flow rate was performed to detect any eventual leakage.

At that time, the temperature of the system was increased by setting the value of the operating temperature on the Eurotherm controllers. When the reactor reached the desired temperature and pressure conditions, the three-way junction valves were turned to switch to the precursor lines. The precursor solutions were pumped and fed to the heated and pressurised reactor. Different flow rates (residence times) of the pumps were used to synthesise xonotlite and tobermorite.

At the end of the synthesis time, the heating system was shut down and the reactor was let cool down to room temperature. Finally, once the system returns to ambient conditions, the filter was disassembled from the reactor and then opened by 15-inch adjustable wrench to collect the synthesised particles (Figure 3.1(a)). The produced materials were dried in an oven at 60 °C overnight before being finely grounded into a powder for the characterisation analyses (Figures 3.1(b) and (c)).

To avoid cross-pollution contamination between different syntheses of xonotlite and tobermorite, a procedure involving several flushing of the system through an open/close valve to expel the eventual retained particles on the reactor wall, and cleaning with an acid solution was employed.

It has to be highlighted that the experimental protocol developed for the synthesis of xonotlite differs slightly from that one of tobermorite. The versatility of the supercritical

water-based technology allows us synthesising different nanomineral phases by changing few parameters as the residence time, the Ca/Si molar ratio, and the presence of Al source in the precursor solutions.

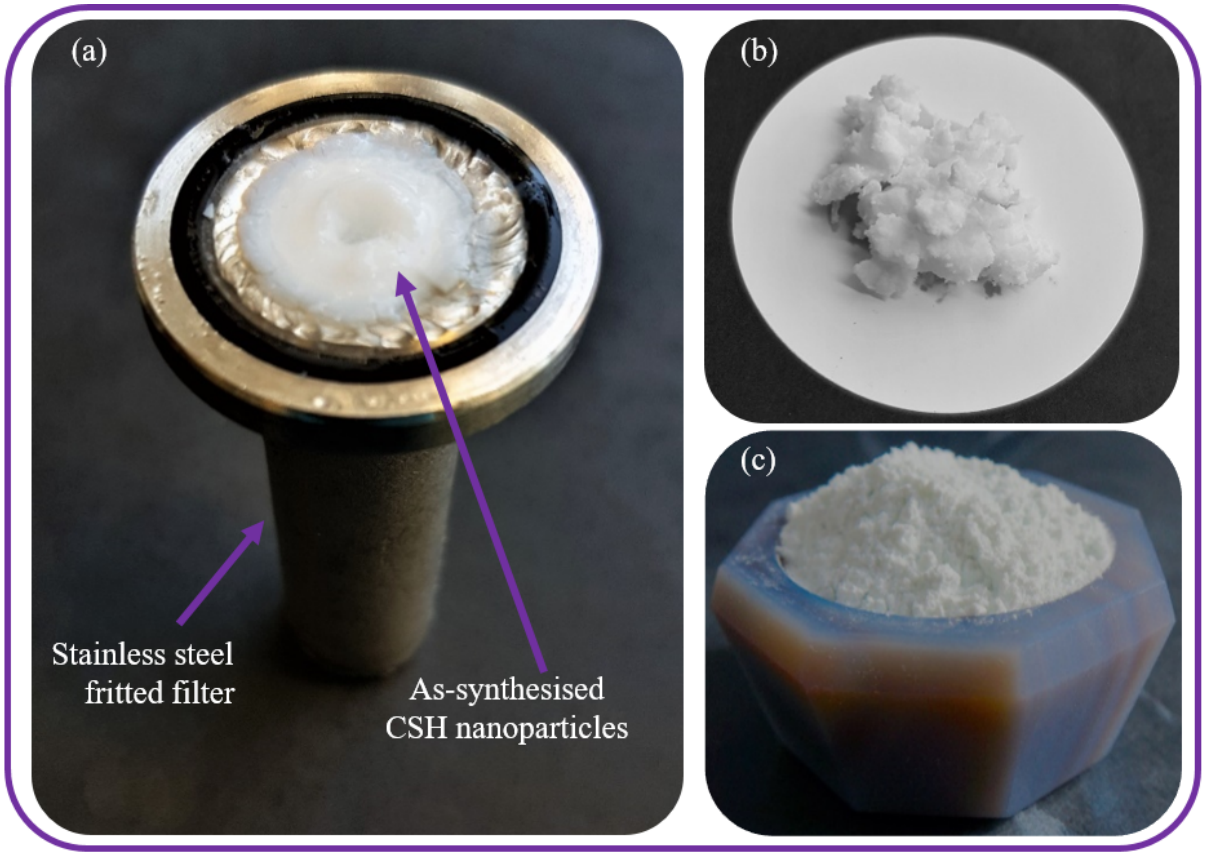

Figure 3.1: Pictures of (a) the stainless steel fritted filter filled with the produced nanomineral particles just after the synthesis, (b) dried solid material and (c) finely grounded material powder.

In the next sections, the influence of the experimental parameters on the synthesised mineral phase, structure, and properties will be presented. From now on, when comparing xonotlite and tobermorite synthesised in supercritical water (SCW) or via a hydrothermal synthesis (HS) to the natural counterparts (N), we will refer to them with the acronyms SCW, HS, and N, respectively.

3.2 Xonotlite synthesised in supercritical water

To investigate the formation of xonotlite via a flow synthesis, two processes were analysed separately:

1. the precipitation at room temperature of the Ca- and Si-precursors in the T-mixing piece at the inlet of the reactor to form a calcium silicate hydrate compound,
2. the crystallisation of xonotlite particles inside the tubular reactor kept under near- or supercritical conditions.

In the following, these two steps will be discussed.

3.2.1 Investigation of the mixing procedure

First, an experiment in which the precursors solutions (Ca/Si molar ratio equal to 1) are injected through the pumps line into the reactor kept under atmospheric conditions was performed. As shown in Figure 3.2(a), the precipitation at room temperature of the Ca- and Si-solutions in the T-mixing piece of the reactor gives rise to the formation of a gel. After drying, the material was analysed by powder X-ray diffraction and transmission electron microscopy to study the mineral phase and its morphology.

The PXRD pattern of the sample, Figure 3.2(b), can be mainly identified according to PDF file no. 34-0002 reported for C-S-H(I) compound in the International Centre for Diffraction Data (ICDD) database. The material exhibits an intense diffraction peak at around 29.2° (2θ), which is the principal peak in both C-S-H(I) and calcite. Other peaks that confirm the formation of calcium silicate hydrate phase are 16.7° (2θ), 31.9° (2θ), 37.4° (2θ), 49.8° (2θ). These results are in agreement with those reported in previous studies for C-S-H(I) prepared with a Ca/Si ratio between 0.5 and 1.5 by mixing calcium and silicate ions in dilute aqueous suspension at temperatures below $\sim 60\,^{\circ}\mathrm{C}$ [68, 151], or by mechanochemically procedure [152, 153]. However, as both the production and the drying of the sample were not performed in an inert atmosphere free of carbon dioxide, other peaks related to calcium carbonate, in the form of its polymorphs calcite and vaterite, were detected.

Regarding the morphology, at lower magnification, Figure 3.2(c), an aggregation of C-S-H(I) particles can be observed. At higher magnification, the C-S-H compound obtained for precipitation shows a foil-like morphology, Figures 3.2(d) and 3.2(e).

This poorly crystalline material can be considered as the starting precursor for the syn-

thesis of xonotlite under near- and supercritical conditions. To study the chemical process that results in the formation of crystalline xonotlite, syntheses at different temperatures were performed, as will be discussed in the following.

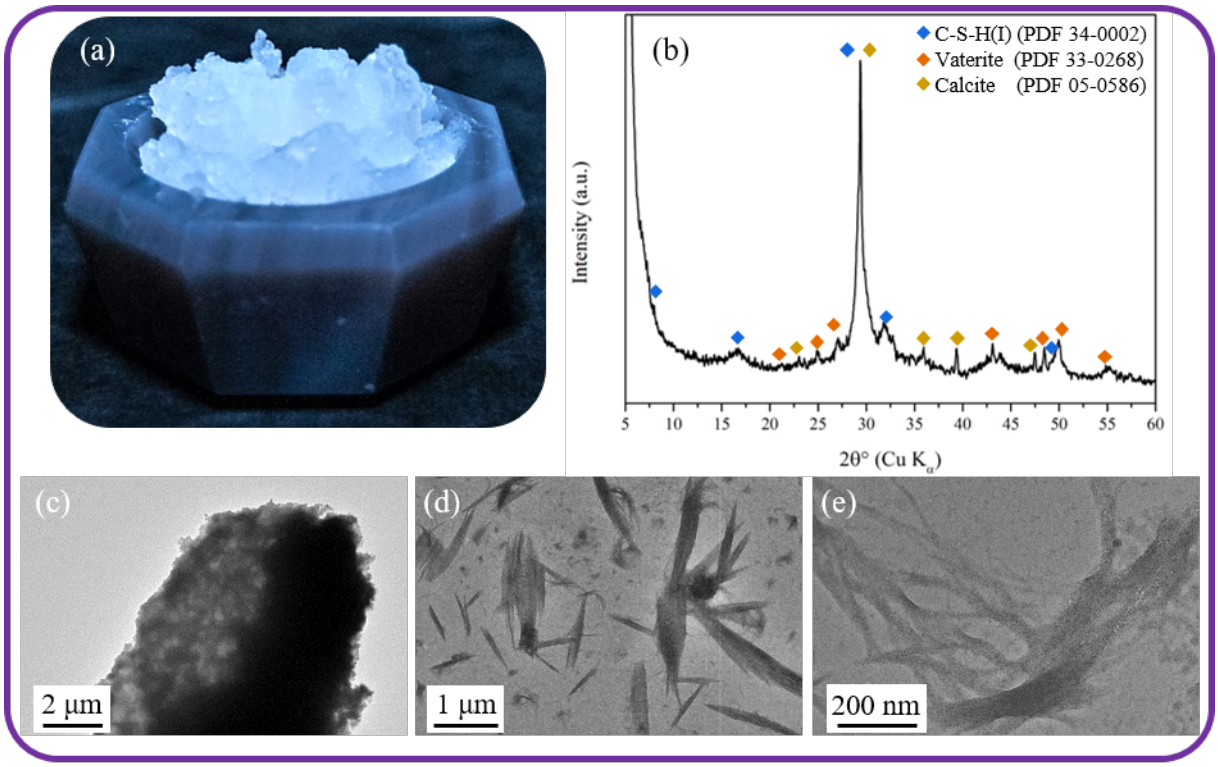

Figure 3.2: (a) Picture, (b) powder X-ray diffraction pattern, and (c)-(e) TEM images of C-S-H compound formed as precipitation product of the Ca- and Si-precursors mixing at the inlet of the reactor and at room temperature. In the PXRD pattern, three phases were detected: C-S-H(I) (PDF file no. 34-0002), vaterite (PDF file no. 33-0268), and calcite (PDF file no. 05-0586).

3.2.2 Crystallisation of xonotlite: influence of the synthesis parameters

a) Influence of temperature

The conventional hydrothermal synthesis of xonotlite has been investigated, in the literature, in a wide range of temperatures, times, and precursors, as reported in chapter 1. The most common temperature ranges between 150 and 250 °C [98]. However, in the case of low temperature, the synthesis time is very long (133 days at 150 °C) [95], and can be reduced to several hours ($\sim$ 17 h to obtain crystalline single phase material) at 250 °C [7].

In this work, we studied the effect of temperature, in the near- or supercritical domain, on the crystallinity and structural properties of xonotlite, to then compare them with those reported in the literature so far. The samples were prepared via hydrothermal flow synthesis at 23.5 MPa and different temperatures: 250, 300, 350, and 400 °C. The syntheses were performed keeping the flow rate of each pump at 2.8 mL/min, that corresponds, depending on the temperature, to distinct residence time values (according to Equation 2.3). From now on, in the text we refer to these samples with the label T250, T300, T350, and T400. The list of parameters employed in these experiments is reported in Table 4.3.

Table 3.1: Experimental parameters employed during the synthesis at different temperatures of T250, T300, T350, and T400.

Sample name	T250	T300	T350	T400
Temperature (°C)	250	300	350	400
Pressure (MPa)	23.5	23.5	23.5	23.5
Residence time (s)	$\sim$ 115	$\sim$105	$\sim$ 88	$\sim$ 20

Powder X-ray diffraction patterns of the samples are shown in Figure 3.3. The majority of the peaks, in all samples, are coincident in positions and intensities with those of xonotlite, as reported in PDF file no. 00-023-0125 of monoclinic xonotlite (space group P2/a) in the ICDD database. Furthermore, in all the diffraction patterns, the most intense diffraction peak, centred at 28.9° (2θ), is related to the (320) reflection.

Comparing the diffraction patterns of T250, T300, T350, and T400 samples, the effect of temperature is clear: higher temperature, despite the shorter time that growing particles spend in the reactor, results in an increasing of the material crystallinity. In fact, T350 and T400 exhibit sharper and less broadened diffraction peaks in respect to samples synthesised at a lower temperature. Furthermore, it is possible to observe that in these conditions of low flow rate (high residence time), the increasing of the temperature leads to the crystallisation of wollastonite (principal diffraction peak centred around 30° (2θ)) and calcium carbonate polymorphs, as calcite and vaterite. The presence of vaterite and wollastonite is responsible for the broadening of the (202) peak in T250 and T300, which at higher temperature (T300 and T400) results in three different diffraction peaks. Whereas, the diffraction peaks at 43.4°, 44.3°, and 50.4° (2θ) came from the sample holder in stainless steel.

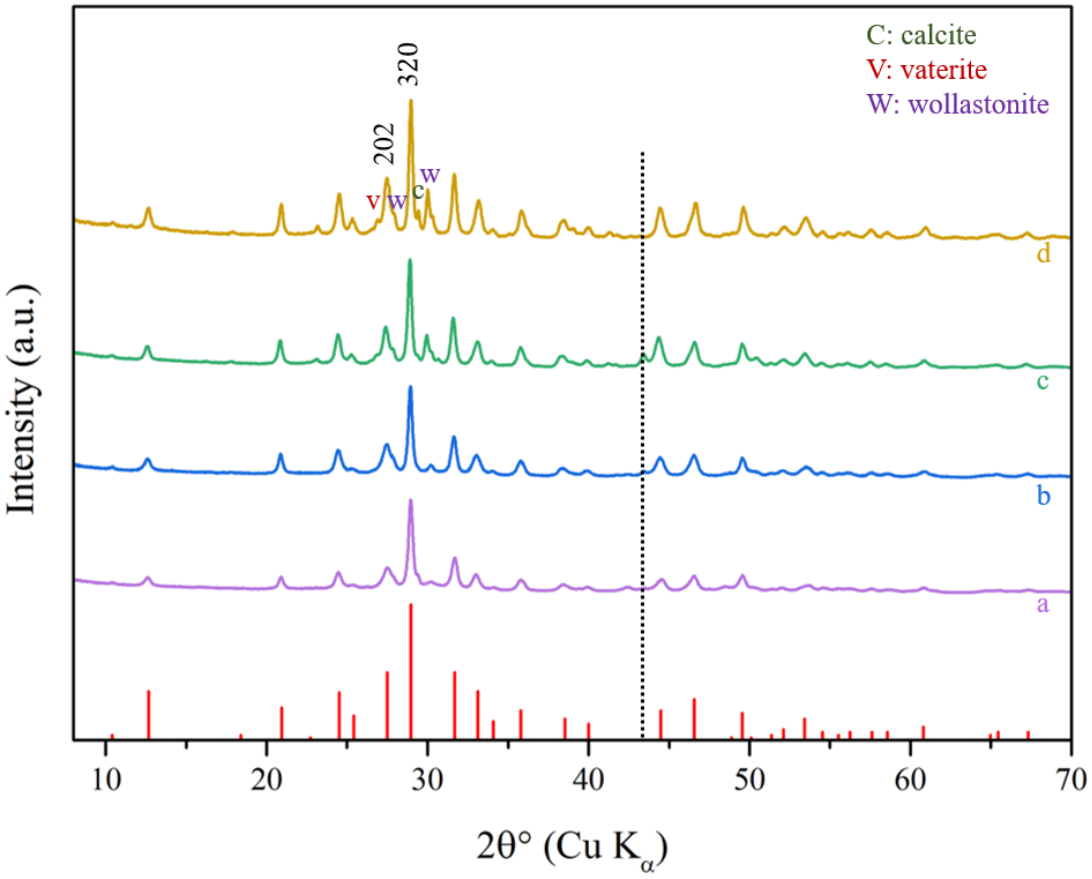

Figure 3.3: Powder X-ray diffraction patterns of samples T250, T300, T350 and T400 synthesised under near- and supercritical conditions at 23.5 MPa and (a) 250 °C, (b) 300 °C, (c) 350 °C and (d) 400 °C, respectively. In red, the positions and intensities of the diffraction peaks as reported in PDF file no. 00-023-0125 of monoclinic xonotlite (space group P2/a) are shown. The letters C, V, and W indicate diffraction peaks of calcite, vaterite or wollastonite phases, respectively. The vertical black dot line indicates diffraction from the stainless steel sample holder.

These findings represent the first proof of xonotlite synthesis under nearcritical conditions (250 - 350 °C) in only tens of seconds in a continuous process. In fact, even if the reaction yields and the crystallinity of the samples are reduced if compared to the specimen synthesised at 400 °C, these results at lower temperatures are very promising. Suffice it to say that several hours are required for the conventional hydrothermal synthesis at 250 °C. In this way, for some applications in which is not needed an excellent degree of crystallinity, the methodology developed for the first time in this work can represent a real innovation for the production of xonotlite.

The effect of temperature on the formation of xonotlite was further analysed through the investigation of the local environment of protons at the atomic nearest neighbour and next-nearest neighbour scale. Figure 3.4 displays the ^{1}H MAS NMR spectra of samples

T250, T300, T350 and T400. All the spectra show two peaks at 1.9 and 2.3 ppm which are attributed to the presence of Si–OH and Ca–OH groups, respectively. In contrast, the broad signal around 5 ppm can be assigned to molecular water adsorbed on the mineral particle surface. Although the ideal crystal structure of xonotlite should contain only Ca–OH units like in portlandite, previous research studies have shown deviations from the ideal model. As a consequence, our results are in agreement with the existence of two different types of proton environments already detected in both natural and synthetic xonotlite synthesised under conventional hydrothermal conditions [45, 58, 154, 155].

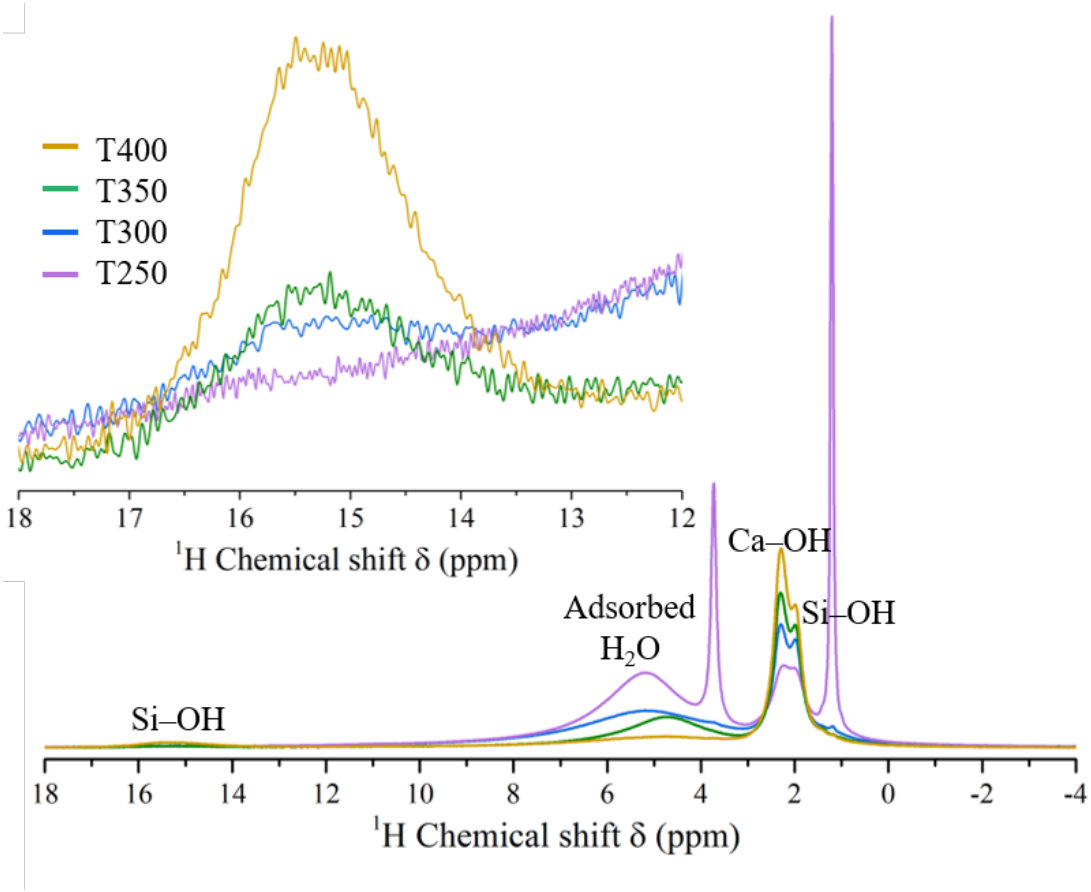

Figure 3.4: ^{1}H MAS NMR spectra of samples T250, T300, T350, and T400 synthesised under near- and supercritical conditions at 23.5 MPa and 250, 300, 350 and 400 °C, respectively. The spectra are normalised for the material mass and the number of scans, and thus comparable to each other. The inset shows a zoom in the range within 12 and 18 ppm of the spectra.

Furthermore, the spectrum of the sample T250 shows two more intense peaks at 1.2 and 3.7 ppm which can be assigned to the presence of unreacted C-S-H precursor due to the low synthesis temperature. Small contributions of these peaks are also observed in the sample T300. The inset in Figure 3.4 shows that by increasing the temperature, another peak at around 15 ppm appears. This signal can be assigned to strongly hydrogen-bonded

protons involving Si–OH groups, as already reported for other silicate minerals [156]. From the deconvolution of the spectra, this contribution has been calculated to be equal to 5% in T400, and around 1 - 2% in T300 and T350, whereas it was not detected in T250.

More information can be obtained from the comparison between these spectra. First, by increasing the temperature, the quantity of xonotlite in the sample increases (especially, the amount of Ca–OH increases), NMR giving semi-quantitative information. That result is in agreement with the PXRD analyses of the samples previously reported. Second, the quantity of molecular water adsorbed on the mineral surface decreases. Third, the peak at around 15.2 ppm becomes more intense the higher the temperature is. These findings suggest that higher temperature, and thus higher crystallinity of the structure, result in an increase in the H-bond network strength and a lower wettability of the mineral surface.

The silicate structure and the local chemical environment of Si atoms in xonotlite samples, synthesised at different temperatures, were investigated by ^{29}Si MAS NMR. To interpret the results, we must recall the structure of this mineral phase. As shown in Figure 3.5, three different silicon sites are present in the silicate chains of xonotlite. Among them, two are in bridging positions, Si(1) and Si(2), and the third one is located in branching position, Si(3).

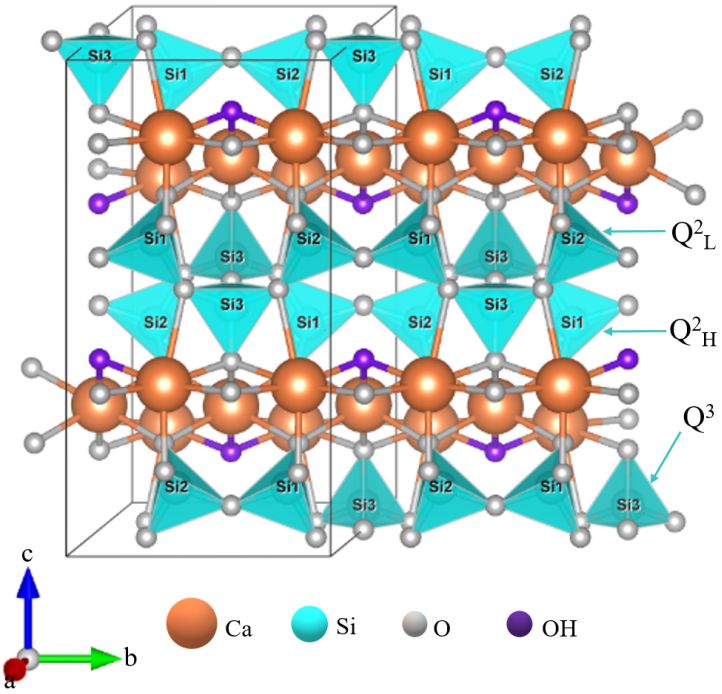

Figure 3.5: Crystal structure of xonotlite determined from the crystallographic information framework (CIF) file reported by Kudoh *et al.* [45] in the NIST Inorganic Crystal Structure Database (ICSD) [157]. In the structure, the Si(1), Si(2), and Si(3) atoms, which give rise to three different contributions (Q^2_H, Q^2_L and Q^3) to the SSNMR xonotlite spectrum can be distinguished. The black rectangle represents the limits of the unit cell.

As a consequence, three contributions, namely Q^2_H, Q^2_L and Q^3, appear into the SSNMR xonotlite spectrum. The presence of two Q^2 components is because the bridging Si atoms have different Si–O bond lengths and Si–O–Si bond angles, in agreement to the model proposed by Kudoh and Takeuchi [45].

In Figure 3.6(a), the signal centred around -86 ppm is attributed to the Q^2 Si sites, and the other at -97 ppm to the presence of Q^3 silicon tetrahedra in branching positions.

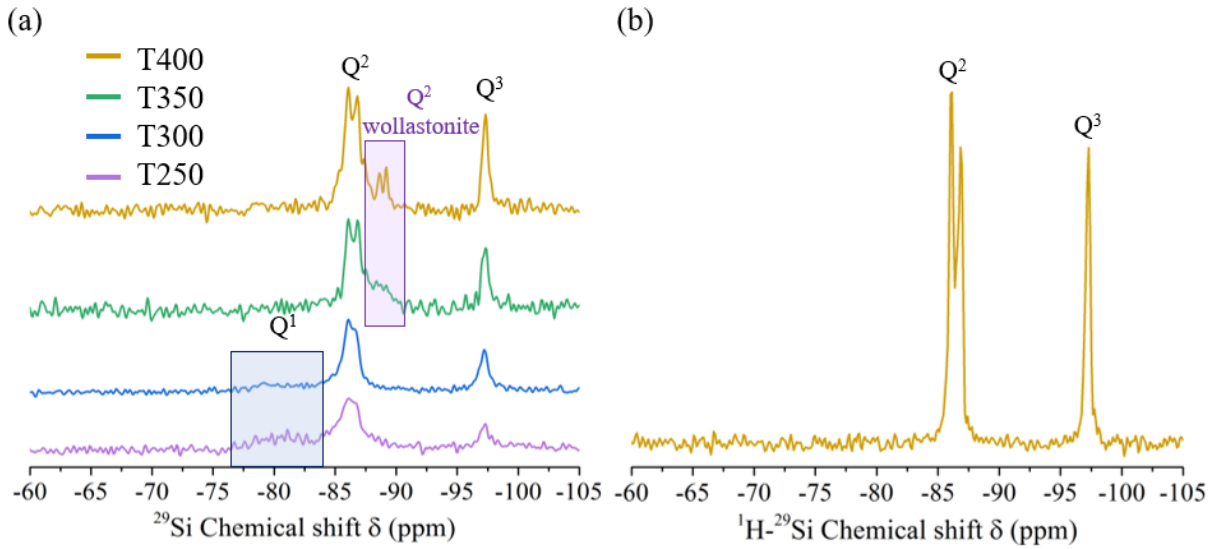

Figure 3.6: (a) ^{29}Si MAS NMR spectra of samples T250, T300, T350, and T400 synthesised under near- or supercritical conditions at 23.5 MPa and 250, 300, 350, and 400 °C, respectively. The spectra are normalised for the material mass and the number of scans, and thus comparable to each other. (b) ^{1}H-^{29}Si CP/MAS NMR spectrum of T400.

We can observe that the splitting of the Q^2 peak into two components becomes much more clear at high temperature; on the contrary, it is less detectable due to the broadening of the signals when decreasing the temperature. The sharpness of SSNMR peaks in T350 and T400 samples is the proof of their higher crystallinity, in agreement with the PXRD results. Furthermore, another peak appears in T250 and T300 at around -80 ppm due to the Q^1 contribution, related to end site of the silicate anion chains. The presence of Q^1 Si sites is the direct evidence of defects, and a more defective and low crystalline material. In this sense, it is interesting to observe that the Q^1 contribution decreases by increasing the temperature. On the other hand, the spectra of samples synthesised at higher temperatures, T350 and T400, show another signal at around -88 ppm which can be associated with the wollastonite presence in the sample. The proof that this contribution comes from wollastonite was obtained through ^{1}H-^{29}Si CP/MAS NMR experiment, that is sensitive only to Si in close proximity to H atoms. Being protons absent in wollastonite structure, ^{1}H-^{29}Si CP/MAS NMR spectrum of T400 does not exhibit the peak a -88 ppm,

Figure 3.6(b). In this sense, SSNMR confirms the formation of wollastonite in T350 and T400, already observed by powder X-ray diffraction.

The presence of wollastonite in samples synthesised at low flow rate (high residence time) and temperature equal to 350 and 400 °C, even if in small traces, is interesting, as in the literature the formation of that dehydrated phase is reported by calcination of xonotlite at 800 °C for 2 h. More details regarding the dehydration process of xonotlite to form wollastonite will be reported in chapter 4.

In this section, the results related to xonotlite synthesis via the developed near- or supercritical flow process were discussed. Two crucial experimental findings should be highlighted. First, the formation of xonotlite is stable over a wide range of temperatures, from 250 to 400°C at 23.5 MPa. These results reported for the first time here make this methodology very profitable in terms of very fast production even at mild temperature. In fact, the developed process allows to produce xonotlite at 250 °C in 115 s, contrarily to the conventional hydrothermal route reported in the literature which at the same temperature requires several hours.
Second, PXRD and SSNMR results have shown that by increasing the temperature, the crystallisation of the material increases. However, under these conditions the formation of a secondary phase, wollastonite, takes place. Consequently, to synthesise highly crystalline single phase xonotlite, the residence time has to be decreased to avoid its dehydration.
In additions to the parameters investigated so far, also pressure plays an important role in the dehydration process, as it will be investigated more in detail in the next chapter.

b) Influence of residence time

To avoid as much as possible the crystallisation of wollastonite and obtain single phase xonotlite, the synthesis was performed at 400 °C, and 25 MPa, reducing the residence time down to 7 s. In Figure 3.7, the PXRD pattern of this sample shows well-defined diffraction peaks corresponding, in positions and intensities, to those reported in PDF file no. 00-023-0125 of monoclinic xonotlite. Under these synthesis conditions, the presence of wollastonite is reduced to a neglectable amount.

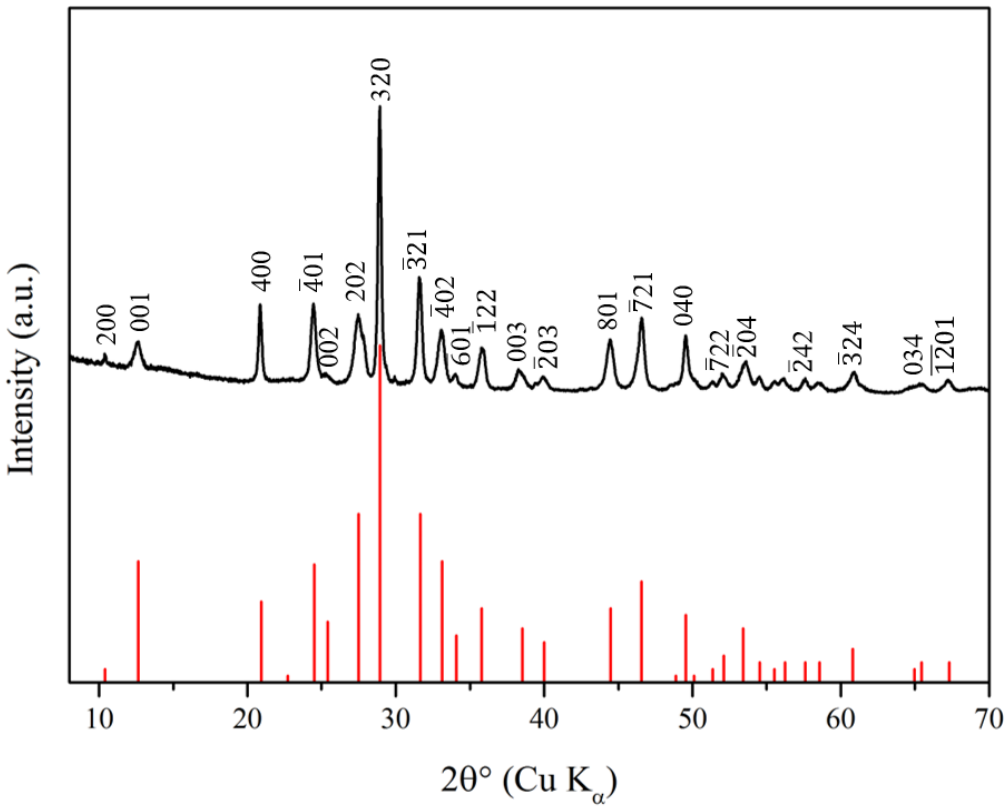

Figure 3.7: Powder X-ray diffraction pattern of xonotlite synthesised under supercritical conditions at 25 MPa, 400 °C and 7 s. In red, the positions and intensities of the diffraction peaks as reported in PDF file no. 00-023-0125 of monoclinic xonotlite (space group P2/a) are shown. Each peak is identified by the corresponding Miller indices as reported in PDF file no. 00-023-0125.

The morphology of the as-synthesised xonotlite was investigated by scanning electron microscopy. As shown in Figure 3.8(a), the crystals mainly consist of tiny flat fibres that are approximately 10 - 30 μm long and 50 - 200 nm wide. Previously, Lin and coworkers reported similar results for synthetic xonotlite prepared by conventional hydrothermal treatment at 200 °C for 24 h [106]. The EDS mapping, acquired for Ca and Si, confirms that xonotlite fibres exhibit a very uniform elemental distribution, Figures 3.8(b)-(d). HR-TEM analysis was performed to get information on the preferential growing direction of the crystals. Figures 3.9(a) and (b) show well crystalline xonotlite fibres, which confirm the PXRD results. It is possible to observe the (2,0,0) atomic planes characteristic of xonotlite structure, suggesting that the fibre grows along the direction of the silicate chains parallel to **b**-axis (Figure 3.9(d)). The interlayer distance between these planes was measured be equal to 8.6 Å (Figure 3.9(c)) in agreement to the (200) reflection observed in the PXRD pattern.

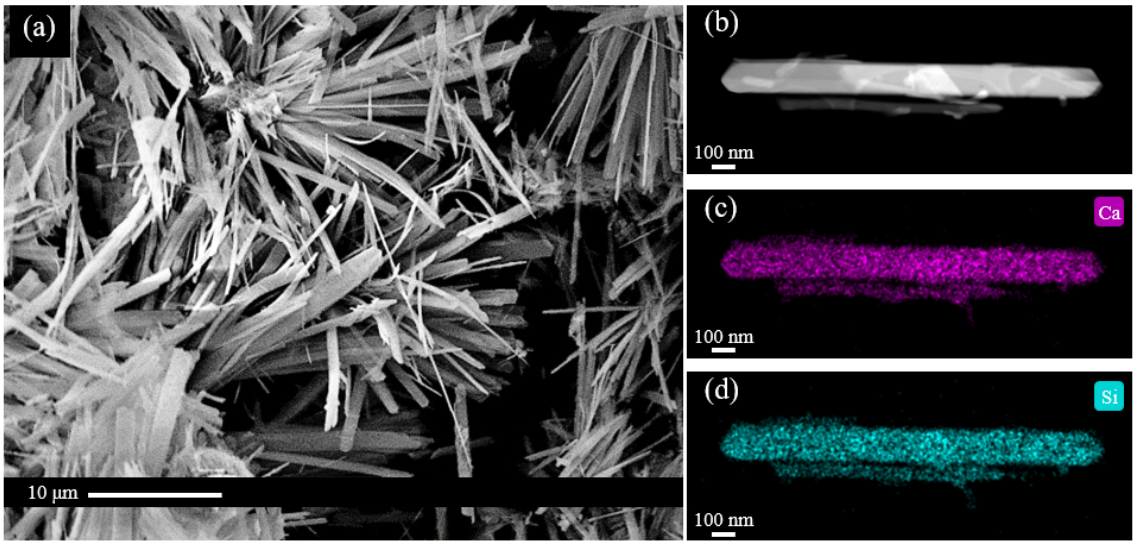

Figure 3.8: (a) SEM image of xonotlite fibres; (b) xonotlite fibre analysed by EDS shows uniform distribution of calcium and silicon atoms in (c) and (d), respectively.

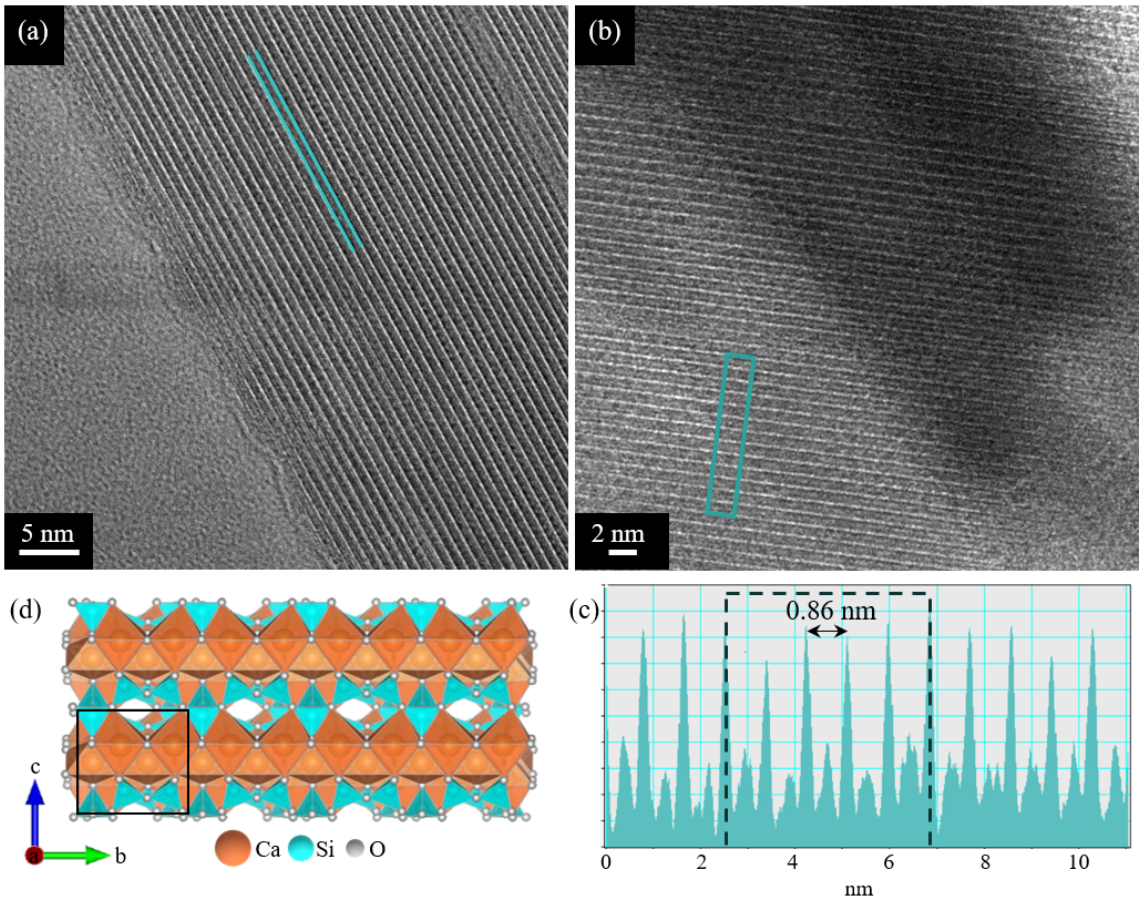

Figure 3.9: (a) and (b) HR-TEM images of xonotlite fibres, synthesised under supercritical conditions, showing the ordered and well-arranged crystal lattice of the material. (c) Distance profile derived from the light blue region in (b) to measure the interlayer distance between planes related to reflection (200) and perpendicular to the fibre's length. (d) Crystal structure of xonotlite as reported in the CIF file of the ICSD database [157] by Hejny *et al.* [44].

Whit the aim of studying the effect of the residence time shortening (from 20 to 7 s) on the silicate structure of xonotlite, ^{29}Si MAS NMR was performed, Figure 3.10. The ^{29}Si MAS NMR spectrum of xonotlite synthesised in supercritical water in only 7 s show three signals assigned to Q^2_H, Q^2_L and Q^3, in agreement with the silicate structure of xonotlite reported in Figure 3.5.

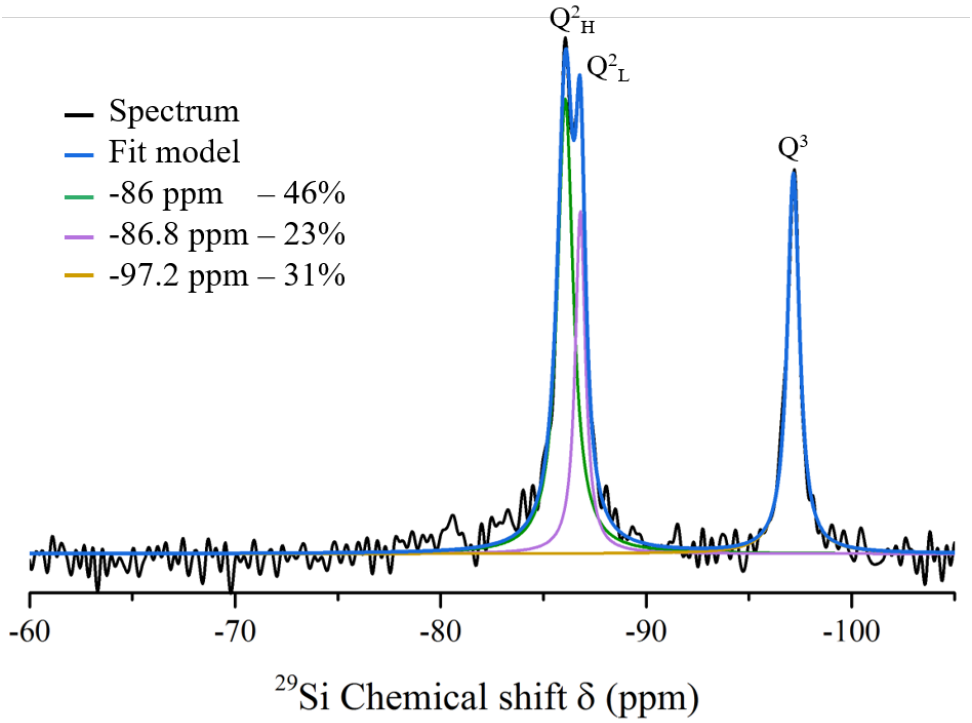

Figure 3.10: (a)^{29}Si MAS NMR spectrum of xonotlite synthesised under supercritical conditions at 25 MPa and 400 °C in 7 s.

The areas of Q^2 and Q^3 signals were calculated through the deconvolution of the peaks, as reported in Figure 3.10. The ratio between the areas, Q^2:Q^3, was approximately 2:0.9. However, the ideal crystal structure of xonotlite is built by parallel silicate chains in "dreiereinfachketten" arrangement with two "paired" Q^2 tetrahedra (Si(1), Si(2)) and one Q^3 site (Si(3)); consequently, Q^2:Q^3 ratio should be equal to 2:1. That difference implies that in xonotlite synthesised under supercritical conditions, some Q^3 silicon sites are missing. Similar results were also found in other studies on synthetic and natural xonotlite [158]. Furthermore, the absence of wollastonite in this sample, as already observed by PXRD, is here confirmed by ^{29}Si MAS NMR, as the peak characteristic for the dehydrated phase at -88 ppm is not anymore detectable, if compared to Figure 3.6(a). Another technique that gives detailed information on the chemical structure of a mineral is the infrared spectroscopy. The characteristic IR spectrum of xonotlite is shown in Figure 3.11. The spectrum, acquired in the range 1800-400 cm^{-1}, can be divided into two

groups of bands related to vibrations of: (i) water molecules, and (ii) octahedral Ca and tetrahedral Si, as commonly observed in calcium silicate hydrates [154, 159]. The peak at 1632 cm^{-1} is attributed to the scissoring bending mode of water [159]. Instead, the bending mode vibration of CaO–H, typical of xonotlite structure, is observed at 631 cm^{-1}. The band around 1202 cm^{-1} is assigned to Si–O stretching vibrations involving Q^3 branching sites (ν(Si–O)Q^3) [159]. Instead, the spectral features of silicates, which appear around 978 and 930 cm^{-1} are attributed to Si–O stretching of Q^2 sites (ν(Si–O)Q^2). It is worth mentioning that in the spectrum does not appear the vibration band ν(Si–O)Q^1, commonly detected around 828 cm^{-1} [159], confirming the SSNMR results.

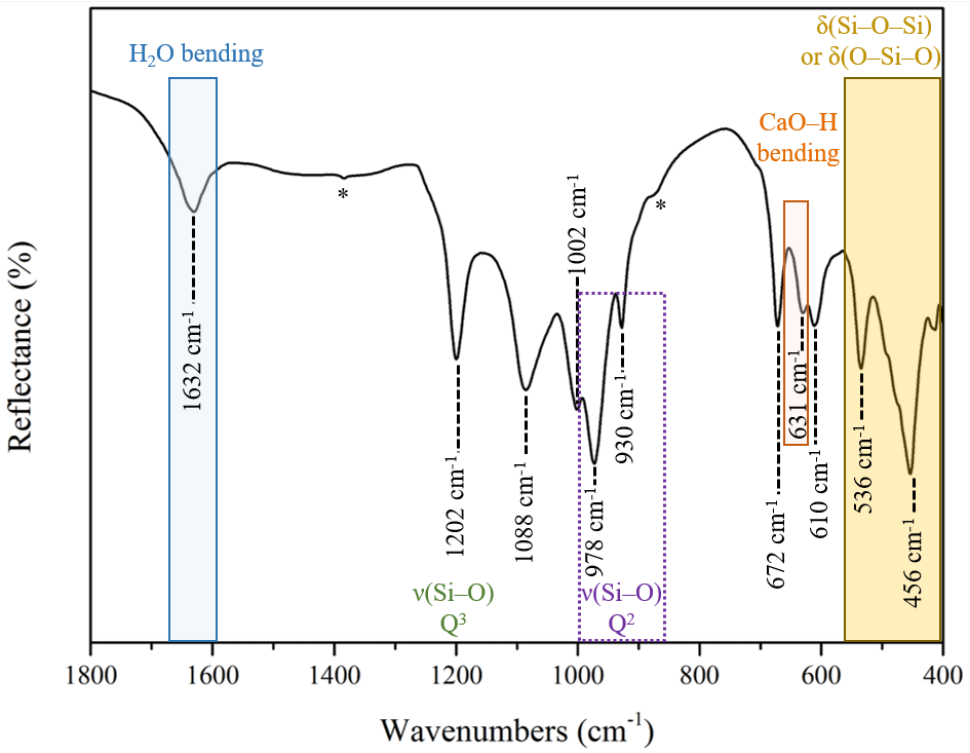

Figure 3.11: IR spectrum of xonotlite synthesised in supercritical water at 25 MPa and 400 °C in 7 s. The asterisk denotes CO_3^{2-} vibration bands related to carbonate impurity.

The signal observed at 1088 could be assigned to the asymmetric (ν_{as}(Si–O-Si)) vibration of Si–O–Si bridges; the respective symmetric stretching bands (ν_s(Si–O-Si)) appear at 672 and 610 cm^{-1}. Lastly, the band at 536 cm^{-1} is assigned to Si–O–Si bending mode (δ_s(Si–O–Si)); on the contrary, the O–Si–O bending mode (δ_s(O–Si–O)) appear at 456 cm^{-1} [159]. Although no peaks related to carbonates were observed in the diffraction pattern, in the IR spectrum of xonotlite small contributions related to CO_3^{2-} vibration bands were detected and marked with an asterisk. The presence of small carbonates traces in xonotlite is commonly reported in the literature [159].

3.3 Fingerprint of xonotlite nanomineral synthesised in SCW

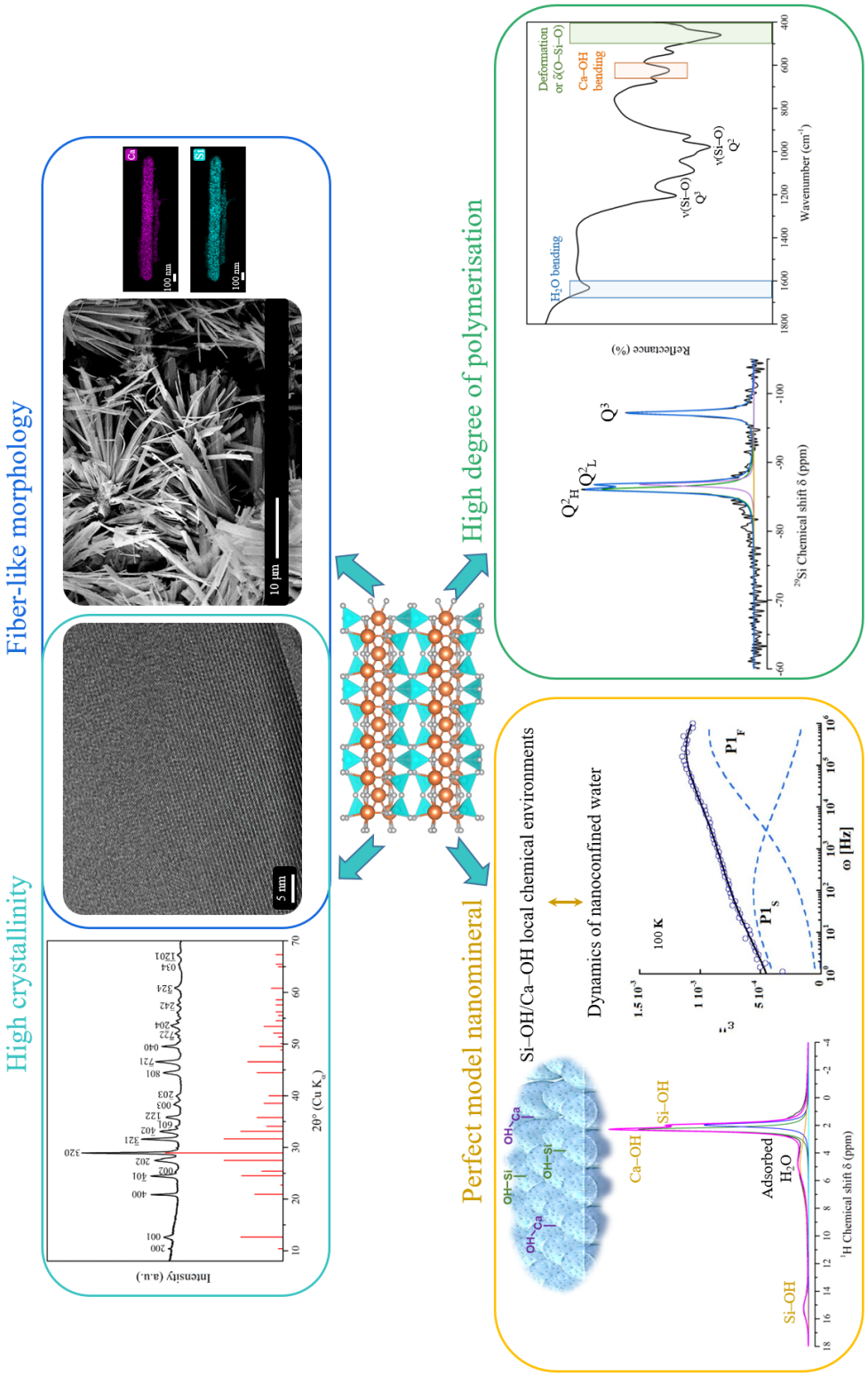

Figure 3.12: Fingerprint of xonotlite nanomineral synthesised in supercritical water (400 °C and 25 MPa, in 7 s).

In this first part of the chapter, the results related to xonotlite crystallisation via a near- and supercritical hydrothermal flow synthesis were presented. Several tests were conducted to optimise the experimental parameters and obtain high crystalline and single phase material. Our findings have shown that temperature, residence time and pressure play a fundamental role in the synthesis process, highlighting the importance of controlling the reaction kinetics to avoid secondary phases, as wollastonite. In this work, xonotlite nanoparticles synthesised at 25 MPa, 400 °C in 7 s show fibre-like morphology and well crystallised structure. Based on these results, it appears clear the interest in using the SHFS as a fast, profitable, and scalable manufacturing route for producing synthetic xonotlite fibres to replace the very long conventional hydrothermal methodology.
In the next section, the synthesis and characterisation of tobermorite will be reported and discussed.

3.4 Tobermorite synthesised in supercritical water

The conventional hydrothermal synthesis of tobermorite has been widely reported in the literature. Among the numerous studies, Shaw *et al.* proposed a two stages mechanism for tobermorite formation based on an *in situ* energy-dispersive X-ray diffraction analysis within the temperature range 235 and 310 °C [92]. The proposed mechanism involves the first formation at room temperature of poorly crystalline C-S-H, characterised by a good periodicity parallel to the *ab* plane but a low order along the [001] direction. This step is followed by an increase of the order in the CaO layers and of the periodicity along the *c* direction until tobermorite crystallises at a higher temperature. Based on this proposed model [92], and on the observation related to the mixing of reagents for xonotlite (section 3.2.1), we assume that this mechanism applies also to the formation of tobermorite via SHFS, where poorly crystalline phase forms at the T-mixing point and then the crystallisation of the mineral takes place in the reactor.

In chapter 1, a detailed description of the tobermorite-xonotlite phase boundary was reported. The several studies present in the literature have shown that tobermorite is thermodynamically unstable at high temperature. Thus, that parameter plays an important role in the formation of single phase tobermorite. Furthermore, also the aluminium content and the synthesis time are important experimental factors. Consequently, the complex synthesis of tobermorite does not allow to play with the experimental parameters in a wide range of values, as it was done for xonotlite. For the formation of tobermorite at 400 °C and 25 MPa, the residence time should be as fast as possible to avoid the formation of other species as xonotlite, but long enough to allow the crystallisation of the material. In this work, to meet the needs for the production of highly crystalline tobermorite, a residence time of 8 s was used. Furthermore, molar ratios of Ca/Al+Si = 0.83 and a Al/Al+Si = 0.15 in the precursor solutions were employed.

3.4.1 Crystal structure and physicochemical properties of tobermorite

Powder X-ray diffraction was used to identify the mineral phase and to investigate the crystallinity of tobermorite synthesised in supercritical water. In Figure 3.13(a), PXRD pattern shows well-defined peaks coincident with those reported in the PDF file no. 00-083-1520 for orthorhombic 11Å tobermorite in the ICDD database. The most intense diffraction peak of the pattern is centred at 7.8° (2θ) which corresponds to a basal distance $d_{002} = 11.4$ Å, in agreement whit what reported for natural 11Å tobermorite

specimens [50, 53, 55]. It must be emphasised that we are synthesising tobermorite at a temperature (400 °C) far above its stability limit, which is approximately 140 °C [160]. The formation of a thermodynamically unstable phase under these conditions is allowed because of the fine control of the reaction kinetics.

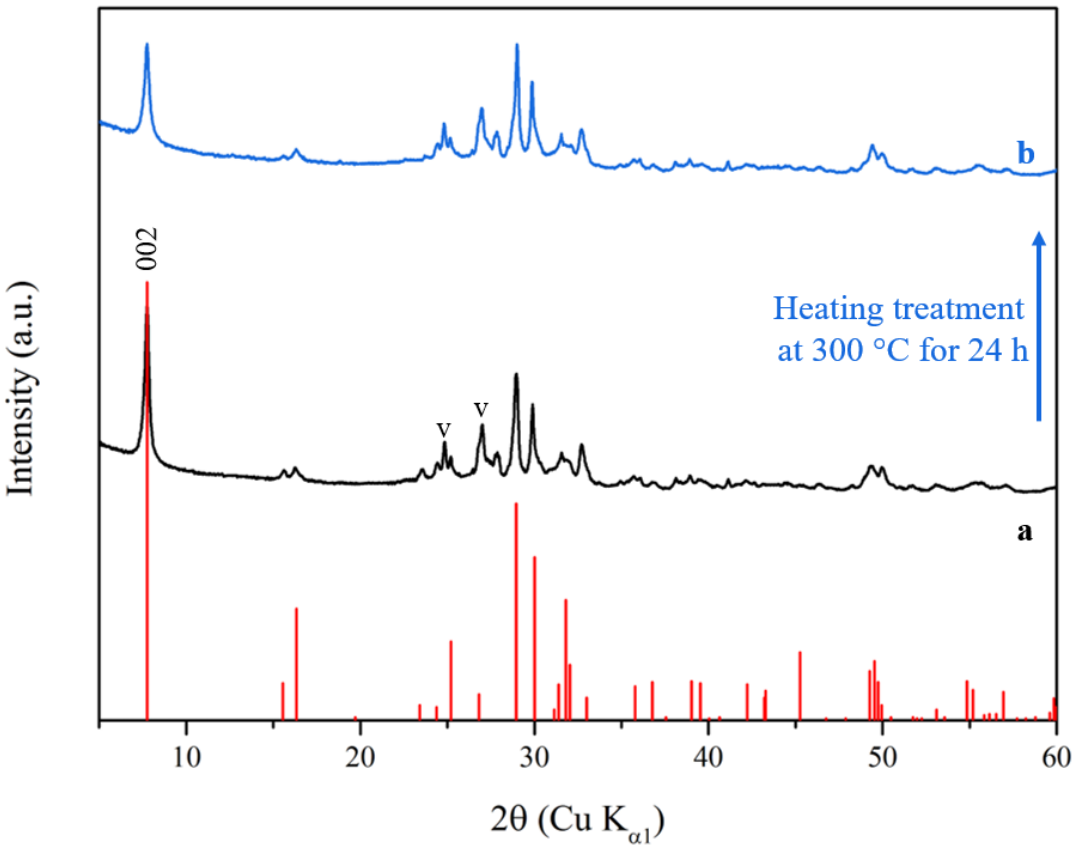

Figure 3.13: (a) Powder X-ray diffraction pattern of tobermorite synthesised under supercritical conditions at 25 MPa, 400 °C in 8 s. In red, the positions and intensities of the diffraction peaks as reported in PDF file no. 00-083-1520 of orthorhombic 11Å tobermorite are shown. Small traces of vaterite were detected from 2 diffraction peaks, indicated with a letter V, partially overlapped to those of tobermorite. (b) Powder X-ray diffraction pattern of the tobermorite sample after a further thermal treatment at 300 °C in an oven for 24 h.

In chapter 1, we discussed the existence of two types of 11Å tobermorite, described as 'normal' or 'anomalous' depending on their dehydration behaviour. The normal specimen dehydrates to the 9Å form when heated at 300 °C. On the other hand, despite the anomalous variant dehydrates under similar conditions, its basal distance does not decrease. To study the nature of our 11Å tobermorite, either normal or anomalous, the sample synthesised in supercritical water was further subjected to dehydration at 300 °C in an oven for 24 h. As shown in Figure 3.13(b), after the thermal treatment the basal peak (002) has not shifted, suggesting that via SHFS we have synthesised 11Å anomalous tobermorite. The behaviour of anomalous tobermorite upon dehydration has been correlated by Mitsuda *et*

al. to the existence of cross-linkages of silicate layers across the interlayer, which prevents a reduction in the interlayer space when water molecules are lost [51].

The morphology of tobermorite crystals was investigated by scanning electron microscopy. As shown in Figures 3.14(a), 3.14(b), and 3.14(c), the mineral phase continuously synthesised in supercritical water exhibits a fibre-like morphology with a size of approximately 2 - 20 μm in length and 10 - 20 nm in width. This result confirms the similarity of the tobermorite synthesised under supercritical conditions to the natural mineral, which also crystallises in the form of fibres or plates [161]. In contrast, tobermorite prepared by conventional hydrothermal synthesis shows a foil-like morphology unless templates are employed to induce fibre formation [111, 161].

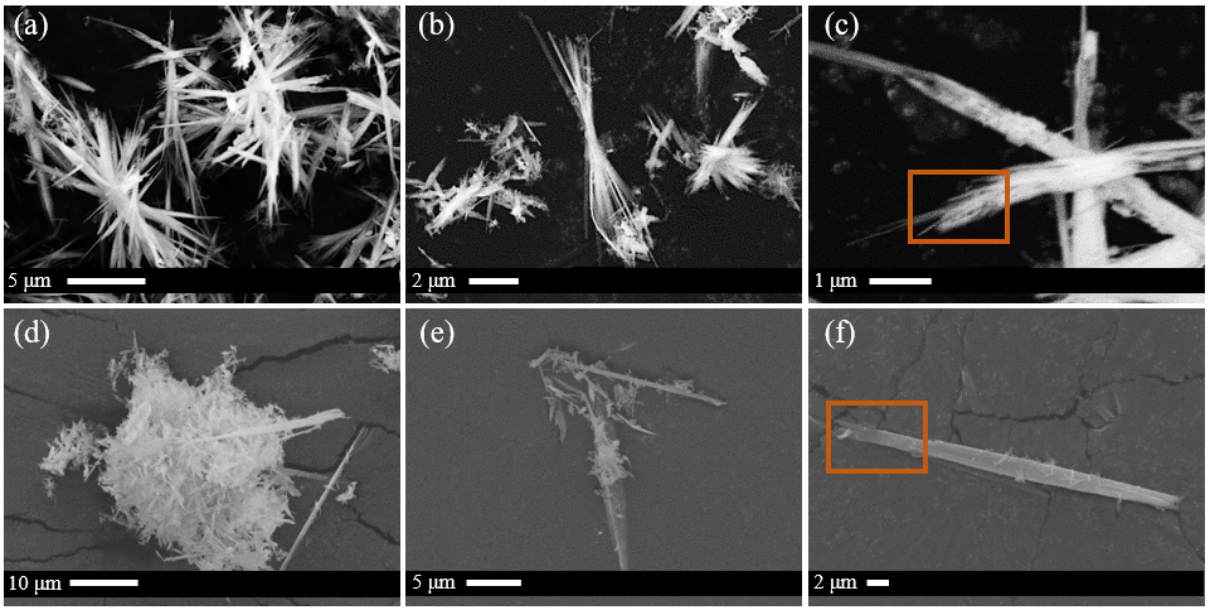

Figure 3.14: SEM images of tobermorite fibres synthesised under supercritical conditions (25 MPa and 400 °C in 8 s) at different magnifications: both aggregates of small fibres as well as large single fibres are present.

To explain these findings, we should consider the kinetic effects: the formation of natural tobermorite occurs at low temperature, due to its unstable character, over many years, while synthetic varieties have to form in a much shorter time. As a result, the reaction temperature must be increased in the laboratory to trigger a faster crystallisation process. However, at higher temperature, only an accurate control on the reaction time can inhibit the formation of other mineral phases. That control is difficult to be achieved in a traditional batch method, where the mild temperatures typically used (≤ 250 °C) could lead to the crystallisation of other stable phases during the synthesis of tobermorite. Consequently, in a conventional subcritical hydrothermal synthesis, the process has to be

prematurely interrupted to avoid xonotlite crystallisation, resulting in the formation of foil-like structures often accompanied by amorphous or poorly ordered materials [7]. On the other hand, using the supercritical water-based technology the control on the ultra-fast kinetic is achieved, allowing fibre-like tobermorite synthesis.

SEM analysis provides further information. Figure 3.14(d) shows the presence of both aggregates of small fibres as well large individual fibres. That evidence confirms that the growth of fibres occurs through a homogeneous nucleation process, as previously observed [8, 162]. According to that formation model, at first, the crystallisation of small fibres takes place, then they can aggregate and evolve to form large single units in a second step, Figures 3.14(e) and 3.14(f). In fact, in the orange rectangular inset regions of Figures 3.14(c) and 3.14(f), it is possible to observe that both small aggregates and large fibres are constituted of several single units.

This experimental evidence proves that our methodology, mimicking the environments of the geological process, allows producing model nanominerals very close to the natural counterpart in terms of crystallinity and morphologies.

Tobermorite crystals were further characterised by high-resolution transmission electron microscopy. HR-TEM analysis allows the investigation of the preferential growth direction and to confirm the high crystallinity of the material, observed by PXRD. Figures 3.15(a) and (b) show the well ordered arranged lattice of the material, where different atomic planes can be distinguished. Thanks to high-resolution imaging, the interlayer distance between calcium layers was determined being approximately 11.4 Å, Figure 3.15(c), in agreement with the value, 11.3 Å, reported for natural specimens [50, 53]. Therefore, HR-TEM confirms, through the measurement of the basal distance, that supercritical hydrothermal synthesis leads to the formation of the 11Å tobermorite variety. Furthermore, considering the crystal structure of 11Å tobermorite in Figure 3.15(d), it can be noticed that the **c**-axis is perpendicular to the growth direction of the fibre.

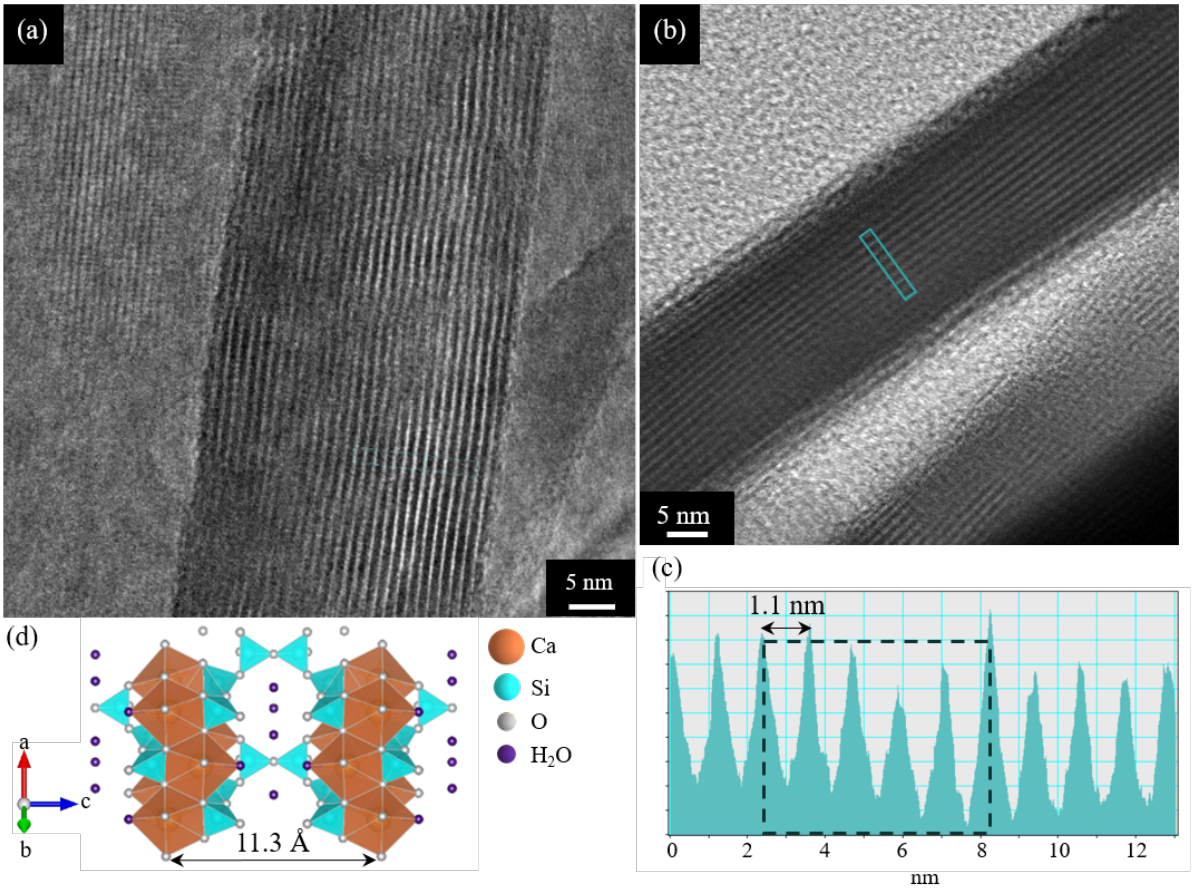

Figure 3.15: (a) and (b) HR-TEM images of 11Å tobermorite fibres, synthesised under supercritical conditions (25 MPa and 400 °C in 8 s), showing the ordered and well-arranged crystal lattice of the material. (c) Distance profile derived from the light blue region in (b) to measure the basal distance between (002) planes along **c**-axis perpendicular to the length of the fibre. (d) Crystal structure of 11Å tobermorite as reported in the CIF file of the ICSD database [157] by Merlino *et al.* [50].

The aluminosilicate structure of Al-substituted tobermorite was investigated by SS-NMR, which is an excellent technique to obtain information on the polymerisation degree of the chains. The ^{29}Si MAS NMR spectrum of Al-tobermorite is shown in Figure 3.16(b). The conventional $Q^n(m\text{Al})$ nomenclature was used to indicate silicate tetrahedra connected via oxygen to n adjacent tetrahedra (SiO_4 or AlO_4), m of which are Al sites and the remaining $n - m$ Si sites. The deconvolution of the spectrum in six components was performed to obtain quantitative information on the content of silicon and aluminium ions in sites with different connectivities. First, a signal centred at -79.6 ppm was detected and assigned to Q^1 sites. This contribution is commonly related to end-of-chain silicon tetrahedra, thus indicating a defective silicate chain structure. The low value of this contribution, only 4%, implies a high degree of polymerisation related to the presence of long silicate chains in Al-tobermorite synthesised via SHFS. It is worth mentioning that

the fraction of end-of-chain silicon Q^1 found in our sample is much lower than what previously reported, 14 - 17%, for other synthetic Al-tobermorite obtained by conventional hydrothermal synthesis [7, 163].

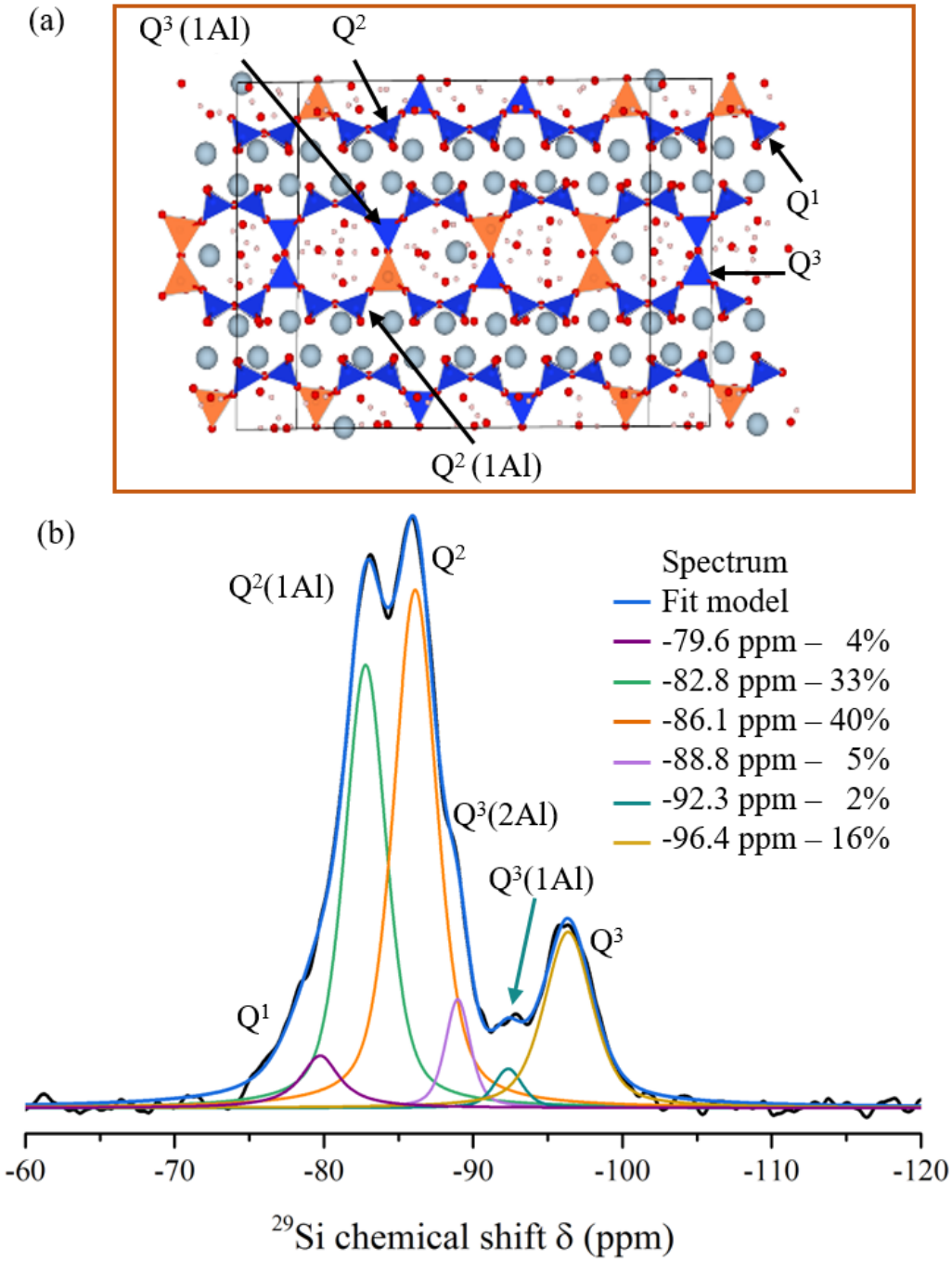

Figure 3.16: (a) Structural model proposed for Al-anomalous tobermorite, thanks to a combination of NMR and simulation results, by Dupuis *et al.* [164]. (b) ^{29}Si MAS NMR spectra of Al-tobermorite synthesised under supercritical conditions at 25 MPa and 400 °C in 8 s. The fitted curves are presented together with the respective contributions percentage.

Two more broad signals appear at -92.3 and -96.4 ppm, assigned to chain branching

sites Q^3(1Al) and Q^3(0Al), respectively.

The presence of Q^2(1Al) confirms that Al^{3+} is present in the bridging tetrahedra positions. However, the fraction of Q^2, 40%, is higher than Q^2(1Al), 33%, implying that these sites allocate a higher number of Si atoms than Al atoms. The replacing of silicon atoms (Si^{4+}) by aluminium atoms (Al^{3+}) generates in the structure a negative charge excess, which is excepted to be compensated by Ca^{2+} cations placed in the interlayer or by single proton.

Interestingly, the addition of aluminium in the mineral structure gives rise to alumina cross-linking sites, which can be detected by the presence of Q^3(2Al) at -88.8 ppm. The Löwenstein's rule states that –Al–O–Al-bond formation should be forbidden. However, violations of that rule have been documented in several systems, such as mica [165], zeolite [166], and calcium aluminosilicates [167], when the Al content is sufficiently high. Furthermore, the presence of Q^3(2Al) has been detected in natural Al-tobermorite [164] as well as in Al-tobermorite in ancient Roman seawater concrete [57]. Consequently, Dupuis *et al.* proposed that the Löwenstein's rule might be circumvented under some kinetic constraints [164], which could be the case of the formation of Al-tobermorite under supercritical conditions.

To fully elucidate the aluminosilicate structure of Al-tobermorite, it was crucial to perform ^{27}Al MAS NMR analysis. In fact, this technique gives more precise information on enter position of Al atoms rather than the ^{29}Si MAS NMR, for two main reasons. First, ^{29}Si MAS NMR signals are often overlapped, making complicated the fitting procedure. Second, $Q^n(m\text{Al})$ sites could have different relaxation times giving rise to an over- or underestimation of their contribution. On the contrary, during ^{27}Al MAS NMR measurements, aluminium atoms have shown faster relaxation time than silicon sites. Therefore, a recycling delay parameter of 1 s is enough to recorder all the contributions coming from these atoms. In Figure 3.17, the peaks centred at 64 and 56.3 ppm were assigned to two resonances of tetracoordinated Al sites, Al[4], as previously reported for Al-substituted 11Å tobermorite [61, 168, 169]. The presence of two distinct Al[4] can be related to the replacing of Si by Al in two different lattice environments: the resonances at 64 and 56.3 ppm correspond to the substitution in the middle chain bridging Q^2 and the branching Q^3 sites, respectively [170, 171]. Considering the deconvolution of the ^{27}Al MAS NMR spectrum, it can be stated that Al atoms preferentially enter into branching tetrahedral sites of Al-tobermorite synthesised under supercritical conditions. Based on this analysis, it appears clear that Al atoms connect silicate polymeric chains together during the growth mechanism, creating silicate units that are linked by bridging

and, mostly, branching AlO_4 units. These results are in agreement with those previously reported for Al-tobermorite [60, 170].

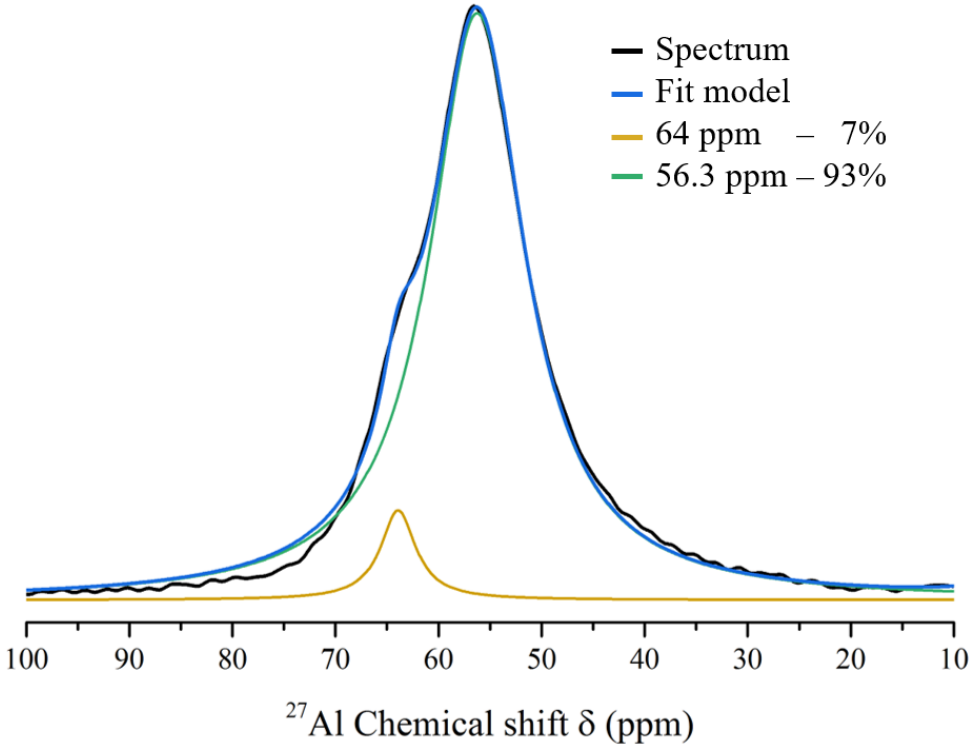

Figure 3.17: ^{27}Al MAS NMR spectra of Al-tobermorite synthesised under supercritical conditions at 25 MPa and 400 °C in 8 s. The fitted curves are presented together with the respective contributions percentage.

It is worth mentioning that ^{27}Al MAS NMR of tobermorite synthesised via SHFS is reported in this work for the first time. In fact, in the study of Diez-Garcia [7, 8], the low amount of material did not allow to perform it, highlighting the importance of developing a suitable user-customised reactor.

The SSNMR results were further confirmed by Raman analysis. Raman spectrum in Figure 3.18 shows several well-resolved bands from which it is possible to obtain structural interpretations. The principal band appears at 678 cm^{-1} and is attributed to linkages involving Q^2 tetrahedra, more specifically to symmetrical Si–O–Si bending vibration [163, 172]. The main contributor of this Raman signal intensity is the bending of Si–O_b bond between a silicon atom and a bridging oxygen atom. Consequently, the high polymerisation degree of the chains, observed by ^{29}Si MAS NMR, is here confirmed by the high intensity of that signal, related to the large number of bridging oxygen atoms that vibrate in phase. The band at 621 cm^{-1} is characteristic of Si–O–Si symmetrical bending involving Q^3 cross-linking Si tetrahedra [163, 172]. The broad shoulder on the low-frequency side, around 570 cm^{-1}, could be related to the contribution of Al–O–Si vibrational modes,

as previously observed in hydrothermally synthetic Al-tobermorite [163].

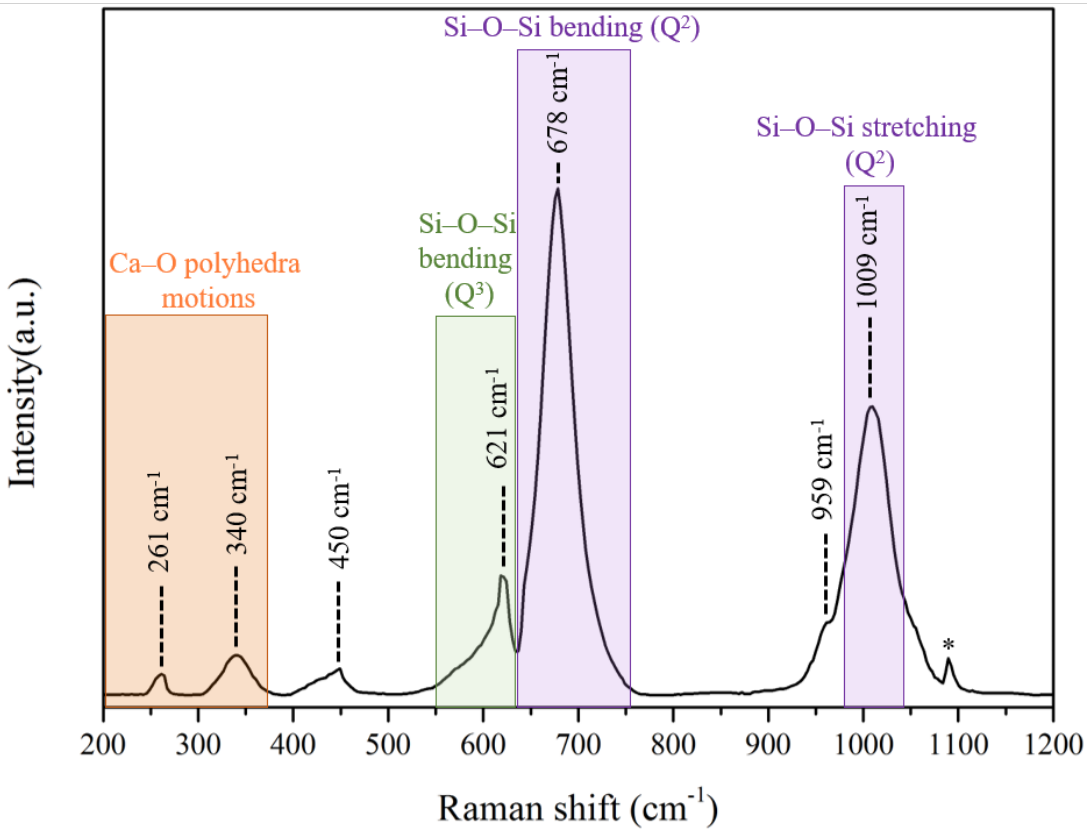

Figure 3.18: Raman spectrum, acquired in the range 200 - 1200 cm^{-1}, of Al-tobermorite synthesised under supercritical conditions at 25 MPa and 400 °C in 8 s. The asterisk denotes C–O stretching mode related to carbonate impurity.

The intense band at 1009 cm^{-1} represents the symmetrical Si–O–Si stretching mode assigned to Q^2 Si sites [173]. On the low-frequency side of this band, the signal around 959 cm^{-1} is attributed to Si–OH stretching vibrations, as previously reported [163]. Furthermore, the symmetrical Si–O–Si stretching band shows a broad shoulder on the high-frequency side, around $\sim$1050 cm^{-1}, probably related to symmetrical stretching involving Q^3 silicate units [173]. Vibrations related to Q^1 sites commonly appear in the region within 800 and 890 cm^{-1} [172], and as previously observed in ^{29}Si MAS NMR spectrum, that contribution is very small in our sample.

The band characterised by an asymmetrical feature to higher frequencies with intensity extending to about 450 cm^{-1}, can be related to internal deformations of the silicon tetrahedra [172]. More specifically, it has been assigned to O–Si–O bending vibrations, where non-bridging oxygen atoms linked to Si atoms are the main contributor [174]. Lastly, the peaks within the region 250 and 350 cm^{-1} are associated to Ca–O lattice vibrations [175].

The presence of a low-intensity peak centred at 1090 cm^{-1} is related to the very Raman-

sensitive symmetrical C–O stretching mode of $CaCO_3$, as vaterite [175]. This peak is commonly detected in both natural and synthetic tobermorite specimens [163].

The characteristic reflection spectrum of Al-tobermorite obtained through FTIR measurement confirms the Raman results and gives more information, Figure 3.19.

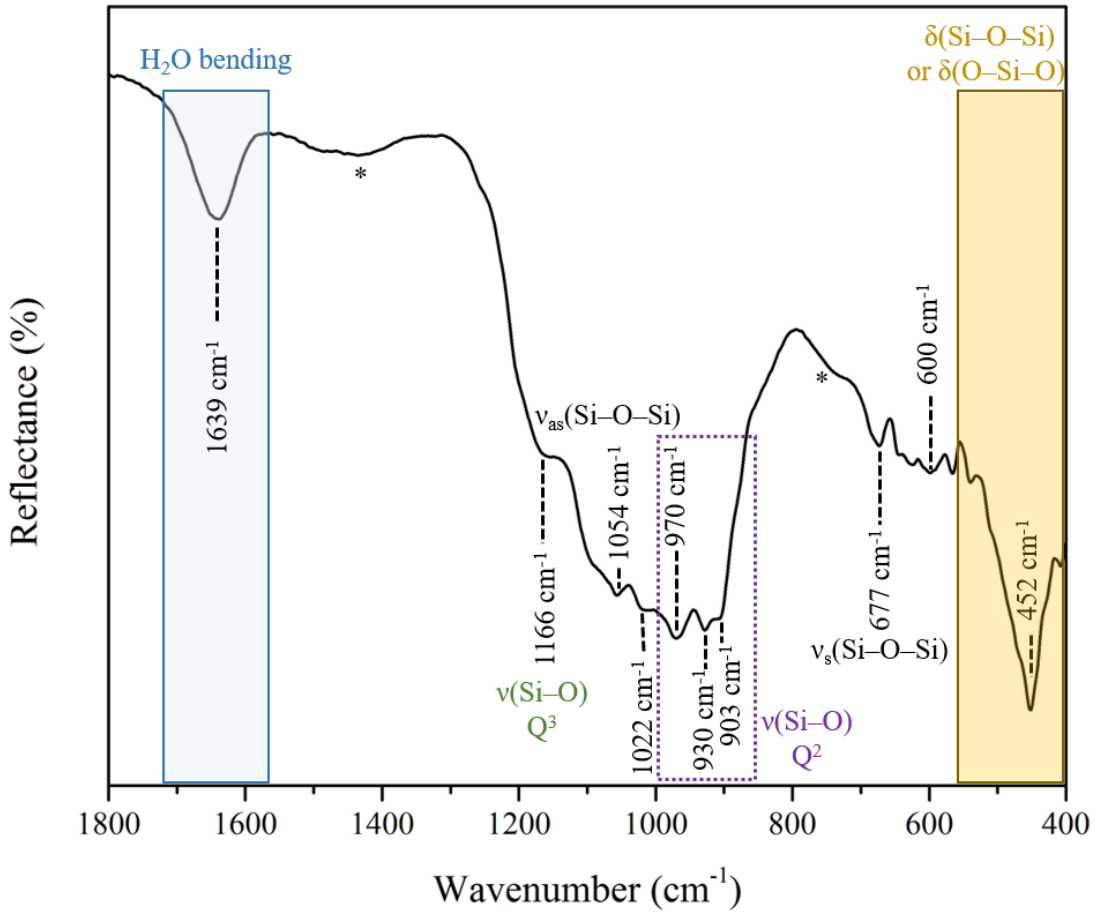

Figure 3.19: IR spectrum, recorded in the range 1800 - 400 cm^{-1}, of Al-tobermorite synthesised under supercritical conditions at 25 MPa and 400 °C in 8 s. The asterisk denotes C–O stretching mode related to carbonate impurity.

In the spectrum of tobermorite, as for xonotlite, the band related to the bending vibration of water is centred around 1639 cm^{-1}. In the range 1100 - 1200 cm^{-1}, a band at 1166 cm^{-1} and a small bump around 1200 cm^{-1} are related to Si–O stretching (O-links between bridging tetrahedra, ν(Si–O)Q^3). Some authors suggested that the band around 1166 cm^{-1} might be characteristic of anomalous tobermorite [7, 8, 176]. The spectral features related to Si–O stretching of Q^2 sites (ν(Si–O)Q^2) appear around 970, 930, and 903 cm^{-1} [159]. The signal observed at 1054 corresponds to the asymmetrical (ν_{as}(Si–O–Si)) stretching vibration of Si–O–Si bridges, respectively [159]. Instead, the peaks centred at 677 and 600 cm^{-1} are assigned to the respective symmetrical stretching

vibrations bands (ν_s(Si–O–Si)). Lastly, the presence of small traces of vaterite contribute to the IR spectra around 1400 and 780 $^{-1}$.

The spectral features at 1022 cm^{-1} can be assigned to Si–O stretching (in SiO_2) in agreement for what is reported for natural tobermorite [82]. In the frequency region within 550 and 400 cm^{-1}, the bands related to O–Si–O deformation or bending modes (δ_s(O–Si–O), (δ(Si–O-Si)) appear [159].

3.4.2 Intrinsic mechanical properties of tobermorite synthesised in supercritical water

As discussed in chapter 1, Al-tobermorite is considered as a model for calcium aluminosilicate hydrate, the glue in concrete, and it has also been found in ancient Roman concrete. The service life of Roman structures is about two orders of magnitude longer than that of modern structures [177], and their high durability (over 2000 years) has been related to the presence in it of Al-tobermorite. In this context, the investigation of the mechanical proprieties of this material can be of crucial importance for designing cement-based materials containing Al-tobermorite. In this work, the characterisation of intrinsic mechanical properties of Al-tobermorite was performed through a synchrotron radiation-based high pressure X-ray diffraction. HP-XRD experiments were carried out at the beamline 12.2.2 of the Advanced Light Source at the Lawrence Berkeley National Laboratory to test the crystallinity and the lattice deformation of Al-tobermorite under hydrostatic load. The measurements and the data processing were carried out in collaboration with Jiaqi Li, postdoctoral researcher in the research group led by Paulo J. M. Monteiro at University of California, Berkeley.

In Figure 3.20, the powder X-ray pattern of Al-tobermorite acquired at ambient pressure exhibits the characteristic diffraction peaks of the mineral phase identified by the corresponding Miller indices. During the HP-XRD experiments, diffraction patterns were acquired at different hydrostatic pressures: 1.1, 2.8, 4.4, 5.1, 6.1, 7.2 and 8.3 GPa. Another diffraction pattern was recorded at atmospheric pressure when the sample was unloaded after the experiments, to investigate if the effects of the compression on the structure are permanent or not.

Two main effects of the compression on the material structure can be observed from Figure 3.20. First, by increasing the applied hydrostatic load, the diffraction peaks monotonically shift to higher d^{-1} values. This experimental evidence is the consequence of a systematic decreasing of the interplanar distances, in fact, closing interlayer spacing are

indicated by the shift of (002) peaks, as shown in the inset of Figure 3.20. Furthermore, the X-ray powder pattern acquired when the sample was unloaded shows that such deformations are purely elastic, as the diffraction peaks return to their original positions at the end of the experiment. Second, the applied compression results in a broadening of all diffraction peaks, which can be related to the mineral structure's amorphisation in terms of reduction in the structural order and/or the development of microstrains. This pressure-induced amorphisation phenomena has been previously detected in several other HP-XRD experiments, including studies on synthetic tobermorite [163], natural tobermorite [164], tobermorite in Roman concrete [57], jennite [178], calcium aluminosilicate hydrate [179], and cementitious material phases [180, 181].

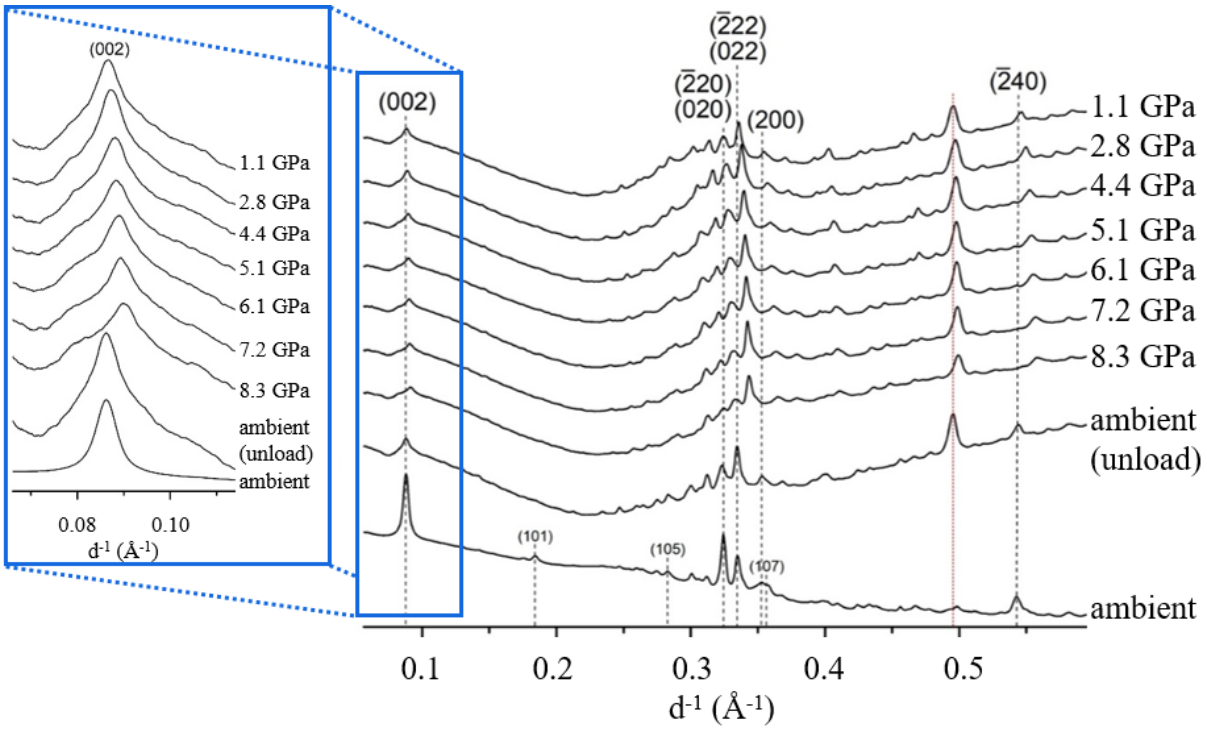

Figure 3.20: Powder X-ray diffraction patterns of Al-tobermorite, synthesised under supercritical conditions, as a function of applied hydrostatic pressure. Vertical black dashed lines correspond to the reference peaks positions at ambient pressure, whereas the vertical red dot line indicates the diffraction from the gasket. The inset shows a zoom-in where the effect of hydrostatic pressure on the position and broadening of (002) peak is noticeable.

Thanks to this study, unit cell parameters of the material were refined using *CelRef* software with Merlino's tobermorite structure, space group B11m [182]. In Table 3.2 the unit cell parameters of Al-tobermorite measured for the different pressure values are reported. As already shown from the XRD patterns, the applied hydrostatic pressure impacts the crystal structure producing a gradual decreasing of the unit cell parameters and the cell volume. These results agree with those previously reported for 11Å tobermorite

synthesised under subcritical conditions [163].

Table 3.2: Cell parameters of 11Å tobermorite measured at different pressure values: ambient, 1.1, 2.8, 4.4, 5.1, 6.1, 7.2 and 8.3 GPa.

Pressure (GPa)	a (Å)	b (Å)	c (Å)	γ (°)	V (Å^3)
Ambient	6.746	7.365	22.760	123.08	947.6
1.1	6.729	7.336	22.719	123.03	940.4
2.8	6.686	7.293	22.566	123.05	922.4
4.4	6.650	7.259	22.396	123.08	906
5.1	6.636	7.242	22.351	123.07	900.3
6.1	6.613	7.222	22.206	123.1	888.5
7.2	6.577	7.201	22.198	123.19	879.9
8.3	6.558	7.189	22.009	123.24	868

The HP-XRD results can be used to obtain information on the intrinsic mechanical properties of Al-tobermorite synthesised under supercritical conditions. First, the definitions of Biot strain and bulk modulus must be introduced. Biot strain of the unit cell is defined as:

$$\text{Biot Strain} = \frac{L - L_0}{L_0} \tag{3.1}$$

where L and L_0 are the lattice parameters of the unit cell at the applied and ambient pressure, respectively. Biot strain along each axis as a function of applied hydrostatic pressure can be fitted with a linear trendline, as displayed in Figure 3.21. The results have shown that the incompressibilities along **a**- and **c**-axes of tobermorite synthesised in SCW are -1/283 and -1/241 GPa^{-1}, respectively, highly comparable to previous studies on cross-linked C-A-S-H [179] and hydrothermally synthetic Al-tobermorite with similar Al content [163]. Whereas, the incompressibility value along the **b**-axis was estimated to be higher than that reported by Li *et al.* for tobermorite synthesised with a similar Al content, Al/(Al+Si) = 0.16, in autoclaves under subcritical conditions at 170 °C for 22 h followed by additional 2 h at 180 °C [163]. This significant result suggests that the **b**-axis of Al-tobermorite synthesised in SCW is stiffer than that of hydrothermally synthetic Al-tobermorite. This phenomenon could be explained by considering the high polymerisation degree of the aluminosilicate chains observed by SSNMR, which in turn can be related to a more crystalline and ordered structure of our sample.

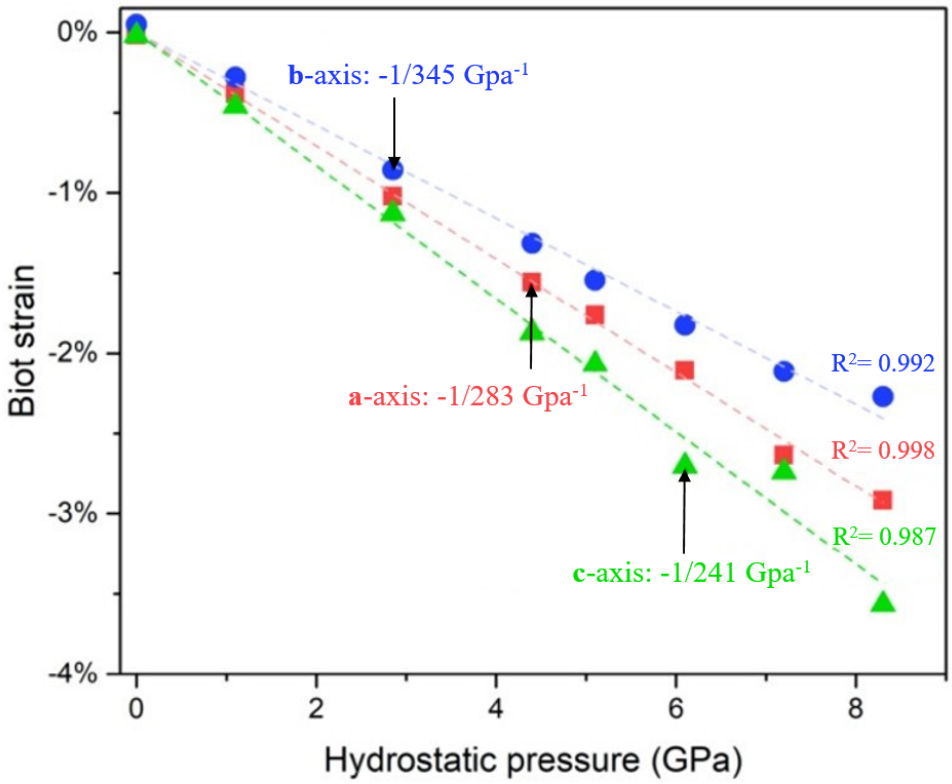

Figure 3.21: (a) Biot strain as a function of applied hydrostatic pressure along the **a**-, **b**-, and **c**-axes. The uncertainty of pressure is estimated to be about ± 0.15 GPa. The uncertainty of the Biot stain is below $\sim 0.15\%$. R^2 of the fittings are above 0.987.

The third-order Birch-Murnaghan equation of state (BM-EoS, Equation 3.2) describes the relationship between the pressure-induced volumetric change and the bulk modulus of an unit cell [183]:

$$P = \frac{3}{2} K_0 \left[(V/V_0)^{-\frac{7}{3}} - (V/V_0)^{-\frac{5}{3}}\right] \left[1 + \frac{3}{4}\left(K_0' - 4\right)\left((V/V_0)^{-\frac{2}{3}} - 1\right)\right] \tag{3.2}$$

where P is the applied hydrostatic pressure in the chamber, K_0 is the bulk modulus at ambient pressure, V is the volume of unit cell under pressure, V_0 is the initial volume of unit cell at ambient pressure, and K_0' is the pressure derivative of K_0, typically fixed at 4 for cement-related phases [178, 180]. In our work, the second-order BM-EoS was employed, as commonly done for these materials in previous studies [163, 178, 180, 184]:

$$P = \frac{3}{2} K_0 \left[(1-\epsilon_V)^{-\frac{7}{3}} - (1-\epsilon_V)^{-\frac{5}{3}}\right] \tag{3.3}$$

where ϵ_V is the volumetric strain of a unit cell, defined as $\epsilon_V = (V_0 - V)/V_0$. Figure 3.22 shows the linear trendline of hydrostatic pressure versus the volumetric strain. Pressure-volume data were fitted using the 2^{nd} order Birch-Murnagnan Equation of State to determine the isothermal bulk modulus at atmospheric pressure.

In this work, the K_0 value of Al-tobermorite synthesised in SCW was determined to be 75 ± 2 GPa, which corresponds exactly with the theoretical value predicted through simulations by Manzano *et al.* for anomalous 11Å tobermorite [185]. In a recent HP-XRD study on natural 11Å tobermorite samples reported by Dupuis *et al.* the bulk modulus of a normal and an anomalous specimens were found being equal to 71 ± 4 GPa and 63 ± 2 GPa, respectively [164]. In their work, the lower K_0 value of anomalous tobermorite was associated to the higher Al content in that sample (Al/Si = 0.25) than in the normal one (Al/Si = 0.1). In fact, it has been proposed that the Al–O bond is softer and longer than the Si–O bond, and at the same time, the Al–O–Al angles are more malleable than the Si–O–Si or Si–O–Al bonds [164].

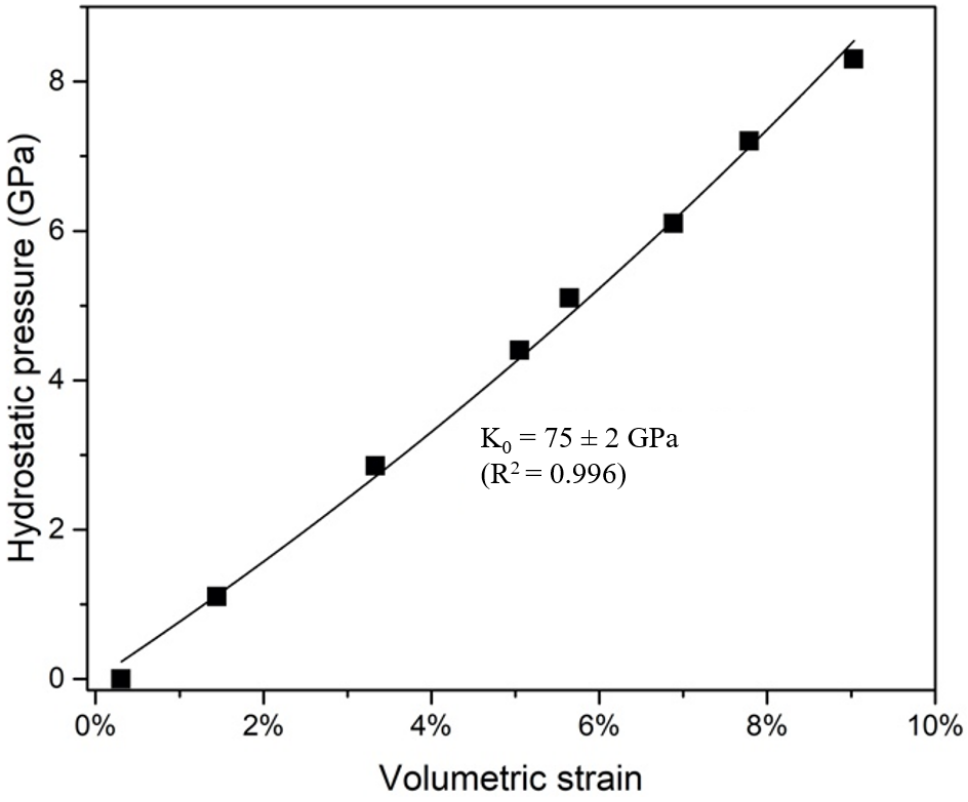

Figure 3.22: Volumetric strain determined at different hydrostatic pressure values. The data were fitted with 2^{nd} order BM-EoS to determine K_0. The uncertainty of pressure is estimated to be about ± 0.15 GPa. R^2 of the fitting is 0.996.

Furthermore, the value of K_0 measured in this work agrees well with values reported for tobermorite hydrothermally synthesised with different Al contents, more specifically: 63 ± 3 GPa for Al-free tobermorite, 70 ± 2 GPa for tobermorite with Al/(Al+Si) = 0.083, and 71 ± 2 GPa for tobermorite with Al/(Al+Si) = 0.16 [186]. Another interesting comparison could be made between the values of K_0 measured in this work and that measured for Al-tobermorite found in ancient Roman seawater concrete, 55 ± 5 GPa [57]. The lower

K_0 value of tobermorite in ancient Roman concrete could be related to the presence in the structure of some distortion due to Na^+ and K^+ incorporation in the interlayer, which results in lower mechanical properties.

The relevant results on the intrinsic mechanical properties of 11 Å tobermorite found in this work are summarised and compared with those previously reported in the literature for several natural and synthetic tobermorite specimens in Table 3.3 [57, 163, 164].

Table 3.3: Comparison between the bulk modulus and the incompressibility values along the **b**-axis determined for 11 Å tobermorite synthesised in supercritical water (SCW), and other specimens: natural [164], product of ancient Roman seawater concrete [57], and synthetic obtained via conventional hydrothermal synthesis (HS) [163]. For the natural samples, the letters n and a refer to a normal or an anomalous specimen.

	Tobermorite specimens			
	Natural [164]	Roman Concrete [57]	Synthetic (HS) [163]	Synthetic (SCW)
Bulk Modulus (GPa)	71 ± 4 (n) 63 ± 2 (a)	55 ± 5	71 ± 2	75 ± 2
Incompressibility along **b**-axis (GPa^{-1})	-	-	-1/260	-1/345

To conclude, anomalous Al-substituted 11 Å tobermorite was synthesised in this work via a hydrothermal flow process in supercritical water at 400 °C and 25 MPa in 8 s. The main advantage to use this methodology relies on boosted reaction kinetics, allowing the synthesis of high crystalline tobermorite fibres in only 8 s. The in-depth characterisation analysis has shown that, despite the curtail of reaction times, our material is very close to the natural mineral in crystallinity and morphologies. Furthermore, by using techniques as SSNMR, Raman and HP-XRD, we have shown that 11 Å tobermorite synthesised in SCW exhibits aluminosilicate chains with high polymerisation degree, a less defective structure, and better intrinsic mechanical properties if compared to samples produced via conventional hydrothermal synthesis. These findings suggest that this innovative technology more accurately captures the formation process of minerals that takes place in nature.

3.5 Fingerprint of tobermorite nanomineral synthesised in SCW

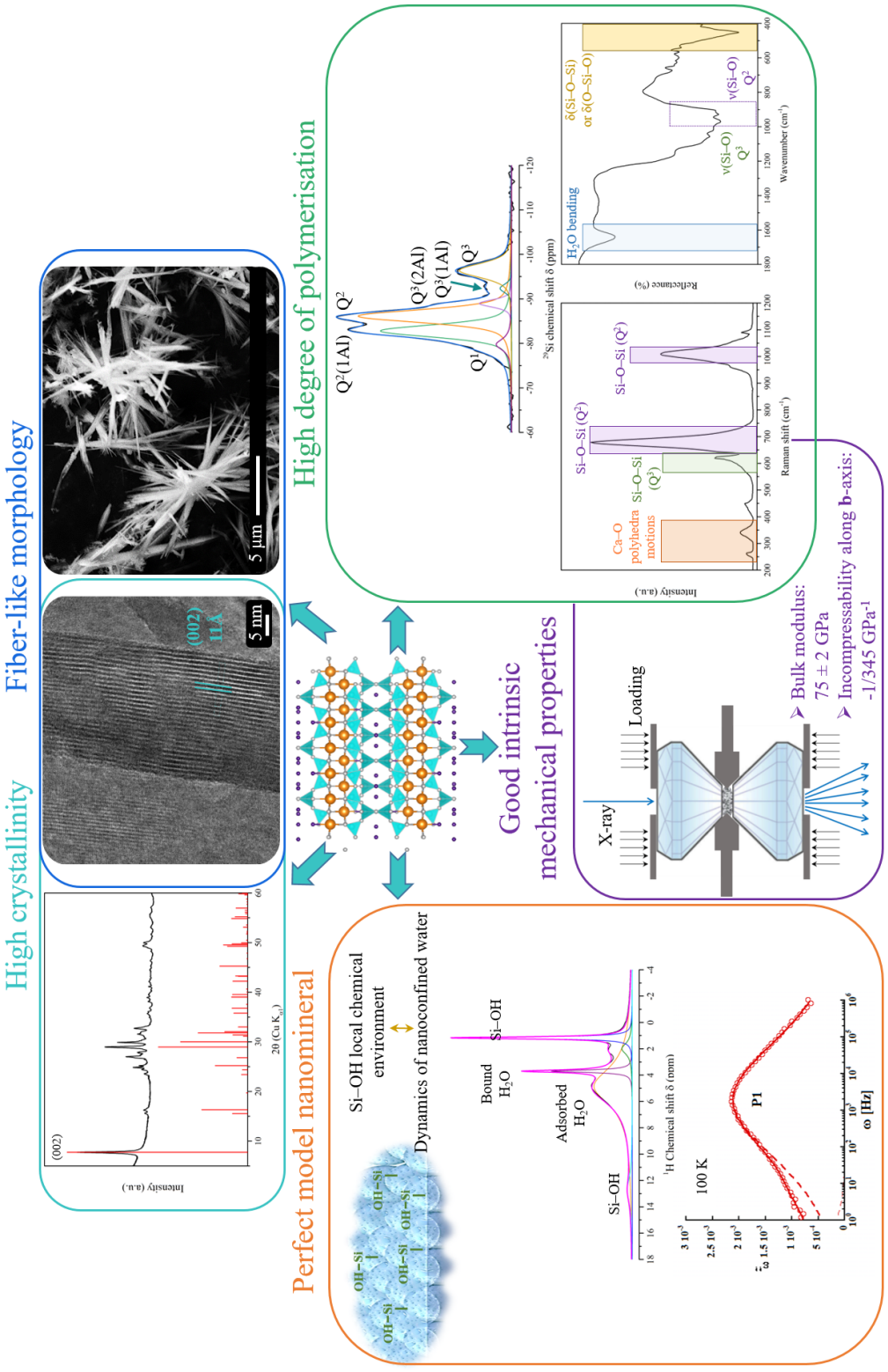

Figure 3.23: Fingerprint of tobermorite nanomineral synthesised in supercritical water (400 °C and 25 MPa, in 8 s).

As a conclusion of these results, it can be stated that the supercritical hydrothermal flow synthesis allows producing model nanominerals by mimicking natural environments at high temperatures and pressures. As-synthesised xonotlite and tobermorite represent two synthetic highly crystalline materials characterised by different physicochemical properties that depend on the presence of calcium hydroxide and silicon hydroxide groups. Therefore, these model systems offer the opportunity to rigorously describe the relationship between the dynamics of nanoconfined water and the local material chemistry in calcium silicate hydrates. In particular, the effect of the local chemical environments, either Si–OH or Ca–OH, on the hydrogen bond network and on dynamics of nanoconfined water will be discussed in the next section.

3.6 Correlation between the dynamics of nanoconfined water and the local chemical environments in xonotlite and tobermorite

In chapter 1 (section 1.2.4), the extensive interest in studying the dynamics of nanoconfined water in calcium silicate hydrate nanominerals has been highlighted. Despite previous studies on C-S-H gel [79, 80, 187] and tobermorite [81, 82], the definitive origin of the relaxation processes in these systems is difficult to ascertain, and an appropriate assignment is still incomplete. This lack of knowledge can be attributed to two main reasons. First, the description of C-S-H gel structure, which accommodates both Ca–OH and Si–OH groups at the nanoscale, is very complex due to its heterogeneous and amorphous nature. Second, the tobermorite mineral, even if more crystalline than C-S-H gel, contains only Si–OH groups and thus does not allow to investigate the effect of different chemical environments on the dynamics of water molecules.

In this work, to further elucidate the relationship between the dynamics of nanoconfined water and the local material chemistry in calcium silicate hydrates, two appropriate synthetic model nanominerals, xonotlite and tobermorite, were studied. Tobermorite is an optimal candidate to explore the effect of the silicon hydroxide environment on water dynamics, and xonotlite is expected to be a good mineral archetype to study the additional contribution of the Ca–OH chemical environment.

The study was conducted in 2 steps: first, the hydrogen bond network of the minerals was investigated, and then the dielectric spectroscopy data were interpreted to explain the nanoconfined water dynamics in xonotlite and tobermorite. We refined the picture of the dynamics of confined water and hydroxyl groups in calcium silicate hydrates, through a combination of spectroscopic techniques, which could be potentially applied to other water-containing materials.

3.6.1 Study of the hydrogen bond network in xonotlite and tobermorite structures

Three powerful techniques for the investigation of the hydrogen bond networks in nanominerals are Fourier transform infrared, Raman, and nuclear magnetic spectroscopies. The characteristic IR spectra of xonotlite and tobermorite within the range 2800 - 4000 cm^{-1} are shown in Figure 3.24. The sharp absorption peak at 3610 cm^{-1} is attributed to the Ca–OH vibration and appears only in the spectrum of xonotlite; this bonding is exclusively

contained in the xonotlite structure and thus is characteristic of this mineral. In the range of OH stretching frequencies from 2600 to 4000 cm^{-1}, both spectra show a broad band at approximately 3400 cm^{-1}, which is presumably linked to the stretching contributions of both structurally incorporated OH groups and surface-adsorbed water (Si–OH···H_2O), as reported in the simulation results of Churakov *et al.* [154]. The broadening of this band, if compared of that one of xonotlite at 3610 cm^{-1}, is related to hydrogen bonding with a wide range of strengths [159]. Furthermore, a more intense peak attributed to adsorbed and interlayer water was observed in the tobermorite phase rather than in xonotlite. It is interesting to highlight the similarity of our results for tobermorite synthesised in supercritical water with those reported by Monasterio *et al.* for the natural specimen [82]. In their work, the IR spectrum of synthetic tobermorite synthesised at 200 °C in 4 h was compared with that of a natural sample. Their results have shown a shift of the broad peak attributed to OH towards lower wavenumbers in the natural tobermorite mineral. That effect was related to the higher crystallinity of the natural structure, which results in lower OH bond strength [82].

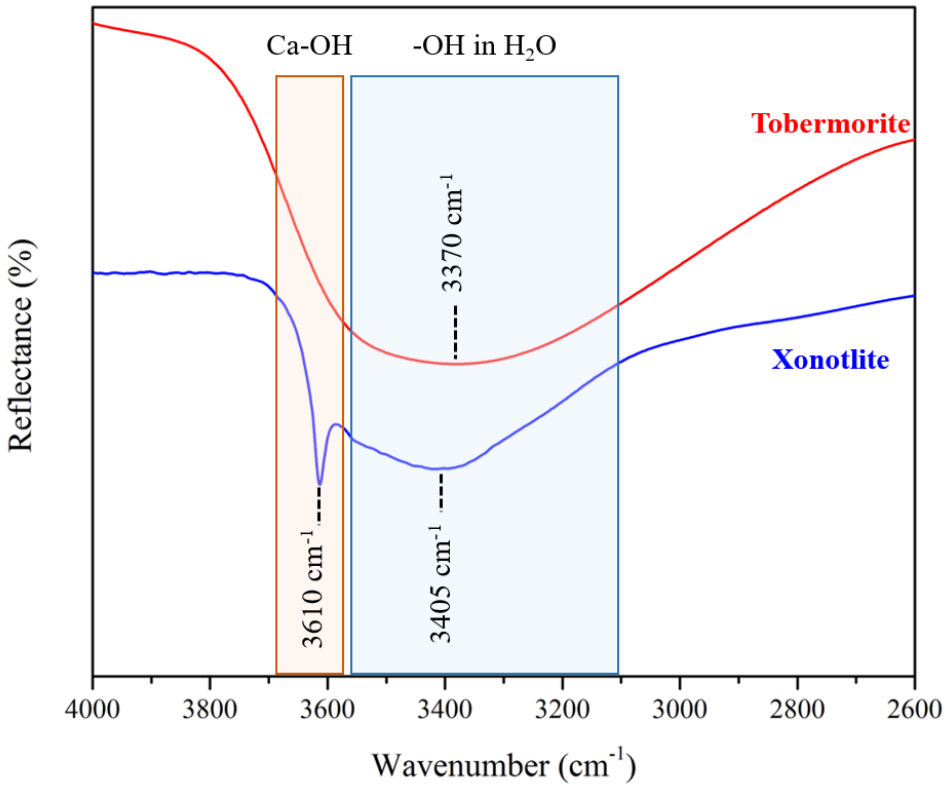

Figure 3.24: IR spectra of tobermorite (red curve) and xonotlite (blue curve) synthesised under supercritical conditions at 400 °C and 25 MPa [188].

Full comprehension of the hydrogen bond network in xonotlite and tobermorite has

been obtained with further investigation in the 2800 - 3800 cm^{-1} region by micro-Raman spectroscopy. The spectrum of xonotlite shown in Figure 3.25 displays two groups of Raman-active vibrations.

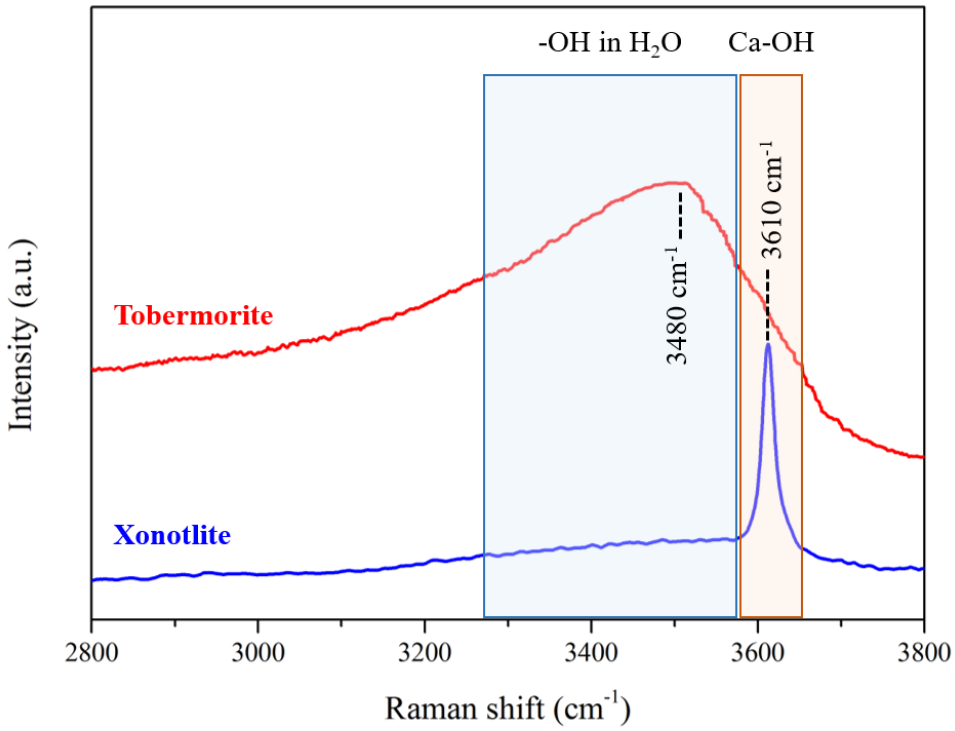

Figure 3.25: Raman spectra of tobermorite (red curve) and xonotlite (blue curve) synthesised under supercritical conditions at 400 °C and 25 MPa [188].

The most intense and sharp signal, centred at 3610 cm^{-1}, is attributed to hydroxyl stretching bands of Ca–OH units in the mineral, similar to those of portlandite ($Ca(OH)_2$), where the A_{1g} (OH) mode appears at 3618 cm^{-1} [174, 189]. At lower frequencies, the broad band centred at approximately 3500 cm^{-1} is assigned to OH stretching vibrations of surface-adsorbed water molecules [174]. In contrast, the Raman spectrum of tobermorite in Figure 3.25 shows only one broad signal centred at approximately 3480 cm^{-1}. This band is attributed to water stretching vibrations and has a much greater intensity than that observed in xonotlite. As already suggested from FTIR spectroscopy, the Raman results confirm the absence of hydroxyls linked to the Ca–O sheets in the tobermorite structure. These findings are in agreement with the results of several studies on natural minerals and confirm that both xonotlite and tobermorite prepared in SCW exhibit very close structural characteristics to those of their natural counterparts [173, 174].

The difference between the hydrogen bond networks in xonotlite and tobermorite were further investigated by ^1H SSNMR. In Figure 3.26 the xonotlite spectrum was deconvoluted into four signals (fitted curves) centred at 1.9, 2.3, 5.1 and 15.2 ppm, in agreement

with the interpretation reported in the previous section 3.2.2.

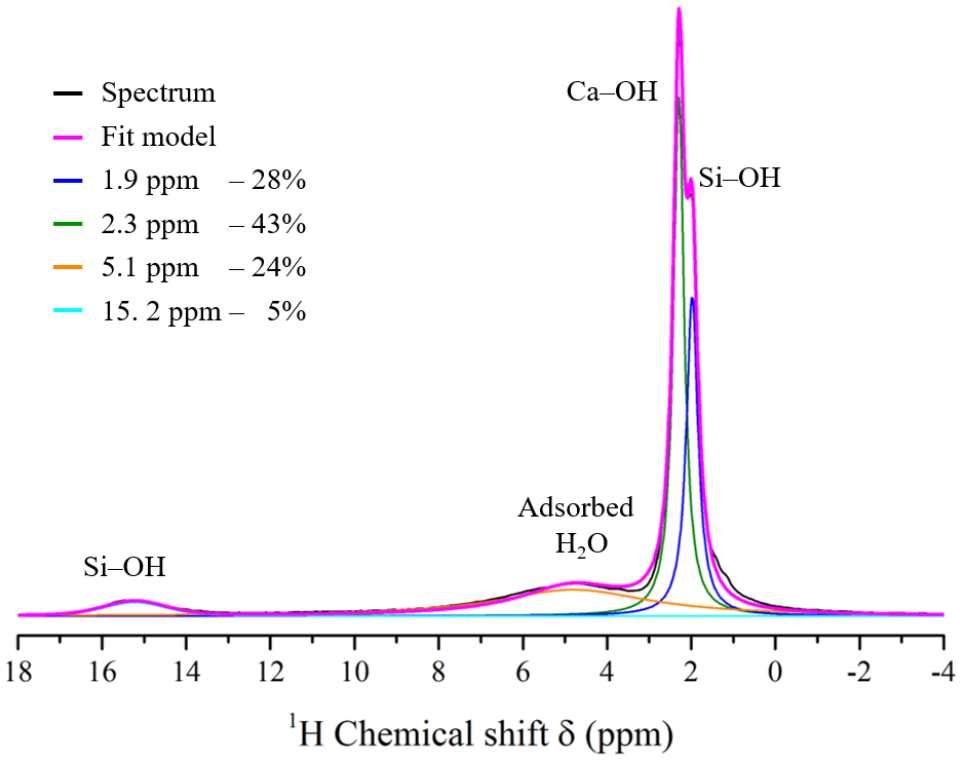

Figure 3.26: ^{1}H MAS NMR spectrum of xonotlite. The fitted curves are presented together with the respective contributions percentage [188].

To our knowledge, any study that focuses on the local environment of hydrogen species in tobermorite structure, determined with ^{1}H SSNMR, is reported in the literature. Peak assignments and data analysis are a challenge due to the complexity of the structure and possible proton configurations multiplicity. In Figure 3.27, the ^{1}H MAS NMR spectrum of tobermorite formed in SCW exhibits two sharp peaks centred at 1.2 and 3.7 ppm and three broad shoulder signals at 2.2, 5 and 12.8 ppm. All these peaks are related to the presence of structural OH and molecular water, as well as interlayer water in tobermorite. Despite the similarity of the xonotlite and tobermorite structures, the comparison between the ^{1}H MAS NMR spectra shows several differences. First, the slight shift towards higher values of the Si–OH signal in xonotlite (1.9 ppm) rather than in tobermorite (1.2 ppm). This experimental evidence could be explained by considering that hydroxyl groups with stronger hydrogen bonding exhibit larger chemical shifts than those with weaker hydrogen bonding [190]. Thus, the downfield shift of the Si–OH bond peak in the tobermorite spectrum occurs mainly due to the decrease in the electronic charge of the hydrogen bonded proton. This result is in accordance with previous studies on silica particles, which reported the observation of a peak at 1.1 ppm assigned to isolated (i.e., not hydrogen

bonded) silanols at the SiO_2 surface [191]. Therefore, the intense peak at 1.2 ppm was assigned to protons in structural and weakly bonded Si–OH groups.

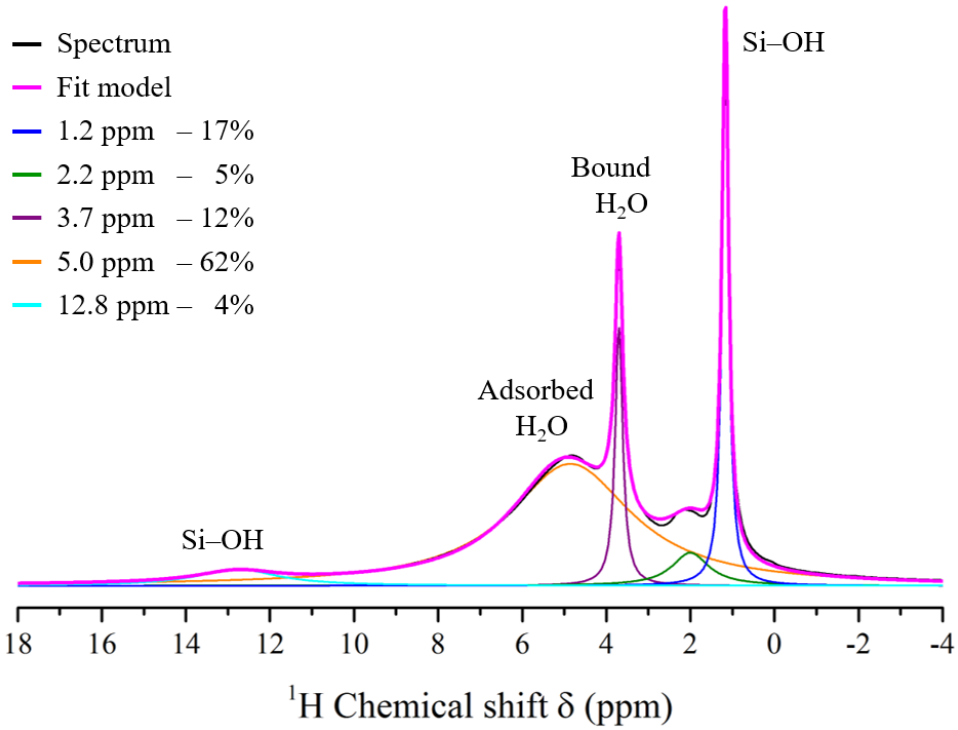

Figure 3.27: ^{1}H MAS NMR spectrum of tobermorite. The fitted curves are presented together with the respective contributions percentage [188].

On the other hand, the broad resonances at 2.2, 5.0 and 12.8 ppm can be related to protons linked to Ca–OH, water on hydrated surfaces and strongly hydrogen-bonded protons in Si–OH groups, respectively [155, 156, 191, 192]. These findings are in accordance with the results reported by Colombet *et al.* for numerous polycrystalline calcium hydrosilicate materials [193].

Lastly, to explain the origin of the signal at 3.7 ppm, some knowledge discussed in chapter 1 must be recalled. Water molecules within minerals can be present in zeolitic sites or interlayer regions, as well as on the surface in the form of macroscopic fluid inclusions or microscopic cracks in the crystal [71]. Yesinowski *et al.* investigated numerous hydrous species in minerals by ^{1}H MAS NMR and reported that only minerals, such as analcite and hemimorphite, containing hydrogen in the form of stoichiometric amounts of water exhibit peaks at approximately 3.1 and 3.6 ppm [71]. These chemical shift values are very close to the value of 3.7 ppm found in this work. Consequently, this peak appearing in the tobermorite spectrum and absent from that of xonotlite might be probably related to the presence of stoichiometric amounts of water located in the cavities between double silicate chains. This assignment proposed in our work would be in agreement with the

presence of water molecules in the structure of 11Å tobermorite proposed by Merlino *et al.* [50].

The investigation of the water content in xonotlite and tobermorite minerals was also conducted by thermogravimetric analysis, as shown in Figure 3.28. Nonevaporable water is defined as the H_2O molecules distributed throughout the sample in capillary pores and/or both small and big gel pores [79]. The nonevaporable water content in weight, c_w (wt.%), was calculated as $c_w = (m_{105} - m_{300})/m_{300}$, where m_{105} and m_{300} represent the mass weight of the sample at 105 and 300 °C, respectively. We have observed that the amount of nonevaporable water is double in xonotlite, $c_w = 0.95$ wt.%, in respect to tobermorite, $c_w = 0.48$ wt.%. As we will show later, the presence of different nonevaporable water content in the two mineral phases affects their dielectric properties.

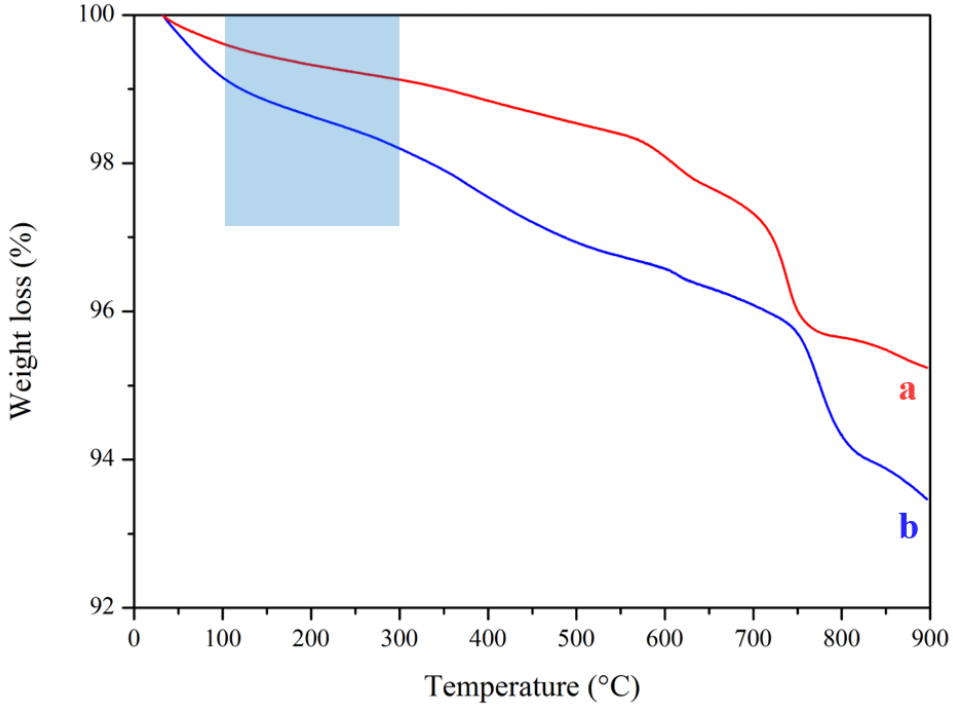

Figure 3.28: Thermogravimetric curves of (a) tobermorite and (b) xonotlite synthesised under supercritical conditions [188].

3.6.2 Dynamic of nanoconfined water in xonotlite and tobermorite

One of the most useful techniques for investigating the structure and the dynamics of nanoconfined water is broadband dielectric spectroscopy due to its sensitivity to the high dipolar moment of water molecules. In this work, the measurements and the data analysis were carried out in collaboration with Guido Goracci, Postdoctoral researcher in

the *Ceramic and Cement-Based Materials* group led by Jorge S. Dolado at CFM.

In the case of minerals with close distributions of hydrous species in the structure, such as xonotlite and tobermorite, water molecules and hydroxyl groups are expected to contribute to the dielectric signal similarly. However, BDS analysis, conducted on xonotlite for the first time in this work, revealed some specific and different properties between the two mineral structures that cannot be detected with other conventional techniques.

In Figure 3.29, the imaginary part of the tobermorite and xonotlite complex permittivity (ϵ'') is shown at representative temperatures (100, 160 and 200 K).

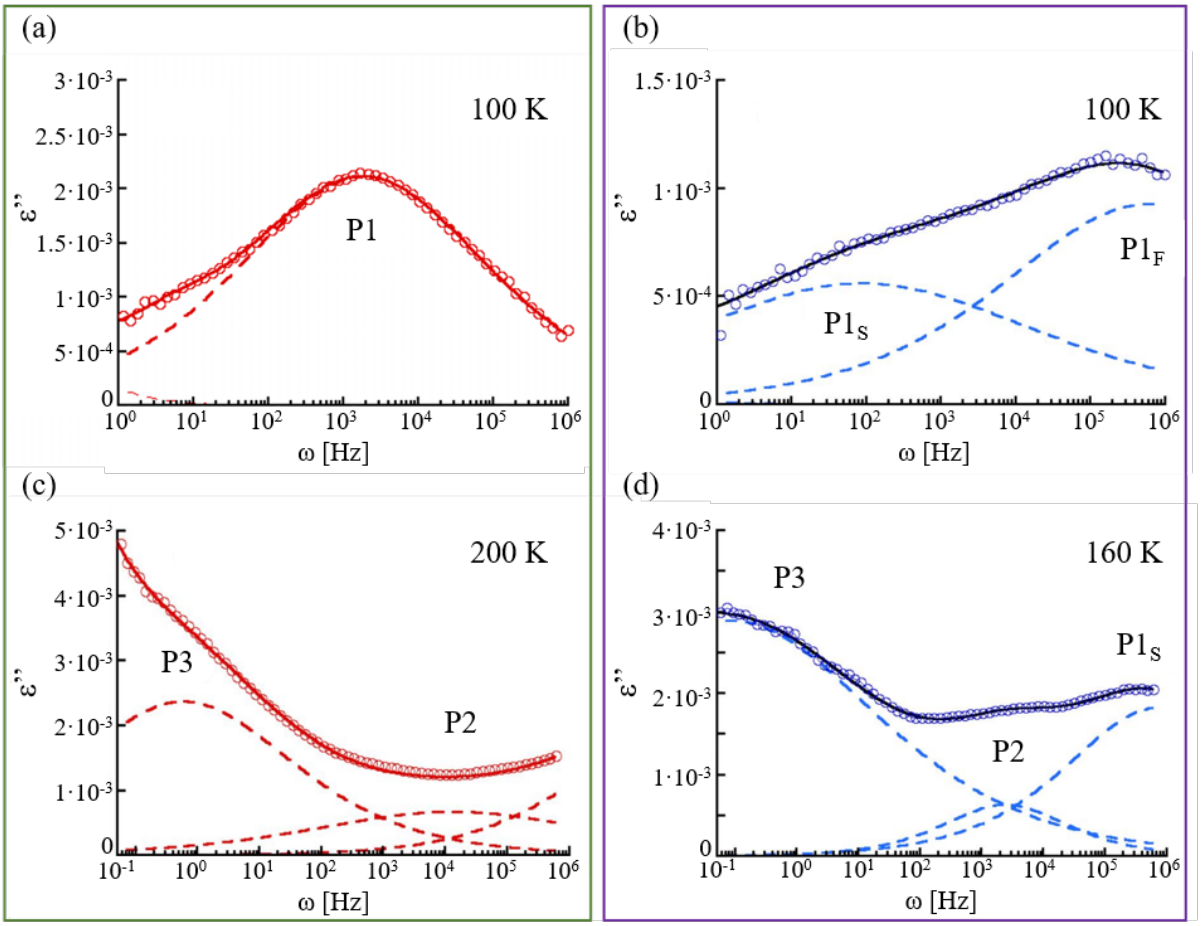

Figure 3.29: Imaginary part (ϵ'') of the dielectric spectra of nanominerals at different temperatures: tobermorite at (a) 100 K and (c) 200 K and xonotlite at (b) 100 K and (d) 160 K. The solid lines represent the fits to the experimental data. The dashed lines represent the relaxation corresponding to processes 1, 2, and 3 [188].

The complex non-Debye dielectric behaviour of these nanominerals can be represented in terms of different distributed relaxation processes, in distinct temperature and frequency ranges, and labelled as P1, P2, and P3 in accordance to their appearance during the heating process. Starting from the low-temperature region, the tobermorite signal

is characterised by a well-defined peak (P1), as shown in Figure 3.29(a). Contrarily, in Figure 3.29(b) xonotlite shows two components at the same temperature, slower (P1S) and faster (P1F) than that observed in tobermorite. Upon increasing the temperature, a new weak process is observed in both samples (P2). Finally, at higher temperatures, process P3 enters in the frequency range of the dielectric spectrometer, as shown in Figure 3.29(c) and 3.29(d). All the processes shift towards higher frequencies as the temperature increases, suggesting that the process is thermally activated. To extract information on the relaxation times, the dielectric response can be described by using standard fit functions. In that case, as commonly done for confined water, the data were analysed in terms of Cole-Cole functions, Equation 2.21. Through this analysis, the Cole-Cole shape parameter was determined ranging between 0.4 and 0.6.

The temperature dependence of the extracted relaxation times for each dynamic observed in tobermorite and xonotlite is shown in Figure 3.30. All the processes exhibit an Arrhenius-type temperature dependence within the entire temperature range.

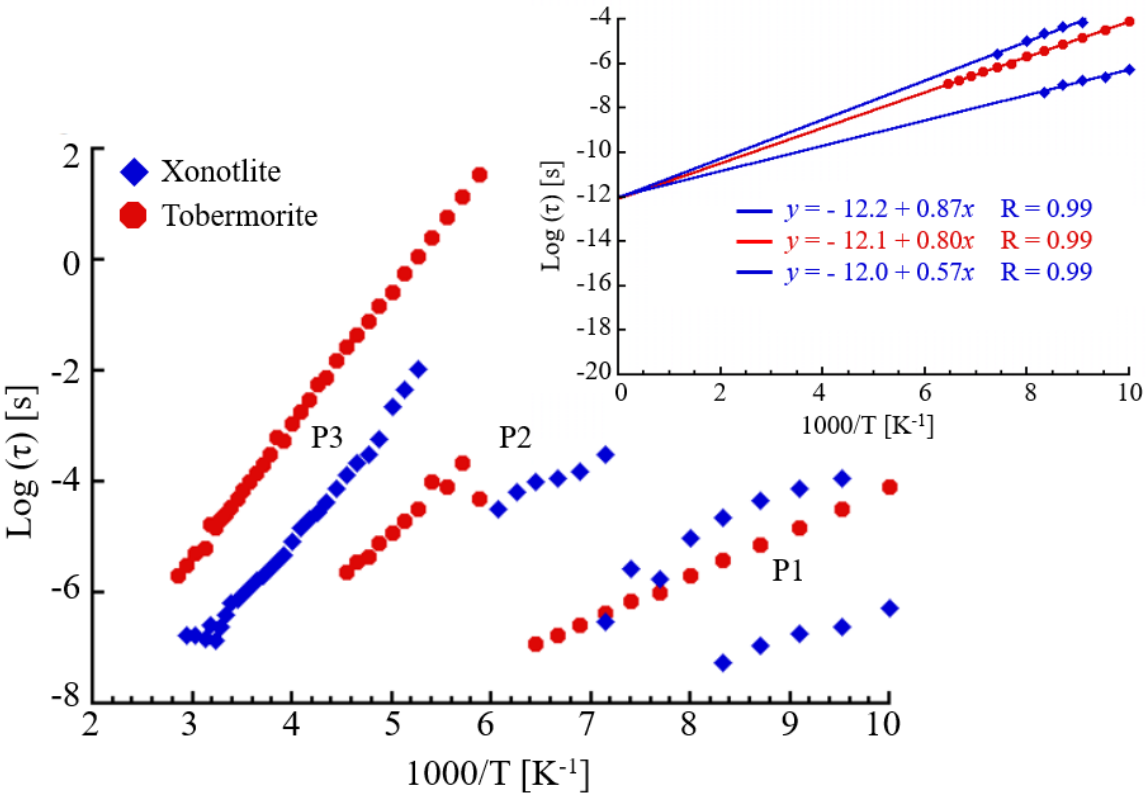

Figure 3.30: Temperature dependence of relaxation times related to the observed dynamics in tobermorite (in red) and xonotlite (in blue) synthesised in SCW. The inset shows the fit for each P1 process, together with the calculated fit equations used to determine the τ_0 and E_a values [188].

The linearisation of the Arrhenius law, Equation 2.24, allows plotting $\log \tau$ versus

the inverse temperature, 1/T, in a so-called Arrhenius plot. This form of the Arrhenius equation makes easier to determine the activation energy (E_a) and the pre-exponential factor ($\log \tau_0$) as the slope and y-intercept, respectively. The interpretation of these data provides information about the nature of the motions involved in relaxation processes. The value of τ_0 and E_a determined for each process by fitting the experimental data with the Arrhenius function, are reported in Table 3.4.

Table 3.4: Activation Energy, E_a, and pre-exponential factor, $\log \tau_0$, obtained from the Arrhenius equation applied to the data in Figure 3.29 [188].

Material	Process 1		Process 2		Process3	
	E_a (eV)	$\log \tau_0$ (s)	E_a (eV)	$\log \tau_0$ (s)	E_a (eV)	$\log \tau_0$ (s)
Xonotlite	0.12 P1F 0.18 P1S	-12.0 P1F -12.2 P1S	0.16	-9.3	0.42	-13.5
Tobermorite	0.16	-12.1	0.33	-13.3	0.48	-12.6

Starting from the faster process, P1 is characterised by a low energy activation (between 0.12 and 0.18 eV) and a characteristic time $\tau_0 \sim 10^{-12}$ s typical of vibrational dynamics. A similar process was previously observed in the investigation of natural and synthetic tobermorite by Monasterio *et al.* [81, 82]. In their work, this process was associated with the fast dynamics of water molecules in aluminium-rich zeolitic cavities. However, xonotlite does not have this kind of cavity, and therefore, such interpretation is not consistent with the results obtained in our work. Moreover, in this time and temperature range, a broad and weak contribution was found even in silica nanoparticles [194] and other cementitious materials, synthetic C-S-H [80] and a cement matrix [79]. In particular, in the latter systems, the origin of this contribution was associated with the rotational dynamics of hydroxyl groups. Considering that it is generally accepted that the C-S-H phase has a tobermorite-like structure, we suggest that process 1 is related to the dynamics of hydroxyl groups. The well-defined shape of this component can be attributed to the ordered distribution of OH groups on tobermorite layers, while the disordered environment in C-S-H gel is reflected in the broadening of process P1.

To understand the differences observed in tobermorite and xonotlite, we must recall the ^{1}H SSNMR results. In the xonotlite spectrum, we observed a double peak related to two different populations of hydroxyl groups, Ca–OH and Si–OH, while in the tobermorite spectrum, a single peak was observed at a lower chemical shift associated with isolated silanol groups. Hence, the presence of two P1 processes in xonotlite can be related to the presence of two hydroxyl group populations with different chemical environments.

Regarding process 2, the Arrhenius fitting procedure results suggest a different nature and origin of this process in tobermorite and xonotlite (Table 3.4). In fact, in tobermorite, these dynamics show energy activation and characteristic times similar to those of strongly bound water, as already observed in several dried or low-relative-humidity systems, such as titanate nanowires [195], zeolites [196, 197, 198], and silica nanoparticles (SNPs) [194]. According to the ^{1}H SSNMR results, only tobermorite exhibits the characteristic peak related to hydrated hydroxyl groups. Therefore, we might expect a scenario similar to that studied by Cerveny *et al.* in SNPs dried at 373 K, and P2 can be associated with the dynamics of water molecules hydrating the silanol groups [194]. On the other hand, in the xonotlite process, P2 has a lower activation energy and $\tau_0 \sim 10^{-9.3}$ s, suggesting the diffusional nature of this process. This different behaviour can be related to a distinct interaction between water molecules and the surface of the layer, as already observed by ^{1}H SSNMR. Sulpizi *et al.* have shown that the orientation and distribution of hydroxyl groups on the surface of SiO_2 affect the arrangement of water molecules on the surface [199]. In particular, according to those authors, it is possible to have a "liquid-like" distribution of water molecules instead of the more ordered "ice-like" distribution. Since process 2 is normally associated with the presence of a tetrahedrally coordinated distribution of water molecules, the diffusive behaviour dynamics in xonotlite indicate the absence of such water coordination. We suggest that the presence of Ca–OH affects the distribution of hydroxyl groups on the surface of xonotlite, giving rise to a more disordered arrangement of water molecules, that is "liquid-like", where a diffusive dynamic appears to be more favourable than the typical vibration behaviour observed in tobermorite.

Finally, process P3 has similar activation energy and pre-exponential factors, suggesting that it originates from the same dynamic in both tobermorite and xonotlite. However, in xonotlite, the relaxation is faster than those in tobermorite. A process with values of τ_0 and relaxation times similar to those found in this work has been observed even in zeolites [196, 197]. In these studies, such dynamics were related to the migration of cations in supercages. Furthermore, contributions from charge migration in the same frequency and temperature range have been observed in titanate nanowires [195] and CaFe-layered double hydroxide [200]. In this scenario, the faster dynamics observed in xonotlite could be explained by taking into account the higher amount of nonevaporable water detected through TGA measurements in the two specimens (Figure 3.28). The presence of higher nonevaporable water content enhances the cation mobility, resulting in a shift towards shorter relaxation times in xonotlite [201].

A schematic representation of the funding of this study is presented in Figure 3.31:

the ordered "ice-like" solvation water found in the Si–OH-rich environments (tobermorite structure) is converted to a disordered "liquid-like" distribution in the Ca–OH-rich environment (xonotlite structure).

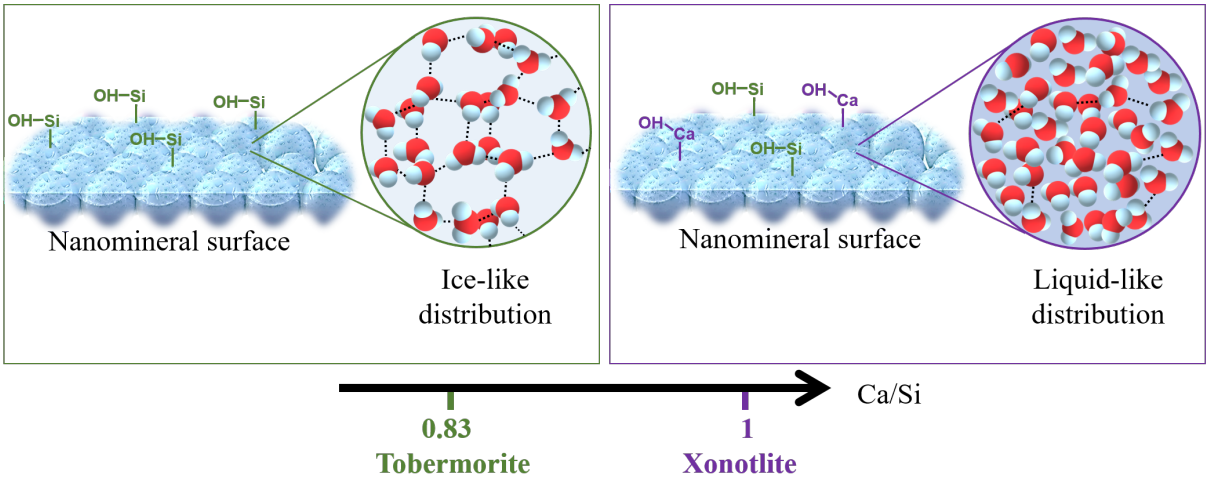

Figure 3.31: Schematic representation of the correlation between the chemical structure of xonotlite and tobermorite and its effect on nanoconfined water dynamics based on the results of this work [188].

In this work, the hydrogen bond network and the dynamics of nanoconfined water in xonotlite and tobermorite have been thoroughly studied. We have shown that they are highly dependent on the interactions and confinement geometry, and are modified by different chemical environments. These findings allow us refining the picture of the dynamics of confined water and hydroxyl groups in calcium silicate hydrate systems, which can also be applied to other water-containing materials, with a significant impact in many fields of materials science.

3.7 Conclusions and perspectives

In this chapter, the hydrothermal flow synthesis of xonotlite and tobermorite were investigated, highlighting the effect of several experimental parameters.

The first technical challenge of this work was focused on the design and development of a suited, innovative, home-made user-customised set-up which allows the production of significant quantities of CSH particles, $\sim 2.9\,g/h$ of xonotlite (at $M = 0.1\,mol/L$ and $7\,s$) and $\sim 1.4\,g/h$ (at $M = 0.05\,mol/L$ and $8\,s$) of tobermorite. In this reactor, the synthesis of xonotlite and tobermorite occurred in only a few seconds, as a promising alternative to the very long conventional hydrothermal route which requires several hours, or even days. The reactor prototype and the protocol developed in this work represent the first proof of the scale-up of a supercritical water-based methodology for synthesising CSH minerals. In this context, the new and fast synthesis route could be further implemented for a more effective production at the industrial scale.

For the synthesis of xonotlite, we have investigated the effect of temperature, pressure, and residence time. We have shown that, at high temperature (from $350\,°C$) to avoid forming a second phase (a calcium silicate, namely wollastonite) it is crucial to reduce the residence time down to $7\,s$ and to increase the pressure up to $25\,MPa$. As we will show in chapter 4, the value of pressure (i.e. the value of water density) has an important impact on the dehydration process from xonotlite to wollastonite.

Regarding the synthesis of Al-tobermorite under supercritical conditions, we deeply studied the material's structure thanks to a combination of SSNMR, Raman and FTIR spectroscopies. In this work, the intrinsic mechanical properties of Al-tobermorite synthesised in supercritical water were investigated for the first time by HP-XRD. We have found that our material is characterised by a high polymerisation degree and shows a less defective structure and higher bulk modulus K_0 than what is commonly observed for other synthetic tobermorite. The study of the mechanical properties provides information for predicting the mineral's long-term behaviour, relevant in applications concerning the design of cement-based materials with Al-tobermorite.

Following this line, future work could be focused on the synthesis of other calcium silicate hydrate minerals with different Ca/Si ratios. It would be advisable to test different residence time and temperature values to determine the optimal synthesis conditions. Furthermore, it could be interesting to try various water density values, as that parameter could play an essential role in stabilising and forming the mineral phases.

One of the most critical objectives achieved from this work relies on the in-depth char-

acterisation of hydrogen bond networks and nanoconfined water in these minerals. Despite the similarities in their stoichiometric layered structures, the chemical environments of xonotlite and tobermorite minerals are dominated by Ca–OH and Si–OH groups, respectively. Based on a combination of spectroscopic techniques such as Raman, FTIR, SSNMR and BDS, a refined picture of the dynamics of water in these materials was possible, allowing univocal assignments of each dielectric relaxation process to a specific structural origin. The fastest relaxation dynamic (P1) found in the calcium silicate hydrate phases was previously hypothesised to arise from the hanging hydroxyl ions. Still, this work confirms this assignment by distinguishing the Ca–OH and Si–OH environments. Our results also reveal that the second fastest processes (P2) are intimately related to hydration/solvation water dynamics and that these processes are susceptible to local chemical environment. In that respect, the ordered "ice-like" solvation water found in the Si–OH-rich environments of tobermorite transforms into a disordered "liquid-like" solvation water found in the Ca–OH-enriched environment of xonotlite. Finally, our experiments suggest that the slowest process (P3) is related to bulky nonevaporable water and coupled to ion mobilities. Overall, this work might serve as a starting point for understanding the water dynamics in more complex calcium silicate hydrates, such as cementitious C-S-H gel, and provides a solid fundamental knowledge body for other water-containing materials.

CAPITULO 4 SUJETO A CONFIDENCIALIDAD POR LA AUTORA

Chapter 5

Life cycle assessment of xonotlite and tobermorite production via supercritical hydrothermal flow synthesis

In the previous chapters, we have highlighted the advantages of using supercritical water-based technology to produce high crystalline minerals. As already discussed, performing the synthesis under high temperature and pressure conditions boosts the nucleation, accelerates the reaction kinetics and reduces the synthesis time down to a few seconds. Furthermore, we have shown that our xonotlite and tobermorite result more similar, in morphologies, crystallinity and structures, to the natural phases than the other synthetic minerals reported so far in the literature.

Beyond these attractive aspects of SCF technology, it became of high relevance to evaluate the chemical synthesis process in terms of sustainability and environmental impacts. With this in mind, during this work, a question arose firstly: what is the method to estimate how green a process is? The optimal tool for a comprehensive evaluation of the pros and cons of a manufacturing route is provided by the life cycle assessment analysis (LCA). LCA offers the opportunity to estimate the impacts across precursors, solvent, and energy associated with materials processing, highlighting which contribution could be adjusted to improve the environmental profile.

In the frame of this work, an anticipatory life cycle assessment has been used to estimate the potential environmental impacts leading from the supercritical hydrothermal synthesis of 1 kg of xonotlite or tobermorite at the lab-scale as well as extrapolated at the industrial scale. This analysis was carried out in collaboration with the Ph.D. student Alexandre Charpentier Poncelet and the Assistant Professor Philippe Loubet of the research group *Life cycle Assessment and Sustainable Chemistry* (CyVi) at Institute of Molecular Sciences (ISM) led by Prof. Guido Sonnemann.

This chapter is divided into two parts. The first one is devoted to the presentation of the life cycle assessment, in terms of definition and methodologies; afterwards, a brief review of the LCA studies on the SCF synthesis, reported in the literature, will be presented.

The second part will discuss the goal and scope of this study, the inventory realised for the acquisition of the data, and lastly, the interpretation of the analysis. The LCA results are useful for highlighting the attractiveness of the supercritical fluid technology and identifying where improvements could be realised to further enhance its perspectives as an environmentally sustainable synthesis methodology.

5.1 Life cycle assessment

5.1.1 Definition

LCA is the most appropriate tool for assessing the overall environmental impact of products, services, or processes [272]. The LCA methodology was developed in the early 1960s in response to a growing concern about the limitations of energy sources and raw materials. Later, this methodology was standardised in the guidelines ISO 14040-14044 which define the life cycle assessment as "the compilation and evaluation of the inputs and outputs and the potential impacts of a product system through its life cycle" [273]. This analysis considers the entire life cycle of a product, from the extraction of raw materials to the end-of-life and waste disposal/recycling, through the manufacturing process and the use-phase (Figure 5.1). For each phase of the product life cycle, the content of inputs (materials, energy, *etc.*) and the relative outputs (emissions, by-products, water, *etc.*) are estimated.

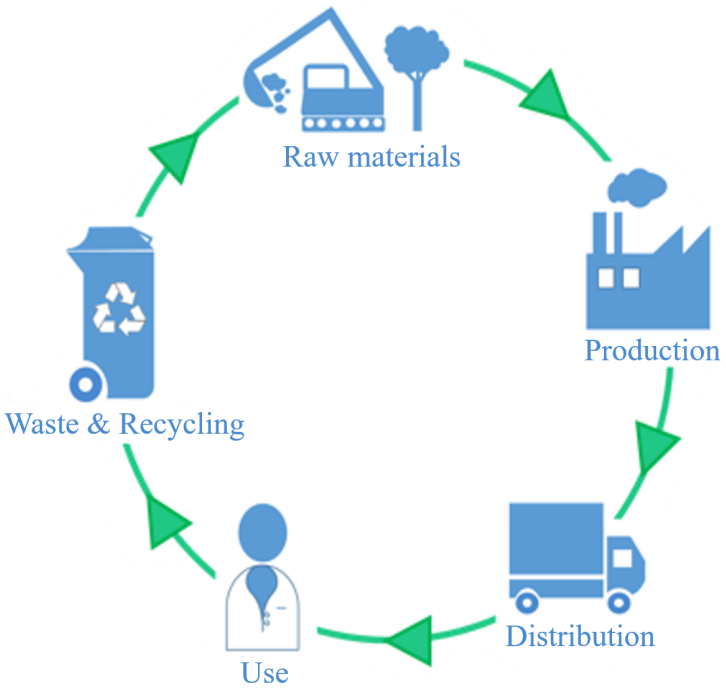

Figure 5.1: Scheme of the life cycle assessment of a product.

A life cycle assessment study involves the iteration of the following four steps (Figure 5.2):

1. **Goal and scope definition** identifies the purpose of the LCA analysis, determining the key LCA elements, such as the functional unit, the system boundaries, and which environmental concerns will be included in the study.

2. **Life cycle inventory (LCI)** quantifies the life cycle for all the inputs and outputs, in terms of mass and energy flows, involved in the system boundaries.

3. **Life cycle impact assessment (LCIA)** converts the mass and energy flows from the inventory to indicators for a given category, evaluating the magnitude and significance of the potential environmental impacts of the system under study.

4. **Interpretation of the results** analyses the data, estimating the opportunities to reduce environmental impact at each step of the product life cycle.

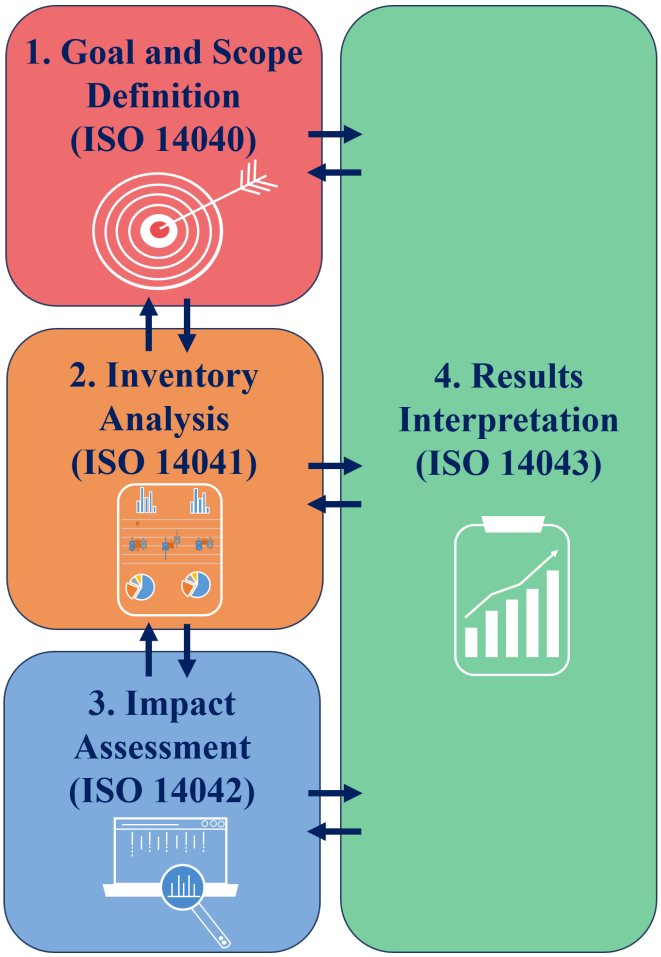

Figure 5.2: Schematic representation of the life cycle assessment methodology and its 4 phases, as reported in ISO 14040 [273].

In the next section, a brief summary of the studies reported so far on the evaluation of the environmental profile of the SCF synthesis will be reported. Afterwards, the LCA analysis conducted in this work will be presented following the four steps included in its methodology.

5.1.2 Life cycle assessment of supercritical fluid-based synthesis

In the last years, the relevance in using the supercritical fluids technology has been recognised by the United States Environmental Protection Agency (US EPA), which promotes projects to develop environmentally sustainable chemical processes [274]. The wide range of applications covers different fields, from materials, semiconductors, energy, synthetic chemistry science to waste treatment, pharmaceuticals and medical science.

Regarding material synthesis, only three contributions to understanding the environmental profile of the SHFS of nanoparticles have been discussed in the literature. Among them, two are the results of the collaboration between the *Supercritical Fluids Group* at ICMCB and *CyVi Group* at ISM. Tsang *et al.* reported the first known attempt to assess the environmental impact of the SCF synthesis through the LCA study. In that work, the analysis was performed on the production of $Ba_{0.6}Sr_{0.4}TiO_3$ nanoparticles in a continuous reactor kept at 400 °C and 23 MPa [275]. The LCA was used to investigate the environmental impacts of solvent (ethanol-water mixture) and precursors (barium isopropoxide, strontium isopropoxide, and titanium isopropoxide) to figure out the one resulting in the lowest effect. They have shown that at the lab-scale (precursors molar concentration: 0.017 mol/L) the use of precursors was negligible, around 3% of the total impacts. At the same time, the average contribution from manufacturing, processing and disposing of the ethanol was about 90% of the total life cycle impacts. Consequently, their work investigated how further improvement could be achieved at the industrial scale. They concluded that by increasing the precursor concentrations up to 0.1 and 1.0 mol/L, the average life-cycle impacts decreases by nearly 81% and 95%, respectively. Furthermore, the additional recovery and reuse of solvents, with an efficiency of 90%, could further reduce the average life-cycle impacts by 56%. They also investigated the environmental impact of three different solvents: ethanol-water mixture, methanol-water mixture and isopropanol-water mixture. Such analysis has shown that the replacing of ethanol with methanol, in the alcohol-water mixture, allows to reduce the total impact categories. Contrarily, the use of isopropanol turns out greater life cycle impacts.

In a later work, life cycle assessment was employed to analyse the environmental profile of TiO_2 nanoparticles production via supercritical solvothermal flow synthesis using water-ethanol solution as solvent [276]. The analysis was particularly focused on comparing two production processes of TiO_2 nanoparticles: the supercritical fluid synthesis and the conventional precipitation method. The results have shown that the climate change potential and cumulative energy demand for the SHFS were reduced of 55% and 30%,

respectively, compared with that evaluated for the precipitation method. Furthermore, these values were also significantly lower than those determined by Caramazana and coworkers for the continuous solvothermal production of TiO_2 [277]. Considering that similar synthesis conditions were used, these discrepancies could be explained as follows. First, Caramazana *et al.* employed isopropanol, which leads to higher environmental impact, if compared with ethanol used by Tsang *et al.* Second, the precursor molar concentration employed by Caramazana *et al.* was lower, 0.5 mol/L, than in the first study, 1.0 mol/L. Operating at lower concentrations requires higher energy and solvent amounts for the same quantity of product, resulting in an adverse effect on the environmental profile.

To conclude, these previous studies have highlighted that the most critical parameters in evaluating the environmental impact of the SCF synthesis at the lab-scale are: the type of solvent, the energy consumption, the type of chemical precursors, and the precursor concentration. At the industrial-scale, the precursor concentration, the amount of water and energy can be optimised; in this case, the precursors play the most crucial role. With this in mind, these parameters have been considered in our study, as will be exposed in the next sections.

5.2 Goal and scope definition

In this work, the goal and scope were to evaluate the cradle-to-gate environmental impact related to the production under supercritical hydrothermal conditions of xonotlite and tobermorite nanominerals. In the analysis, we considered the lab-scale production, and we further took into account some prospective synthesis alternatives that could be used at the industrial scale. A preliminary LCA study allowed to identify potential environmental impact hotspots, which were found to be dominated by the heat generation, and precursors required for the reaction. Therefore, several parameters were considered in the LCA study: nature and concentration of precursors, and operating temperature.

5.2.1 System boundaries for the supercritical hydrothermal production of xonotlite and tobermorite

Once identified the goal and scope of the work, the system boundaries were determined. In this step, it is crucial to define the functional unit as the reference basis to which the LCA results are related. The function of a manufacturing chemical process is to provide a product, and thus commonly the functional unit is defined as 1 kg of the chemical product. In this study, the functional unit is 1 kg of dry calcium silicate hydrate nanoparticles (xonotlite or tobermorite).

The analysis conducted in this work covers the manufacturing and transport of precursors, heat and water consumption related to the functional unit, as well as wastewater treatment. The capital equipment (i.e. equipment and building infrastructure) was not encompassed in the study as this has been shown to have a negligible contribution to life cycle impacts, in general, over the long-term [274, 275]. Furthermore, considerations on use-phase and end-of-life of xonotlite and tobermorite particles were not considered as they will not influence the production route, and thus they fall outside of the scope of evaluating the environmental profile of SHFS. The energy required to run the pumps, filtrate and dry the materials at the lab-scale level was not considered, as the main aim of this anticipatory LCA was to identify where improvements in the manufacturing methodology can be realised.

The system boundaries of this LCA analysis is shown in Figure 5.3. The processes included in the study can be summarised as follows:

1. Production and transport of precursors,

2. Supercritical hydrothermal flow synthesis,

3. Wastewater treatment.

The elementary flows represent the interactions between the technosphere and the environment: they are related to all the extracted resources and all the environmental emissions, as shown in Figure 5.3. As it will be discussed in the next section, background and foreground data required to build the life cycle inventories were collected by lab-scale experiments and/or modelled through the use of wastewater LCI (WW LCI) tool [278] and the ecoinvent database. The detailed LCI are provided in section 5.3.

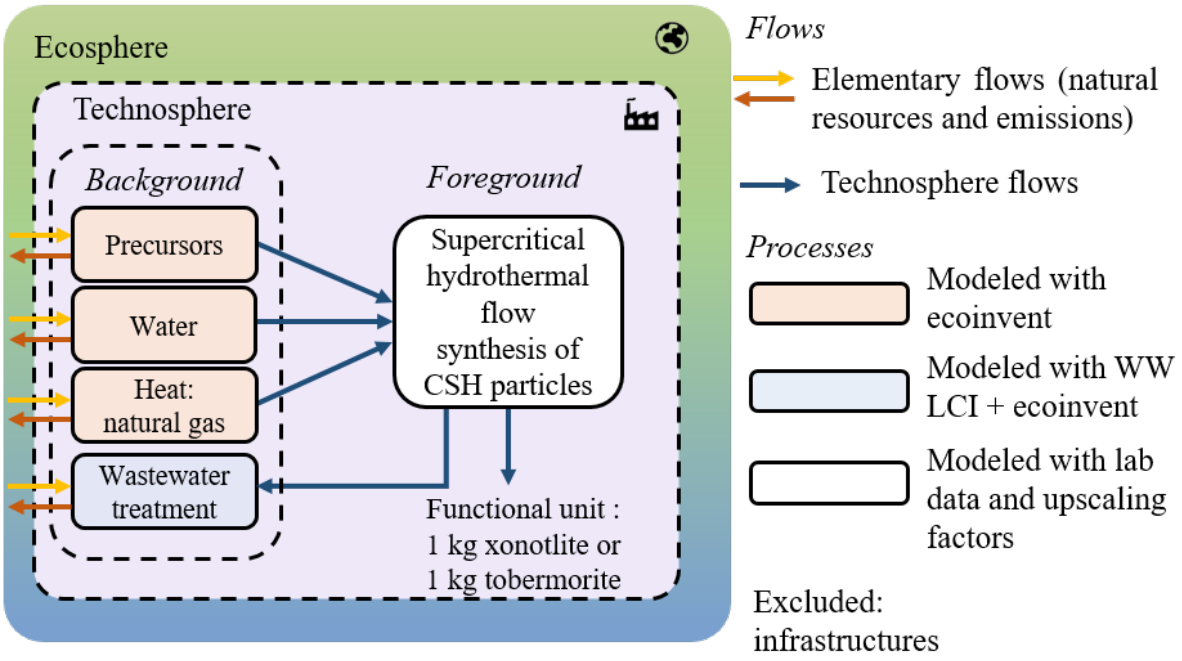

Figure 5.3: System boundaries for the SHFS production of xonotlite and tobermorite minerals. The system analysed in this work encompassed raw materials and energy used during the entire process, and the emissions up to the point of the material production, while excluding both the use and end-of-life phases.

5.3 Life cycle inventory analysis

The life cycle inventory allows to determine the totality of the elementary flows linked to a product system under study. For the production of xonotlite and tobermorite, foreground data (weight of precursors, water consumption, process efficiency) were collected during lab-scale experiments. Background data regarding the impacts of both production and transport of precursors, and the SHFS synthesis, were collected from the ecoinvent database and the WW LCI tool by considering lab experiments and upscaling factors.

For xonotlite, to identify a scenario with the lowest environmental impact, the influence of different parameters was investigated, namely the synthesis temperature, the concentration of precursors and their nature. The parameters for the production of xonotlite were compiled in five different scenarios in order to capture the evolution of the results over different options. Instead, for the production of tobermorite, a lab-scale and an industrial scale scenario were modelled. The parameters for the lab-scale experiments and scenarios 1 to 6 for xonotlite and tobermorite productions are identified in Tables 5.1 and 5.2, respectively.

Table 5.1: Parameters considered in this analysis for the production of 1 kg of xonotlite according to 5 production scenarios (Sc).

Scenario (Sc)	**Lab-scale**	**Sc1**	**Sc2**	**Sc3**	**Sc4**
Functional unit	1 kg of xonotlite				
Parameters					
Material concentration (g/L)	5.2	5.2	69.3	66.1	69.3
Temperature (°C)	400	400	400	325	400
Use of heat exchanger	NO	YES	YES	YES	YES
Yield (%)	87	87	87	83	87
Ca-source	$Ca(NO_3)_2$	$Ca(NO_3)_2$	$Ca(NO_3)_2$	$Ca(NO_3)_2$	$CaCl_2$

Table 5.2: Parameters considered in this analysis for the production of 1 kg of tobermorite according to 3 production scenarios (Sc).

Scenario (Sc)	**Lab-scale**	**Sc5**	**Sc6**
Functional unit	1 kg of tobermorite		
Parameters			
Material concentration (g/L)	2.9	2.9	76.8
Temperature (°C)	400	400	400
Use of heat exchanger	NO	YES	YES
Yield (%)	82	82	82

For the synthesis of xonotlite, calcium nitrate and sodium metasilicate were used as Ca- and Si-source for all scenarios, exception being sc4 in which calcium chloride was employed for replacing calcium nitrate. Instead, for tobermorite the same precursors were employed in all scenarios: calcium nitrate as Ca-source, sodium metasilicate as Si-source, and aluminium nitrate as Al-source.

In the following, the impact of the experimental parameters that are predominant in each scenario will be investigated.

5.3.1 Heat recovery

In the life cycle inventory, we investigated through scenario Sc1 and sc5 the use, in the lab-scale experiments, of a heat exchanger with a recovery efficiency of 90% as reasonable value for a well-designed and insulated heat exchanger according to the literature [279]. Considering that, the 90% of the energy coming from the outlet flow can be used to further heat up the input water flow. At the industrial scale (Sc2, Sc3, Sc4, and Sc6), the use of a heat exchanger with a heat loss of only 10% was always included.

5.3.2 Concentration of precursors

In the case of xonotlite, the lab-scale scenario considered the synthesis of the mineral using calcium nitrate and sodium metasilicate with a $Ca/Si = 1$. The molar concentration of each precursor was 0.1 mol/L, which results in approximately 5.2 g of xonotlite per litre of injected solution, taking into account a reaction rate of 87%. The temperature and the pressure during the reaction were 400 °C and 25 MPa. The most significant parameter to be optimised is the precursor concentration, as it drastically lowers the volume of water that would need to be heated. Therefore, it was assumed that the industrial production process would aim to run at the maximal possible concentration. Hence, the upper limit for the precursors concentration was determined by considering the solubility of the precursors employed for the synthesis of xonotlite, i.e. sodium metasilicate nonahydrate and calcium nitrate tetrahydrate. The precursor with the lower solubility is $Na_2SiO_3 \cdot 9H_2O$ (380 g/L), which limits at the industrial scale the maximal molar concentration at 1.3 mol/L. The LCA analysis was thus performed for two different concentrations of xonotlite production to investigate the effect of the precursor concentrations. The lab-scale default scenario involves the production of 5.2 g/L of xonotlite, whereas the industrial scale scenario allows to produce 69.3 g/L (Sc2).

In the case of tobermorite synthesis, the lab-scale scenario considers the use of calcium

nitrate, sodium metasilicate and aluminium nitrate with Ca/Al+Si and Al/Al+Si molar ratios equal to 0.83 and 0.15, respectively. The molar concentration of Si-precursor was 0.05 mol/L, which results in the production of approximately 2.9 g of tobermorite per litre of injected solution, by considering a reaction rate of 82%. The temperature and the pressure during the reaction were 400 °C and 25 MPa. Among the three employed precursors, the one with lower solubility is, also in this case, the $Na_2SiO_3 \cdot 9H_2O$. Consequently, 2.9 g/L is the concentration of produced tobermorite in the lab-scale scenario, to use as reference for the industrial scale scenario (Sc6) which involves the production of 76.8 g/L.

5.3.3 Reaction temperature

The energy consumption in the flow synthesis is mostly entirely related to water heating. This term is related to the heat energy used to bring the reaction to the desired temperature in the near- or supercritical domain. Therefore, it was calculated directly as the energy, E, needed to heat the water content, m, at the desired synthesis temperature, T, in agreement with:

$$E = m \int_{20}^{T} C_p \, dT \tag{5.1}$$

where C_p is the heat capacity of water (J/kg °C) at a fixed pressure. The evolution of heat capacity is not linear within the range of temperature 20 - 400 °C, as shown in Figure 5.4.

The environmental profile of xonotlite synthesis was further investigated by taking into account the impact of reaction temperatures, namely 400 and 325 °C, to compare at the industrial scale the two respective scenarios, Sc2 and Sc3. In this case, an important parameter to consider is the effect of the reaction temperature on the production yield. In fact, the energy demand is definitively higher when the temperature increases, but that value should be determined by kilogram of xonotlite nanoparticles, as an increase of temperature could also give rise to higher conversion rate of precursors, as previously observed [277, 280]. In the literature, this phenomenon is related to greater nucleation of the nanoparticles due to the increase of the reaction energy at higher temperatures. The yield of the xonotlite nanoparticles after drying was determined in agreement with the following equation:

$$Y = \frac{m_p}{m_t} \cdot 100 \tag{5.2}$$

where m_p and m_t are the practical and theoretical quantities, in grams, of the produced xonotlite particles, respectively. The yields were calculated based on the average of three experimental runs. The observed yields were of 83% and 87% at 325 and 400 °C, respec-

tively. Furthermore, the yield value for each temperature was confirmed by ICP-OES analysis on the outlet water containing the reaction by-products. Powder X-ray diffraction patterns of xonotlite synthesised at these two temperature values are reported in Figures 5.5(a) and (b) to confirm the good crystallinity of the material phase.

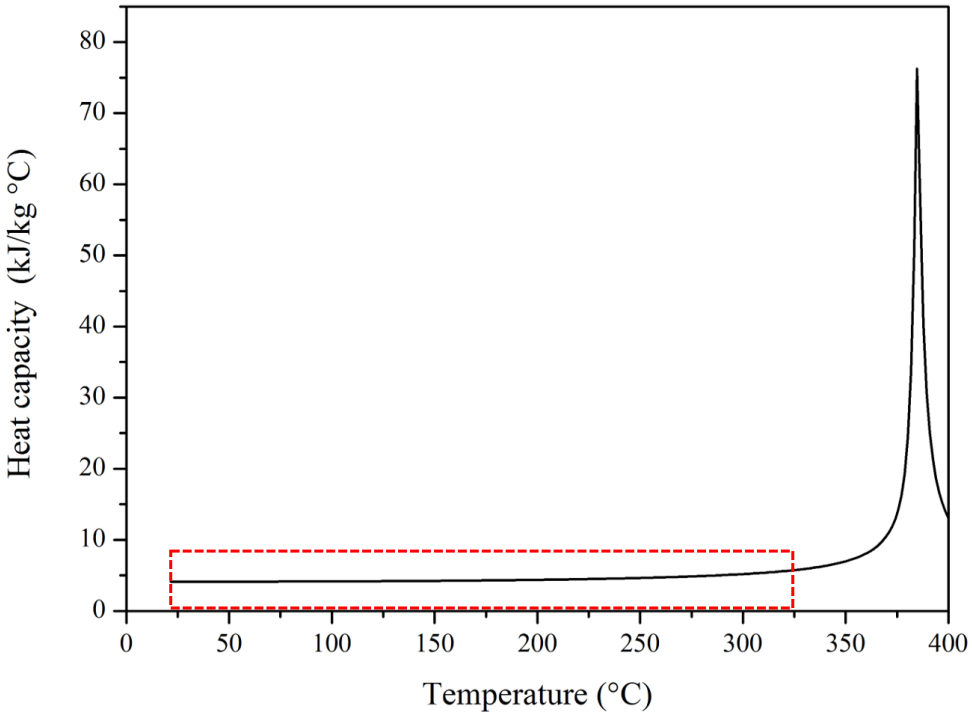

Figure 5.4: Evolution of the heat capacity from 20 to 400 °C at P = 25 MPa. The red line defines the limited temperature region, 20 - 325 °C, used to calculate the evolution of C_p for the synthesis at 325 °C (Sc3). The data were collected from the NIST database [126].

Instead for tobermorite, due to the challenge in synthesising an unstable phase, the temperature reaction was kept equal to 400 °C for all scenarios. Through lab-scale experiments the yield for the synthesis of tobermorite was calculated to be of 82% at 400 °C.

5.3.4 Type of precursors

Finally, while the initial reaction considered calcium nitrate as Ca-source, it was observed from preliminary results that this precursor contributed significantly to the overall impacts of the process. Consequently, another potential compound that could be used for the production of xonotlite was identified, namely calcium chloride. The use of $CaCl_2$ as promising alternative to $Ca(NO_3)_2$ was experimentally tested for xonotlite production, and considered in scenario Sc4. The PXRD pattern of the as-synthesised sample is shown in Figure 5.5(c).

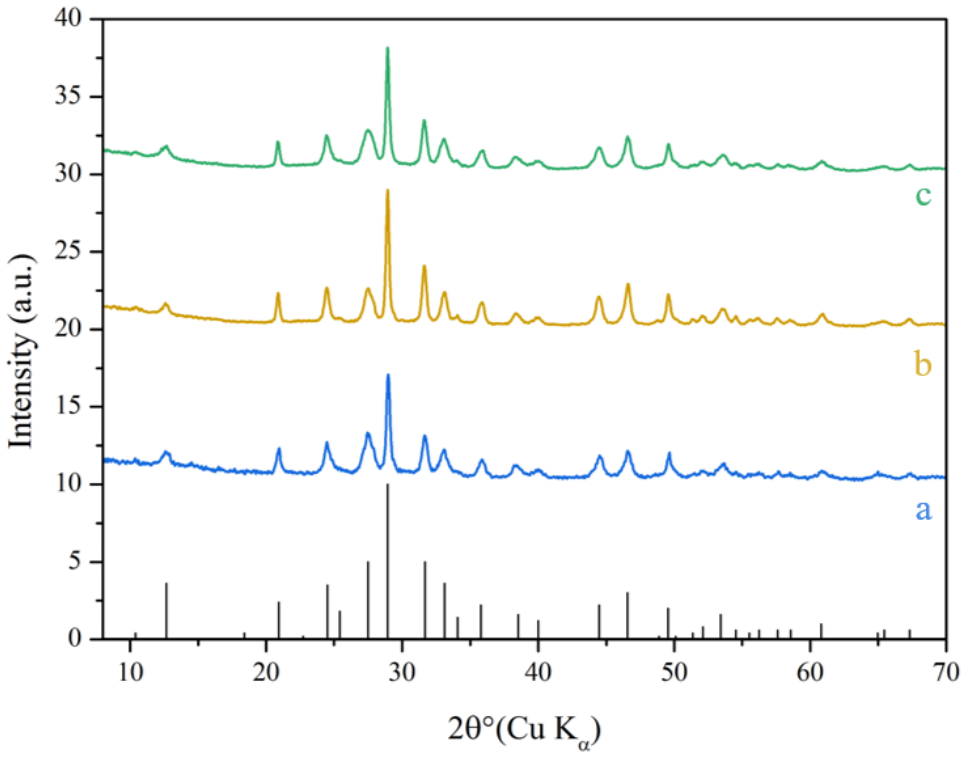

Figure 5.5: Powder X-ray diffraction patterns of xonotlite synthesised at (a) 325 and (b) 400 °C by using calcium nitrate tetrahydrate, and (c) 400 °C employing calcium chloride dihydrate, respectively. In black, the positions and intensities of the diffraction peaks as reported in PDF file no. 00-023-0125 of monoclinic xonotlite (space group P2/a) are shown.

5.3.5 Research of data not available in the ecoinvent database

In the lab-scale experiments $Ca(NO_3)_2 \cdot 4\,H_2O$, $CaCl_2 \cdot 2\,H_2O$, and $Na_2SiO_3 \cdot 9\,H_2O$ were used as Ca- and Si-precursors. However, in the ecoinvent database only calcium nitrate, sodium metasilicate pentahydrate and calcium chloride were present. Here, these compounds were used for the inventory by simply adjusting the input quantities from stoichiometric calculations.

Furthermore, aluminium nitrate (used as Al-source in the tobermorite synthesis) was not available in the ecoinvent database. Consequently, the inventory data were estimated based on a potential synthesis process for the production of $Al(NO_3)_3$ as reported in the literature. It was found that aluminium nitrate is obtained from the reaction of aluminium oxide with nitric acid, in agreement with the following equation:

$$1\,Al_2O_3 + 6\,HNO_3 \longrightarrow 2\,Al(NO_3)_3 + 3\,H_2O \tag{5.3}$$

To approximate the inputs required for this reaction at the industrial scale, we considered the same yield (95%), water, energy and other inputs required for the synthesis of alu-

minium chloride from the reaction of the aluminium compound with hydrochloric acid, already present in the ecoinvent database.

5.3.6 Wastewater treatment

Up to now, we explained how the inputs for each category (precursors, water and energy) were estimated in the life cycle inventory. As previously mentioned, in the global LCA study, the outputs must also be considered in terms of water plus by-products.

In our model, it was assumed that the output process water containing unreacted chemicals is sent to a wastewater treatment facility. The simulation to consider the wastewater treatment was modelled with the WW LCI v2 tool [278]. WW LCI is an excel-based model for calculating life cycle inventories of wastewater discharges by inserting the concentrations and the characteristics of the chemical presents in the water. The model predicts how wastewater will be treated in the plant, and also, determines to what level wastewater is treated and considers the local sludge disposal practices, whether wastewater is discharged to groundwater, rivers, or sea. The model takes also into account methane emissions and the energy demand of the wastewater treatment plant.

In our study, the concentration of chemical waste (unreacted precursors) contained in the output water was determined theoretically from stoichiometric calculations (considering the reaction yield for each scenario) and also confirmed by ICP-OES analysis for the lab-scale scenario. However, this technique does not allow to measure the content of nitrogen in the solution. In this work, during the deep characterisation of the samples (through TGA-MS and PXRD), any traces in NO_x were observed in the xonotlite and tobermorite powders. For that reason, we have considered that 100% of NO_x content in the precursor is injected in the outlet solution.

5.3.7 Life cycle inventory data

The LCA study was performed with the SimaPro 9 software. Foreground inventory data for the supercritical hydrothermal synthesis of CSH particles were collected in-house from lab-scale experiments and stoichiometric calculations. Background data were gathered from the ecoinvent v3.5 database [281, 282].

The inventories for the industrial scale production were extrapolated from the lab-scale inventories based on various prospective parameters that could be employed at that scale, as heat recovery and high precursor concentration. The mass balance as well as the selection of LCI data were realised accordingly.

Detailed life cycle inventories, according to 8 production scenarios, are reported in Tables 5.3 and 5.4 for the production of 1 kg of xonotlite or tobermorite, respectively.

Table 5.3: Parameters and life cycle inventories for the production of 1 kg of xonotlite according to 5 production scenarios (Sc).

Scenario (Sc)	**Lab-scale**	**Sc1**	**Sc2**	**Sc3**	**Sc4**
Functional unit	1 kg of xonotlite				
Inputs					
Deioniside water (L)	192.96	192.96	14.43	15.13	14.43
Energy (MJ)	477.13	47.71	3.57	2.06	3.57
Sodium metasilicate pentahydrate (kg)	2.04	2.04	2.04	2.14	2.04
Calcium nitrate (kg)	1.58	1.58	1.58	1.65	-
Calcium chloride (kg)	-	-	-	-	1.07
Outputs (water and by-products)					
Water (L)	192.96	192.96	14.43	15.13	14.43
Sodium metasilicate pentahydrate (kg)	0.24	0.24	0.24	0.33	0.24
Calcium nitrate (kg)	0.21	0.21	0.21	0.28	-
Calcium chloride (kg)	-	-	-	-	0.14

Table 5.4: Parameters and life cycle inventories for the production of 1 kg of tobermorite according to 3 production scenarios (Sc).

Scenario (Sc)	**Lab-scale**	**Sc5**	**Sc6**
Functional unit	1 kg of tobermorite		
Inputs			
Deioniside water (L)	348.06	348.06	13.02
Energy (MJ)	860.63	86.06	3.22
Sodium metasilicate pentahydrate (kg)	2.16	2.16	2.16
Calcium nitrate (kg)	1.67	1.67	1.67
Aluminium nitrate (kg)	0.39	0.39	0.39
Outputs (water and by-products)			
Water (L)	348.06	348.06	13.02
Sodium metasilicate pentahydrate (kg)	0.36	0.36	0.36
Calcium nitrate (kg)	0.30	0.30	0.30
Aluminium nitrate (kg)	0.07	0.07	0.07

5.4 Life cycle impact assessment: evaluation of impact categories

In the first part of this chapter, the life cycle assessment analysis was defined as a tool to quantify the environmental impacts of the complete life cycle of a product. The life cycle of a synthetic mineral is related to many resources and emissions, which can considerably vary in their potential environmental impacts. To interpret the LCA study, the raw materials, energy, and emissions flows identified in the LCI must be converted into potential consequences for human health and the environment. The tool used to perform this third phase of the LCA analysis is the so-called life cycle impact assessment (LCIA) [283]. LCIA consists of three mandatory steps, as reported in ISO 14042, ISO 14040, and ISO 14044 [273, 284, 285]:

1. Selection of: impact categories of interest, indicators for each category and characterisation models;
2. Classification: assignment of LCI data to the selected impact categories;
3. Characterisation: calculation of impact category indicators results through characterisation factors.

These three steps will be explained in details in the following part.

The impact categories and category indicators are selected to properly reflect the LCI results on the category endpoints. According to ISO 14042, there are three broad groups of category endpoints which define the main areas of protection as: damage to human health, damage to ecosystems and damage to resource availability [285]. Multiple impact categories may lead to damage on these areas of protection, such as global warming, stratospheric ozone depletion, human toxicity, water consumption, *etc.* The impact categories can be classified as shown in Figure 5.6.

Once the environmental impact categories are defined, the classification step assigns each elementary flows of the inventory (extraction flows and emission flows) to a corresponding impact category. As an example, the impacts related to NO_x emissions can be classified to contribute to both ozone formation and acidification categories. Finally, the third step converts the elementary flows of LCI into a limited number of environmental impact scores and aggregates the converted results within the same impact category. This conversion is done by multiplying the inventory results by the respective characterisation factors, which specify the environmental impact per unit of resource extracted or emission

released. As a results, different emissions and resources consumption can be expressed in terms of a mass released, as 1 kg, per functional unit into the environment, and can thus be aggregated, compared and evaluated. For example, the relative contributions of several gases to climate change are usually grouped and compared in terms of CO_2-equivalent using global warming potentials [286].

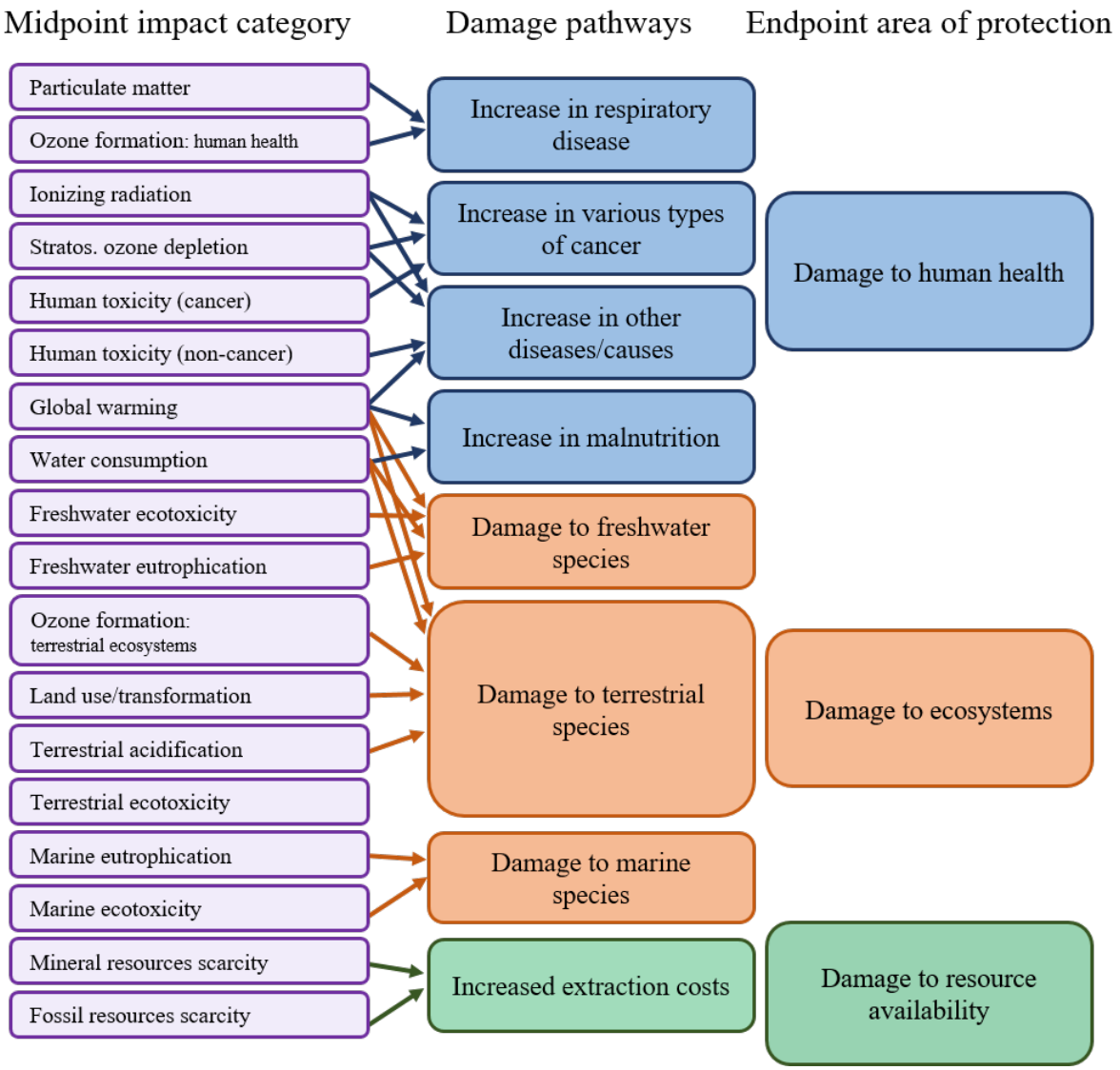

Figure 5.6: Overview of the impact categories considered in the ReCiPe2016 method (on the left) and their related areas of protection (on the right).

LCIA methods generally allow to measure midpoint impacts or endpoint damage [287]. The midpoint impacts represent an intermediary step between the LCI and the endpoint damage, and it is calculated based on a cause-effect impact pathway. An example of midpoint impact is the global warming. The endpoint methods allow to measure the damage of such midpoint impacts on the three areas of protection previously defined: human

health, ecosystems and natural resources. For example, global warming can be linked to two endpoint damages, human health and ecosystems, as shown in Figure 5.6. In this work, we have employed the midpoint approach to perform the impact assessment related to the production via a supercritical water-based synthesis of xonotlite and tobermorite. The impact assessment were conducted using the ReCiPe2016 midpoint which involves 18 midpoint impact categories, as shown in Figure 5.6 and in Table 5.5 [283].

Table 5.5: List of impact categories as included in ReCiPe 2016 midpoint (H) considered in the LCA. CFC-11: chlorofluorocarbon, Co-60: Cobalt-60, PM2.5: particulate matter $< 2.5\,\mu$m, N: nitrogen, S: sulfur, P: phosphorus, 1,4-DCB: dichlorobenzene, Cu: copper.

Recipe impact category	Unit
Global warming	kg (CO_2-eq to air)
Ozone depletion	kg (CFC-11-eq to air)
ionizing radiation	kBq (Co-60-eq to air
Fine particulate matter formation	kg (PM2.5-eq to air)
Ozone formation: terrestrial ecosystems	kg (NOx-eq to air)
Ozone formation: human health	kg (NOx-eq to air)
Terrestrial acidification	kg (SO_2-eq to air)
Freshwater eutrophication	kg (P-eq to freshwater)
Human toxicity: cancer	kg (1,4-DCB-eq to urban air)
Human toxicity: non-cancer	kg (1,4-DCB-eq to urban air)
Terrestrial ecotoxicity	kg (1,4-DCB-eq to industrial soil)
Freshwater ecotoxicity	kg (1,4-DCB-eq to freshwater)
Marine ecotoxicity	kg (N-eq to marine water)
Marine eutrophication	kg (1,4-DCB-eq to marine water)
Land use	m^2 year
Water use	m^3 water-eq consumed
Mineral resource scarcity	kg (Cu-eq)
Fossil resource scarcity	kg (oil-eq)

Furthermore, three different cultural perspectives can be applied in the analysis, namely individualist (I), egalitarian (E), and hierarchist (H) [283]. The individualist is based on the short-term interest, neglecting the hazard of a near fossil fuels depletion, takes into account only a short time frame (i.e. 20 years) for global warming. The hierachist perspective involves the most common policy principles regarding time frame and other issues, using the medium time frame (i.e. 100 years) for global warming. Lastly, the egalitarian is the most precautionary perspective considering the most prolonged time frame for global warming (i.e. 1000 years) and giving more importance to the ecosystem quality. In this work we employed the hierarchist assessment to perform the analysis. The

potential environmental impacts for the production of 1 kg of xonotlite and tobermorite are shown in Appendix B, Tables B.1 and B.2, respectively.

In this section, the most important concepts related to the life cycle assessment analysis were introduced. We have discussed the goal and scope of this study, and the inventory realised for the acquisition of the data for each considered scenario. In the next part, the results related to the production on 1 kg of xonotlite and tobermorite via SHFS will be discussed, highlighting the impact of several experimental parameters.

5.5 Interpretation of results

5.5.1 Life cycle assessment for production of 1 kg of xonotlite

In this section, the contributions of precursors, heat generation, as well as water consumption and wastewater treatment will be analysed for each scenario.

a) Lab-scale scenario

The results for the lab-scale inventory, shown in Figure 5.7, reveal that precursors and heat generation contribute significantly to the impacts of the manufacturing route of xonotlite synthesis. In particular, production and transport of precursors and heat generation have a cumulative contribution of over 90% of the total impacts for 12 of the 18 impact categories. Considering the great amounts of energy (477.13 MJ) required to heat the water for producing 1 kg of xonotlite at the lab-scale, energy strongly contributes to most impact categories with notably 74.8% of global warming and 87.8% of the fossil resource scarcity, due to the combustion of natural gas. Finally, the marine eutrophication impacts are dominated by the wastewater treatment, with 99.7% of the impacts. This is due to the presence in the wastewater of NO_3^- as a by-product of the calcium nitrate precursor.

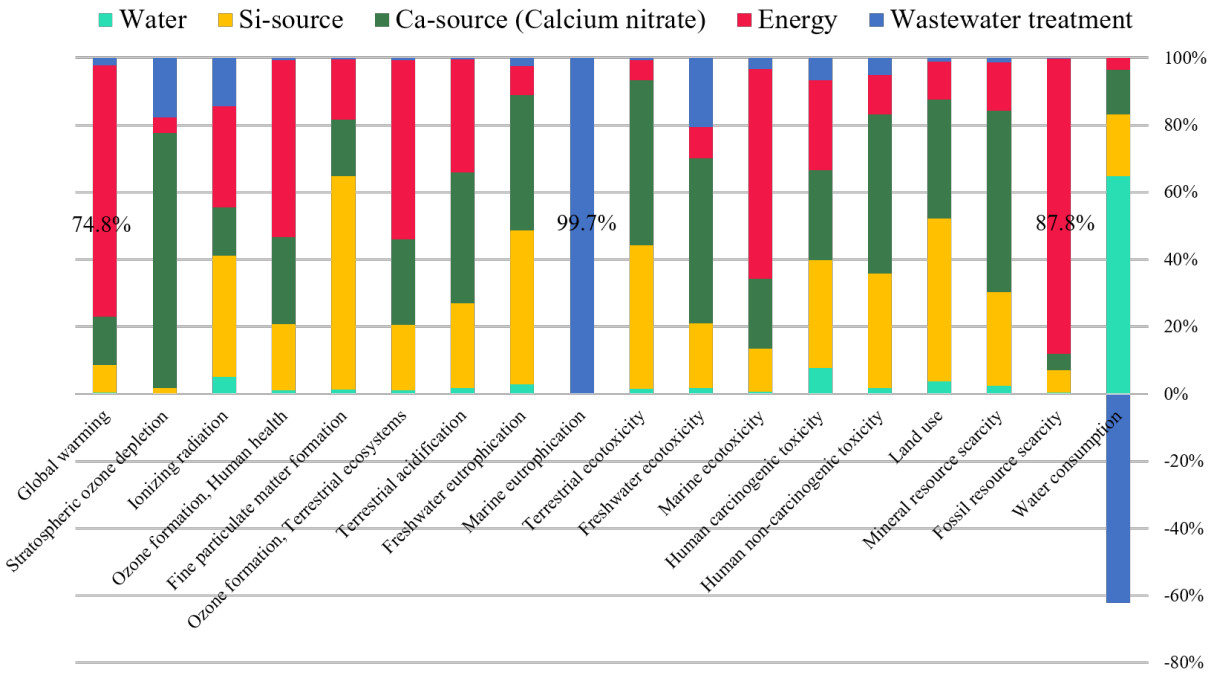

Figure 5.7: Relative contributions from critical life cycle stages to the default lab-scale scenario (no heat recovery) for the production of 1 kg of xonotlite via the supercritical hydrothermal flow pathway (400 °C, 25 MPa) using calcium nitrate as Ca-source.

b) Scenario 1: minimising the heat consumption

The main objective of this LCA study was to identify the categories which more impact the environmental profile of the manufacturing route, and thus, determine where further improvements can be made. Consequently, the analysis was conducted on a scenario 1, considering the same parameters as the lab-scale experiment but with an additional heat exchanger (heat recovery efficiency of 90%). The results for scenario 1, in Figure 5.8, show that considering a potential heat recovery of 90%, the heat generation for the supercritical process can be reduced below 10% for 13 out of 18 categories, exceptions being global warming (22.9%), ozone formation (10% for human health and 10.2% for terrestrial ecosystems, respectively), marine ecotoxicity (14.2%) and fossil resource scarcity (41.8%). The impact contributions arising from the precursors became the most dominant for most of the impact categories, with an average contribution of 34.9% and 41.5% for sodium metasilicate and calcium nitrate, respectively (Figure 5.8).

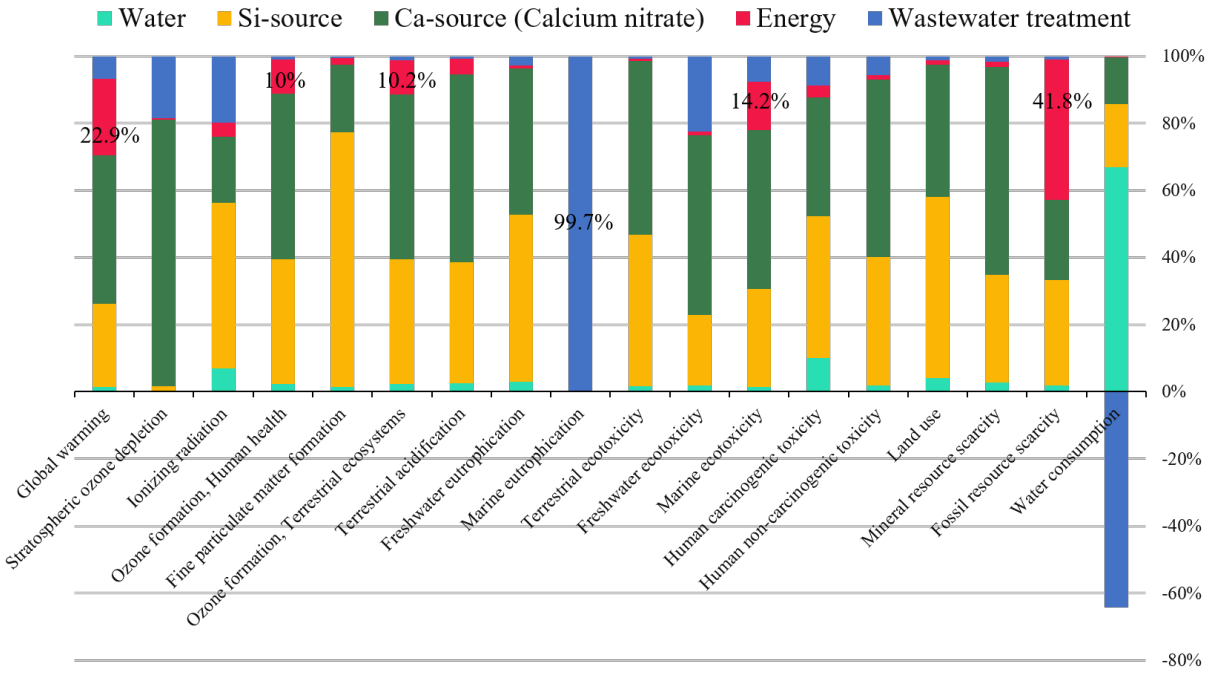

Figure 5.8: Relative contributions from critical life cycle stages to scenario 1: lab-scale production of 1 kg of xonotlite via the supercritical hydrothermal flow pathway (400 °C, 25 MPa) using calcium nitrate as Ca-source and including a heat exchanger (90% efficiency).

To anticipate the impacts of the supercritical hydrothermal synthesis of calcium silicate hydrate nanoparticles at the industrial scale, we always considered the use of heat exchanger in all scenarios at the industrial scale, which reduced the impacts of heat generation by 90%.

c) Scenario 2: optimising the precursors concentration

At the industrial scale, a change that is expected to be feasible is the use of the optimal amount of reactants to reduce as much as possible the volume of water to be heated. As discussed previously, the maximal theoretical concentration of reactants and/or products was calculated according to precursors solubility limit. As a consequence of this consideration, the industrial scale scenario included the use of a much lower water volume, 14.43 L, compared to the lab-scale synthesis, 192.96 L, to produce 1 kg of xonotlite. The impact results for scenario 2, covering the maximal concentration of precursors to generate an output of 69.3 g/L of xonotlite, are shown in Figure 5.9. As the required volume of water is reduced by 92.5% in comparison to scenario 1, the relative contributions of heat generation to the total impacts, and those of water treatment, are further reduced for most categories. Consequently, precursors have the most crucial contribution to life cycle impacts in this scenario.

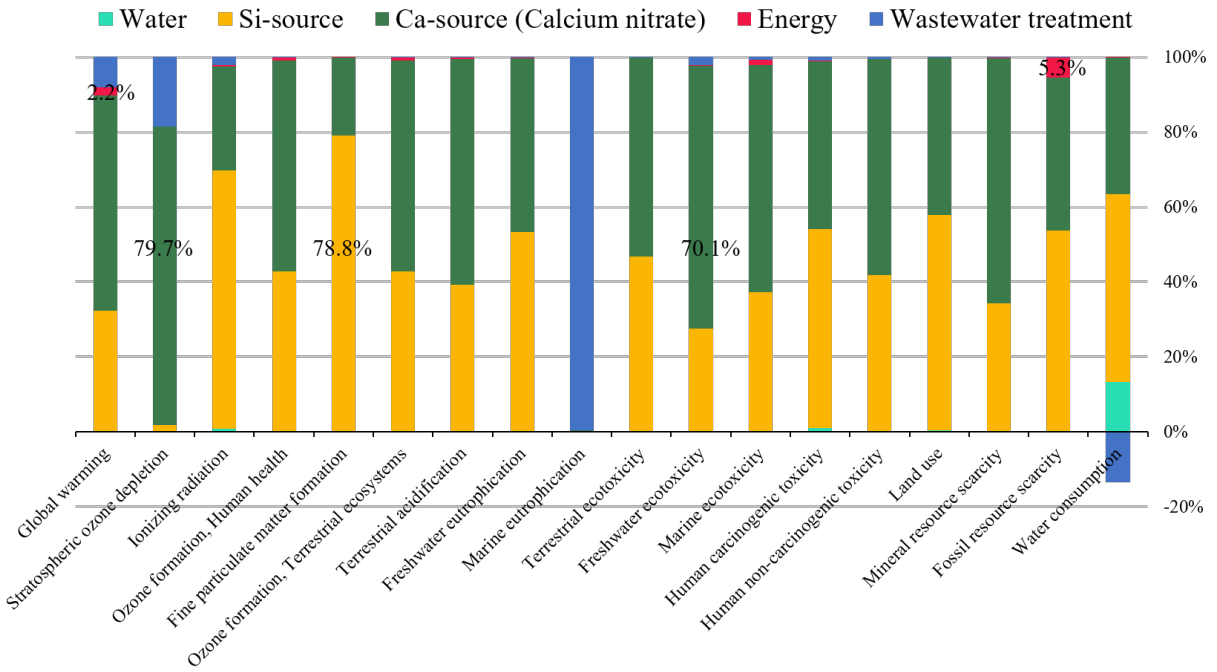

Figure 5.9: Relative contributions from critical life cycle stages to scenario 2: industrial scale synthesis for the production of 1 kg of xonotlite via the supercritical hydrothermal flow pathway (400 °C, 25 MPa) using calcium nitrate as Ca-source and including a heat exchanger (90% efficiency).

The cumulated impacts of precursors are now found to be over 90% for 15 out of 18 categories, exceptions being stratospheric ozone depletion, marine eutrophication and water consumption. In particular, the average total impacts across all categories were 42.2% and 48.7% for sodium metasilicate and calcium nitrate, respectively. The lowest

and the highest relative contributions of Si-source were 0.2% and 78.8% to marine eutrophication and fine particulate matter formation, respectively. On the other hand, the use of Ca nitrate impacts 0.1% and 79.7% to marine eutrophication and stratospheric ozone depletion, respectively.

d) Scenario 3: optimising the operating temperature value

In scenario 3, we further investigated whether or not reducing the operating temperature of the process could be a viable option (Figure 5.10). The results have shown that by decreasing the temperature of 75 °C the average impact of energy across the 18 categories is reduced from 0.7% for Sc2 to 0.4% for Sc3, giving rise to energy savings of 42.9% due to heat reduction. More in details, lower temperature impacts the relative contribution of energy, with a relative decrease of ∼1% and ∼2% for global warming and fossil resource scarcity categories, respectively.

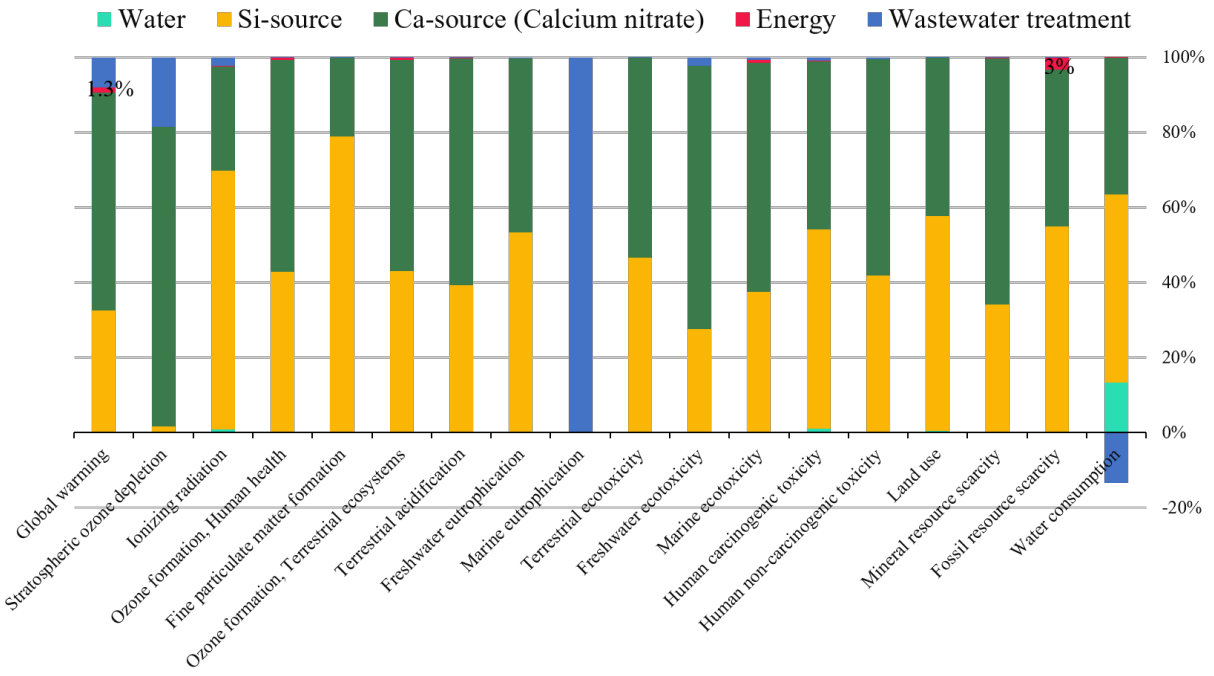

Figure 5.10: Relative contributions from critical life cycle stages to scenario 3: industrial scale synthesis for the production of 1 kg of xonotlite via the nearcritical flow synthesis pathway (325 °C, 25 MPa) using calcium nitrate as Ca-source and including a heat exchanger (90% efficiency).

However, from the experimental results, the reaction yield was determined to be 83% when operating at 325 °C, compared to 87% at 400 °C. This parameter has to be taken into account to establish which scenario between Sc2 and Sc3 has a better environmental profile. The comparison shows that the potential gains from reducing the temperature

are offset by the lower reaction yield, leading to an increase of approximately 5% for all categories. This result implies that the higher volumes of process water and precursors required for producing 1 kg of xonotlite at a lower yield, as well for the associated amounts of wastewater and unreacted precursors, counterbalance the energy savings of heat reduction.

e) Scenario 4: replacing the Ca-precursor source

Overall, it can be stated from the results of previous scenarios, that precursors are the most important contributors to the potential environmental impacts of SHFS at the industrial scale. On the other hand, energy, water consumption and wastewater treatment have relatively low contributions to the total impacts. Specifically, the results suggest that nitrates are particularly harmful for the marine eutrophication (due to nitrates in the wastewater treatment) and the stratospheric ozone depletion (due to nitrates in producing the calcium nitrate precursor) categories.

Hence, it was attempted to find suitable alternatives to calcium nitrate, which was initially used for the reactions, namely calcium chloride. A preliminary comparative LCA analysis has shown that the production of 1 kg of calcium chloride has an advantageous impact profile compared to the production of the same quantity of calcium nitrate. The potential environmental impacts for the synthesis of 1 kg of precursors are reported in Appendix B, Table B.3. As shown in Figure 5.11, calcium chloride exhibits the lowest environmental impact per kilogram for all the considered impact categories, except for land use category. Notably, calcium nitrate contributes about 6 and 327 times more to global warming (62.7% against 10.1%) and stratospheric ozone depletion (98.1% against 0.3%) impacts categories, respectively. The average total impacts across all categories was decreased from 47.5% for calcium nitrate to 18.49% for calcium chloride. Contrarily, no alternative to sodium metasilicate was investigated, as it was considered less problematic than calcium nitrate, with an average total impacts across all categories of 34.1%. This result has suggested that the production of 1 kg of $Ca(NO_3)_2$ is approximately 40% more environmentally harmful than that of 1 kg of $Na_2SiO_3 \cdot 5\,H_2O$. Furthermore, the sodium content is non-toxic and has shown to contribute negligibly to the wastewater treatment impacts compared to nitrates. However, sodium metasilicate pentahydrate has a greater environmental impact than calcium nitrate for 5 out of 18 categories, namely ionizing radiation, fine particulate matter formation, marine eutrophication, fossil resource scarcity and water consumption, Figure 5.11. Consequently, in future studies will be interesting to search for more sustainable chemical precursor as Si-source to replace sodium metasilicate.

After the comparative LCA analysis of chemical precursors, experimental runs were performed to confirm that calcium chloride was a viable alternative for xonotlite synthesis (as shown by PXRD in Figure 5.5).

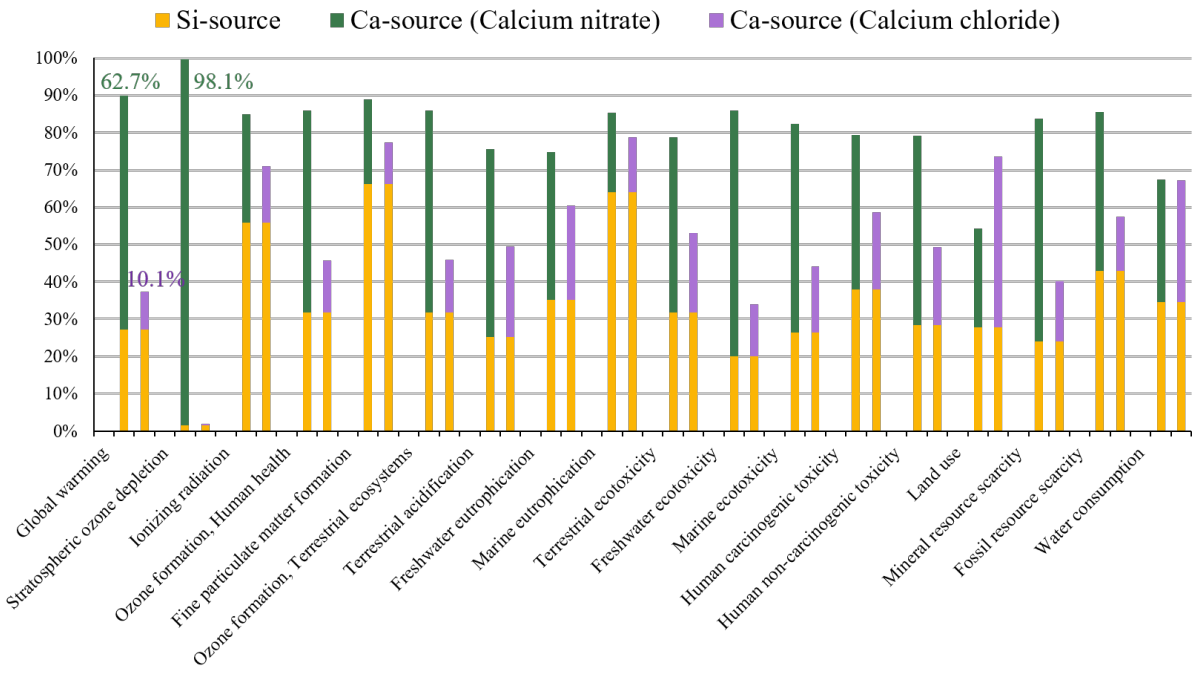

Figure 5.11: Environmental impacts related to the production of 1 kg of chemical precursors: sodium metasilicate pentahydrate, calcium nitrate and calcium chloride.

For scenario 4, the calcium chloride precursor was used to replace calcium nitrate. The impact profile for this scenario, Figure 5.12, shows that the contribution of the calcium precursor to the total impacts diminishes significantly in comparison to that of calcium nitrate in Figure 5.9. For example, the relative impacts of Ca precursor decreased from 79.7% to 9.1% for stratospheric ozone depletion and from 70.1% to 25.3% for freshwater ecotoxicity. In average, the use of calcium chloride has a total impact across all categories of 22%, representing a reduction of 55.1% compared to calcium nitrate (total impact across the 18 impact categories in sc2 equal to 49%). Additionally, the use of calcium chloride, instead of calcium nitrate, drastically reduces the potential impacts related to nitrates present in the wastewater treatment, with a decrease of over 99% for the impact of wastewater treatment on global warming, stratospheric ozone depletion, and marine eutrophication categories comparing to scenario 2. However, these observed improvements are partly counterbalanced by an average increase of 2.5% for other impact categories, such as freshwater ecotoxicity and marine ecotoxicity. To conclude the evaluation analysis of the environmental impacts related to precursors, in Figure 5.13 the relative impacts of sodium metasilicate, calcium nitrate and calcium chloride for the synthesis of 1 kg of

xonotlite are shown.

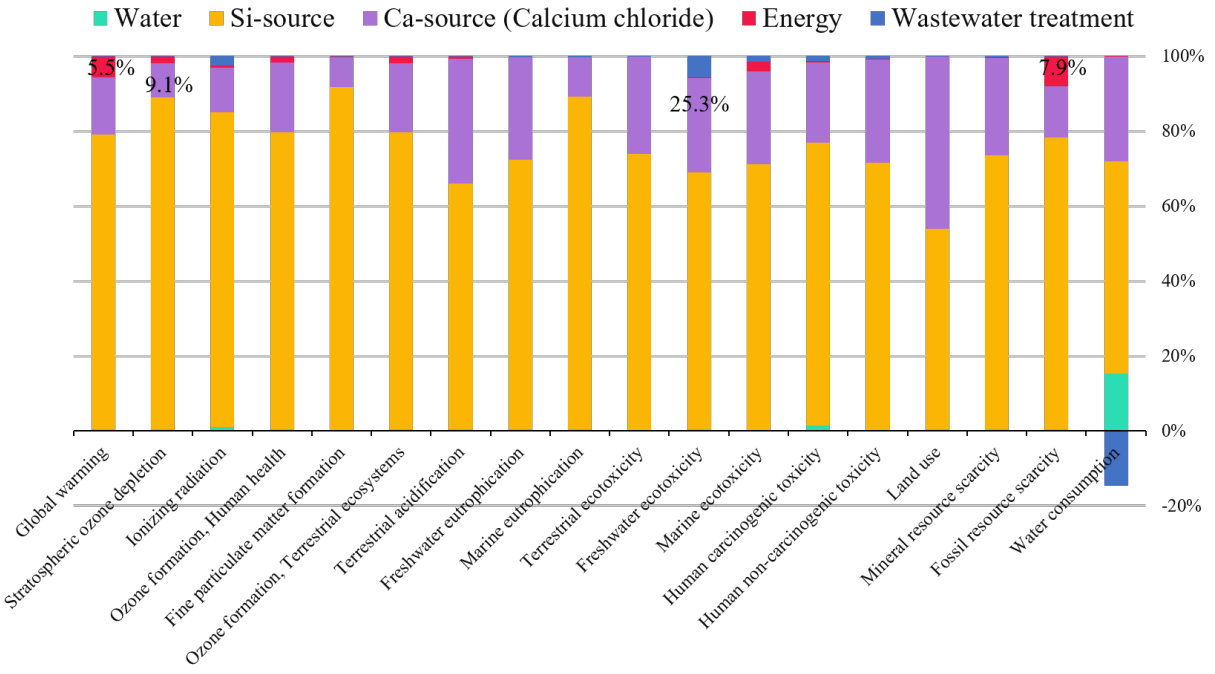

Figure 5.12: Relative contributions from critical life cycle stages to scenario 4: industrial scale synthesis for the production of 1 kg of xonotlite via the supercritical hydrothermal flow pathway (400 °C, 25 MPa) using calcium chloride as Ca-source and including a heat exchanger (90% efficiency).

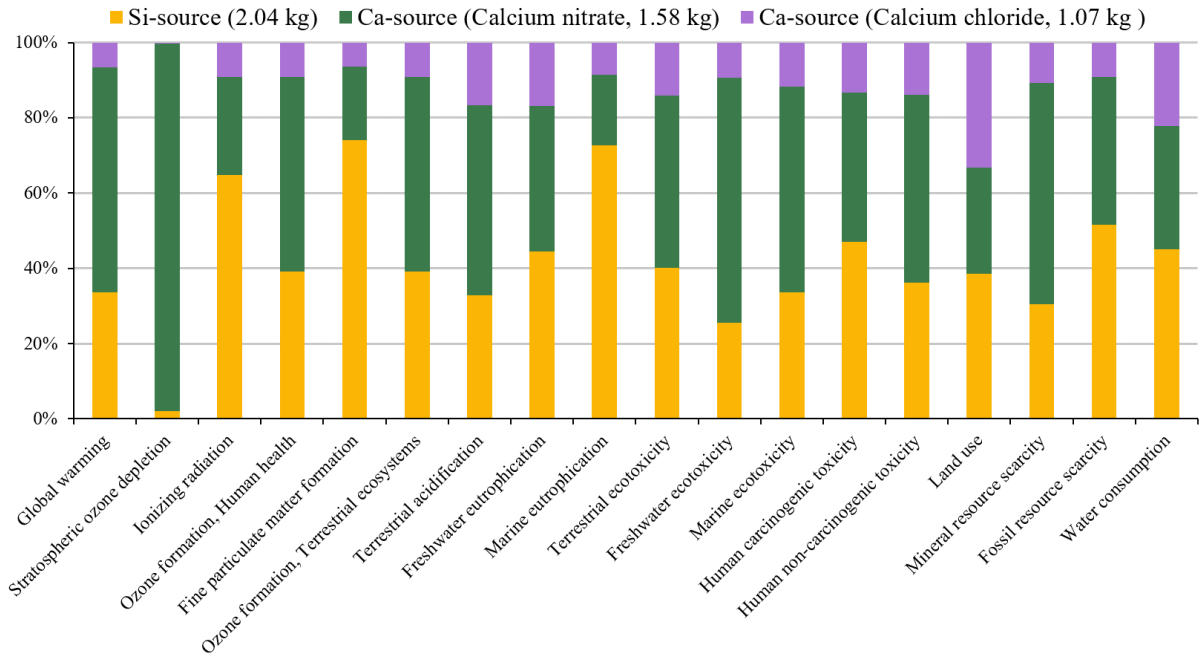

Figure 5.13: Comparison between the environmental impacts related to the three different precursors (sodium metasilicate pentahydrate, calcium nitrate and calcium chloride) for the production of 1 kg of xonotlite via the supercritical hydrothermal flow pathway.

The comparison shows that calcium chloride has the lower impacts, per kilogram of xonotlite, for all categories except land use category. Notably, 1.07 kg of calcium chloride compares favourably to the 1.58 kg calcium nitrate necessary to generate 1 kg of xonotlite (considering the yield efficiency of 87%). In particular, calcium nitrate contributes to about 9 and 466 times more to global warming and stratospheric ozone depletion impact categories, respectively, compared to calcium chloride.

The LCA results obtained in this work for the synthesis of 1 kg of xonotlite via SHFS have shown that a proper choice for chemical precursors is of fundamental importance to develop an environmentally sustainable synthesis methodology. In the next section, the analysis of the environmental profile related to the synthesis of 1 kg of tobermorite will be reported.

5.5.2 Life cycle assessment for the production of 1 kg of tobermorite

As described above, the complex synthesis of tobermorite does not allow to play with the experimental parameters in a wide range of values, as it was done for xonotlite. Consequently, for this mineral phase, the LCA analysis was performed for only three scenarios, in which the environmental benefits related to heat recovery and high precursors concentration were investigated. First, the comparison between the lab-scale scenario, with and without the use of a heat exchanger, will be presented.

a) Lab-scale scenario

Figure 5.14 shows the environmental impacts related to the synthesis of 1 kg of tobermorite at the lab scale scenario, which results in the production of 2.9 g of material particles per litre of water.

As already observed for xonotlite in Figure 5.7, the heat process is an important contributor to most impact categories, due to the high consumption of required energy (860.63 MJ) if no heat recovery is considered. In particular, the contribution of energy to the total impacts was found to be over 50% for 5 out of 18 categories. Notably, it is responsible for 81% of global warming impacts, 60.8% of the ozone formation, 69.9% of the marine ecotoxity, and 91.3% of the fossil resource scarcity. Furthermore, the employment of 0.39 kg of aluminium nitrate to synthesise tobermorite, rather than in the case of xonotlite, generates supplementary impacts. It contributes significantly, over 10%, for 4 out of 18 categories, specifically stratospheric ozone depletion, freshwater ecotoxicity,

human carcinogenic toxicity and mineral resource scarcity categories with relative impacts equal to 17.1%, 13.1%, 29.2% and 23.1%, respectively.

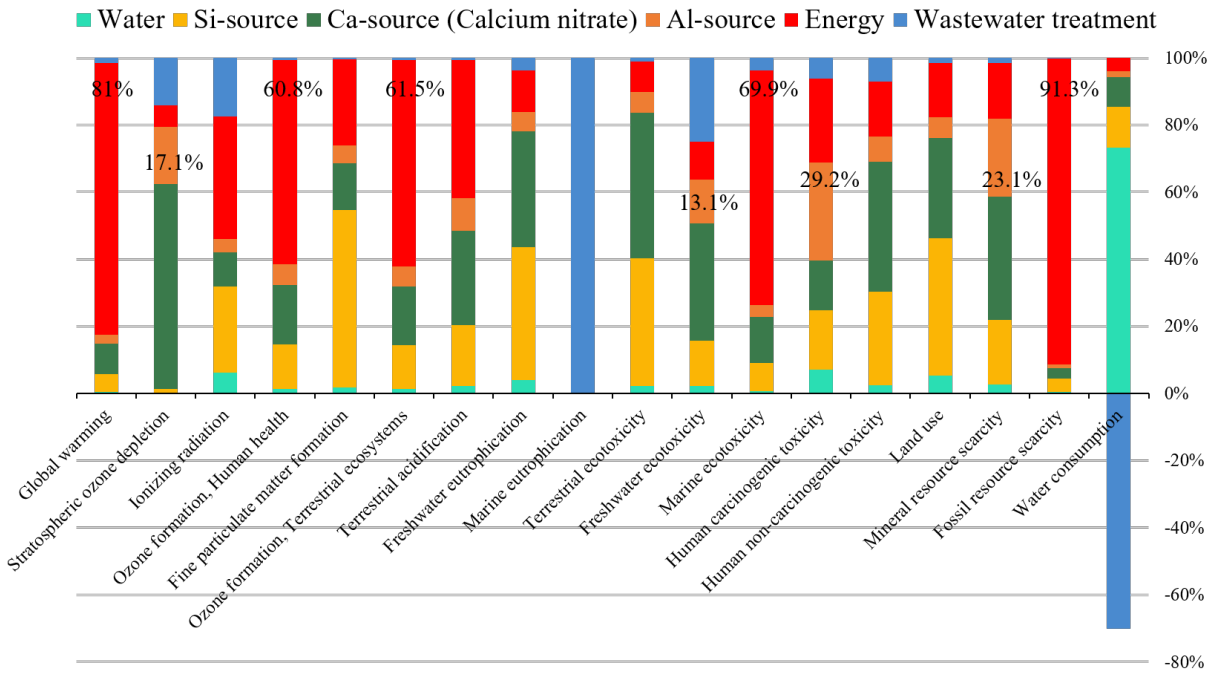

Figure 5.14: Relative contributions from critical life cycle stages to the default lab-scale scenario (no heat recovery) for the production of 1 kg of tobermorite via the supercritical hydrothermal flow pathway (400 °C, 25 MPa).

From these results, it appears clear that the first improvement to be realised to enhance the environmental perspectives of this process is related to the heat recovery. In the following, this consideration will be taken into account in scenario 5.

b) Scenario 5: minimising the heat consumption

After considering the use of a heat exchanger (90% efficiency), the impact of energy was reduced to less than 15% for 15 out of 18 categories, exceptions being global warming, marine ecotoxicity and fossil resources scarcity categories, as shown in Figure 5.15. On the contrary, sodium metasilicate and calcium nitrate became the greatest contributors for most impact categories, with an average contribution of 27.8% and 32.5% for Si-source and Ca-source, respectively. These results are in agreement with those previously discussed for the case of xonotlite (Figure 5.8). However, aluminium nitrate entails additional effects that influence the total potential impacts of the reaction. It contributes by an average of 12% to the different impact categories, principally to the stratospheric ozone depletion, terrestrial acidification, human carcinogenic toxicity, and mineral resource scarcity categories, with relative impacts of 18.1%, 15.4%, 37.7% and 27.2%, respectively.

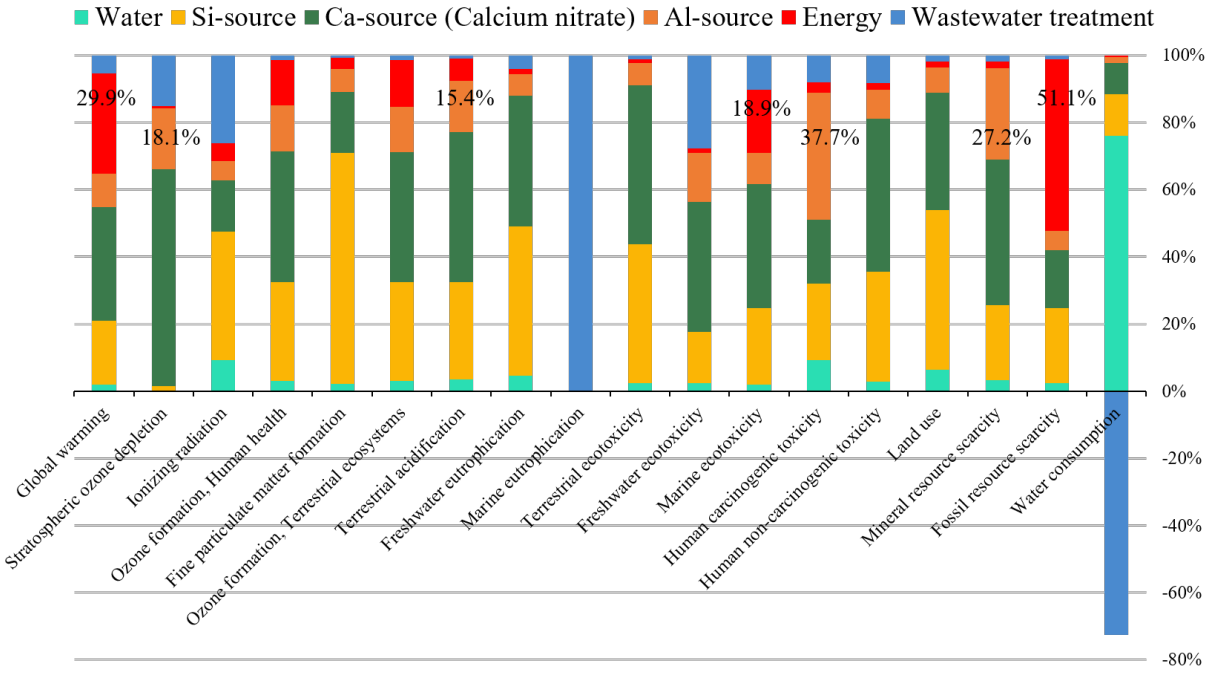

Figure 5.15: Relative contributions from critical life cycle stages to scenario 5: lab-scale production of 1 kg of tobermorite via the supercritical hydrothermal flow pathway (400 °C, 25 MPa) including a heat exchanger (90% efficiency).

Another strategy that can be considered to further improve the environmental profile of the tobermorite supercritical flow synthesis relies on the use of the maximal precursor concentration. This case was analysed in scenario 6, which corresponds to the industrial scale production of tobermorite at 76.8 g per litre of injected solution.

c) Scenario 6: optimising the precursors concentration

In Figure 5.16 the relative contributions from critical life cycle stages to the industrial scale production of 1 kg of tobermorite via SHFS pathway are shown.

As for scenario Sc2, the highest contribution to life cycle impacts comes from precursors. In particular, aluminium nitrate has the most important relative impact on human carcinogenic toxicity (46.9%) if compared to calcium nitrate (23.8%) and sodium metasilicate (28.3%). The cumulated impacts of precursors are found to be over 90% for 14 out of 18 categories, exceptions being global warming, stratospheric ozone depletion, marine eutrophication and water consumption.

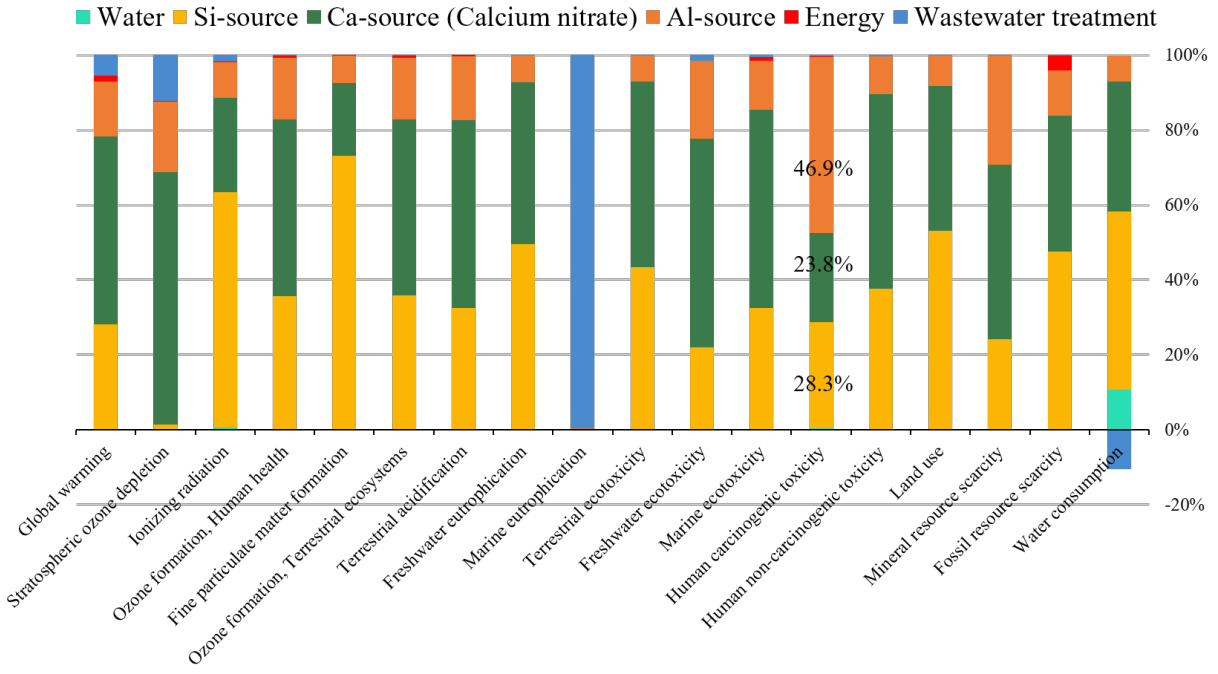

Figure 5.16: Relative contributions from critical life cycle stages to scenario 6: industrial scale synthesis for the production of 1 kg of tobermorite via the supercritical hydrothermal flow pathway (400 °C, 25 MPa) including a heat exchanger (90% efficiency).

5.5.3 Comparison between LCA analyses for producing 1 kg of xonotlite and 1 kg of tobermorite at the industrial scale

At this stage, the comparison between the impacts of the industrial scale scenarios for producing 1 kg of xonotlite and 1 kg of tobermorite, gives some interesting information. Figure 5.17 shows that the impacts difference increase from a minimum of 14.1% to a maximum value of 99.4% for the different impact categories. The largest differences are observed for the freshwater ecotoxicity (+ 33.6%), mineral resource scarcity (+ 49.7%) and human carcinogenic toxicity (+ 99.4%). This would imply that despite the synthesis of 1 kg of tobermorite results in a gain in terms of water and energy consumption of 1.41 L and 0.35 MJ, respectively, some parameters offset these benefits if compared to the production of 1 kg of xonotlite. These results are related to the addition of aluminium nitrate as a precursor for producing tobermorite, and the 5% decrease in the observed reaction efficiency. The later involves the additional injection of precursors to the wastewater, which in turn gives rise to other impacts associated with its treatment and additional release of nitrates and aluminium to the environment.

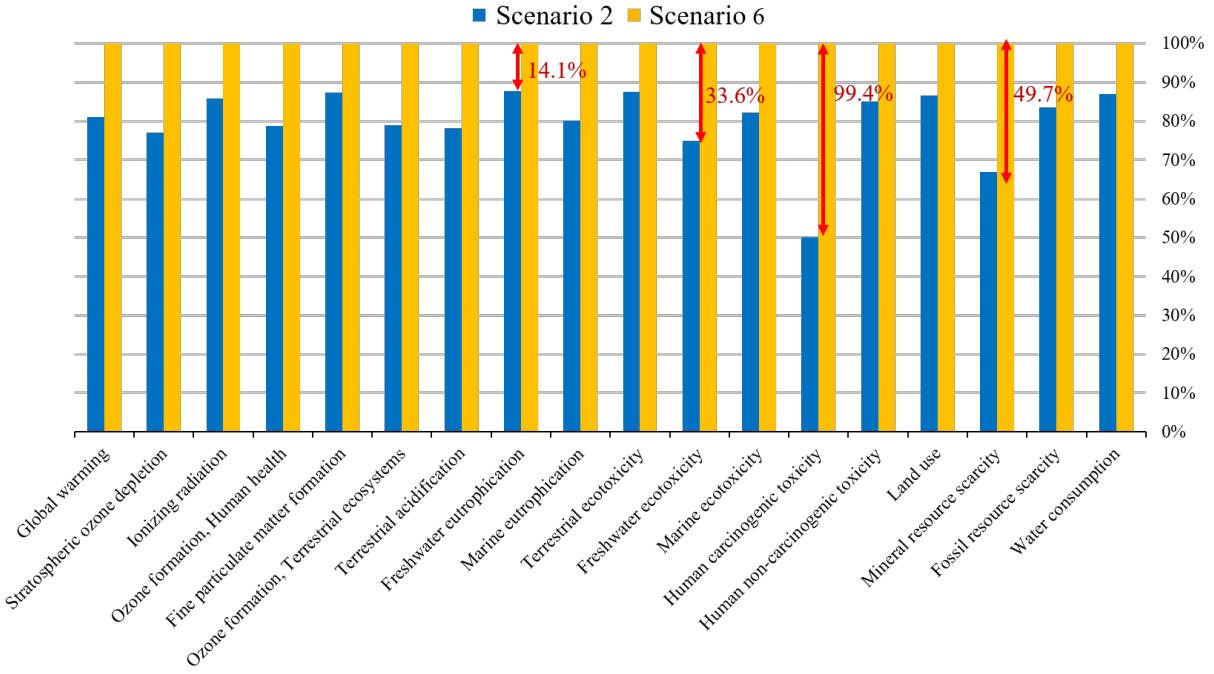

Figure 5.17: Comparison between impacts related to scenario 2 (industrial scale of xonotlite production) and scenario 6 (industrial scale of tobermorite production).

This LCA study provides a basic understanding of the contributions of each parameter that take part in the life cycle of xonotlite and tobermorite syntheses via a supercritical water-based methodology.

5.5.4 Impact to global warming category: comparison between scenarios

Another interesting comparison that can be done is related to the impact of different factors (precursors, energy, water and wastewater) on the global warming category. The results obtained for this study are reported in Figure 5.18. As expected, the lab-scale scenarios for xonotlite and tobermorite are the most relevant contributor to global warming, mostly due to the heat generation impacts which accounted for 27.06 and 48.8 kg (CO_2-eq to air), respectively. Once the energy consumption was optimised through heat recovery, in sc1 and sc5, the absolute impacts to global warming related to heat were reduced to 2.71 and 4.88 kg (CO_2-eq to air), respectively. The theoretical energy saving obtained with the employment of heat exchanger would allow to reduce the total impacts of global warming from 36.17 and 60.27 kg (CO_2-eq to air) for the lab-scale scenarios of xonotlite and tobermorite to 11.81 and 16.35 kg (CO_2-eq to air) for sc1 and sc5, respectively. To further reduce the impacts of energy consumption, the maximal precursor concentration

should be used, as shown in Figure 5.18 for sc2, sc3, and sc6. For these scenarios, the highest contribution to global warming comes from the precursors which account for 8.14, 8.53 and 10.25 kg (CO_2-eq to air), respectively.

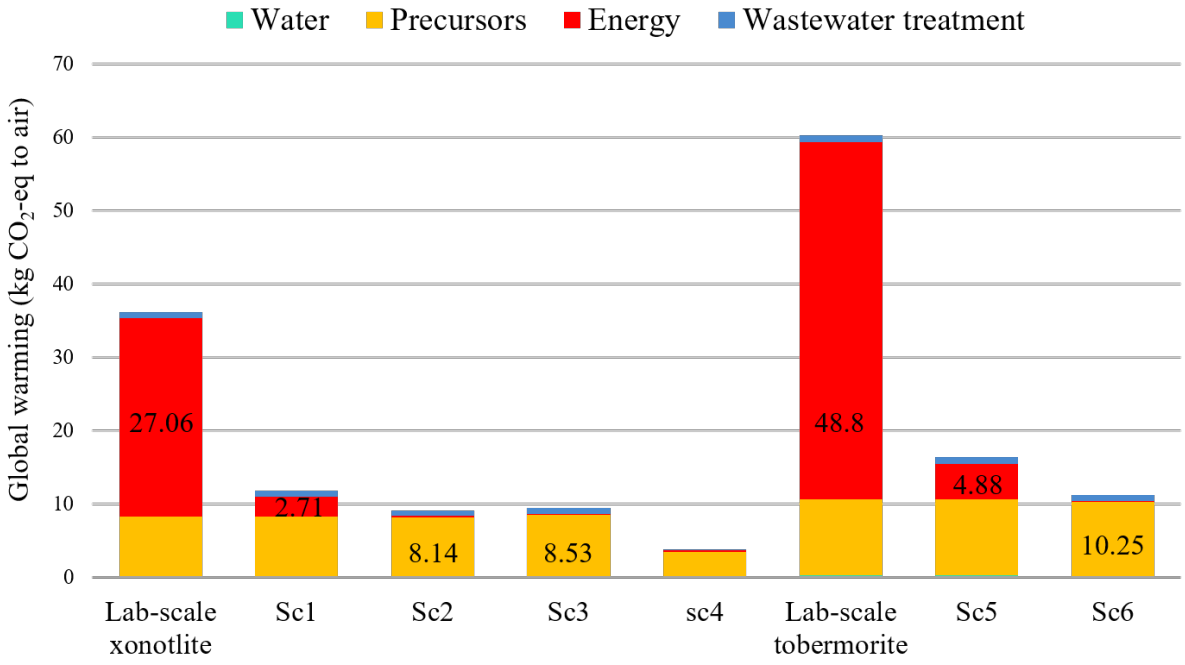

Figure 5.18: Comparison between the absolute impacts of water, precursors, energy, and wastewater treatment on the global warming category.

In general, tobermorite synthesis affects more the global warming impact due to the lower conversion yield of the reaction. On the contrary, the xonotlite synthesis as reported in sc4 has the lowest total impact to global warming, 3.72 kg (CO_2-eq to air), thanks to the proper choice of Ca precursor.

In this work, the cradle-to-gate environmental impacts related to the production of xonotlite and tobermorite via the supercritical hydrothermal flow synthesis were analysed through LCA. The results have shown that to improve the environmental profile of this manufacturing route, three main factors must be optimised: the heat recovery, the precursors concentration, and the type of chemical precursors. In the field of synthetic nanomineral production, this study could serve as a starting point for developing a sustainable and scalable synthesis methodology.

test the dehydration process on other CSH mineral, considering both natural and synthetic specimens as pristine materials.

Lastly, we have focused our attention on evaluating the environmental profile of the supercritical hydrothermal flow synthesis. The cradle-to-gate environmental impacts related to xonotlite and tobermorite production via SHFS were investigated through life cycle assessment analysis. The results have shown that the most significant impacts are precursors and heat consumption for both mineral phases at the lab-scale. It has been found that the production of 1 kg of tobermorite has a more significant environmental impact, in term of global warming, due to the lower conversion yield of the reaction. Furthermore, in that case, aluminium nitrate generates supplementary impacts if compared to 1 kg of xonotlite production. The use of Al-source significantly affects categories as stratospheric ozone depletion, freshwater ecotoxicity, human carcinogenic toxicity and mineral resource scarcity.

The main objective of this study was to identify where improvements could be realised to further enhance the attractiveness of SHFS as an environmentally sustainable synthesis methodology. Consequently, we have considered heat recovery and precursors molar concentration as parameters to be optimised at the industrial scale. First, by adding a heat exchanger (90% efficiency), the energy consumption decreased from 477.13 and 860.63 MJ to 47.71 and 86.06 MJ for xonotlite and tobermorite, respectively. Second, by considering the maximal precursor concentrations, the water amount was drastically reduced, and consequently also the required energy amount (3.57 and 3.22 MJ for xonotlite and tobermorite production, respectively). At the industrial scale, the maximal concentration of produced material was estimated to be 69.3 g/L and 76.8 g/L for xonotlite and tobermorite, respectively. At that level, once optimised the amounts of energy and water, the chemicals contributed significantly to the overall impacts of the process. In particular, we estimated that calcium nitrate had the most significant effect, and therefore we identified another compound, calcium chloride, which could be used for the production of xonotlite. The results have shown that the $CaCl_2$ dramatically reduces the potential impacts linked to nitrates, i.e. eutrophication and ozone depletion.

This work represents the first investigation through LCA of the environmental profile of supercritical hydrothermal flow synthesis to produce synthetic calcium silicate hydrate nanominerals. In this context, having stressed the crucial importance of choosing proper chemicals, further studies could be focused on the search for more sustainable chemical precursors to replace sodium metasilicate and aluminium nitrate.

Appendix A

Description of characterisation techniques

A.1 Electron microscopy techniques

A.1.1 Scanning electron microscopy

Scanning electron microscopy uses an electron beam of energy within 5 and 100 keV to probe the surface of the specimen. During the measurement, the electron beam is firstly generated by an electron gun and then focused by a series of lenses and apertures on the sample under study. The interaction between the electron beam and atoms, at various depths, produces various types of signals. Among them, there are high-energy back-scattered electrons, low-energy secondary electrons, light (cathodoluminescence), heat or characteristic X-ray. Both secondary and back-scattered electrons can be detected, giving access to different information such as topography and chemical composition, respectively.

A.1.2 Transmission electron microscopy

The working principles of transmission electron microscopy are similar to those of SEM, but in that case, a beam of energetic electrons is transmitted through the sample. The transmission geometry allows getting information about the morphology, the crystallinity, and the elemental composition of the material. High resolution-TEM allows to resolve details at the atomic scale and distinguish different families of planes and even individual atoms. High resolution imaging is achieved thanks to the interference between the wavefunctions of transmitted and diffracted electrons. As a result, it is possible to

identify the crystalline phase(s) of the material by measuring the interlattice spacing, d_{hkl}, as the distance between the interference fringes observed in the crystalline grains.

A.2 Powder X-ray diffraction technique

A crystalline solid can be described as a crystal lattice formed by atomic planes regularly spaced with long-range order. X-ray diffraction is a powerful and non-destructive technique for characterising crystalline materials. This methodology reveals accurate information on the chemical composition, unit cell dimensions, arrangement of atoms in the crystalline structure, and identification of the phase(s). In addition, it allows determining several other structural parameters, such as strain and crystalline domain size.

The working principle of PXRD is based on the Bragg diffraction which occurs when a monochromatic X-ray beam, with wavelength comparable to the interplanar distance, interacting with a crystalline sample is scattered by different crystal planes and undergoes constructive interferences (Figure A.1).

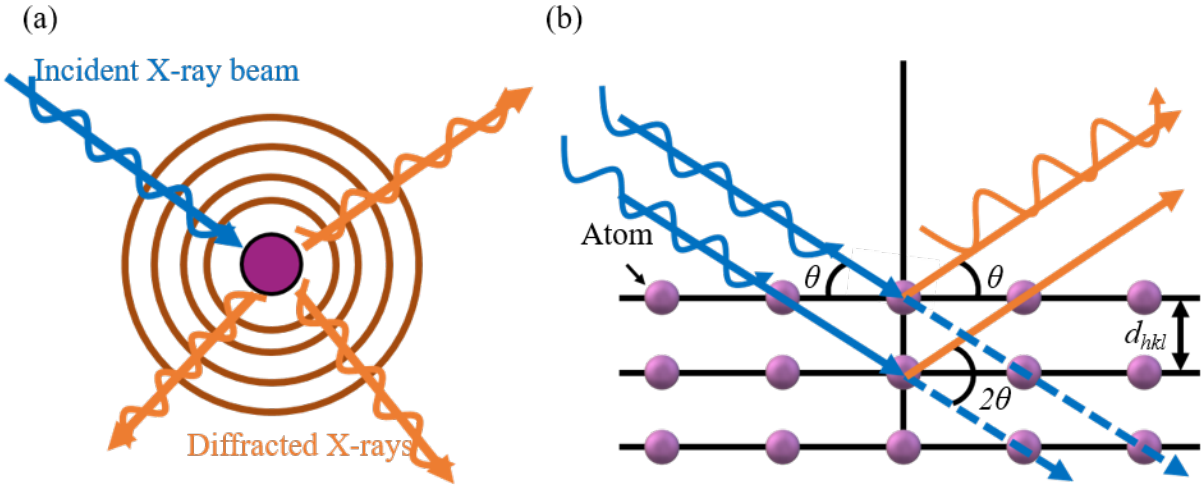

Figure A.1: Working principle of X-ray diffraction: (a) interaction between X-ray beam and atom, (b) interaction between X-ray beam and atomic planes.

The Bragg law defines the conditions for which the first, second, third, *etc.*, order reflections occur (Equation A.1):

$$2d \cdot \sin\theta = n\lambda \tag{A.1}$$

where d represents the spacing in a family of lattice planes, θ is the angle of incidence between the X-ray beam and the scattering planes, n is a positive integer related to the

order of reflection, and λ the wavelength of the incident beam (Figure A.1(b)).

During the PXRD analysis, the sample is irradiated by the electromagnetic beam at an angle θ in respect to the sample plane. The X-ray detector acquires the intensity of the diffracted X-rays at an angle of 2θ. Consequently, by scanning the sample within a wide range of 2θ angles, an unique fingerprint of the mineral can be obtained. The identification of the mineral phase(s) is then determined by the comparison of the d-spacings, measured from the position of the diffraction peaks, with standard reference patterns.

A.3 Spectroscopy techniques

A.3.1 Fourier transform infrared spectroscopy

The basic principle of Fourier transform infrared spectroscopy is based on the approximation of the chemical bonds within molecules to quantum harmonic oscillators. During the analysis, the sample is exposed to electromagnetic radiation and the chemical bonds vibrate at certain frequencies, depending on the elements and the type of bonds. According to quantum mechanics, for any given bond there are various specific frequencies at which it can vibrate. These frequencies correspond to the ground state (lowest frequency) and numerous other excited states (higher frequencies). An oscillating electric field with the same frequency as the chemical bond induces a vibrational resonance. Consequently, the absorption of energy occurs due to an excitation of molecular vibration. Thus, the resonant frequency is a unique characteristic of the chemical bond, since different chemical bonds absorb different frequencies of radiation. In addition, polyatomic molecules, or functional groups, have several vibrational modes, symmetric and asymmetric stretching, wagging, rocking, and bending modes, which correspond to different characteristic resonant frequencies. By varying the frequency of the radiation over a desired range, a mineral can be identified by comparing its absorption peaks to a data bank of spectra, and the response can be used to identify its chemistry.

A.3.2 Raman spectroscopy

Raman spectroscopy is a complementary tool to infrared absorption spectroscopy, providing further vibrational information of the molecules. Contrary to FTIR, Raman spectroscopy is based on an inelastic scattering process. Furthermore, Raman spectroscopy reveals vibrations involving a change in polarizability, instead of FTIR, which reveals vibrations involving a change in the dipole moment. Consequently, the two spectroscopic

techniques detect phenomena, inelastic scattering and absorption, which respond to different selection rules.

A.3.3 Solid-state nuclear magnetic resonance spectroscopy

Solid-state nuclear magnetic resonance relies on the quantum mechanical property of some atomic nuclei to have an overall nuclear spin. The basic working principle of NMR is schematically represented in Figure A.2.

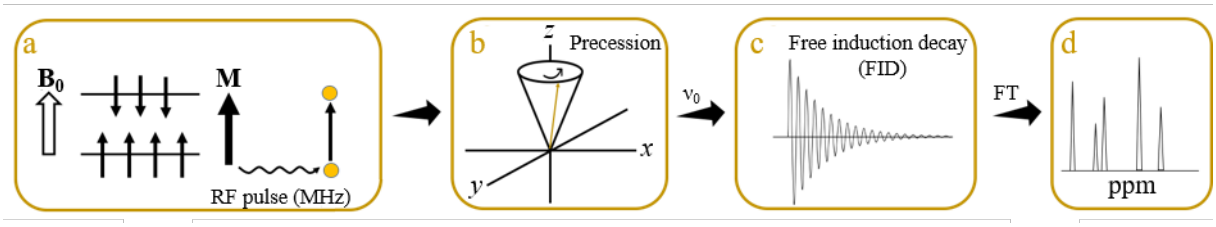

Figure A.2: Schematic representation of NMR working principle. (a) The whole spin system at equilibrium shows a net magnetisation, **M**, aligned along the direction of the external magnetic field $\mathbf{B}_0$; a radio frequency (RF) pulse excites the nuclei generating a transition in the spin energy levels. (b) The magnetisation is subjected to a precessional motion, which in turn gives rise to the emission of a (c) free induction decay signal. (d) The Fourier Transform (FT) of such signal provides the NMR spectrum.

In the presence of an external magnetic field of strength B_0, the nucleus develops a quantised number of energy levels. The transitions across different levels are allowed by respecting the selection rule: $\Delta m = \pm 1$, with m the magnetic quantum number. In addition, under the effect of $\mathbf{B}_0$, the ensemble of spins generates a net magnetisation, **M**, parallel to the magnetic field along the z-direction (Figure A.2a). If **M** is perturbed and tilted away from the z-axis, a net transverse component is induced on the x-y plane. The precession of such component about the field $\mathbf{B}_0$ with a frequency ν_0 (termed the Larmor frequency) generates the emission of an exponentially decaying sine wave signal, the Free Induction Decay (FID) (Figure A.2b and c). The manipulation of **M** is achieved by exciting the nuclei through a radio frequency (RF) pulse oscillating at the Larmor frequency, and thus on resonance conditions. In addition, the magnetisation **M** is tilt away from the equilibrium state by an angle θ during a certain time. Therefore, parameters that must be optimised during the measurement are the magnitude and the duration of the RF pulse. NMR analysis allows detecting the FID electromagnetic signal produced from the nuclei, and then converts it to a NMR spectrum by applying a Fourier transform (FT), Figure A.2d.

The magnetic field experienced by a molecule will depend on the local chemical en-

vironment; therefore, different chemical environments will result in different resonances within the spectrum. When using NMR, it is more convenient to define a chemical shift δ, typically reported in ppm, which is measured relative to a known frequency of a reference compound.

A.4 Chemical analysis techniques

A.4.1 Thermogravimetric analysis

The thermogravimetric analysis relies on a high degree of precision in the measurement of the sample mass changes as a function of the temperature. During the analysis, the sample is placed in a microbalance sensitive to any weight loss during the heating performed in a controlled atmospheric environment (inert or reducing). The combination of the TGA with a mass spectrometer allows obtaining further qualitative information on the chemical composition, in terms of m/z, of the evolved decomposition or vaporisation products.

A.4.2 Inductively coupled plasma/optical emission spectrometry

Inductively Coupled Plasma Optical Emission Spectroscopy is an elemental analysis technique that allows to identify and quantify the elements present in a material. More in details, ICP-OES exploits the high temperatures in plasma to break down the sample into atoms and measures the characteristic energy for ionisation and excitation.

Appendix B

Absolute midpoint life-cycle impact results

Table B.1: List of impacts for the production of 1 kg of xonotlite particles for the lab-scale process with and without the use of a heat exchanger (lab-scale and Sc1 scenarios) and the three other potential industrial scale scenarios (Sc2, Sc3, Sc4).

Impact category	**Unit**	**Lab-scale**	**Sc1**	**Sc2**	**Sc3**	**Sc4**
Global warming	kg CO_2-eq	$3.62 \cdot 10$	$1.18 \cdot 10$	9.08	9.43	3.72
Ozone depletion	kg CFC-11-eq	$1.50 \cdot 10^{-4}$	$1.44 \cdot 10^{-4}$	$1.43 \cdot 10^{-4}$	$1.50 \cdot 10^{-4}$	$2.70 \cdot 10^{-6}$
Ionizing radiation	kBq Co-60-eq	$8.02 \cdot 10^{-2}$	$5.84 \cdot 10^{-2}$	$4.18 \cdot 10^{-2}$	$4.38 \cdot 10^{-2}$	$3.43 \cdot 10^{-2}$
Ozone formation: human health	kg NOx-eq	$3.53 \cdot 10^{-2}$	$1.86 \cdot 10^{-2}$	$1.63 \cdot 10^{-2}$	$1.70 \cdot 10^{-2}$	$8.73 \cdot 10^{-3}$
Fine particulate matter formation	kg PM2.5-eq	$2.79 \cdot 10^{-2}$	$2.34 \cdot 10^{-2}$	$2.25 \cdot 10^{-2}$	$2.36 \cdot 10^{-2}$	$1.94 \cdot 10^{-2}$
Ozone formation: terrestrial ecosystems	kg NOx-eq	$3.62 \cdot 10^{-2}$	$1.88 \cdot 10^{-2}$	$1.65 \cdot 10^{-2}$	$1.72 \cdot 10^{-2}$	$8.85 \cdot 10^{-3}$
Terrestrial acidification	kg SO_2-eq	$4.41 \cdot 10^{-2}$	$3.75 \cdot 10^{-2}$	$2.84 \cdot 10^{-2}$	$2.97 \cdot 10^{-2}$	$1.69 \cdot 10^{-2}$
Freshwater eutrophication	kg P-eq	$6.85 \cdot 10^{-4}$	$6.32 \cdot 10^{-4}$	$5.93 \cdot 10^{-4}$	$6.21 \cdot 10^{-4}$	$4.37 \cdot 10^{-4}$
Marine eutrophication	kg N-eq	$1.78 \cdot 10^{-2}$	$1.78 \cdot 10^{-2}$	$1.78 \cdot 10^{-2}$	$2.13 \cdot 10^{-2}$	$4.15 \cdot 10^{-5}$
Terrestrial ecotoxicity	kg 1,4-DCB-eq	$3.37 \cdot 10$	$3.19 \cdot 10$	$3.10 \cdot 10$	$3.25 \cdot 10$	$1.96 \cdot 10$
Freshwater ecotoxicity	kg 1,4-DCB-eq	$8.92 \cdot 10^{-3}$	$8.18 \cdot 10^{-3}$	$6.26 \cdot 10^{-3}$	$6.56 \cdot 10^{-3}$	$2.51 \cdot 10^{-3}$
Marine ecotoxicity	kg N-eq	$7.82 \cdot 10^{-2}$	$3.43 \cdot 10^{-2}$	$2.69 \cdot 10^{-2}$	$2.80 \cdot 10^{-2}$	$1.41 \cdot 10^{-2}$
Human toxicity: cancer	kg 1,4-DCB-eq	$8.52 \cdot 10^{-2}$	$6.47 \cdot 10^{-2}$	$5.13 \cdot 10^{-2}$	$5.37 \cdot 10^{-2}$	$3.61 \cdot 10^{-2}$
Human toxicity: non-cancer	kg 1,4-DCB-eq	$9.90 \cdot 10^{-1}$	$8.85 \cdot 10^{-1}$	$8.12 \cdot 10^{-1}$	$8.50 \cdot 10^{-1}$	$4.74 \cdot 10^{-1}$
Land use	m^2 year	$1.64 \cdot 10^{-1}$	$1.47 \cdot 10^{-1}$	$1.38 \cdot 10^{-1}$	$1.45 \cdot 10^{-1}$	$1.48 \cdot 10^{-1}$
Mineral resource scarcity	kg Cu-eq	$5.04 \cdot 10^{-2}$	$4.39 \cdot 10^{-2}$	$4.15 \cdot 10^{-2}$	$4.34 \cdot 10^{-2}$	$1.93 \cdot 10^{-2}$
Fossil resource scarcity	kg oil-eq	$1.20 \cdot 10$	2.52	1.48	1.51	1.01
Water consumption	m^3 water-eq	$1.17 \cdot 10^{-1}$	$1.07 \cdot 10^{-1}$	$9.75 \cdot 10^{-2}$	$1.02 \cdot 10^{-1}$	$8.46 \cdot 10^{-2}$

Table B.2: List of impacts for the production of 1 kg of tobermorite particles for the lab-scale process with and without the use of a heat exchanger (lab-scale and Sc5 scenarios) and industrial scale scenario (Sc6).

Impact category	**Unit**	**Lab-scale**	**Sc5**	**Sc6**
Global warming	kg CO_2-eq	$6.03 \cdot 10$	$1.63 \cdot 10$	$1.11 \cdot 10$
Ozone depletion	kg CFC-11-eq	$1.99 \cdot 10^{-4}$	$1.87 \cdot 10^{-4}$	$1.80 \cdot 10^{-4}$
Ionizing radiation	kBq Co-60-eq	$1.19 \cdot 10^{-1}$	$8.01 \cdot 10^{-2}$	$4.87 \cdot 10^{-2}$
Ozone formation: human health	kg NOx-eq	$5.51 \cdot 10^{-2}$	$2.50 \cdot 10^{-2}$	$2.07 \cdot 10^{-2}$
Fine particulate matter formation	kg PM2.5-eq	$3.56 \cdot 10^{-2}$	$2.74 \cdot 10^{-2}$	$2.58 \cdot 10^{-2}$
Ozone formation: terrestrial ecosystems	kg NOx-eq	$5.66 \cdot 10^{-2}$	$2.53 \cdot 10^{-2}$	$2.09 \cdot 10^{-2}$
Terrestrial acidification	kg SO_2-eq	$6.47 \cdot 10^{-2}$	$4.07 \cdot 10^{-2}$	$3.64 \cdot 10^{-2}$
Freshwater eutrophication	kg P-eq	$8.45 \cdot 10^{-4}$	$7.49 \cdot 10^{-4}$	$6.77 \cdot 10^{-4}$
Marine eutrophication	kg N-eq	$2.22 \cdot 10^{-2}$	$2.22 \cdot 10^{-2}$	$2.00 \cdot 10^{-2}$
Terrestrial ecotoxicity	kg 1,4-DCB-eq	$4.04 \cdot 10$	$3.71 \cdot 10^{1}$	$3.45 \cdot 10$
Freshwater ecotoxicity	kg 1,4-DCB-eq	$1.33 \cdot 10^{-2}$	$1.20 \cdot 10^{-2}$	$8.63 \cdot 10^{-3}$
Marine ecotoxicity	kg N-eq	$1.26 \cdot 10^{-1}$	$4.66 \cdot 10^{-2}$	$3.27 \cdot 10^{-2}$
Human toxicity: cancer	kg 1,4-DCB-eq	$1.64 \cdot 10^{-1}$	$1.27 \cdot 10^{-1}$	$1.02 \cdot 10^{-1}$
Human toxicity: non-cancer	kg 1,4-DCB-eq	1.28	1.09	$9.55 \cdot 10^{-1}$
Land use	m^2 year	$2.06 \cdot 10^{-1}$	$1.76 \cdot 10^{-1}$	$1.59 \cdot 10^{-1}$
Mineral resource scarcity	kg Cu-eq	$7.83 \cdot 10^{-2}$	$6.66 \cdot 10^{-2}$	$6.20 \cdot 10^{-2}$
Fossil resource scarcity	kg oil-eq	$2.08 \cdot 10^{1}$	3.72	1.77
Water consumption	m^3 water-eq	$1.47 \cdot 10^{-1}$	$1.30 \cdot 10^{-1}$	$1.12 \cdot 10^{-1}$

Table B.3: List of impacts for the production of 1 kg of sodium metasilicate pentahydrate, calcium nitrate and calcium chloride.

Impact category	**Unit**	**Sodium metasilicate pentahydrate**	**Calcium nitrate**	**Calcium chloride**
Global warming	kg CO_2-eq	1.43	3.31	$5.35 \cdot 10^{-1}$
Ozone depletion	kg CFC-11-eq	$1.17 \cdot 10^{-6}$	$7.23 \cdot 10^{-5}$	$2.29 \cdot 10^{-7}$
Ionizing radiation	kBq Co-60-eq	$1.41 \cdot 10^{-2}$	$7.33 \cdot 10^{-3}$	$3.83 \cdot 10^{-3}$
Ozone formation: human health	kg NOx-eq	$3.40 \cdot 10^{-3}$	$5.81 \cdot 10^{-3}$	$1.51 \cdot 10^{-3}$
Fine particulate matter formation	kg PM2.5-eq	$8.70 \cdot 10^{-3}$	$2.97 \cdot 10^{-3}$	$1.45 \cdot 10^{-3}$
Ozone formation: terrestrial ecosystems	kg NOx-eq	$3.44 \cdot 10^{-3}$	$5.85 \cdot 10^{-3}$	$1.53 \cdot 10^{-3}$
Terrestrial acidification	kg SO_2-eq	$5.43 \cdot 10^{-3}$	$1.09 \cdot 10^{-2}$	$5.26 \cdot 10^{-3}$
Freshwater eutrophication	kg P-eq	$1.54 \cdot 10^{-4}$	$1.74 \cdot 10^{-4}$	$1.11 \cdot 10^{-4}$
Marine eutrophication	kg N-eq	$1.81 \cdot 10^{-5}$	$5.99 \cdot 10^{-6}$	$4.11 \cdot 10^{-6}$
Terrestrial ecotoxicity	kg 1,4-DCB-eq	7.09	$1.05 \cdot 10$	4.74
Freshwater ecotoxicity	kg 1,4-DCB-eq	$8.40 \cdot 10^{-4}$	$2.78 \cdot 10^{-3}$	$5.94 \cdot 10^{-4}$
Marine ecotoxicity	kg N-eq	$4.90 \cdot 10^{-3}$	$1.03 \cdot 10^{-2}$	$3.27 \cdot 10^{-3}$
Human toxicity: cancer	kg 1,4-DCB-eq	$1.34 \cdot 10^{-2}$	$1.45 \cdot 10^{-2}$	$7.25 \cdot 10^{-3}$
Human toxicity: non-cancer	kg 1,4-DCB-eq	$1.66 \cdot 10^{-1}$	$2.96 \cdot 10^{-1}$	$1.22 \cdot 10^{-1}$
Land use	m^2 year	$3.89 \cdot 10^{-2}$	$3.68 \cdot 10^{-2}$	$6.39 \cdot 10^{-2}$
Mineral resource scarcity	kg Cu-eq	$6.90 \cdot 10^{-3}$	$1.72 \cdot 10^{-2}$	$4.67 \cdot 10^{-3}$
Fossil resource scarcity	kg oil-eq	$3.87 \cdot 10^{-1}$	$3.83 \cdot 10^{-1}$	$1.31 \cdot 10^{-1}$
Water consumption	m^3 water-eq	$2.76 \cdot 10^{-2}$	$2.61 \cdot 10^{-2}$	$2.59 \cdot 10^{-2}$

Bibliography

[1] R. M. Hazen and J. H. Ausubel, "On the nature and significance of rarity in mineralogy," *American Mineralogist*, vol. 101, pp. 1245–1251, 2016.

[2] M. Claverie, M. Diez-Garcia, F. Martin, and C. Aymonier, "Continuous synthesis of nanominerals in supercritical water," *Chemistry – A European Journal*, vol. 25, pp. 5814–5823, 2019.

[3] X. Li and J. Chang, "A novel hydrothermal route to the synthesis of xonotlite nanofibers and investigation on their bioactivity," *Journal of Materials Science*, vol. 41, pp. 4944–4947, 2006.

[4] G. Wei, Y. Liu, X. Zhang, F. Yu, and X. Du, "Thermal conductivities study on silica aerogel and its composite insulation materials," *International Journal of Heat and Mass Transfer*, vol. 54, pp. 2355–2366, 2011.

[5] N. Low and J. Beaudoin, "Mechanical properties and microstructure of cement binders reinforced with synthesized xonotlite micro-fibres," *Cement and Concrete Research*, vol. 23, pp. 1016–1028, 1993.

[6] G. Land and D. Stephan, "Controlling cement hydration with nanoparticles," *Cement and Concrete Composites*, vol. 57, pp. 64–67, 2015.

[7] M. Diez-Garcia, "Synthesis by supercritical fluids methods of advanced additions for cementitious materials.," *Ph.D. Thesis, Universidad del País Vasco and Univerité de Bordeaux*, 2017.

[8] M. Diez-Garcia, J. J. Gaitero, J. S. Dolado, and C. Aymonier, "Ultra-fast supercritical hydrothermal synthesis of tobermorite under thermodynamically metastable conditions," *Angewandte Chemie (International Ed. in English)*, vol. 56, pp. 3162–3167, 2017.

[9] M. Diez-Garcia, J. J. Gaitero, J. I. Santos, J. S. Dolado, and C. Aymonier, "Supercritical hydrothermal flow synthesis of xonotlite nanofibers," *Journal of Flow Chemistry*, vol. 8, pp. 89–95, 2018.

[10] P. Hewlett and M. Liska, *Lea's chemistry of cement and concrete*. Butterworth-Heinemann, 2019.

[11] Bentur Arnon, "Cementitious materials-Nine millennia and a new century: past, present, and future," *Journal of Materials in Civil Engineering*, vol. 14, pp. 2–22, 2002.

[12] R. Malinowski and Y. Garfinkel, "Prehistory of concrete," *Concrete International*, vol. 13, pp. 62–68, 1991.

[13] A. Moropoulou, A. Bakolas, and S. Anagnostopoulou, "Composite materials in ancient structures," *Cement and Concrete Composites*, vol. 27, pp. 295–300, 2005.

[14] J. Elsen, K. Van Balen, and G. Mertens, "Hydraulicity in historic lime mortars: A review," in *Historic Mortars* (J. Válek, J. J. Hughes, and C. J. W. P. Groot, eds.), (Dordrecht), pp. 125–139, Springer Netherlands, 2012.

[15] G. Artioli and J. W. Bullard, "Cement hydration: the role of adsorption and crystal growth," *Crystal Research and Technology*, vol. 48, pp. 903–918, 2013.

[16] A. Ulrik Nilsen and P. Monteiro, "Concrete: A three phase material," *Cement and Concrete Research*, vol. 23, pp. 147–151, 1993.

[17] P. J. M. Monteiro, S. A. Miller, and A. Horvath, "Towards sustainable concrete," *Nature Materials*, vol. 16, pp. 698–699, 2017.

[18] R. Andrew, "Global CO_2 emissions from cement production, 1928-2017," *Earth System Science Data*, vol. 10, pp. 2213–2239, 2018.

[19] "Activity report," *Cembureau, The European Cement Association, http://www.cembureau.eu/library/reports/*, 2018.

[20] "Activity report," *Cembureau, The European Cement Association, http://www.cembureau.eu/library/reports/*, 2019.

[21] "World cement association," *https://worldcementassociation.org/*.

[22] M. S. Imbabi, C. Carrigan, and S. McKenna, "Trends and developments in green cement and concrete technology," *International Journal of Sustainable Built Environment*, vol. 1, pp. 194–216, 2012.

[23] P. K. Mehta and P. Monteiro, "Concrete, microstructure, properties and materials," p. 239, 2001.

[24] H. Le Chatelier, *Recherches experimentales sur la constitution des mortiers hydrauliques*. 2nd Edition, Dunod, 1904.

[25] N. Thomas and D. Double, "Calcium and silicon concentrations in solution during the early hydration of portland cement and tricalcium silicate," *Cement and Concrete Research*, vol. 11, pp. 675–687, 1981.

[26] D. Marchon and R. J. Flatt, "Impact of chemical admixtures on cement hydration," in *Science and Technology of Concrete Admixtures* (P.-C. Aïtcin and R. J. Flatt, eds.), pp. 279–304, Woodhead Publishing, 2016.

[27] P. Barret, D. Ménétrier, and D. Bertrandie, "Mechanism of C_3S dissolution and problem of the congruency in the very initial period and later on," *Cement and Concrete Research*, vol. 13, pp. 728–738, 1983.

[28] M. Grutzeck and A. Ramachandran, "An integration of tricalcium silicate hydration models in light of recent data," *Cement and Concrete Research*, vol. 17, pp. 164–170, 1987.

[29] J. F. Young, H. S. Tong, and R. L. Berger, "Compositions of solutions in contact with hydrating tricalcium silicate pastes," *Journal of the American Ceramic Society*, vol. 60, pp. 193–198, 1977.

[30] M. E. Tadros, J. Skalny, and R. S. Kalyoncu, "Early hydration of tricalcium silicate," *Journal of the American Ceramic Society*, vol. 59, pp. 344–347, 1976.

[31] B. J. Dalgleish, P. L. Pratt, and E. Toulson, "Fractographic studies of microstructural development in hydrated Portland cement," *Journal of Materials Science*, vol. 17, pp. 2199–2207, 1982.

[32] H. F. W. Taylor, *Cement chemistry*. Thomas Telford Publishing, 1997.

[33] K. L. Scrivener and P. L. Pratt, "Characterisation of portland cement hydration by electron optical techniques," *MRS Online Proceedings Library (OPL)*, vol. 31, 1983.

[34] M. Voltolini, N. Marinoni, and L. Mancini, "Synchrotron X-ray computed microtomography investigation of a mortar affected by alkali–silica reaction: a quantitative characterization of its microstructural features," *Journal of Materials Science*, vol. 46, pp. 6633–6641, 2011.

[35] L. B. Skinner, S. R. Chae, C. J. Benmore, H. R. Wenk, and P. J. M. Monteiro, "Nanostructure of Calcium Silicate Hydrates in Cements," *Physical Review Letters*, vol. 104, p. 195502, 2010.

[36] P. E. Stutzman, "Scanning electron microscopy in concrete petrography," pp. 59–72, 2000.

[37] T. C. Powers, "Structure and physical properties of hardened portland cement paste," *Journal of the American Ceramic Society*, vol. 41, pp. 1–6, 1958.

[38] R. F. Feldman and P. J. Sereda, "A new model for hydrated portland cement and its practical implications," *Engineering Journal (Canada)*, 1970.

[39] P. D. Tennis and H. M. Jennings, "A model for two types of calcium silicate hydrate in the microstructure of Portland cement pastes," *Cement and Concrete Research*, vol. 30, pp. 855–863, 2000.

[40] H. M. Jennings, "A model for the microstructure of calcium silicate hydrate in cement paste," *Cement and Concrete Research*, vol. 30, pp. 101–116, 2000.

[41] A. J. Allen, J. J. Thomas, and H. M. Jennings, "Composition and density of nanoscale calcium–silicate–hydrate in cement," *Nature Materials*, vol. 6, pp. 311–316, 2007.

[42] R. Taylor, I. G. Richardson, and R. M. D. Brydson, "Composition and microstructure of 20-year-old ordinary Portland cement–ground granulated blast-furnace slag blends containing 0 to 100% slag," *Cement and Concrete Research*, vol. 40, pp. 971–983, 2010.

[43] H. F. W. Taylor, "Proposed structure for calcium silicate hydrate gel," *Journal of the American Ceramic Society*, vol. 59, pp. 464–467, 1986.

[44] C. Hejny and T. Armbruster, "Polytypism in xonotlite $Ca_6Si_6O_17(OH)_2$," *Zeitschrift für Kristallographie - Crystalline Materials*, vol. 216, pp. 396–408, 2001.

[45] Y. Kudoh and Y. Takéuchi, "Polytypism of xonotlite: (I) Structure of an A-1 polytype," *Mineralogical Journal*, vol. 9, pp. 349–373, 1979.

[46] K. Mamedov and N. Belov, "Structure of xonotlite," *Dokl. Akad. Nauk SSSR*, vol. 104, pp. 615–618, 1955.

[47] A.-R. Grimmer and W. Wieker, "Bestimmung der art der wasserbindung im xonotlit $6CaO_6SiO_2$-H_2O," *Zeitschrift für anorganische und allgemeine Chemie*, vol. 384, pp. 34–42, 1971.

[48] O. Anton, A. Eckert, and A. Eckert, "Brake linings," *United States Patent, Patent number 4,994,506*, 1991.

[49] K. Luke and G. Quercia, "Formation of tobermorite and xonotlite fiber matrices in well cementing and impact on mechanical properties," *Journal of Sustainable Cement-Based Materials*, vol. 5, pp. 91–105, 2016.

[50] S. Merlino, E. Bonaccorsi, and T. Armbruster, "The real structure of tobermorite $11\dot{A}$: normal and anomalous forms, OD character and polytypic modifications," pp. 1643–1621, 2001.

[51] T. Mitsuda and H. F. W. Taylor, "Normal and anomalous tobermorites," *Mineralogical Magazine*, vol. 42, pp. 229–235, 1978.

[52] I. G. Richardson, "Tobermorite/jennite- and tobermorite/calcium hydroxide-based models for the structure of C-S-H: applicability to hardened pastes of tricalcium silicate, β-dicalcium silicate, Portland cement, and blends of Portland cement with blast-furnace slag, metakaolin, or silica fume," *Cement and Concrete Research*, vol. 34, pp. 1733–1777, 2004.

[53] J. D. C. McConnell, "The hydrated calcium silicates riversideite, tobermorite, and plombierite," *Mineralogical magazine and journal of the Mineralogical Society*, vol. 30, pp. 293–305, 1954.

[54] H. Megaw and C. Kelsey, "Crystal structure of tobermorite," *Nature*, vol. 177, pp. 390–391, 1956.

[55] S. A. Hamid, "The crystal structure of the $11\dot{A}$ natural tobermorite $Ca_{2.25}[Si_3O_{7.5}(OH)_{1.5}] \cdot 1\,H_2O$," *Zeitschrift für Kristallographie - Crystalline Materials*, vol. 154, pp. 189–198, 1981.

[56] S. Merlino, E. Bonaccorsi, and T. Armbruster, "Tobermorites: their real structure and order-disorder (OD) character," *American Mineralogist*, vol. 84, pp. 1613–1621, 1999.

[57] M. D. Jackson, J. Moon, E. Gotti, R. Taylor, S. R. Chae, M. Kunz, A.-H. Emwas, C. Meral, P. Guttmann, P. Levitz, H.-R. Wenk, and P. J. M. Monteiro, "Material and elastic properties of Al-tobermorite in ancient roman seawater concrete," *Journal of the American Ceramic Society*, vol. 96, pp. 2598–2606, 2013.

[58] G. L. Kalousek, "Crystal chemistry of hydrous calcium silicates: I, substitution of aluminum in lattice of tobermorite," *Journal of the American Ceramic Society*, vol. 40, pp. 74–80, 1957.

[59] S. Diamond, J. L. White, and W. L. Dolch, "Effects of isomorphous substitution in hydrothermally-synthesized tobermorite," *American Mineralogist*, vol. 51, pp. 388–401, 1966.

[60] J. R. Houston, R. S. Maxwell, and S. A. Carroll, "Transformation of meta-stable calcium silicate hydrates to tobermorite: reaction kinetics and molecular structure from XRD and NMR spectroscopy," *Geochemical Transactions*, vol. 1-14, p. 1, 2009.

[61] X. Guo, F. Meng, and H. Shi, "Microstructure and characterization of hydrothermal synthesis of Al-substituted tobermorite," *Construction and Building Materials*, vol. 133, pp. 253–260, 2017.

[62] M. S. Z. S. Wang, Z. and X. Wang, "Incorporation of Al and Na in hydrothermally synthesized tobermorite," *Journal of the American Ceramic Society*, vol. 100, pp. 792–799, 2017.

[63] J. S. Dolado, M. Griebel, J. Hamaekers, and F. Heber, "The nano-branched structure of cementitious calcium-silicate-hydrate gel," *Journal of Materials Chemistry*, vol. 21, pp. 4445–4449, 2011.

[64] H. Manzano, "Atomistic simulation studies of the cement paste componentss," *Ph.D. Thesis, Universidad del Pais Vasco*, 2009.

[65] I. Richardson and G. Groves, "Models for the composition and structure of calcium silicate hydrate (C-S-H) gel in hardened tricalcium silicate pastes," *Cement and Concrete Research*, vol. 22, pp. 1001–1010, 1992.

[66] I. Richardson, "The nature of C-S-H in hardened cements," *Cement and Concrete Research*, vol. 29, pp. 1131–1147, 1999.

[67] J. Bernal, J. Jeffery, and H. F. W. Taylor, "Crystallographic research on the hydration of portland cement. A first report on investigations in progress," *Magazine of Concrete Research*, vol. 4, pp. 4–54, 1952.

[68] L. Heller and H. F. W. Taylor, *Crystallographic Data for the Calcium Silicates*. London: HMSO, 1956.

[69] J. Thomas, J. Chen, H. Jennings, and D. Neumann, "Ca-OH bonding in the C-S-H gel phase of tricalcium silicate and withe portland cement pastes measured by inelastic neutron scattering," *Chemistry of Materials*, vol. 15, pp. 3813–3817, 2003.

[70] C. Roosz, S. Gaboreau, S. Grangeon, D. Prêt, V. Montouillout, N. Maubec, S. Ory, P. Blanc, P. Vieillard, and P. Henocq, "Distribution of water in synthetic calcium silicate hydrates," *Langmuir*, vol. 32, pp. 6794–6805, 2016.

[71] J. P. Yesinowski, H. Eckert, and G. R. Rossman, "Characterization of hydrous species in minerals by high-speed proton MAS-NMR," *Journal of the American Chemical Society*, vol. 110, pp. 1367–1375, 1988.

[72] R. Bergman and J. Swenson, "Dynamics of supercooled water in confined geometry," *Nature*, vol. 403, pp. 283–286, 2000.

[73] M. D. Fayer, "Dynamics of water interacting with interfaces, molecules, and ions," *Accounts of Chemical Research*, vol. 45, pp. 3–14, 2012.

[74] D. Muñoz-Santiburcio and D. Marx, "Chemistry in nanoconfined water," *Chemical Science*, vol. 8, pp. 3444–3452, 2017.

[75] W. P. Gates, H. N. Bordallo, L. P. Aldridge, T. Seydel, H. Jacobsen, V. Marry, and G. J. Churchman, "Neutron time-of-flight quantification of water desorption isotherms of montmorillonite," *The Journal of Physical Chemistry C*, vol. 116, pp. 5558–5570, 2012.

[76] B. Coasne, A. Galarneau, R. J. M. Pellenq, and F. D. Renzo, "Adsorption , intrusion and freezing in porous silica : the view from the nanoscale," *Chemical Society Reviews*, vol. 42, pp. 4141–4171, 2013.

[77] M. A. Vasilyeva, Y. A. Gusev, V. G. Shtyrlin, A. Puzenko, P. B. Ishai, and Y. Feldman, "Dielectric relaxation of water in clay minerals," *Clays and Clay Minerals*, vol. 62, pp. 62–73, 2014.

[78] F. Kremer and A. Schönhals, *Broadband Dielectric Spectroscopy*. Springer Science & Business Media, 2002.

[79] G. Goracci, M. Monasterio, H. Jansson, and S. Cerveny, "Dynamics of nano-confined water in Portland cement - comparison with synthetic C-S-H gel and other silicate materials," *Scientific Reports*, vol. 7, pp. 1–10, 2017.

[80] S. Cerveny, S. Arrese-Igor, J. S. Dolado, J. J. Gaitero, A. Alegría, and J. Colmenero, "Effect of hydration on the dielectric properties of C-S-H gel," *The Journal of Chemical Physics*, vol. 134, p. 034509, 2011.

[81] M. Monasterio, "On the dielectric properties of water confined in cement-like materials," 2015.

[82] M. Monasterio, J. J. Gaitero, H. Manzano, J. S. Dolado, and S. Cerveny, "Effect of chemical environment on the dynamics of water confined in calcium silicate minerals: Natural and synthetic tobermorite," *Langmuir*, vol. 31, pp. 4964–4972, 2015.

[83] K. Byrappa and M. Yoshimura, *Handbook of hydrothermal technology. 1st Edition.* Noyes Publications, 2001.

[84] G. Demazeau, "Solvothermal processes: a route to the stabilization of new materials," *Journal of Materials Chemistry*, vol. 9, pp. 15–18, 1999.

[85] T. Adschiri, Y. Hakuta, and K. Arai, "Hydrothermal synthesis of metal oxide fine particles at supercritical conditions," *Industrial & Engineering Chemistry Research*, vol. 39, pp. 4901–4907, 2000.

[86] G. Demazeau, "Solvothermal reactions: an original route for the synthesis of novel materials," *Journal of Materials Science*, vol. 43, pp. 2104–2114, 2008.

[87] M. Yoshimura and K. Byrappa, "Hydrothermal processing of materials: past, present and future," *Journal of Materials Science*, vol. 43, pp. 2085–2103, 2007.

[88] G. Morey and P. Niggli, "The hydrothermal formation of silicates, a review," *Journal of the American Chemical Society*, vol. 35, pp. 1086–1130, 1913.

[89] R. M. Barrer, "Syntheses and reactions of mordenite," *Journal of the Chemical Society (Resumed)*, pp. 2158–2163, 1948.

[90] H. F. W. Taylor, "Hydrothermal reactions in the system CaO-SiO_2-H_2O and the steam curing of cement and cement-silica," *Chemistry of Cement: Proceedings of the Fourth International Symposium*, pp. 167–186, 1962.

[91] I. Harker, "Dehydration series in the system $CaSiO_3$-SiO_2-H_2O," *Journal of the American Ceramic Society*, vol. 47, pp. 521–529, 1964.

[92] S. Shaw, S. Clark, and C. Henderson, "Hydrothermal formation of the calcium silicate hydrates, tobermorite ($Ca_5Si_6O_{16}(OH)_2 \cdot 4H_2O$) and xonotlite ($Ca_6Si_6O_{17}(OH)_2$): an in situ synchrotron study," *Chemical Geology*, vol. 167, pp. 129–140, 2000.

[93] S. Hong and F. Glasser, "Phase relations in the CaO–SiO_2–H_2O system to 200 °C at saturated steam pressure," *Cement and Concrete Research*, vol. 34, pp. 1529–1534, 2004.

[94] L. Black, K. Garbev, P. Stemmermann, K. R. Hallam, and G. C. Allen, "Characterisation of crystalline C-S-H phases by X-ray photoelectron spectroscopy," *Cement and Concrete Research*, vol. 33, pp. 899–911, 2003.

[95] K. Speakman, "The stability of tobermorite in the system CaO-SiO_2-H_2O at elevated temperatures and pressures," *Mineralogical magazine and journal of the Mineralogical Society*, vol. 36, pp. 1090–1103, 1968.

[96] D. Buckner, D. Roy, and R. Roy, "Studies in the system $CaO-Al_2O_3-SiO_2-H_2O$–[part] 2, the system $CaSiO_3 - H_2O$," *The American Journal of Science*, vol. 258, pp. 132–147, 1960.

[97] E. P. Flint, H. F. McMurdie, and L. S. Wells, "Formation of hydrated calcium silicates at elevated temperatures and pressures," vol. 21, pp. 617–638, 1938.

[98] E. Spudulis, V. Savareika, and Spokauskas, "Influence of hydrothermal synthesis condition on xonotlite crystal morphology," *Materials Science*, vol. 19, pp. 190–196, 2013.

[99] L. Black, K. Garbev, and A. Stumm, "Structure, bonding and morphology of hydrothermally synthesised xonotlite," vol. 108, pp. 137–144, 2009.

[100] M. Hansen, H. Jakobsen, and J. Skibsted, "^{29}Si chemical shift anisotropies in calcium silicates from high-field ^{29}Si MAS NMR spectroscopy," *Inorganic Chemistry*, vol. 42, pp. 2368–2377, 2003.

[101] X. Cong and R. Kirkpatrick, "^{29}Si and ^{17}O NMR investigation of the structure of some crystalline calcium silicate hydrates," *Advanced Cement Based Materials*, vol. 3, pp. 133–143, 1996.

[102] A. Yazdani, H. Rezaie, and H. Ghassai, "Investigation of hydrothermal synthesis of wollastonite using silica and nano silica at different pressures," *Journal of Ceramic Processing Research*, vol. 13, pp. 348–353, 2010.

[103] W. Tan, G. Zhu, Y. Liu, Z. Zhang, and L. Liu, "Effects and mechanism research of the crystalline state for the semi-crystalline calcium silicate," *Cement and Concrete Research*, vol. 72, pp. 69–75, 2015.

[104] J. Cao, F. Liu, Q. Lin, and Y. Zhang, "Hydrothermal synthesis of xonotlite from carbide slag," *Progress in Natural Science*, vol. 18, pp. 1147–1153, 2008.

[105] F. Liu, L. Zeng, J. Cao, B. Zhu, and A. Yuan, "Hydrothermal synthesis of xonotlite fibers and investigation on their thermal property," *Advanced Materials Research*, vol. 105, pp. 841–843, 2010.

[106] K. Lin, J. Chang, G. Chen, M. Ruan, and C. Ning, "A simple method to synthesize single-crystalline β-wollastonite nanowires," *Journal of Crystal Growth*, vol. 300, pp. 267–271, 2007.

[107] N. Coleman, C. Trice, and J. Nicholson, "$11\dot{A}$ tobermorite from cement bypass dust and waste container glass: A feasibility study," *International Journal of Mineral Processing*, vol. 93, pp. 73–78, 2009.

[108] N. Coleman, Q. Li, and A. Raza, "Synthesis, structure and performance of calcium silicate ion exchangers from recycled container glass," *Physicochemical Problems of Mineral Processing*, vol. 50, pp. 5–16, 2014.

[109] J. Reinik, I. Heinmaa, U. Kirso, T. Kallaste, J. Ritamäki, D. Boström, E. Pongrácz, M. Huuhtanen, W. Larsson, R. Keiski, K. Kordás, and J. Mikkola, "Alkaline modified oil shale fly ash: Optimal synthesis conditions and preliminary tests on CO_2 adsorption," *Journal of Hazardous Materials*, vol. 196, pp. 180–186, 2011.

[110] T. Mitsuda and H. F. W. Taylor, "Influence of aluminium on the conversion of calcium silicate hydrate gels into $11\dot{A}$ tobermorite at 90 °c and 120 °C," *Cement and Concrete Research*, vol. 5, pp. 203–209, 1975.

[111] X. Huang, D. Jiang, and S. Tan, "Novel hydrothermal synthesis of tobermorite fibers using Ca(II)-EDTA complex precursor," *Journal of the European Ceramic Society*, vol. 23, pp. 123–126, 2003.

[112] F. Cansell, C. Aymonier, and A. Loppinet-Serani, "Review on materials science and supercritical fluids," *Current Opinion in Solid State and Materials Science*, vol. 7, pp. 331–340, 2003.

[113] M. Besnard, T. Tassaing, Y. Danten, J.-M. Andanson, J.-C. Soetens, F. Cansell, A. Loppinet-Serani, H. Reveron, and C. Aymonier, "Bringing together fundamental and applied science: The supercritical fluids route," *Journal of Molecular Liquids*, vol. 125, pp. 88–99, 2006.

[114] A. Loppinet-Serani, C. Aymonier, and F. Cansell, "Supercritical water for environmental technologies," *Journal of Chemical Technology & Biotechnology*, vol. 85, pp. 583–589, 2010.

[115] F. Cansell and C. Aymonier, "Design of functional nanostructured materials using supercritical fluids," *The Journal of Supercritical Fluids*, vol. 47, pp. 508–516, 2009.

[116] C. Aymonier, G. Philippot, A. Erriguible, and S. Marre, "Playing with chemistry in supercritical solvents and the associated technologies for advanced materials by design," *The Journal of Supercritical Fluids*, vol. 134, pp. 184–196, 2018.

[117] T. Adschiri, K. Kanazawa, and K. Arai, "Rapid and continuous hydrothermal crystallization of metal oxide particles in supercritical water," *Journal of the American Ceramic Society*, vol. 75, pp. 1019–1022, 1992.

[118] C. Aymonier, A. Loppinet-Serani, H. Reverón, Y. Garrabos, and F. Cansell, "Review of supercritical fluids in inorganic materials science," *The Journal of Supercritical Fluids*, vol. 38, pp. 242–251, 2006.

[119] D. Bröll, C. Kaul, A. Krämer, P. Krammer, T. Richter, M. Jung, H. Vogel, and P. Zehner, "Chemistry in supercritical water," *Angewandte Chemie International Edition*, vol. 38, pp. 2998–3014, 1999.

[120] H. Cochran, P. Cummings, and S. Karaborni, "Solvation in supercritical water," *Fluid Phase Equilibria*, vol. 71, pp. 1–16, 1992.

[121] M. Hodes, P. A. Marrone, G. T. Hong, K. A. Smith, and J. W. Tester, "Salt precipitation and scale control in supercritical water oxidation-Part A: fundamentals and research," vol. 29, pp. 265–288, 2004.

[122] E. Duverger-Nédellec, T. Voisin, A. Erriguible, and C. Aymonier, "Unveiling the complexity of salt(s) in water under transcritical conditions," *Journal of Supercritical Fluids*, vol. 165, pp. 1–12, 2020.

[123] H. Weingärtner and E. U. Franck, "Supercritical water as a solvent," *Angewandte Chemie International Edition*, vol. 44, pp. 2672–2692, 2005.

[124] A. Chialvo and P. Cummings, "Simple transferable intermolecular potential for the molecular simulation of water over wide ranges of state conditions," *Fluid Phase Equilib.*, vol. 73, pp. 190–191, 1998.

[125] T. Voisin, A. Erriguible, D. Ballenghien, D. Mateos, A. Kunegel, F. Cansell, and C. Aymonier, "Solubility of inorganic salts in sub-and supercritical hydrothermal environment: application to SCWO processes," *The Journal of Supercritical Fluids*, vol. 120, pp. 18–31, 2017.

[126] "Nist chemistry webbook, srd 69, https://webbook.nist.gov/chemistry/fluid/,"

[127] G. Brunner, "Near critical and supercritical water. Part I. Hydrolytic and hydrothermal processes," *The Journal of Supercritical Fluids*, vol. 47, pp. 373–381, 2009.

[128] A. Dumas, M. Claverie, C. Slostowski, G. Aubert, C. Careme, C. Le Roux, P. Micoud, F. Martin, and C. Aymonier, "Fast-geomimicking using chemistry in supercritical water," *Angewandte Chemie International Edition*, vol. 55, pp. 9868–9871, 2016.

[129] E. Reverchon and R. Adami, "Nanomaterials and supercritical fluids," *The Journal of Supercritical Fluids*, vol. 37, pp. 1–22, 2006.

[130] T. Adschiri, Y.-W. Lee, M. Goto, and S. Takami, "Green materials synthesis with supercritical water," *Green Chemistry*, vol. 13, pp. 1380–1390, 2011.

[131] E. Lester, P. Blood, J. Denyer, D. Giddings, B. Azzopardi, and M. Poliakoff, "Reaction engineering: The supercritical water hydrothermal synthesis of nano-particles," *The Journal of Supercritical Fluids*, vol. 37, pp. 209–214, 2006.

[132] B. Walkley, "Solid-state nuclear magnetic resonance spectroscopy of cements," vol. 1, pp. 1–42, 2019.

[133] D. Massiot, F. Fayon, M. Capron, I. King, S. Le Calve, B. Alonso, J. Durand, B. Bujoli, Z. Gan, and G. Hoatson, "Modelling one- and two-dimensional solid-state NMR spectra," *Magnetic Resonance in Chemistry*, vol. 40, pp. 70–76, 2001.

[134] V. F. Lvovich, *Impedance Spectroscopy: Applications to Electrochemical and Dielectric Phenomena*. John Wiley & Sons, 2012.

[135] S. Thomas, R. Thomas, A. Zachariah, and R. Kumar, *Spectroscopic Methods for Nanomaterials Characterization*. Elvesier, 1st ed., 2017.

[136] F. Kremer, "Dielectric spectroscopy of polymeric materials," *Dielectrics Newsletter*, pp. 5–10, 1997.

[137] G. Schaumburg, "New integrated dielectric analyzer extends accuracy and impedance range for material measurements," *Dielectrics Newsletter*, pp. 4–6, 1999.

[138] K. S. Cole and R. H. Cole, "Dispersion and absorption in dielectrics I. Alternating current characteristics," *The Journal of Chemical Physics*, vol. 9, pp. 341–351, 1941.

[139] K. S. Cole and R. H. Cole, "Dispersion and absorption in dielectrics II. Direct current characteristics," *The Journal of Chemical Physics*, vol. 10, pp. 98–105, 1942.

[140] J. Leys, "Broadband dielectric spectroscopy of confined liquid crystals and hydrogen bonded liquids," *Ph.D. Thesis, Katholieke Universiteit Leuven*, 2007.

[141] D. W. Davidson and R. H. Cole, "Dielectric relaxation in glycerine," *The Journal of Chemical Physics*, vol. 18, p. 1417, 1950.

[142] D. W. Davidson and R. H. Cole, "Dielectric relaxation in glycerol, propylene glycol, and n-propanol," *The Journal of Chemical Physics*, vol. 19, pp. 1484–1490, 1951.

[143] S. Havriliak and S. Negami, "A complex plane analysis of α-dispersions in some polymer systems," *Journal of Polymer Science Part C: Polymer Symposia*, vol. 14, pp. 99–117, 1966.

[144] S. Havriliak and S. Negami, "A complex plane representation of dielectric and mechanical relaxation processes in some polymers," *Polymer*, vol. 8, pp. 161–210, 1967.

[145] H. Vogel *Phys. Z.*, vol. 22, pp. 645–646, 1921.

[146] G. S. Fulcher, "Analysis of recent measurements of the viscosity of glasses," *Journal of the American Ceramic Society*, vol. 8, pp. 339–355, 1925.

[147] G. Tammann and W. Hesse, "Die Abhängigkeit der Viscosität von der Temperatur bie unterkühlten Flüssigkeiten," *Zeitschrift für anorganische und allgemeine Chemie*, vol. 156, pp. 245–257, 1926.

[148] Novocontrol, "Alpha high resolution dielectric / impedance analyzer: User's manual," 2002.

[149] A. A. MacDowell, D. Y. Parkinson, A. Haboub, E. Schaible, J. R. Nasiatka, C. A. Yee, J. R. Jameson, J. B. Ajo-Franklin, C. R. Brodersen, and A. J. McElrone, "X-ray micro-tomography at the Advanced Light Source," in *Developments in X-Ray Tomography VIII*, vol. 8506, p. 850618, International Society for Optics and Photonics, 2012.

[150] "Beamline 8.3.2 manual Advanced Light Source Lawrence Berkeley National Laboratory. http://microct.lbl.gov/manual," 2015.

[151] I. Richardson, "Model structures for C-(A)-S-H(I)," *Acta Crystallogr B Struct Sci Cryst Eng Mater*, vol. 70, pp. 903–923, 2014.

[152] L. Black, K. Garbev, G. Beuchle, P. Stemmermann, and D. Schild, "X-ray photoelectron spectroscopic investigation of nanocrystalline calcium silicate hydrates synthesised by reactive milling," *Cement and Concrete Research*, vol. 36, pp. 1023–1031, 2006.

[153] K. Garbev, G. Beuchle, M. Bornefeld, L. Black, and P. Stemmermann, "Cell dimensions and composition of nanocrystalline calcium silicate hydrate solid solutions. part 1: Synchrotron-based X-ray diffraction," *Journal of the American Ceramic Society*, vol. 91, pp. 3005–3014, 2008.

[154] S. Churakov and P. Mandaliev, "Structure of the hydrogen bonds and silica defects in the tetrahedral double chain of xonotlite," *Cement and Concrete Research*, vol. 38, pp. 300–311, 2008.

[155] F. Méducin, B. Bresson, N. Lequeux, M.-N. Noirfontaine, and H. Zanni, "Calcium silicate hydrates investigated by solid-state high resolution ^{1}H and ^{29}Si nuclear magnetic resonance," *Cement and Concrete Research*, vol. 37, pp. 631–638, 2007.

[156] F. Brunet, P. Bertani, T. Charpentier, A. Nonat, and J. Virlet, "Application of ^{29}Si homonuclear and ^{1}H-^{29}Si heteronuclear NMR correlation to structural studies of calcium silicate hydrates," *The Journal of Physical Chemistry B*, vol. 108, pp. 15494–15502, 2004.

[157] *NIST Inorganic Crystal Structure Database, NIST Standard Reference Database Number 3.* National Institute of Standards and Technology, Gaithersburg MD, 20899.

[158] H. Noma, Y. Adachi, Y. Matsuda, and T. Yokoyama, "^{29}Si and ^{1}H NMR of natural and synthetic xonotlite," *Chemistry letters*, pp. 219–220, 1998.

[159] N. Mostafa, A. Shaltout, H. Omarb, and S. Abo-El-Enein, "Hydrothermal synthesis and characterization of aluminium and sulfate substituted 1.1 nm tobermorites," *Journal of Alloys and Compounds*, vol. 467, pp. 332–337, 2009.

[160] S. A. S. Eℓ-Hemaly, T. Mitsuda, and H. F. W. Taylor, "Synthesis of normal and anomalous tobermorites," *Cement and Concrete Research*, vol. 7, pp. 429–438, 1977.

[161] T. Mitsuda, K. Sasaki, and H. Ishida, "Phase evolution during autoclaving process of aerated concrete," *Journal of the American Ceramic Society*, vol. 75, pp. 1858–1863, 1992.

[162] N. Bell, S. Venigalla, P. Gill, and J. Adair, "Morphological forms of tobermorite in hydrothermally treated calcium silicate hydrate gels," *Journal of the American Ceramic Society*, vol. 79, pp. 2175–2178, 1996.

[163] J. Li, W. Zhang, K. Garbev, G. Beuchle, and P. J. M. Monteiro, "Influences of cross-linking and Al incorporation on the intrinsic mechanical properties of tobermorite," *Cement and Concrete Research*, vol. 136, p. 106170, 2020.

[164] R. Dupuis, J. Moon, Y. Jeong, R. Taylor, S.-H. Kang, H. Manzano, A. Ayuela, P. J. M. Monteiro, and J. S. Dolado, "Normal and anomalous self-healing mechanism of crystalline calcium silicate hydrates," *Cement and Concrete Research*, vol. 142, p. 106356, 2021.

[165] E. Pavón, F. Osuna, M. Alba, and L. Delevoye, "Direct evidence of Löwenstein's rule violation in swelling high-charge micas," *Chemical Communications*, vol. 50, pp. 6984–6986, 2014.

[166] R. Fletcher, S. Ling, and B. Slater, "Violations of Löwenstein's rule in zeolites," *Chemical Science*, vol. 8, pp. 7483–7491, 2017.

[167] S. Dann, P. Mead, and M. Weller, "Löwenstein's rule extended to an aluminum rich framework. The structure of bicchulite, $Ca_8(Al_2SiO_6)_4(OH)_8$, by MAS NMR and neutron diffraction," *Inorganic Chemistry*, vol. 35, pp. 1427–1428, 1996.

[168] W. Wieker, M. Mgi, M. Tarmak, and E. Lippmaa, "Solid-state high-resolution ^{29}Si NMR spectroscopy of synthetic $14\dot{A}$, $11\dot{A}$ and $9\dot{A}$ tobermorites," *Cement and Concrete Research*, vol. 12, pp. 333–339, 1982.

[169] R. Gabrovsek, B. Kurbus, D. Mueller, and W. Wieker, "Tobermorite formation in the system CaO, C_3S-SiO_2-Al_2O_3-NaOH-H_2O under hydrothermal conditions," *Cement and Concrete Research*, vol. 23, pp. 321–328, 1993.

[170] S. Komarneni, R. Roy, D. M. Roy, C. A. Fyfe, G. J. Kennedy, A. A. Bothner-By, J. Dadok, and A. S. Chesnick, "^{27}Al and ^{29}Si magic angle spinning nuclear magnetic resonance spectroscopy of Al-substituted tobermorites," *Journal of Materials Science*, vol. 20, pp. 4209–4214, 1985.

[171] K. Sasaki, T. Masuda, H. Ishida, and T. Mitsuda, "Structural degradation of tobermorite during vibratory milling," *Journal of the American Ceramic Society*, vol. 79, pp. 1569–1574, 1996.

[172] J. Kirkpatrick, J. Yarger, P. McMillan, P. Yu, and X. Cong, "Raman spectroscopy of CSH, tobermorite, and jennite," *Advanced Cement Based Materials*, vol. 5, pp. 93–99, 1997.

[173] K. Garbev, "Struktur, eigenschaften und quantitative rietveld analyse von hydrothermal kristallisierten calciumsilikathydraten (C–S–H phasen)- Structure, properties and quantitative rietveld analysis of hydrothermal, crystalline calcium silicate hydrates (C–S–H phases)," *Ph.D. Thesis, University of Heidelberg*, 2004.

[174] K. Garbev, P. Stemmermann, L. Black, C. Breen, J. Yarwood, and B. Gasharova, "Structural features of C–S–H(I) and its carbonation in air—A Raman spectroscopic study. Part I: fresh phases," *Journal of the American Ceramic Society*, vol. 90, pp. 900–907, 2007.

[175] S. Ortaboy, J. Li, G. Geng, R. J. Myers, P. J. M. Monteiro, R. Maboudian, and C. Carraro, "Effects of CO_2 and temperature on the structure and chemistry of C–(A–)S–H investigated by Raman spectroscopy," *RSC Advances*, vol. 7, pp. 48925–48933, 2017.

[176] A. Vidmer, G. Sclauzero, and A. Pasquarello, "Infrared spectra of jennite and tobermorite from first-principles," *Cement and Concrete Research*, vol. 60, pp. 11–23, 2014.

[177] A. Palomo, P. J. M. Monteiro, P. Martauz, V. Bilek, and A. Fernandez-Jimenez, "Hybrid binders: a journey from the past to a sustainable future (opus caementicium futurum)," *Cement and Concrete Research*, vol. 124, p. 105829, 2019.

[178] J. Moon, S. Yoon, and P. J. M. Monteiro, "Mechanical properties of jennite: A theoretical and experimental study," *Cement and Concrete Research*, vol. 71, pp. 106–114, 2015.

[179] G. Geng, R. Myers, J. Li, R. Maboudian, C. Carraro, D. Shapiro, and P. J. M. Monteiro, "Aluminum-induced dreierketten chain cross-links increase the mechanical properties of nanocrystalline calcium aluminosilicate hydrate," *Scientific Reports*, vol. 7, p. 44032, 2017.

[180] J. Moon, J. E. Oh, M. Balonis, F. P. Glasser, S. M. Clark, and P. J. M. Monteiro, "Pressure induced reactions amongst calcium aluminate hydrate phases," *Cement and Concrete Research*, vol. 41, pp. 571–578, 2011.

[181] J. Moon, J. E. Oh, M. Balonis, F. P. Glasser, S. M. Clark, and P. J. M. Monteiro, "High pressure study of low compressibility tetracalcium aluminum carbonate hydrates $3CaO{\cdot}Al_2O_3{\cdot}CaCO_3{\cdot}11H_2O$," *Cement and Concrete Research*, vol. 42, pp. 105–110, 2012.

[182] S. Merlino, E. Bonaccorsi, M. Merlino, F. Marchetti, and W. Garra, "Tobermorite $11\dot{A}$ and its synthetic counterparts: Structural relationships and thermal behaviour," *Minerals as Advanced Materials I*, pp. 37–44, 2008.

[183] F. Birch, "Finite strain isotherm and velocities for single-crystal and polycrystalline NaCl at high pressures and 300 K," *Journal of Geophysical Research: Solid Earth*, vol. 83, pp. 1257–1268, 1978.

[184] J. Moon, "Experimental and theoretical studies on mechanical properties of complex oxides in concrete," *Ph.D. Thesis, University of California, Berkeley*, 2013.

[185] H. Manzano, J. S. Dolado, A. Guerrero, and A. Ayuela, "Mechanical properties of crystalline calcium-silicate-hydrates: comparison with cementitious C-S-H gels," *Physica status solidi (a)*, vol. 204, pp. 1775–1780, 2007.

[186] J. Li, W. Zhang, K. Xu, and P. J. M. Monteiro, "Fibrillar calcium silicate hydrate seeds from hydrated tricalcium silicate lower cement demand," *Cement and Concrete Research*, vol. 137, p. 106195, 2020.

[187] M. Monasterio, J. J. Gaitero, E. Erkizia, A. M. Guerrero Bustos, L. A. Miccio, J. S. Dolado, and S. Cerveny, "Effect of addition of silica- and amine functionalized silica-nanoparticles on the microstructure of calcium silicate hydrate (C–S–H) gel," *Journal of Colloid and Interface Science*, vol. 450, pp. 109–118, 2015.

[188] V. Musumeci, G. Goracci, P. Sanz Camacho, J. S. Dolado, and C. Aymonier, "Correlation between the dynamics of nanoconfined water and local chemical environ-

ments in calcium silicate hydrate nanominerals," *Chemistry - A European Journal*, vol. Submitted, 2021.

[189] G. Renaudin, A. Bertrand, M. Dubois, S. Gomes, P. Chevalier, and A. Labrosse, "A study of water releases in ground (GCC) and precipitated (PCC) calcium carbonates," *Journal of Physics and Chemistry of Solids*, vol. 69, pp. 1603–1614, 2008.

[190] H. Rosenberger, A.-R. Grimmer, U. Haubenreißer, and B. Schnabel, "Investigations on the type of OH-groups in some crystalline silicates by high resolution NMR-spectroscopy in solids," in *Magnetic Resonance and Related Phenomena* (E. Kundla, E. Lippmaa, and T. Saluvere, eds.), pp. 106–106, Springer Berlin Heidelberg, 1979.

[191] I. S. Protsak, Y. M. Morozov, W. Dong, Z. Le, D. Zhang, and I. M. Henderson, "A ^{29}Si, ^{1}H, and ^{13}C solid-state NMR study on the surface species of various depolymerized organosiloxanes at silica surface," *Nanoscale Research Letters*, vol. 14, pp. 1–15, 2019.

[192] C. C. Liu and G. E. Maciel, "The fumed silica surface: A study by NMR," *Journal of the American Chemical Society*, vol. 118, pp. 5103–5119, 1996.

[193] P. Colombet, A.-R. Grimmer, H. Zanni, and P. Sozzani, *Nuclear Magnetic Resonance Spectroscopy of Cement-Based Materials*. Springer Science & Business Media, 2012.

[194] S. Cerveny, G. A. Schwartz, J. Otegui, J. Colmenero, J. Loichen, and S. Westermann, "Dielectric study of hydration water in silica nanoparticles," *The Journal of Physical Chemistry C*, vol. 116, pp. 24340–24349, 2012.

[195] H. Haspel, V. Bugris, and A. Kukovecz, "Water-induced changes in the charge-transport dynamics of titanate nanowires," *Langmuir*, vol. 30, pp. 1977–1984, 2014.

[196] L. Frunza, H. Kosslick, S. Frunza, R. Fricke, and A. Schönhals, "On the mobility of sodium ions and of confined liquid crystals in molecular sieves of faujasite type," *Journal of Non-Crystalline Solids*, vol. 307-310, pp. 503–509, 2002.

[197] L. Frunza, H. Kosslick, I. Pitsch, S. Frunza, and A. Schönhals, "Rotational fluctuations of water inside the nanopores of SBA-type molecular sieves," *The Journal of Physical Chemistry B*, vol. 109, pp. 9154–9159, 2005.

[198] L. Frunza, A. Schönhals, H. Kosslick, and S. Frunza, "Relaxation processes of water confined to AIMCM-41 molecular sieves. Influence of the hydroxyl groups of the

pore surface," *The European Physical Journal. E, Soft Matter*, vol. 26, pp. 379–386, 2008.

[199] M. Sulpizi, M.-P. Gaigeot, and M. Sprik, "The silica–water interface: How the silanols determine the surface acidity and modulate the water properties," *Journal of Chemical Theory and Computation*, vol. 8, pp. 1037–1047, 2012.

[200] V. Bugris, H. Haspel, A. Kukovecz, Z. Kónya, M. Sipiczki, P. Sipos, and I. Pálinkó, "Water types and their relaxation behavior in partially rehydrated CaFe-mixed binary oxide obtained from CaFe-layered double hydroxide in the 155–298 K temperature range," *Langmuir*, vol. 29, pp. 13315–13321, 2013.

[201] J. Jansen and R. Schoonheydt, "Electrical properties of crystalline synthetic zeolites types X and Y, exchanged with monovalent cations," *Journal of the Chemical Society, Faraday Transactions 1: Physical Chemistry in Condensed Phases*, vol. 69, pp. 1338–1355, 1973.

[202] K. Sobolev and M. Gutiérrez, "How nanotechnology can change the concrete world," *American Ceramic Society Bulletin*, vol. 84, pp. 113–116, 2014.

[203] A. C. Institute, *ACI 241R-17, Report on Application of Nanotechnology and Nanomaterials in Concrete*. Noyes Publications, 2017.

[204] P. J. M. Monteiro, G. Geng, D. Marchon, J. Li, P. Alapati, K. E. Kurtis, and M. J. A. Qomi, "Advances in characterizing and understanding the microstructure of cementitious materials," *Cement and Concrete Research*, vol. 124, p. 105806, 2019.

[205] J. Fink, *Petroleum Engineer's Guide to Oil Field Chemicals and Fluids*. Gulf Professional Publishing, 2015.

[206] H. N. Stein and J. M. Stevels, "Influence of silica on the hydration of $3CaO,SiO_2$," *Journal of Applied Chemistry*, vol. 14, pp. 338–346, 1964.

[207] Z.-Q. Wu and J. F. Young, "The hydration of tricalcium silicate in the presence of colloidal silica," *Journal of Materials Science*, vol. 19, pp. 3477–3486, 1984.

[208] W. Kurdowski, *Cement and Concrete Chemistry*. Springer Science & Business, 2014.

[209] R. Alizadeh, L. Raki, J. M. Makar, J. J. Beaudoin, and I. Moudrakovski, "Hydration of tricalcium silicate in the presence of synthetic calcium–silicate–hydrate," *Journal of Materials Chemistry*, vol. 19, p. 7937, 2009.

[210] J. J. Thomas, H. M. Jennings, and J. J. Chen, "Influence of nucleation seeding on the hydration mechanisms of tricalcium silicate and cement," *The Journal of Physical Chemistry C*, vol. 113, pp. 4327–4334, 2009.

[211] P. Bost, "Comparison of the accelerating effect of various additions on the early hydration of Portland cement," *Construction and Building Materials*, vol. 113, pp. 290–296, 2016.

[212] E. John, T. Matschei, and D. Stephan, "Nucleation seeding with calcium silicate hydrate – A review," *Cement and Concrete Research*, vol. 113, pp. 74–85, 2018.

[213] L. Nicoleau, T. Gadt, L. Chitu, G. Maier, and O. Paris, "Oriented aggregation of calcium silicate hydrate platelets by the use of comb-like copolymers," *Soft Matter*, vol. 9, pp. 4864–4874, 2013.

[214] W. Nocuń-Wczelik and P. Czapik, "Use of calorimetry and other methods in the studies of water reducers and set retarders interaction with hydrating cement paste," *Construction and Building Materials*, vol. 38, pp. 980–986, 2013.

[215] G. Land and D. Stephan, "The effect of synthesis conditions on the efficiency of C-S-H seeds to accelerate cement hydration," *Cement and Concrete Composites*, vol. 87, pp. 73–78, 2018.

[216] F. Wang, X. Kong, L. Jiang, and D. Wang, "The acceleration mechanism of nano-C-S-H particles on OPC hydration," *Construction and Building Materials*, vol. 249, p. 118734, 2020.

[217] N. Bossa, P. Chaurand, J. Vicente, D. Borschneck, C. Levard, O. Aguerre-Chariol, and J. Rose, "Micro- and nano-X-ray computed-tomography: A step forward in the characterization of the pore network of a leached cement paste," *Cement and Concrete Research*, vol. 67, pp. 138–147, 2015.

[218] D. Hernández-Cruz, C. W. Hargis, J. Dominowski, M. J. Radler, and P. J. M. Monteiro, "Fiber reinforced mortar affected by alkali-silica reaction: A study by synchrotron microtomography," *Cement and Concrete Composites*, vol. 68, pp. 123–130, 2016.

[219] P.-A. Itty, M. Serdar, C. Meral, D. Parkinson, A. A. MacDowell, D. Bjegović, and P. J. M. Monteiro, "In situ 3D monitoring of corrosion on carbon steel and ferritic stainless steel embedded in cement paste," *Corrosion Science*, vol. 83, pp. 409–418, 2014.

[220] Z. Yang, W. Ren, R. Sharma, S. McDonald, M. Mostafavi, Y. Vertyagina, and T. J. Marrow, "In-situ X-ray computed tomography characterisation of 3D fracture evolution and image-based numerical homogenisation of concrete," *Cement and Concrete Composites*, vol. 75, pp. 74–83, 2017.

[221] M. Voltolini, M. C. Dalconi, G. Artioli, M. Parisatto, L. Valentini, V. Russo, A. Bonnin, and R. Tucoulou, "Understanding cement hydration at the microscale: new opportunities from 'pencil-beam' synchrotron X-ray diffraction tomography," *Journal of Applied Crystallography*, vol. 46, pp. 142–152, 2013.

[222] G. Artioli, L. Valentini, M. Voltolini, M. Dalconi, G. Ferrari, and V. Russo, "Direct imaging of nucleation mechanisms by synchrotron diffraction micro-tomography: Superplasticizer-induced change of C-S-H nucleation in cement," *Crystal Growth & Design*, vol. 15, pp. 20–23.

[223] K. Xu, A. S. Tremsin, J. Li, D. M. Ushizima, C. A. Davy, A. Bouterf, Y. T. Su, M. Marroccoli, A. M. Mauro, M. Osanna, A. Telesca, and P. J. M. Monteiro, "Microstructure and water absorption of ancient concrete from Pompeii: An integrated synchrotron microtomography and neutron radiography characterization," *Cement and Concrete Research*, vol. 139, p. 106282, 2021.

[224] J. Schindelin, I. Arganda-Carreras, E. Frise, V. Kaynig, M. Longair, T. Pietzsch, S. Preibisch, C. Rueden, S. Saalfeld, B. Schmid, J.-Y. Tinevez, D. J. White, V. Hartenstein, K. Eliceiri, P. Tomancak, and A. Cardona, "Fiji: an open-source platform for biological-image analysis," *Nature Methods*, vol. 9, pp. 676–682, 2012.

[225] D. Ushizima, D. Parkinson, P. Nico, J. Ajo-Franklin, A. MacDowell, B. Kocar, W. Bethel, and J. Sethian, "Statistical segmentation and porosity quantification of 3D X-ray microtomography," *SPIE Optics and Photonics, Applications of Digital Image Processing XXXIV*, vol. 8135, p. 813502, 2011.

[226] W. Tsai, "Moment-preserving thresolding: A new approach," *Computer Vision, Graphics, and Image Processing*, vol. 29, pp. 377–393, 1985.

[227] D. Ushizima, X. Ke, and P. J. M. Monteiro, "Materials data science for microstructural characterization of archaeological concrete," *MRS Advances*, vol. 5, pp. 305–318, 2020.

[228] C. Li, J. Li, A. Telesca, D. Marchon, K. Xu, M. Marroccoli, Z. Jiang, and P. J. M. Monteiro, "Effect of polycarboxylate ether on the expansion of ye'elimite hydration

in the presence of anhydrite," *Cement and Concrete Research*, vol. 140, p. 106321, 2021.

[229] B. D. A. Levin, Y. Jiang, E. Padgett, S. Waldon, C. Quammen, C. Harris, U. Ayachit, M. Hanwell, P. Ercius, D. A. Muller, and R. Hovden, "Tutorial on the visualization of volumetric data using tomviz," *Microscopy Today*, vol. 26, pp. 12–17, 2018.

[230] S. Withley, R. Halama, R. Gertisser, K. Preece, F. Deegan, and V. Troll, "Magmatic and metasomatic effects of magma–carbonate interaction recorded in calc-silicate xenoliths from Merapi volcano (Indonesia)," *Journal of Petrology*, vol. 61, pp. 1–38, 2020.

[231] M. Barnick, "Structure study of natural wollastonite," *Naturwissenschaften*, vol. 23, p. 770, 1935.

[232] H. Yang and C. T. Prewitt, "Crystal structure and compressibility of a two-layer polytype of pseudowollastonite ($CaSiO_3$)," *American Mineralogist*, vol. 84, pp. 1902–1905, 1999.

[233] T. Yamanaka and H. Mori, "The structure and polytypes of α-$CaSiO_3$ (pseudowollastonite)," *Acta Cryst B*, vol. 37, pp. 1010–1017, 1981.

[234] Y. V. Seryotkin, E. V. Sokol, and S. N. Kokh, "Natural pseudowollastonite: Crystal structure, associated minerals, and geological context," *Lithos*, vol. 134-135, pp. 75–90, 2012.

[235] E. Mazzucato and A. Gualtieri, "Wollastonite polytypes in the CaO-SiO_2 system," *Physics and Chemistry of Minerals*, vol. 27, pp. 565–574, 2000.

[236] H. Wenk, "Polymorphism of wollastonite," *Contributions to Mineralogy and Petrology*, vol. 22, pp. 238–247, 1969.

[237] C. Henmi, I. Kusachi, A. Kawahara, and K. Henmi, "7T wollastonite from Fuka, Okayama prefecture," *Mineralogical Journal*, vol. 9, pp. 169–181, 1978.

[238] C. Henmi, A. Kawahara, K. Henmi, I. Kusachi, and Y. Takeuchi, "The 3T, 4T and 5T polytypes of wollastonite from Kushiro, Hiroshima Prefecture, Japan," *American Mineralogist*, vol. 68, pp. 156–163, 1983.

[239] J. Tolliday, "Crystal structure of β-wollastonite," *Nature*, vol. 82, pp. 1012–1013, 1958.

[240] F. Trojer, "The crystal structure of parawollastonite," *Zeitschrift für Kristallographie*, vol. 127, pp. 291–308, 1968.

[241] K.-F. Hesse, "Refinement of the crystal structure of wollastonite-2M (parawollastonite)," *Zeitschrift für Kristallographie - Crystalline Materials*, vol. 168, pp. 93–98, 1984.

[242] K. Jürgen Buschow, R. Cahn, M. Flemings, B. Ilschner, K. E.J., and S. V. Mahajan, *Ceramic Crystals and Polycrystals, Hardness of Encyclopedia of Materials: Science and Technology.* Elsevier Ltd., 2nd ed., 2001.

[243] P. De Aza, Z. Luklinska, M. Anseau, F. Guitian, and S. De Aza, "Morphological studies of pseudowollastonite for biomedical application," *Journal of Microscopy*, vol. 1182, pp. 24–31, 1996.

[244] P. De Aza, Z. Luklinska, M. Anseau, F. Guitian, and S. De Aza, "Bioeutectic: a new ceramic material for human bone replacement," *Biomaterials*, vol. 18, pp. 1285–1291, 1997.

[245] X. Liu, C. Ding, and P. K. Chu, "Mechanism of apatite formation on wollastonite coatings in simulated body fluids," *Biomaterials*, vol. 25, pp. 1755–1761, 2004.

[246] Y. Min, Q. Li, M. Voltolini, M. Kneafsey, and Y. Jun, "Wollastonite carbonation in water-bearing supercritical CO_2: effects of particle size," *Environmental Science & Technology*, vol. 51, pp. 13044–13053, 2017.

[247] K. Curry *U.S. Geological Survey, Mineral Commodity Summaries. https://pubs.usgs.gov/periodicals/mcs2020/mcs2020-wollastonite.pdf*, 2020.

[248] *https://geologyscience.com/minerals/wollastonite/.*

[249] *Wollastonite Powder Market (Application: Ceramics, Polymers, Paints, Metallurgy, Friction Products, Construction, and Others)-Global Industry Analysis, Size, Share, Growth, Trends, and Forecast, 2020-2030, https://www.transparencymarketresearch.com/wollastonite-powder-market.html.*

[250] H. Wang, Q. Zhang, H. Yang, and H. Sun, "Synthesis and microwave dielectric properties of $CaSiO_3$ nanopowder by the sol–gel process," *Ceramics International*, vol. 34, pp. 1405–1408, 2008.

[251] C.-C. Chen, C.-C. Ho, S.-Y. Lin, and S.-J. Ding, "Green synthesis of calcium silicate bioceramic powders," *Ceramics International*, vol. 41, pp. 5445–5453, 2015.

[252] T. V. Vakalova, V. M. Pogrebenkov, and N. P. Karionova, "Solid-phase synthesis of wollastonite in natural and technogenic siliceous stock mixtures with varying levels of calcium carbonate component," *Ceramics International*, vol. 42, pp. 16453–16462, 2016.

[253] G. C. Serghiou and W. S. Hammack, "Pressure-induced amorphization of wollastonite ($CaSiO_3$) at room temperature," *J. Chem. Phys.*, vol. 98, pp. 9830–9834, 1993.

[254] R. Abd Rashid, R. Shamsudin, M. A. Abdul Hamid, and A. Jalar, "In-vitro bioactivity of wollastonite materials derived from limestone and silica sand," *Ceramics International*, vol. 40, pp. 6847–6853, 2014.

[255] S. Vichaphund, M. Kitiwan, D. Atong, and P. Thavorniti, "Microwave synthesis of wollastonite powder from eggshells," *Journal of the European Ceramic Society*, vol. 31, pp. 2435–2440, 2011.

[256] X. Li and J. Chang, "Synthesis of wollastonite single crystal nanowires by a novel hydrothermal route," *Chemistry Letters*, vol. 33, pp. 1458–1459, 2004.

[257] S. Tränkle, D. Jahn, T. Neumann, L. Nicoleau, N. Hüsing, and D. Volkmer, "Conventional and microwave assisted hydrothermal syntheses of 11$\dot{A}$ tobermorite," *Journal of Materials Chemistry A*, vol. 1, pp. 10318–10326, 2013.

[258] C. Vakifahmetoglu, "Zeolite decorated highly porous acicular calcium silicate ceramics," *Ceramics International*, vol. 40, no. 8, Part A, pp. 11925–11932, 2014.

[259] E. Tajuelo Rodriguez, K. Garbev, D. Merz, L. Black, and I. G. Richardson, "Thermal stability of C-S-H phases and applicability of Richardson and Groves' and Richardson C-(A)-S-H(I) models to synthetic C-S-H," *Cement and Concrete Research*, vol. 93, pp. 45–56, 2017.

[260] T. Noguchi, K. Matsui, N. M. Islam, Y. Hakuta, and H. Hayashi, "Rapid synthesis of γ-Al_2O_3 nanoparticles in supercritical water by continuous hydrothermal flow reaction system," *The Journal of Supercritical Fluids*, vol. 46, pp. 129–136, 2008.

[261] J. Rodríguez-Carvajal, "Fullprof: A program for rietveld refinement and pattern matching analysis," *Abstracts of the Satellite Meeting on Powder Diffraction of the XV Congress of the IUCr*, vol. 192, p. 127, 1990.

[262] H. Arcis, J. P. Ferguson, J. S. Cox, and P. R. Tremaine, "The Ionization Constant of Water at Elevated Temperatures and Pressures: New Data from Direct Conductivity Measurements and Revised Formulations from T = 273 K to 674 K and p = 0.1 MPa to 31 MPa," *Journal of Physical and Chemical Reference Data*, vol. 49, p. 033103, 2020.

[263] P. Florian, F. Fayon, and D. Massiot, "^{2}J Si-O-Si scalar spin-spin coupling in the solid state: crystalline and glassy wollastonite $CaSiO_3$," *Journal of Physical Chemistry C*, vol. 113, pp. 2562–2572, 2009.

[264] A. Sebald, L. Mewin, W. Dollase, and F. Seifert, "A multinuclear, high-resolution solid-state NMR study of sorensenite ($Na_4SnBe_2(Si_3O_9)\cdot 2H_2O$) and comparison with wollastonite and pectolite," *Physics and Chemistry of Minerals*, vol. 17, pp. 9–16, 1990.

[265] R. P. Sreekanth Chakradhar, B. M. Nagabhushana, G. T. Chandrappa, K. P. Ramesh, and J. L. Rao, "Solution combustion derived nanocrystalline macroporous wollastonite ceramics," *Materials Chemistry and Physics*, vol. 95, pp. 169–175, 2006.

[266] S. Palakurthy, V. G. Reddy, R. K. Samudrala, and P. Abdul Azeem, "In vitro bioactivity and degradation behaviour of β-wollastonite derived from natural waste," *Materials Science and Engineering: C*, vol. 98, pp. 109–117, 2019.

[267] H. Ismail, R. Shamsudin, and M. Hamid, "Effect of autoclaving and sintering on the formation of β-wollastonite," *Materials Science and Engineering: C*, vol. 58, pp. 1077–1081, 2016.

[268] C. Paluszkiewicz, M. Blażewicz, J. Podporska, and T. Gumuła, "Nucleation of hydroxyapatite layer on wollastonite material surface: FTIR studies," *Vibrational Spectroscopy*, vol. 48, pp. 263–268, 2008.

[269] B. Buzatu and N. Buzgar, "The raman study of single-chain silicates," *Geologie. Tomul LVI*, pp. 107–125, 2010.

[270] C. K. Ong, S. Ray, R. P. Cooney, N. R. Edmonds, and A. J. Easteal, "Preparation and characterization of composites of polyethylene with polypyrrole-coated wollastonite," *Journal of Applied Polymer Science*, vol. 110, pp. 632–640, 2008.

[271] E. Huang, C. H. Chen, T. Huang, E. H. Lin, and J.-A. Xu, "Raman spectroscopic characteristics of Mg-Fe-Ca pyroxenes," *American Mineralogist*, vol. 85, pp. 473–479, 2000.

[272] S. Shaked, P. Crettaz, M. Saade-Sbeih, O. Jolliet, and A. Jolliet, *Environmental Life Cycle Assessment*. CRC Press, 2015.

[273] "Environmental management-Life cycle assessment- Principles and framework, ISO 14040:2006," *International Organization for Standardization, ISO, Geneva, Switzerland*, 2006.

[274] "Life cycle assessment: Principles and practice," *U.S. Environmental Protection Agency (USEPA)*, 2006.

[275] M. Tsang, G. Philippot, C. Aymonier, and C. Sonnemann, "Anticipatory life-cycle assessment of supercritical fluid synthesis of barium strontium titanate nanoparticles," *Green Chemistry*, vol. 18, pp. 4924–4933, 2016.

[276] M. Tsang, G. Philippot, C. Aymonier, and C. Sonnemann, "Supercritical fluid flow synthesis to support sustainable production of engineered nanomaterials: case study of titanium dioxide," *ACS Sustainable Chemistry & Engineering*, vol. 6, pp. 5142–5151, 2018.

[277] P. Caramazana-González, P. W. Dunne, M. Gimeno-Fabra, M. Zilka, M. Ticha, B. Stieberova, F. Freiberg, J. McKechnie, and E. H. Lester, "Assessing the life cycle environmental impacts of titania nanoparticle production by continuous flow solvo/hydrothermal syntheses," *Green Chemistry*, vol. 19, pp. 1536–1547, 2017.

[278] P. P. Kalbar, I. Muñoz, and M. Birkved, "WW LCI v2: A second-generation life cycle inventory model for chemicals discharged to wastewater systems," *Science of The Total Environment*, vol. 622-623, pp. 1649–1657, 2018.

[279] B. Pillain, P. Loubet, F. Pestalozzi, J. Woidasky, A. Erriguible, C. Aymonier, and G. Sonnemann, "Positioning supercritical solvolysis among innovative recycling and current waste management scenarios for carbon fiber reinforced plastics thanks to comparative life cycle assessment," *The Journal of Supercritical Fluids*, vol. 154, p. 104607, 2019.

[280] H. Hobbs, S. Briddon, and E. Lester, "The synthesis and fluorescent properties of nanoparticulate ZrO_2 doped with Eu using continuous hydrothermal synthesis," *Green Chemistry*, vol. 11, pp. 484–491, 2009.

[281] E. Moreno-Ruiz, L. Valsasina, F. Brunner, A. Symeonidis, D. FitzGerald, K. Treyer, G. Bourgault, and W. G., "Documentation of changes implemented in ecoinvent database v3.5," *Ecoinvent, Zürich, Switzerland.*, 2018.

[282] G. Wernet, C. Bauer, B. Steubing, J. Reinhard, E. Moreno-Ruiz, and B. Weidema, "The ecoinvent database version 3 (part I): overview and methodology," *International Journal of Life Cycle Assessment*, vol. 21, pp. 1218–1230, 2016.

[283] M. A. J. Huijbregts, Z. J. N. Steinmann, P. M. F. Elshout, G. Stam, F. Verones, M. Vieira, M. Zijp, A. Hollander, and R. van Zelm, "ReCiPe2016: a harmonised life cycle impact assessment method at midpoint and endpoint level," *The International Journal of Life Cycle Assessment*, vol. 22, pp. 138–147, 2017.

[284] "Environmental management-Life cycle assessment-requirements and guidlines, ISO 14044:2006," *International Organization for Standardization, ISO, Geneva, Switzerland*, 2006.

[285] "Environmental management-Life cycle assessment- Life cycle impact assessment, ISO 14042:2002," *International Organization for Standardization, ISO, Geneva, Switzerland*, 2002.

[286] D. W. Pennington, J. Potting, G. Finnveden, E. Lindeijer, O. Jolliet, T. Rydberg, and G. Rebitzer, "Life cycle assessment Part 2: Current impact assessment practice," *Environment International*, vol. 30, pp. 721–739, 2004.

[287] J. Bare, P. Hofstetter, D. Pennington, and H. Udo de Haes, "Midpoints versus endpoints: The sacrifices and benefits," *The International Journal of Life Cycle Assessment*, vol. 5, pp. 319–326, 2012.

[288] J. Reap, F. Roman, S. Duncan, and B. Bras, "A survey of unresolved problems in life cycle assessment part 1: goal and scope and inventory analysis," *The International Journal of Life Cycle Assessment*, vol. 13, pp. 290–300, 2008.

List of Tables

List of Figures